UNIVERSIDADE DE LISBOA
FACULDADE DE CIÊNCIAS

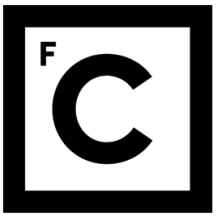

Ciências
ULisboa

Harmonization of Remote Sensing Land Surface Products: correction of clear-sky bias and characterization of directional effects

Doutoramento em Ciências Geofísicas e da Geoinformação
Especialidade de Deteção Remota

Sofia Nunes Lorena Ermida

Tese orientada por:
Professor Doutor Carlos da Camara, Doutora Isabel Trigo e Doutora Catherine Prigent

Documento especialmente elaborado para a obtenção do grau de doutor

2018

UNIVERSIDADE DE LISBOA

FACULDADE DE CIÊNCIAS

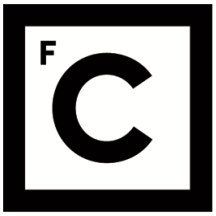

Ciências
ULisboa

Harmonization of Remote Sensing Land Surface Products: correction of clear-sky bias and characterization of directional effects

Doutoramento em Ciências Geofísicas e da Geoinformação

Especialidade de Deteção Remota

Sofia Nunes Lorena Ermida

Tese orientada por:

Professor Doutor Carlos da Camara, Doutora Isabel Trigo e Doutora Catherine Prigent

Júri:

Presidente:

- Doutor João Manuel de almeida Serra, Professor Catedrático, Faculdade de Ciências da Universidade de Lisboa

Vogais:

- Doutora Catherine Prigent, *Senior Research Scientist*, *Laboratoire d'Etudes du Rayonnement et de la Matière en Astrophysique et Atmosphères – Lerma, Unité de Recherche do Centre National de la Recherche Scientifique – CNRS*, França
- Doutor Leonardo de Faria Peres, Professor Adjunto, Instituto de Geociências da Universidade Federal do Rio de Janeiro, Brasil
- Doutora Maria João Costa, Professora Auxiliar, Escola de Ciências e Tecnologia da Universidade de Évora
- Doutor Pedro Manuel Alberto de Miranda, Professor Catedrático, Faculdade de Ciências da Universidade de Lisboa
- Doutor Emanuel Nemésio de Sousa Dutra, Investigador FCT "nível inicial", Faculdade de Ciências da Universidade de Lisboa

Documento especialmente elaborado para a obtenção do grau de doutor

Doutoramento financiado pela Fundação para a Ciência e a Tecnologia (SFRH/BD/96466/2013)

2018

Acknowledgments

First, I would like to express my sincere gratitude to my supervisors for guiding and supporting me throughout this process.

My most sincere thank you to Prof. Carlos da Camara for being always available and supportive during this PhD, in both personal and work-related subjects. I'll forever be grateful for the patience, trust, friendship and knowledge that he shared, making me better at the professional and personal level. This thesis would not be possible without his support.

To Dr. Isabel Trigo a most felt thank you for motivating and incentivizing my work, pushing me to grow and become a better scientist/researcher. Thank you for all the shared knowledge and constructive criticism, and for the trust bestowed in me in all the activities that were carried out within this PhD.

A sincere thank you to Dr. Catherine Prigent for welcoming me and for the shared knowledge that was imperative for the achievement of the goals of this PhD. Thank you for being a teacher and a mentor and for the continuous support and motivation.

Secondly, I'll would like to give a special thank you to my closest friends. A big heartfelt thank you to the friends that have been with me for a long time Catarina Morgado, Mariana Morgado, Joana Morgado, Vânia Silva e Rita Vinagre. Thank you all for the support and friendship, sometimes close and sometimes far away, but nonetheless important. A huge thank you to my goofy friends Andreia Ribeiro e André Amaral. I'm very grateful for all the amazing moments (and the simple ones too) that we have shared.

I would also like to thank all the colleagues at FCUL with whom I've shared discussions, lunch breaks and for all the fun we had in these past years. Thank you to Carlos Jiménez for welcoming me at the Observatoire de Paris and for all the valuable contributions for the research carried out in this PhD. I would also like to thank the team at JPL, Glynn Hulley, Simon Hook and Kerry Cawse-Nicholson, for welcoming me and for all the support and shared knowledge.

Finally, a special thank you to my family, in particular to my parents that have supported and encouraged me to follow my passion and have helped me achieve all my goals, including this PhD.

This PhD was supported by the Portuguese Science Foundation (FCT) through the following grant: SFRH/BD/96466/2013. Research conducted at JPL was partially supported by a Fulbright Research grant.

Abstract

Land surface temperature (LST) is the mean radiative skin temperature of an area of land resulting from the mean energy balance at the surface. LST is an important climatological variable and a diagnostic parameter of land surface conditions, since it is the primary variable determining the upward thermal radiation and one of the main controllers of sensible and latent heat fluxes between the surface and the atmosphere. The reliable and long-term estimation of LST is therefore highly relevant for a wide range of applications, including, amongst others: (i) land surface model validation and monitoring; (ii) data assimilation; (iii) hydrological applications; and (iv) climate monitoring.

Remote sensing constitutes the most effective method to observe LST over large areas and on a regular basis. Satellite LST products generally rely on measurements in the thermal infrared (IR) atmospheric window, i.e., within the 8-13 micrometer range. Beside the relatively weak atmospheric attenuation under clear sky conditions, this band includes the peak of the Earth's spectral radiance, considering surface temperature of the order of 300K (leading to maximum emission at approximately 9.6 micrometer, according to Wien's Displacement Law). The estimation of LST from remote sensing instruments operating in the IR is being routinely performed for nearly 3 decades. Nevertheless, there is still a long list of open issues, some of them to be addressed in this PhD thesis.

First, the viewing position of the different remote sensing platforms may lead to variability of the retrieved surface temperature that depends on the surface heterogeneity of the pixel – dominant land cover, orography. This effect introduces significant discrepancies among LST estimations from different sensors, overlapping in space and time, that are not related to uncertainties in the methodologies or input data used. Furthermore, these directional effects deviate LST products from an ideally defined LST, which should correspond to the ensemble directional radiometric temperature of all surface elements within the FOV. In this thesis, a geometric model is presented that allows the upscaling of in situ measurements to the any viewing configuration. This model allowed generating a synthetic database of directional LST that was used consistently to evaluate different parametric models of directional LST. Ultimately, a methodology is proposed that allows the operational use of such parametric models to correct angular effects on the retrieved LST.

Second, the use of infrared data limits the retrieval of LST to clear sky conditions, since clouds "close" the atmospheric window. This effect introduces a clear-sky bias in IR LST datasets that is difficult to quantify since it varies in space and time. In addition, the cloud clearing requirement severely limits the space-time sampling of IR measurements. Passive microwave (MW) measurements are much less affected by clouds than IR observations. LST estimates can in principle be derived from MW measurements, regardless of the cloud conditions. However, retrieving LST from MW and matching those estimations with IR-derived values is challenging and there have been only a few attempts so far. In this thesis, a methodology is presented to retrieve LST from passive MW observations. The MW LST dataset is examined comprehensively against in situ measurements and multiple IR LST products. Finally, the MW LST data is used to assess the spatial-temporal patterns of the clear-sky bias at global scale.

Keywords: Land surface temperature, directional effects, LST anisotropy, parametric models, microwave observations, microwave LST, clear-sky bias

Resumo

Os mecanismos de transporte de energia na atmosfera são variados, mas a temperatura é uma variável comum a todos. Com exceção da componente de irradiância solar, a maioria dos fluxos na interface superfície-atmosfera apenas podem ser parametrizados usando a temperatura de superfície. A temperatura de superfície do solo (geralmente abreviada LST do inglês *Land Surface Temperature*) constitui a melhor aproximação à temperatura termodinâmica da superfície de Terra, controlando a troca de radiação de longo comprimento de onda e de fluxos turbulentos de calor na interface superfície-atmosfera. Por esta razão, a LST é um dos parâmetros mais importantes na caracterização dos processos físicos no balanço de energia e água à superfície e como tal é extensivamente utilizada numa grande variedade de áreas de estudo, incluindo evapotranspiração, alterações climáticas, ciclo hídrico, monitorização da vegetação, clima urbano e estudos ambientais, entre outros.

Tendo em conta a elevada heterogeneidade da superfície do solo, a LST varia fortemente no espaço e no tempo e, portanto, a sua correta descrição espácio-temporal requer medições com elevado detalhe tanto no espaço como no tempo. Como a obtenção da LST a partir de estações é impraticável em áreas extensas, a deteção remota representa o meio mais eficaz de monitorizar a LST, uma vez que, esta pode fornecer estimativas globais de uma forma uniforme.

Quando os sistemas a ser estudados são complexos ou heterogéneos, é comum surgirem diferentes definições de temperatura. Dada a complexidade de superfícies naturais como o solo ou vegetação, as definições a serem utilizadas devem ter em conta as heterogeneidades inerentes. A temperatura de superfície obtida por deteção remota, nomeadamente usando plataformas no solo, no ar ou no espaço, é uma temperatura radiométrica. Se a superfície é heterogenia e não isotérmica (o que é em geral o caso na deteção remota), essa temperatura radiométrica corresponde ao conjunto das temperaturas radiométricas das diferentes componentes a serem observadas (por exemplo, solo, vegetação, edifícios). É também, por definição, uma temperatura de pele (do inglês *skin temperature*), ou seja, é a temperatura da camada do meio com espessura igual à profundidade de penetração da radiação a um dado comprimento de onda. Consequentemente, a temperatura radiométrica difere fisicamente de outras definições de temperatura, tal como a temperatura termodinâmica que é a temperatura comumente medida por um termómetro. A interpretação física e a medição de uma temperatura radiométrica requerem o conhecimento da natureza da radiação e como esta interage com a matéria.

Qualquer corpo com uma temperatura diferente do zero absoluto (0 K) irradia energia sob a forma de radiação eletromagnética. A radiação emitida por um corpo em função da temperatura e comprimento de onda pode ser obtida através de lei de Planck. Consequentemente, a temperatura de um corpo pode ser obtida através de medições da radiação emitida pelo corpo num dado comprimento de onda. Para o intervalo de temperaturas geralmente observadas na Terra (250-330 K), o pico de emissões encontra-se na zona do espectro do infravermelho térmico (8.8-11.6 μm), tornando esta zona particularmente útil para a deteção remota da temperatura.

A lei de Planck foi formulada para relacionar temperatura e emissões de um corpo negro. Um corpo negro é uma superfície idealizada que tem a propriedade de absorver toda a radiação que nela incide, ou seja, a sua refletividade é nula e a absortividade é máxima. As superfícies naturais não são corpos negros e, portanto, para uma dada temperatura emitem menos do que um corpo negro emitiria. A emissividade espectral é definida como a razão entre a radiância emitida por uma dada superfície e a que seria emitida por um corpo negro à mesma temperatura, sendo por isso uma propriedade da superfície. A emissividade é uma propriedade extramente relevante na deteção remota, uma vez que, a maioria dos algoritmos requer um conhecimento da emissividade da superfície a ser observada.

Para além disso, como os sensores utilizados para realizar medições da radiação emitida pela superfície em geral se encontram afastados da mesma, a radiação que chega ao sensor é afetada, não só pelas emissões da superfície, como também pelas perdas e ganhos que ocorrem quando essa

radiação atravessa a atmosfera. Assim, as principais componentes que contribuem para a radiação que chega ao sensor são: a radiação emitida pela atmosfera na direção do sensor, a radiação emitida pela atmosfera na direção da superfície e que é refletida na direção do sensor e a radiação emitida pela superfície, sendo que estes dois últimos termos são atenuados ao atravessar a atmosfera. A combinação destes termos pode é descrita pela chamada equação de transferência radiativa. Esta é a equação que deve ser resolvida de forma a obter a LST. Apesar da contribuição atmosférica ser pequena comparada com a contribuição da superfície, a correta caracterização da LST depende da correta separação dos diferentes termos acima descritos.

A temperatura medida por deteção remota corresponde à combinação das temperaturas das diferentes superfícies que são observadas pelo sensor. Como tal, variações nas proporções observáveis das diferentes superfícies podem levar a variações na LST. Nesse caso, a anisotropia da LST depende não só da estrutura e localização dos diferentes componentes da superfície em relação uns aos outros, mas também os contrastes de temperatura entre os diferentes componentes. Por exemplo, no caso de uma superfície por árvore dispersas, árvore o solo ao sol e o solo à sombra terão diferentes temperaturas. Consoante a posição do satélite em relação ao sol, as proporções de solo ao sol e sombra e árvore que são observadas irão variar e, portanto, a LST obtida depende da posição do satélite. À escala das componentes individualmente, podem também existir efeitos direcionais associados à emissividade.

A zona espectral do infravermelho próximo é a mais utilizada em deteção remota por corresponder ao pico de emissões na gama de temperaturas comuns na Terra. No entanto, apesar de mais fracas, as emissões na zona das micro-ondas são suficientemente fortes para serem detetadas por sensores no espaço. Devido ao comprimento de onda mais longo, as emissões nas micro-ondas estão associadas a menos energia que no infravermelho. Ao mesmo tempo, o comprimento de onda longo significa que a radiação emitida pela Terra não interage significativamente com a atmosfera e, para os comprimentos de onda mais longos, a dispersão por gotículas de água pode ser desprezada. Isto significa que a superfície da Terra pode ser observada nos comprimentos de onda das micro-ondas mesmo quando há nebulosidade.

As observações de micro-ondas podem, portanto, ser utilizadas para obter a LST sob quase todas as condições atmosféricas, ao contrário do infravermelho que só pode ser utlizado com céu limpo. Como consequência, estudo climáticos baseados em LST obtida do infravermelho são provavelmente afetados pelo o uso limitado a céu limpo. No entanto, este "viés de céu limpo" nunca foi quantificado e o seu verdadeiro impacto em diferentes aplicações não é conhecido.

Esta tese visa os dois pontos em aberto na deteção remota da LST referidos acima: 1) a correta caracterização, e eventual correção, dos efeitos direcionais observados na LST e 2) a análise e quantificação do viés de céu limpo através do uso de LST obtida em quais condições atmosféricas.

Para a caracterização dos efeitos direcionais na LST, um modelo geométrico foi desenvolvido que permite combinar observações *in situ* e estimar a LST que seria observada para uma dada posição do satélite. Este modelo permite gerar uma base de dados sintéticas de LST direcional e que pode ser usada para avaliar modelos paramétricos. Os modelos paramétricos são modelos que descrevem a assinatura direcional de uma dada variável usando formulações matemáticas numa forma simplificada – são modelos estatísticos. Dada a sua simplicidade, são vantajosos em relação aos modelos físicos porque são computacionalmente mais eficientes e requerem menos dados de input, tornando-os particularmente apropriados para uma utilização operacional. Nesta tese, a utilização de diferentes tipos de modelos paramétricos é analisada em detalhe e são propostas metodologias de calibração e aplicação desses modelos.

Com o objetivo de quantificar o viés de céu limpo, nesta tese é apresentada uma metodologia que permite obter a LST a partir de observações efetuadas na zona das micro-ondas. Esta metodologia consiste na utilização de redes-neuronais previamente calibradas com dados e LST de infravermelho. A LST de micro-ondas obtida com este método é então analisada em detalhe por comparação com

medições *in situ* e com LST obtida de diferentes sensores que executam medições no infravermelho. Finalmente, esta base de dados de LST de micro-ondas é utilizada para analisar os padrões espácio-temporais do viés de céu limpo.

Palavras-chave: temperatura de superfície do solo, efeitos direcionais, anisotropia da temperatura de superfície, modelos paramétricos, medições de micro-ondas, viés de céu limpo

Contents

List of Acronyms and Abbreviations

GMASI	Global Multisensor Automated Snow and Ice
AATSR	Advanced Along-Track Scanning Radiometer
AHI	Advanced Himawari Imager
AMSR-E	Advanced Microwave Scanning Radiometer – Earth observation system
BRDF	Bidirectional Reflectance Distribution function
CDR	Climate Data Record
DJF	December-January-February
DEM	Digital Elevation Model
ERS	European Remote Sensing
FOV	Field of view
FVC	Fraction of Vegetation Cover
GO	Geometrical optical
GORT	Geometrical-optical radiative transfer
GOES	Geostationary Operational Environmental Satellites
GEO	Geostationary satellite
GIEMS	Global Inundation Extension from Multi-Satellites
GLOBE	Global Land One-km Base Elevation Project
IR	Infrared
IGBP	International Geosphere-Biosphere Program
ITCZ	Intertropical Convergence Zone
JMA	Japanese Meteorological Association
JAMI	Japanese Meteorological Imager
JJA	June-July-August
KIT	Karlsruhe Institute of Technology
LSE	Land Surface Emissivity
LST	Land Surface Temperature
LAI	Leaf Area Index
LEO	Low Earth Orbit
MAM	March-April-May
MSE	Mean Square Error
MSG	Meteosat Second Generation
MW	Microwave
MODIS	Moderate Resolution Imaging Spectroradiometer
MERRA-2	Modern-Era Retrospective analysis for Research and Applications, Version 2
MTSAT	Multifunction Transport SATellite
NESDIS	National Environmental Satellite, Data, and Information Service
NPP	National Polar-orbiting Partnership
PTC	Percentage of Tree Cover
RT	Radiative transfer
RMSD	Root Mean Square Differences
RMSE	Root Mean Square Error
LSA-SAF	Satellite Application Facility on Land Surface Analysis
SON	September-October-November

SWE	Snow Water Equivalent
SSM/I	Special Sensor Microwave Imager
SEVIRI	Spinning Enhanced Visible and Infrared Imager
STD	Standard deviation
TES	Temperature Emissivity Separation
TIR	Thermal infrared
TOA	Top of the atmosphere
TCWV	Total Column Water Vapour
VZA	View Zenith Angle
VIIRS	Visible Infrared Imaging Radiometer Suite

List of Symbols

A	Emissivity kernel coefficient
$\bar{A}$	Average projected area of an object
B	Kernel-Hotspot model coefficient
B_λ	Spectral radiance
b	Average canopy vertical radius
c	Speed of light
D	Solar kernel coefficient
d	Hemispherical distance
F	Percentage of illuminated surface
F_{sunlit}, F_{shadow}, F_{canopy}	Sunlit background, shaded background and canopy fractions
H	Average height of crown center
h	Planck constant
K	Hotspot model coefficient
k	Boltzmann constant
L_λ	Spectral radiance
$L_{\mathrm{at}_\lambda\downarrow}$, $L_{\mathrm{at}_\lambda\uparrow}$	Atmosphere-emitted downward and upward radiances
L_{avg}	Average within pixel radiance
$L_{\mathrm{diff}_\lambda\downarrow}$, $L_{\mathrm{diff}_\lambda\uparrow}$	Solar diffused downward and upward radiances
L_{s_λ}	Solar spectral radiance
L_{sunlit}, L_{shadow}, L_{canopy}	Sunlit background, shaded background and canopy radiances
L_{sfc}	Composite radiance of the pixel
L_{sky}	Radiance measured by the sky-facing radiometer
q	Gap probability function
R	Average canopy horizontal radius
Rad^*_{TOA}	Daily TOA radiation normalized by the daily solar constant
T	Temperature
T_0, T_H	Surface temperature at nadir and at the hotspot
Tb	Brightness temperature
T_{skin}	Surface skin temperature
α	Coefficient of the soil emissivity model
ΔT_H	Hotspot model coefficient
ε_λ	Spectral emissivity
ε_0	Emissivity at nadir
ε_{eff}	Effective emissivity of the pixel
ζ	Density of object centers
θ_i, θ_v	Sun and satellite view zenith angle
θ_s	Mountain slope
Λ	Amplitude of cycle
λ	wavelength
ρ_λ	Bi-directional spectral reflectivity
σ	Standard deviation
σ_0	Microwave backscattering coefficient

τ_λ	Spectral transmittance
Φ	Emissivity kernel
ϕ_i, ϕ_v	Sun and satellite view zenith angle
ϕ_s	Mountain aspect
χ	Phase of cycle
Ψ	Solar kernel
ω	Frequency of cycle

List of Figures

List of Tables

CHAPTER 1

INTRODUCTION

CONTENTS

1. Introduction

There are different mechanisms for heat transport in the atmosphere, and temperature is a common variable amongst all. Except for solar irradiance components, most of the fluxes at the surface-atmosphere interface can only be parameterized using surface temperature. Land surface temperature (LST) provides the best approximation to the thermodynamic temperature of the Earth's surface, controlling the exchange of longwave radiation and turbulent heat fluxes at the surface-atmosphere interface. For this reason, it is one of the most important parameters characterizing physical processes of surface energy and water balance. It is also a relevant diagnostic parameter of land surface conditions. As such, LST is widely used in a variety of fields including evapotranspiration, climate change, hydrological cycle, vegetation monitoring, urban climate and environmental studies, among others (Kerr et al., 2004; Li et al., 2013).

Given the high heterogeneity of land surface features, LST changes rapidly in space and time and its correct space-temporal description requires, therefore, measurements with detailed spatial and temporal samplings. As it is impractical to obtain LST values from ground measurements over wide areas, remote sensing constitutes the most effective means to monitor LST since it can provide global and uniform estimates.

Different definitions of temperature tend to arise when dealing with complex or heterogeneous systems. Given the complexity of natural surfaces such as soil or vegetation, usable definitions must accommodate the inherent heterogeneities (Norman and Becker, 1995).

When retrieving land surface temperature by remote sensing technologies, namely using ground-based, airborne and space-borne platforms, the obtained variable is a *radiometric temperature*. If the surface is heterogeneous and non-isothermal, which is the general case for remote sensing, it corresponds to an ensemble radiometric temperature of the components within the field of view (e.g. vegetation and soil). It is also by definition a *skin temperature*, i.e. the temperature of a layer of medium with depth equal to the penetration depth of radiation at the given wavelengths (Norman and Becker, 1995). Therefore, radiometric temperature physically differs from other definition of temperatures, such as the thermodynamic temperature defined for a medium in thermal equilibrium and measured by a thermometer. Both the physical understanding of radiometric temperature and of its retrieval require knowing about the nature of radiation and how it interacts with matter.

1.1 Fundamentals of thermal land surface remote sensing

THERMODYNAMIC TEMPERATURE

From the point of view of thermodynamics, a working definition of temperature is obtained as a consequence of the Zeroth Law (Steane, 2016). Two systems are said to be unequal in temperature if there is a heat interaction when they are brought into contact. When they reach equilibrium and the interaction ceases, then the systems are said to be equal in temperature. According to the Zeroth Law, all systems in thermal equilibrium with a given one form an equivalence class whose common temperature may therefore be attributed by means of a prototype system called a thermometer (Hatsopoulos and Keenan, 1965).

Results from experiments indicate that the *absolute zero*, i.e. the temperature at which the volume of a given gas is null, does not depend on the value of the constant pressure and on the nature of the gas. *Absolute temperature* may then be defined based on the absolute zero and a reproducible temperature level. The SI scale of temperature is the Kelvin scale that uses the triple point of water (273.16 K) as the reproducible temperature level (Hatsopoulos and Keenan, 1965).

From a microscopic point of view, temperature has to do with the kinetic energy of the molecules. In the case of an ideal gas, the *kinetic temperature* is proportional to the average translational kinetic energy of the molecules (Schroeder, 2000).

BLACKBODY RADIATION

According to Prévost's principle of exchange if a body at a temperature greater than 0 K is placed in surroundings at the same temperature as itself, its temperature does not change; however, the body radiates energy in the form of electromagnetic radiation at the same rate as it receives energy from its surroundings (Gray et al., 1974).

One of the most important definitions of radiometric remote sensing is the formula for spectral emission from a blackbody radiator. A blackbody is an idealized surface that has the property of absorbing all the radiation impinging upon it, i.e., the reflectivity and transmissivity are zero and the absorptivity is one. The spectral radiance, $B_\lambda(T)$, emitted by a blackbody in thermal equilibrium is completely determined by its absolute temperature T according to Planck's law (Li et al., 2013):

$$B_\lambda(T) = \frac{2hc^2}{\lambda^5(e^{\frac{hc}{k\lambda T}} - 1)} \tag{1.1.1}$$

where $k = 1.3806 \times 10^{-23} JK^{-1}$ is the Boltzmann constant, $h = 6.6261 \times 10^{-34} Js$ is the Planck constant and $c = 2.9979 \times 10^{8} ms^{-1}$ is the speed of light. Besides being a perfect absorber, a blackbody in thermal equilibrium is also a perfect emitter, i.e. it emits more radiance than any non-blackbody radiator in thermal equilibrium at the same temperature, and it's a perfect diffuser, i.e., emits radiation isotropically in all directions. Since for long wavelengths $hc/k\lambda T \ll 1$ and therefore $e^{\frac{hc}{k\lambda T}} \approx 1 + \frac{hc}{k\lambda T}$, Planck's law may be approximated by Rayleigh-Jeans law:

$$B_\lambda(T) = \frac{2ckT}{\lambda^4} \tag{1.1.2}$$

i.e. the spectral radiance of a blackbody for long wavelengths is directly proportional to the temperature. The above approximation is very useful in the microwave (MW) domain; it is mathematically simpler than Planck's law and yet its fractional deviation from Planck's expression is less than 1% if $\lambda T > 0.77\text{mK}$, which for a temperature of 300 K corresponds to $\lambda > 2.57\text{mm}$ (Ulaby et al., 1981).

The wavelength corresponding to the maximum intensity of blackbody radiation ($\lambda_{\max}$) is inversely proportional to the temperature, as given by Wien's displacement law:

$$T\lambda_{\max} = 2897.9 \text{ K } \mu\text{m} \tag{1.1.3}$$

Following this equation, for the range of surface temperatures observed on Earth (approximately 250-330 K), the maximum emission occurs between 8.8-11.6 μm (Figure 1.1.1). The wavelength region between 8 and 13 μm is often called the Thermal Infrared (TIR) region and is particularly useful for remote sensing of the temperature (Li et al., 2013).

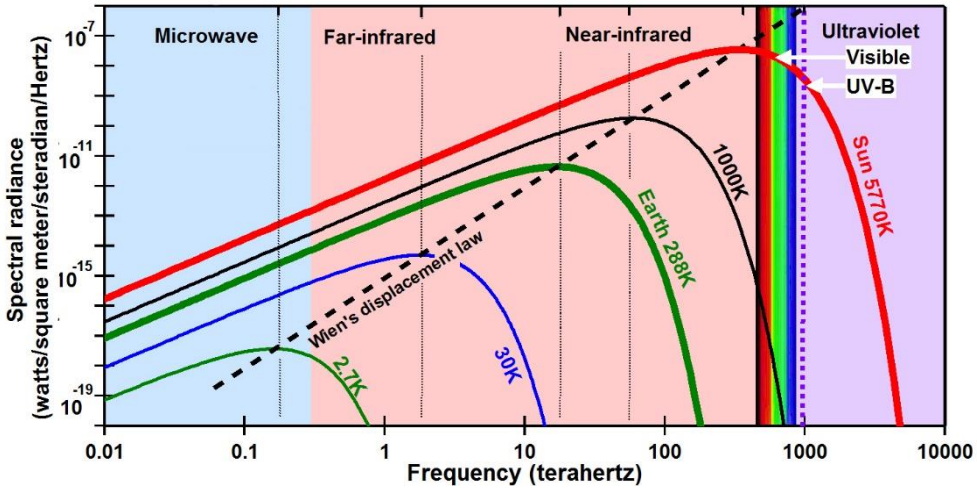

Figure 1.1.1 – Spectral radiance as function of frequency given by Planck's law for bodies of different temperatures (in http://ozonedepletiontheory.info)

NON-BLACKBODY RADIATION

Natural objects are not blackbody radiators (often referred to as grey bodies) and therefore when in thermodynamic equilibrium they emit less spectral radiance than a blackbody does at the same temperature, and do not necessarily absorb all the energy incident upon them. Spectral emissivity, ε_λ, of a given surface is defined as the ratio of spectral radiance emitted by the surface to the spectral radiance of a blackbody in thermal equilibrium at the same temperature of the body (Schott, 2007).

The *brightness temperature* of an object is a fictitious temperature that is defined as the temperature of a blackbody that in thermal equilibrium would emit the same spectral radiance as the object. Since spectral emissivity in general depends on wavelength, direction of emitted radiation and polarization, the same will happen with brightness temperature.

In the general case of heterogeneous and non-isothermal surfaces, it is possible to define a bulk temperature that is measurable from space and is related to the surface heat fluxes. Based on brightness temperature measurements, this temperature, referred to as *radiometric temperature*, depends on the distributions of surface temperature and emissivity, as well as on the channel used to measure it (Becker and Li, 2009). In the case of small variations within the pixel of the surface emissivity and surface temperature, then the radiometric temperature is equivalent to the average of surface temperatures within this pixel.

As pointed out, emissivity is a directional quantity and most natural surfaces are anisotropic emitters. Therefore, different emissivities can be defined for a surface, depending on the effects considered. The spectral dependence of emissivity is usually accounted for in algorithms for LST retrieval. The more complex angular dependence, however, is not.

Experimental studies show that for homogeneous surfaces like water, bare soils, sand and clay the emissivity decreases with view zenith angle (García-Santos et al., 2012; Labed and Stoll, 1991; Sobrino and Cuenca, 1999). However, at the scale of satellite observations, this is not always the case.

For instance, surface roughness modifies the angular dependence of such surfaces. For the general case of a rough boundary, the radiation emitted by the natural surface will partly be scattered as diffuse radiation in all directions (Figure 1.1.2). The rougher the surface, the larger the diffusely scattered portion will be, with the roughness of the surface depending on the wavelength being detected. In these cases, the term surface scattering is used to describe the transfer of energy across the boundary between two dissimilar media (Ulaby et al., 1981). The scatter behavior of rough surfaces has been intensively studied in terms of reflectivity, that is of particular interest when treating the albedo (visible bands) and for MW active methods. Although this effect was less studied in the case

of the emissivity, the same principles may be applied (Pampaloni and Paloscia, 2000; Schanda, 1986; Ulaby et al., 1981). Indeed, modeling studies show that the rugosity of the surface tends to attenuate the angular dependence of emissivity, and for surfaces covered by grass or dense canopy, this dependence is negligible (Sobrino et al., 2005).

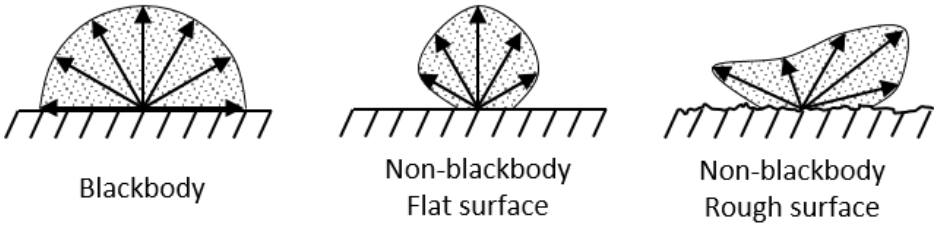

Figure 1.1.2 – Specular and rough surface emission (adapted from Ulaby et al., 1981).

Moreover, since the sensed area is usually quite heterogeneous, geometric effects may also occur. The effective emissivity of a heterogeneous area will be then a combination of the emissivities of the different components of the scene. A change in viewing geometry that results in a change in the observed amount of each of the components will change the effective emissivity of the area (Ren et al., 2011; Sobrino et al., 2005).

Furthermore, when performing observations in the MW region of the spectrum, it is also important to consider emissivity dependence on the dielectric properties of the material and the polarization of the detector. In the MW range, emissivity is inversely proportional to the relative permittivity (or dielectric constant) of the surface. This is particularly relevant because there is a high contrast between the relative permittivity of soil/rock materials (that generally present very low values, in the range 1-4) and that of liquid water (that presents high values: about 30 for frequencies around 30 GHz, reaching 80 for frequencies around 3 GHz). This means that, unlike IR emissivity, MW emissivity will be highly sensitive to soil water content (Ulaby et al., 1986).

These effects may be critical in the remote sensing of surface temperature because most algorithms require an a priori estimation of the surface emissivity. Therefore, a correct simulation of these effects will directly impact the accuracy of the retrieved LST (Li et al., 2013).

PROPAGATION OF RADIATION

As discussed in the previous sections, the temperature of a given object may be retrieved from the emitted radiation making use of Planck's law together with the appropriate emissivity. However, the radiation reaching a remote sensor is affected not only by the emitted radiation from the surface, but also by all gains and losses that occur within the intervening atmosphere as a result of attenuation and scattering effects. The scheme in Figure 1.1.3 summarizes the different contributions to the radiation reaching a remote sensor, for a cloud-free atmosphere under local thermodynamic equilibrium. The spectral radiance at the sensor may be described by the radiative transfer equation, given by

$$L_\lambda = \{L_{s_\lambda} \cos(\theta_i)\, \tau_\lambda(\theta_i, \phi_i)\rho_\lambda(\theta_v, \phi_v, \theta_i, \phi_i) + \varepsilon_\lambda(\theta_v, \phi_v)B_\lambda(T_{\text{skin}}) + [1 - \varepsilon_\lambda(\theta_v, \phi_v)]\left(L_{\text{diff}_\lambda\downarrow} + L_{\text{at}_\lambda\downarrow}\right)\}\tau_\lambda(\theta_v, \phi_v) + L_{\text{diff}_\lambda\uparrow} + L_{\text{at}_\lambda\uparrow} \quad (1.1.4)$$

where (θ_i, ϕ_i) are the sun zenithal and azimuthal angles and (θ_v, ϕ_v) are the sensor zenithal and azimuthal angles. L_{s_λ} is the solar spectral radiance at the top of the atmosphere (TOA), τ_λ is the effective spectral transmittance of the atmosphere and ρ_λ is the bi-directional reflectivity of the surface. The first term on the right hand side corresponds to the direct solar radiance reflected by the surface (path 1 of Figure 1.1.3). ε_λ and T_{skin} are the effective spectral surface emissivity and

temperature. $\varepsilon_\lambda(\theta_v, \phi_v)B_\lambda(T_{\text{skin}})$ represents the radiance emitted directly by the surface (path 2 of Figure 1.1.3). $L_{\text{diff}_\lambda\downarrow}$ and $L_{\text{at}_\lambda\downarrow}$ correspond to the downward radiance that is reflected by the surface, the first representing solar diffusion radiance and the second the atmospheric emitted radiance (paths 3 and 4 of Figure 1.1.3, respectively). Here the surface reflectivity was replaced by $[1 - \varepsilon_\lambda(\theta_v, \phi_v)]$ by assuming that the downward atmospheric and solar diffuse radiation are isotropic (Li et al., 2013). $L_{\text{diff}_\lambda\uparrow}$ and $L_{\text{at}_\lambda\uparrow}$ represent the solar diffusion radiance and the atmospheric emitted radiance, respectively, that propagate upward (paths 5 and 6 of Figure 1.1.3, respectively).

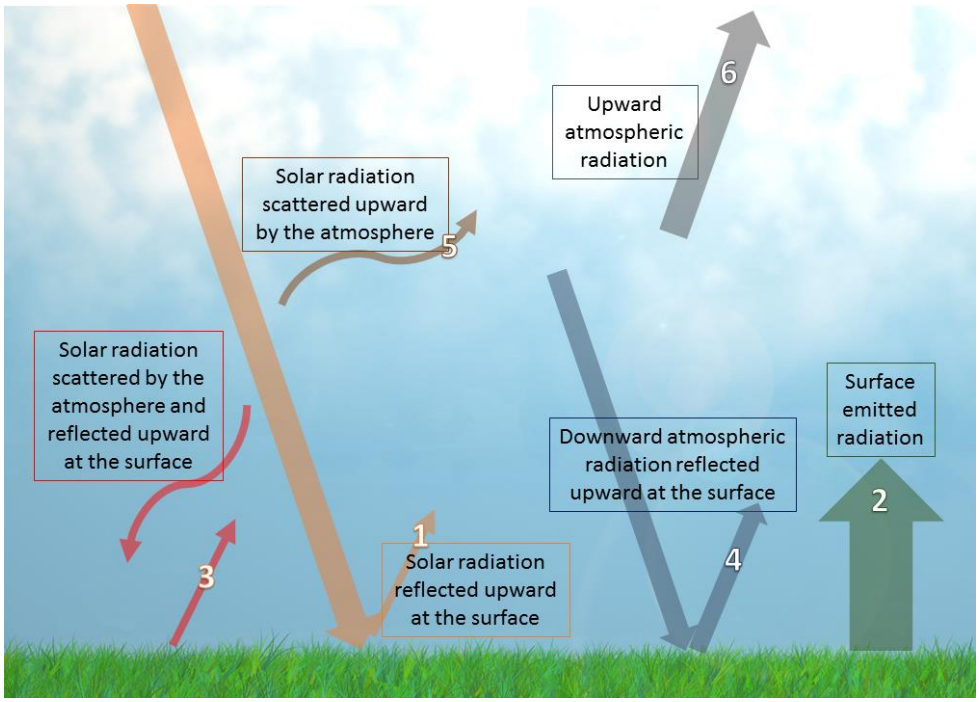

Figure 1.1.3 – Illustration of the radiative transfer occurring in the atmosphere between the surface and a remote sensor (adapted from Li et al., 2013).

For both the IR and the MW regions, the amount of solar energy arriving at the surface is negligible compared to the energy emitted by the earth's surface (Li et al., 2013; Schott, 2007; Ulaby et al., 1981). As a result, the solar-related items (paths 1, 3 and 5 of Figure 1.1.3) may be neglected without loss of accuracy and the effective radiance reaching the sensor may therefore be simplified to

$$L_\lambda = \left\{\varepsilon_\lambda(\theta_v, \phi_v)B_\lambda(T_{\text{skin}}) + [1 - \varepsilon_\lambda(\theta_v, \phi_v)]L_{\text{at}_\lambda\downarrow}\right\}\tau_\lambda(\theta_v, \phi_v) + L_{\text{at}_\lambda\uparrow} \quad \textbf{(1.1.5)}$$

Most satellite sensors measure radiation with a finite spectral-bandwidth. Therefore, the expression for the spectral radiance reaching the sensor must then be cascaded with the sensor response function.

The spectral bands at which a satellite sensor operates are related to the intended application. In the case of thermal remote sensing, it is important to consider the relative absorption of radiation by the atmosphere in order to reduce the uncertainties associated to the atmospheric correction (Figure 1.1.4). In the case of IR radiation, high radiation transmission may be found in the window between about 8 and 14 μm. For MW radiation, the most used window in thermal applications is the one centered at approximately 35GHz. As it may be seen in Figure 1.1.4, there is a significant decrease in the scattering of radiation as the wavelength increases. The amount of scattering depends on the size of the scattering particles in relation to the wavelength. This is why it is possible to use MW remote sensing for thermal applications in cloudy-sky conditions. Nevertheless, there may be contributions from clouds associated to absorption/emission, especialy for frequencies up to 40 GHz.

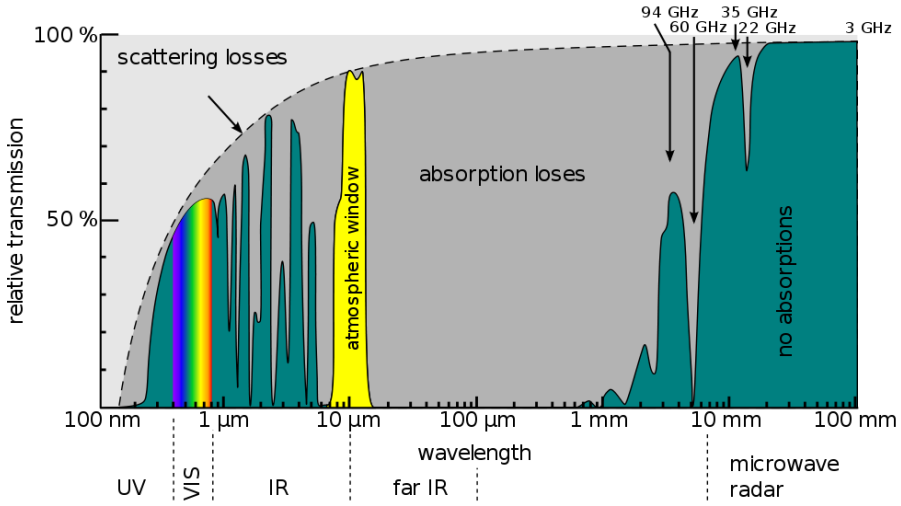

Figure 1.1.4 - Absorption spectrum during atmospheric transition of electromagnetic radiation (in Wikipedia Commons).

1.2 Radiative properties of the Earth's surface

INFRARED REGION

In the IR range, radiation emitted from the surface corresponds to the first few micrometres of the sensed objects (soil, vegetation, roads, buildings, etc). As discussed before, the radiation emitted by a surface depends on surface temperature and its emissivity, but the amount of radiation leaving the surface also includes a portion of the radiation emitted by the surroundings and reflected by the surface. Furthermore, the radiance at the sensor is also modified by absorption, emission and scattering by the atmosphere.

The emitted thermal radiation tends to be highly anisotropic. Remotely sensed surface temperatures in the IR only indicate the mean temperature of the surfaces that can actually be seen by the sensor. As such, the retrieved LST may vary as a result of varying proportions of the different surfaces within the field of view. In this case, LST anisotropy depends not only on structure and location of the surface components relative to each other, but also to the temperature contrasts between the components. Figure 1.2.1 shows an example of the different proportions of different surface components sensed for a nadir and off-nadir observation of the same surface region. In the nadir case, the signal reaching the sensor is composed by approximately one third of radiation emitted by shaded soil, while for the off-nadir view the canopy emitted radiation represents about three fifths of the total. In most cases the temperature of sunlit and shaded soil and of the canopy present large differences, which will result in differences in the retrieved temperature that are only associated to the viewing geometries. If the sensor is positioned in the direction of the sun, the amount of shaded soil radiation sensed is virtually null resulting in the highest LST possibly retrieved for that region. Such configuration is referred to as the hot-spot.

At the scale of the individual surface components, directional effects may also arise from the anisotropy of the emissivity (as discussed in section 1.2). These may be significant for some surface materials, resulting in emissivity variations of more than 5% (Cuenca and Sobrino, 2004; Labed and Stoll, 1991; Snyder et al., 1997; Sobrino et al., 2005; Sobrino and Cuenca, 1999). This will be particularly relevant in the cases where the emissivity is not obtained from measurements with the same viewing configuration as the LST estimates. Furthermore, the emissivity tends to vary with wavelength, which means that emissivity directional effects are likely to also depend on wavelength (Labed and Stoll, 1991; Snyder et al., 1997).

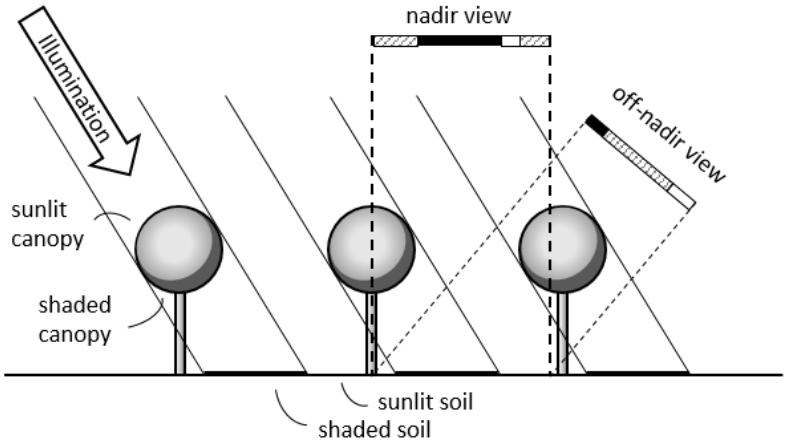

Figure 1.2.1 – Schematic representation sun-view geometry configurations for nadir and off-nadir views, for areas with sparse tree coverage.

MICROWAVE REGION

Although the conventional diagrammatic representation of Planck's function on a linear scale suggests a very reduced proportion of radiation being emitted in the MW region, from a logarithmic representation it is possible to verify that there is a tail of emission in this region (Figure 1.1.1). Although weak, MW emissions from earth are strong enough to be used in passive remote sensing.

Due to the relatively longer wavelengths than IR, MW radiation is associated to significantly less energy. Also, the long wavelength means that at this region radiation is not substantially scattered by the atmosphere. At low frequencies, scattering by cloud droplets may also be neglected. Emission and absorption by water in the atmosphere may, however, not always be neglected. For instance, deep convective clouds generally have significant contributions at frequencies below 40 GHz.

Another factor that is important in MW sensing is the polarization of the radiation. The way in which a polarized MW interacts with a surface may depend on the angle of polarization because of the orientation or roughness of the structure and on its dielectric constant, and hence moisture content.

As in the IR, the MW radiation emitted from a surface depends mainly on the temperature of the surface and on the emissivity, which in turn depends on structure and moisture content of the surface. The dielectric constant is a particularly important determinant of the emissivity, and as water presents an especially high dielectric constant (ranging ~30-80 for terrestrial temperatures and low frequencies) compared with soil minerals (ranging ~1-4), the dielectric constant of a surface is strongly dependent on water content (Jones and Vaughan, 2010). The strong interaction between dielectric constant, incidence angle, frequency, and polarization make MW emissivity particularly difficult to estimate.

Another consequence of the long wavelength is that it makes MW radiation particularly prone to penetration. Longer wavelengths penetrate further into the soil, and for dry soils the penetration depth depends on the size of the soil grains relative to the wavelength. The aggregation of the soil grains is also an important factor, and in general water content decreases the penetration depth. Furthermore, vegetation canopies are also prone to some penetration, depending on the density of foliage and its water content. This means that the skin temperature as measured with MW or IR may not correspond to the same surface layer.

1.3 Context and objectives of this thesis

As discussed in the previous sections, the theoretical ground for remote sensing of LST is that the total radiative energy emitted by the ground surface increases strictly with an increase in temperature according to Planck's law, the surface being whatever is viewed by the sensor at some nominal skin depth. It can be determined from thermal emissions at wavelengths in either IR or MW atmospheric windows.

IR skin temperature is defined as the temperature measured by an IR radiometer in cloud-free conditions typically operating at wavelengths 3.7-12 μm. For bare soil surfaces, IR LST is the temperature of the top few micrometres of the soil surface, whereas for densely vegetated ground it is that of the leaves of the canopy. For sparse vegetation, it is the ensemble temperature of the canopy, the understory, and the soil surface. Currently, the goal for IR LST retrieved data is to achieve accuracies of better than 1 K. Uncertainties have been consistently reduced as knowledge of the involved quantities and their effects have improved. The most relevant variables that impact LST uncertainty are the presence of water vapour, clouds, and aerosols in the atmosphere as well as the satellite viewing geometry, and the variability of the surface emissivity.

MW LST, unlike IR LST, represents the surface temperature at depths up to a few centimeters depending on wavelength, view angle and surface conditions (Prigent et al., 1999). Passive MW instruments use detectors centered on the Ku (18 GHz) and Ka (37 GHz) bands with vertical and horizontal polarization. Retrievals in the IR are generally more accurate than MW retrievals due to smaller variation of surface emissivities, independence of measurements from other temperature datasets and stronger dependence of the radiance on temperature. Also, their Instantaneous Field of Views (FOV) are significantly larger than in the IR. Nevertheless, MW measurements have been shown to complement those in the IR due to their lower sensitivity to clouds thus increasing sampling in cloudy conditions to nearly full sampling.

In the past few years, the LST requirements have become stricter specially because of climate applications, as LST constitutes an independent temperature data set for quantifying climate change complementary to the near-surface air temperature. A long, stable record of LST would be particularly useful for model evaluation in regions where few *in situ* measurements of surface air temperature exist and for attribution of observed changes in such regions to their possible causes.

As such, integrated products can take advantage of the strengths of each data set (IR and MW; polar orbiting and geostationary; and *in situ* where available) to provide sub-daily near-global coverage to better understand the diurnal, seasonal and climate variability of LST. This can be achieved through utilization of existing sensors, continued global deployment of new LST sensors, improved calibration and inter-calibration of satellite sensors, increased validation of derived products, and further advancement of blending methodologies exploiting the synergy benefit of different LST observations.

With the goal of contributing to the harmonization of the LST products, this thesis targets some of the open issues in remote sensing of LST, namely:

- In the IR, the variable viewing geometry between the different platforms may lead to discrepancies in the retrieved surface temperature that depends on the surface heterogeneity of the pixel – dominant land cover, orography. Furthermore, these directional effects deviate IR LST products from an ideally defined LST, which should correspond to the ensemble directional radiometric temperature of all surface elements within the FOV (Norman and Becker, 1995).
- The use of IR data limits the retrieval of LST to clear-sky conditions, since clouds “close” the atmospheric window. This introduces a clear-sky bias, which is difficult to quantify since it varies in space and time. In addition, the cloud clearing requirement severely limits the space-time sampling of IR measurements. Passive MW measurements are much less affected by clouds than IR observations. LST estimates can in principle be derived from MW

measurements, regardless of cloud conditions (e.g. Aires et al., 2001). However, retrieving LST from MW information and matching those estimations with IR-derived values is challenging and there have been only a few attempts so far.

- The validation of LST retrievals is far from trivial, given the high variability in space and time, along with the anisotropic effects mentioned above that characterize this variable. Validation exercises are commonly performed through comparisons of LST against ground-based measurements or through a radiance-based method (e.g. Wan and Li, 2008).

Taking into consideration the issues, the objectives of this thesis are as follows:

1. Develop a methodology for the upscaling of *in situ* observations that allows a correct characterization of directional effects, allowing a more appropriate validation of satellite retrieved LST. This will allow building an *in situ* database of directional LST.
2. Use the *in situ* database of directional LST to assess the potential of using parametric models to simulate LST anisotropy.
3. Assess the potential use of such parametric models at global scale and the impact of a calibration with satellite data.
4. Develop a methodology for the operational use of the parametric models to correct LST angular dependence.
5. Build a database of collocated IR and MW LST and compare LST retrievals from different sensors and with *in situ* LST, taking into account the uncertainty of algorithms. This database will allow a better understanding of the differences in the physical variable "land surface temperature" measured by IR and MW sensors.
6. Characterize the clear-sky bias of IR LST products through the comparison of LST averages obtained with MW LST products, with the aim of quantifying the differences for daytime and night-time observations, over different biomes and seasons.

STRUCTURE OF THE THESIS

This thesis is organized around the two main topics of research, namely the directional effects in IR LST (Chapter 2) and the clear-sky bias of satellite retrieved LST (Chapter 3). The sections of the two chapter are mainly structured according to the contents of the five papers (see following section) that were produced in the framework of this PhD. The papers are almost integrally reproduced as they were published, but changes were made in order to avoid repetitions in the description of datasets and methodologies. The order of presentation does not follow the chronological order of publication in some cases. This occurred because of the need for further investigation of the performance of the parametric models (section 2.3) that aroused after the first attempt of their use with satellite data (section 2.4). The methodology proposed in section 2.5 has not yet been published but it is being used in the production of the Merged LST product disseminated within the GlobTemperature project. Research presented in sections 3.2 and 3.3 was carried out at the Observatoire de Paris (France). It is also emphasizing that although the full algorithm development has been presented in section 3.2 (to follow the published paper), the algorithm was already set up by the team at the Observatoire de Paris. The main contribution of this thesis was to make an assessment of the MW LST with *in situ* and IR LST data that lead to small modifications to the algorithm.

The structure of the thesis is as follow:

- Chapter 1 introduces the physical concepts involved in the retrieval of LST from satellite observations.
- Chapter 2 addresses the problem of the directionality of LST, namely
    - Section 2.1 introduces this chapter.
    - Section 2.2 describes a methodology to generate a synthetic database of directional LST from *in situ* measurements that may be used for the evaluation of parametric models (Ermida et al., 2014).

  - Section 2.3 presents a detailed analysis of previously proposed parametric model of LST anisotropy using the synthetic database of *in situ* LST (Ermida et al., 2018).
  - Section 2.4 presents an assessment of the use of satellite data to calibrate one of the parametric models, addressing the advantages and difficulties in the use of such data (Ermida et al., 2017a).
  - Section 2.5 proposes a methodology for the operational use of the parametric models at global scale and calibrated with satellite data, considering the added knowledge that resulted from the previous sections.
  - Section 2.6 summarizes the findings presented in this chapter.
- Chapter 3 addresses the use of MW observations to derive all-weather LST and to characterize the clear-sky bias of satellite-retrieved LST, namely
  - Section 3.1 introduces this chapter.
  - Section 3.2 describes a methodology to retrieve LST from MW observations and its evaluation against ground data (Jiménez et al., 2017).
  - Section 3.3 presents a detailed comparison between multiple IR LST products and the MW LST developed in section 3.2 (Ermida et al., 2017b).
  - Section 3.4 presents a characterization of the clear-sky bias at seasonal and global scale, making use of the developed MW LST dataset.
  - Section 3.5 summarizes the findings presented in this chapter.
- Chapter 4 summarizes the main findings that resulted from the research carried out during this PhD, indicating also topics that remain open.
- In Appendix A results are shown for an ongoing study on the retrieval of emissivity directionality from collocated satellite observations performed by different sensors.

CHAPTER 2

DIRECTIONAL EFFECTS ON IR LST

CONTENTS

2. DIRECTIONAL EFFECTS ON IR LST

2.1 Introduction

LST estimated from infrared satellite observations correspond to the radiometric temperature of the surface as seen within the sensor field of view (FOV), therefore remotely sensed LST is a directional variable (Norman and Becker, 1995). Given the high spatial heterogeneity of land surface, such directionality may lead to significant differences among LST products obtained for the same area and observation time, but with different viewing geometries (Barroso et al., 2005; Duffour et al., 2016, 2015; Ermida et al., 2014; Lagouarde et al., 2004, 2000, Pinheiro et al., 2006, 2004; Trigo et al., 2008a). This effect contributes to enhance the differences among LST satellite products, and therefore increasing the challenge of using multi-sensor and multi-decadal data to provide harmonized LST datasets suitable for long-term climate observations. Accurate estimates of the angular effects on retrieved LST are also crucial when performing *in situ* and cross-sensor validation exercises (Ermida et al., 2014). Quantification of these effects may also be relevant when using LST for model assessment (e.g. Trigo et al., 2015; Wang et al., 2014) and data assimilation (e.g. English, 2008; Ghent et al., 2010).

The impact of the viewing geometry on LST estimations is related to a large extent with contrasts in the radiometric temperature of the various surface elements. In savannah-like landscapes, the measured difference between tree canopy and sunlit background during the dry season may reach over 20 K (Ermida et al., 2014; Rasmussen et al., 2011). Other factors such as orography or emissivity anisotropy may also play an important role (Trigo et al., 2008a). The angular dependency of satellite observed LST should therefore be taken into account when combining LST products retrieved by different sensors, e.g., in order to obtain a harmonized variable.

The approaches to model and to understand the variability of LST with angle depend on surface type and scales being represented. For the case of tree covered surfaces, several methodologies have been developed to study the directional properties of TIR radiance of vegetation canopies that allow the simulation of the radiometric temperature of canopy–soil combinations. These models can generally be grouped in three categories: geometric optics (GO), radiative transfer (RT), and hybrid (GORT).

1. GO models were designed to describe the radiative transfer within vegetation canopies by assuming simplified opaque sub-canopies that can adopt different geometric shapes (e.g. cubic, cylindrical, conical, ellipsoidal). Examples of such models may be found in the studies presented by Caselles et al. (1992), Kimes (1983), Kimes and Kirchner (1983), Sobrino et al. (1990), and Sobrino and Caselles (1990). These models are appropriate to model clumped or row-structured canopies, however the comprised physical processes are generally limited.
2. RT models are centralized on the directional scattering and absorption of radiation by canopy elements (e.g. leaves), by means of various analytical and numerical approaches. These models relay on various degrees of detail in physical processes, requiring a comprehensive characterization of the vegetation canopy by a leaf density distribution, leaf inclination distribution, amongst others, and they often also assume canopies as homogeneous turbid media composed of layers with different temperatures. Some of the models that fall into this category are the ones proposed by Kimes (1981), Kimes et al. (1981), McGuire et al. (1989), Otterman et al. (1999, 1992), and Smith and Goltz (1994).
3. In the GORT category, 3-D modeling approaches rely on numerical techniques and are suitable to be combined with GO modeling (Li and Strahler, 1985, 1992). Some numerically based models have been proposed to simulate TIR scenes of 3-D canopies (e.g., (Guillevic et al., 2003)). These types of models are capable of representing the thermal heterogeneity of a canopy resulting from the contrast of sunlit/shaded leaves and soil with high accuracy, however they require many parameters to define the 3-D geometric structure of a canopy, which makes it difficult to deal with the inversion problem. Other GORT models combine gap

probabilities and RT for homogeneous and row-structured canopies (Chen et al., 2000; Niu et al., 2000; Yan et al., 2003).

Parallel to these physically based models, there are also models which only describe the angular signature of the bidirectional properties by mathematical kernels: parametric models (Rahman et al., 1993; Roujean et al., 1992; Wanner et al., 1995).

Physical models simulate the canopy physical properties and the radiative transfer between the different layers of the media, soil background inclusive. As a result, they provide accurate simulations of the radiometric temperature for the canopy-soil system. However, those physical models require detailed knowledge of surface characteristics, which is not readily available at the continental or global scale. Parametric models, on the other hand, are computationally more efficient and require few input data, which makes them particularly appropriate for operational use in satellite LST retrieval.

In section 2.2 a geometric model is presented that allows estimating the projected areas of the different components using parallel-ray geometry to describe the illumination of a three-dimensional vegetation element and the shadow it casts. The proposed model not only allows the correction of LST differences between sensors associated with their viewing geometries, but it is also an effective means for the validation of satellite-derived LST with ground-based measurements.

This type of geometric-optical model has been used by several authors to solve radiative transfer problems associated with surface heterogeneities related to vegetation (Franklin and Strahler, 1988; Lagouarde et al., 1995; Li and Strahler, 1985, 1992; Ni et al., 1999; Strahler and Jupp, 1990), as well as in studies of surface temperature anisotropy (Guillevic et al., 2013; Minnis and Khayer, 2000; Pinheiro et al., 2006; Rasmussen et al., 2010). Instead of relying on a rigid analytical approach, the procedure developed here has the advantage of using a simple computational method to calculate the geometrical projections, while making very few a priori assumptions. The method consists of projecting a three-dimensional vegetation object onto a fine grid, which allows the use of any vegetation shape and size or the combination of different shapes and sizes.

The model is applied to *in situ* measurements of brightness temperature gathered at Évora validation site to obtain the ground temperature corresponding to any observation and illumination angles. It can therefore be used as a tool to upscale temperature measurements of various site elements to an integrated temperature value at pixel scale, as viewed from any given angle. However, it can only be used in areas where surface characteristics are well documented and where an array of observations are available, such as in Évora. The site is located in a region dominated by sparse canopies of evergreen oak trees (Southern Portugal; Kabsch et al., 2008).

In section 2.3 this geometric model is used to analyze the performance of parametric models under different settings of surface conditions. One of the models analyzed is the one developed by Vinnikov et al. (2012). The model follows a kernel approach that has successfully been used to describe the Bidirectional Reflectance Distribution function (BRDF) in the optical domain (e.g. Jupp, 2000). Here the LST directionality is modeled by two kernels composed of trigonometric functions of the viewing and sun geometries. Another approach is the one proposed by Lagouarde and Irvine (2008) that is engendered by the hot spot formulation proposed by Roujean (2000) for the optical domain where reflectance is formally replaced by surface temperature. The model has been successfully evaluated against RT models and experimental setups that revealed its potential to properly describe directional LST for both urban and vegetated areas (Duffour et al., 2016; Lagouarde and Irvine, 2008).

The two approaches are worth being compared in a systematic way. For instance, the model by Vinnikov et al. (2012) allows an effective simulation of LST directionality associated not only to shadowing effects but also to emissivity anisotropy. However, Duffour et al. (2016) have pointed out a possible underestimation by the model of the LST anisotropy near the hot-spot geometry. In turn, the model by Lagouarde and Irvine (2008) performs better in simulating anisotropy related to shadowing

effects (Duffour et al., 2016), but the model is unable to account for emissivity anisotropy and could potentially fail for surfaces with low vegetation cover.

As such, the aim of section 2.3 is threefold: 1) to consistently evaluate the performance of the models proposed by Vinnikov et al. (2012) and by Lagouarde and Irvine (2008); 2) to assess their respective potential to correct directional effects on LST for a wide range of surface conditions (tree coverage, vegetation density, surface emissivity); and 3) to optimize the correction of directional effects by proposing an approach based on a synergistic use of both models.

In section 2.4 we assess the potential of the parametric models at global scale and when calibrated with multi-sensor retrievals of LST. For this purpose, the models are applied to LST from sensors on board geostationary and polar-orbit platforms obtained over a large area and over a multi-year time period. The models are evaluated for landscape-level thermal LST directionality, including vegetation and landcover-induced impacts as well as topographic effects. The calibration is evaluated in two different settings: 1) pixel-by-pixel calibration and 2) calibration to pixels' clusters. The clustering based on surface characteristics allows a reduction of calibration issues related to limitations in the sampling of viewing and illumination angles and to unresolved local biases between the LST products.

DATA DESCRIPTION

SATELLITE LST DATA

In this chapter we consider satellite-observed LST obtained from two sensors: 1) the LST product retrieved from Spinning Enhanced Visible and Infrared Imager (SEVIRI) on-board Meteosat Second Generation (MSG) satellites provided by the EUMETSAT Satellite Application Facility on Land Surface Analysis (LSA-SAF) (Trigo et al., 2011); and 2) level 2 daily LST obtained from the Moderate Resolution Imaging Spectroradiometer (MODIS) on-board Aqua (product MYD11, collection 5) and Terra (product MOD11, collection 5) (Wan and Li, 2008). SEVIRI and MODIS LST were obtained from the GlobTemperature portal (http://data.globtemperature.info/), which provides LST data in a standardized format, facilitating collocation in space and time and organization of needed auxiliary variables (including viewing geometry and sun angles).

The LSA-SAF LST is estimated with a generalized split-window algorithm (Freitas et al., 2010) from top-of-atmosphere brightness temperatures measured by MSG/SEVIRI in the thermal infrared, namely in SEVIRI channels IR10.8 and IR12.0. It is produced at full SEVIRI spatial and temporal resolutions, with a 15-minute sampling interval and a spatial resolution of 3 km at the sub-satellite point, which degrades with increasing distance from nadir, reaching a size of about 4 km over Southern Europe. The product is available for all land pixels within the MSG disk under clear sky conditions; the actual area coverage depends on product uncertainty (LST retrievals with uncertainty estimates above 4K are masked out) and can reach view zenith angles (VZA) up to 70° (Freitas et al., 2010). According to Göttsche et al. (2016), comparisons with four LSA-SAF dedicated stations resulted in a mean absolute bias of SEVIRI LST of 0.1 K, with daytime and night-time biases up to 0.7 K (but with opposite signs). Land Surface Emissivity (LSE) used by the LSA-SAF in the derivation of LST is estimated with the Vegetation Cover Method (Caselles and Sobrino, 1989; Peres and DaCamara, 2005; Trigo et al., 2008b). The method allows the determination of effective LSE as the weighted average of the emissivities of the dominant bare ground and vegetation type within a scene, using daily values of Fraction of Vegetation Cover (FVC) to obtain the respective weights. Emissivity values for vegetation and soil types were obtained from the International Geosphere-Biosphere Program (IGBP) land cover classes (Belward and Office, 1996; Peres and DaCamara, 2005; Trigo et al., 2008b).

The MODIS LST product is derived with a Split Window Algorithm (Wan et al., 2002; Wan and Dozier, 1996) applied to bands 31 and 32 with a formulation similar to that adapted by the LSA-SAF team for SEVIRI (Trigo et al., 2011). The product (MOD/MYD11) is available at a spatial resolution of 1 km with a maximum of four clear sky observations per day. Information on viewing geometry was obtained from MODIS products MOD03 and MYD03, collection 5 (http://modis.gsfc.nasa.gov/). Radiance-based validation of the collection 5 of MODIS LST level-2 products at 42 sites indicated that LST uncertainties

are within ±2 K, being within ±1 K in most cases (Wan, 2014). In the case of MODIS, LSE is estimated with a similar method to the SEVIRI but using (static) land cover types (Wan and Dozier, 1996).

IN SITU MEASUREMENTS

Ground observations are gathered at LSA-SAF's Évora validation site maintained by the Karlsruhe Institute of Technology (KIT). The station is located in Southern Portugal (8.00° W; 38.54°N) within an area characterized by a uniform landscape at the SEVIRI pixel scale (Dash et al., 2004; Kabsch et al., 2008), which consists of Quercus woodland and an understory dominated by herbs and grasses (David et al., 2004). At smaller scales, the variability in temperature is quite high, particularly during summer months when the understory desiccates and leads to large temperature differences between the ground and tree canopies. Therefore, comparisons between satellite and *in situ* observations require an appropriate up-scaling of the latter to satellite pixel-scale: the respective up-scaling technique has to account for the different temperatures and fractions of the main surface cover elements, i.e. sunlit ground, shaded ground and tree canopies for each viewing geometry (Pinheiro et al., 2006).

The *in situ* measurements are collected every minute by three infrared radiometers (Heitronics KT-15.85 IIP), observing the sunlit background, a tree crown and the sky at 53° zenith angle, which is used to estimate down-welling reflective components (Göttsche et al., 2013). The radiometers provide measurements of brightness temperatures within the 9.6 – 11.5 µm spectral interval, with an absolute accuracy of 0.3K (Göttsche et al., 2013). Here we will consider observations made between October 2011 and September 2012.

COMPLEMENTARY DATA

A hill shading algorithm was applied to DEM data as provided by NOAA's Global Land One-km Base Elevation Project (GLOBE) which are available at 1 km resolution (http://www.ngdc.noaa.gov/mgg/topo/globe.html). The hill shading algorithm allows the estimation of the fraction of shaded surface in mountainous areas and, for that reason, allows the evaluation of the kernel model over these regions.

Information on Percentage of Tree Cover (PTC) was obtained from MODIS Vegetation Continuous Fields (MOD44B, collection 5) provided on a yearly basis with a 250m resolution (Townshend et al., 2011). The data corresponds to the years of 2013 and 2014 and was re-projected onto the SEVIRI grid using plain average.

Surface topography is also obtained from Digital Elevation Model (DEM) data from Shuttle Radar Topography Mission (SRTM) provided by NASA (http://www2.jpl.nasa.gov/srtm/). Data is provided by the GlobTemperature project for the full globe at a resolution of 0.05^{o}x0.05^{o}, which was regridded from the original $1/120^{o}$ grid.

Land cover type is obtained from the Advanced Along-Track Scanning Radiometer (AATSR) LST Biome V2 (ALB2) land clover data from University of Leicester, also provided by GlobTemperature at a 0.05^{o}x0.05^{o} resolution.

The FVC for the globe is obtained from Copernicus FCover product version 2 at 1 km resolution. The product is based on SPOT-VEGETATION 1km data and generated by the Global Land Service of Copernicus (http://land.copernicus.eu/global/products/fcover), corresponding to 10-day composites. Global data for the 2011 year was retrieved and averaged monthly to allow a characterization of the typical inter-annual variability of the vegetation. The data was also reprojected onto the 0.05^{o}x0.05^{o} grid.

2.2 A Geometric model of directional LST

DATA PRE-PROCESSING

OBTAINING THE TEMPERATURE OF SHADED GROUND

Due to experimental difficulties, the temperature of shaded background is not directly measured and needs to be estimated. Since there is no direct incoming solar radiation on shaded surfaces, their temperature can usually be expected to be close to radiative equilibrium with the near-surface air. Therefore, it can commonly be assumed that the temperature of shaded ground is close to near-surface air temperature or to the temperature of tree canopies; the latter was the approach used by Guillevic et al. (2013), for the Évora site. Here we opted for the former, but additionally applied a phase correction to account for the time lag between shaded ground temperature and near-surface air temperature. The phase adjustment accounts for the difference in heat capacity between air and ground (Figure 2.2.1). For this purpose, we assume that the shaded ground temperature is proportional to sunlit ground temperature with a proportionality given by the ratio of daily maximum air temperature $T_{air}^{\max}$ to daily maximum sunlit background temperature $T_{sunlit}^{\max}$. The shaded ground temperature cycle for each day is estimated with the following empirical model:

$$T_{shadow}(\theta_i) = K(\theta_i) T_{sunlit}(\theta_i) \tag{2.2.1}$$

where

$$K(\theta_i) = \begin{cases} T_{air}^{\max}/T_{sunlit}^{\max} + \dfrac{1 - T_{air}^{\max}/T_{sunlit}^{\max}}{90° - \theta_i^{\min}}\left(\theta_i - \theta_i^{\min}\right), \theta_i < 90° \\ 1 \qquad\qquad\qquad\qquad\qquad\qquad\qquad\qquad\qquad\qquad , \theta_i \geq 90° \end{cases} \tag{2.2.2}$$

and units for temperature are °C.

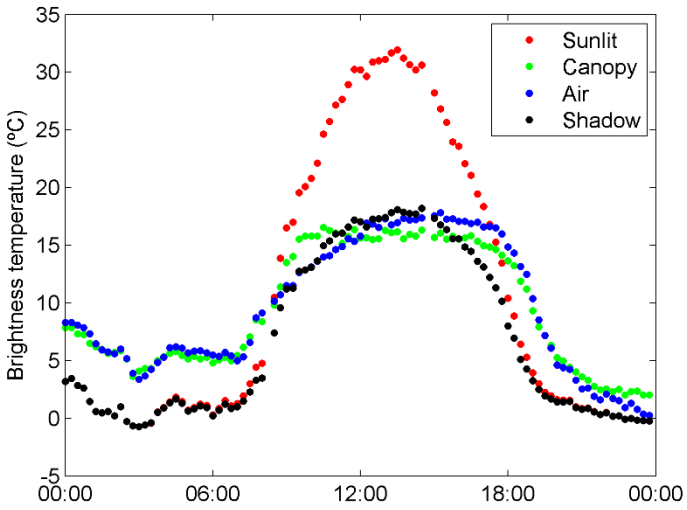

Figure 2.2.1 - Diurnal cycle of near-surface air, canopy, and sunlit ground temperatures (°C) measured at Évora, on the 20th of March 2011. The temperature of the shaded background (Shadow) was estimated using eqs. (2.2.1) and (2.2.2).

When compared with actual *in situ* observations of shaded ground temperature (available for a few hours of the day and during a limited period of the year), the empirical model described by eqs. (2.2.1) and (2.2.2) leads to a bias of 0.5°C and Root Mean Square Error (RMSE) of 3.4°C, which are both about 1°C smaller than the result obtained with the most common approaches of simply equating shaded ground temperature either with tree canopy or with near-surface air temperature.

SHADOW CONTAMINATION OF SUNLIT BACKGROUND MEASUREMENTS

At Évora station there are two radiometers measuring the sunlit background temperature of two different points. During autumn and winter (from October to March) the daily brightness temperature cycle of one of the radiometers sharply drops in the afternoon, which is caused by tree shadow falling into the radiometer's FOV (see "Rad2" in Figure 2.2.2). The other radiometer ("Rad1") does not contain this "shadow contamination", but its measurements are less reliable: the team responsible for the maintenance of Évora LST validation station reported that the grass within the FOV of Rad1 had been accidentally grazed so that it was no longer representative for the typical ground surface found in the area. However, radiometer Rad1 may be used to correct the time series of radiometer Rad2. The two time-series may be linearly correlated, to a good approximation, by the following model:

$$T_{Rad2} - T_{Rad1}^{\min} = \alpha\left(T_{Rad1} - T_{Rad1}^{\min}\right) + \beta \qquad (2.2.3)$$

where subscripts Rad1 and Rad2 identify each radiometer and $T^{\min}$ are the daily minimum temperatures. Parameters α and β are estimated using robust regression. The period of the day when Rad2 is contaminated by shadow was directly estimated by the geometric model.

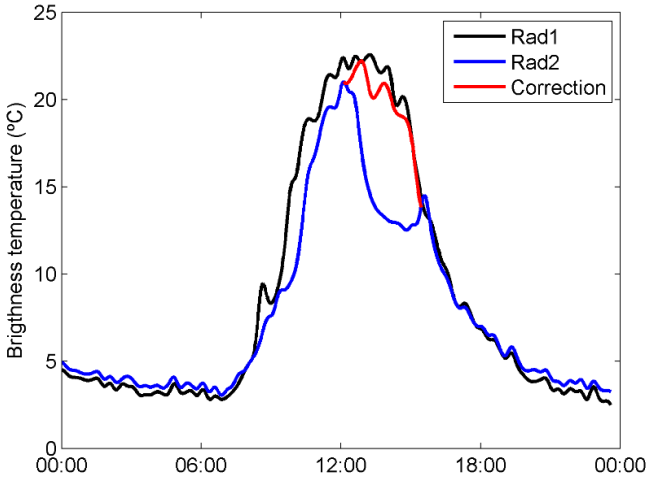

Figure 2.2.2 - Correction of observed shadow contamination in the radiometer's time series, on the 25th of November of 2011. Blue (Rad2) and black (Rad1) curves represent brightness temperatures measured by the two radiometers observing the background; the red line represents the corrected ("shadow-free") sunlit background temperatures obtained for the more representative radiometer Rad2.

THE GEOMETRIC MODEL

Appropriate *in situ* directional LST may be obtained by compositing the *in situ* temperatures of the scene components (i.e. sunlit background, shaded background and tree canopy, as described in the previous section), e.g. by weighing the individual component temperatures with the respective cover fractions seen by the sensor. The dynamic cover fractions needed for this procedure obtained by means of a geometric model that accounts for the viewing and illumination conditions. Here we propose a model based on the GO part of the GORT model (Ni et al., 1999) that allows estimating the scene proportions within a given pixel, assuming that the main components are sunlit background, shaded background and canopy. The sunlit and shaded parts of canopy should in principle also be treated separately (Jones and Vaughan, 2010). However, because of tree's ability to regulate its temperature, differences between the two parts are negligible when compared to the differences between sunlit background, shaded background and canopy at the satellite's pixel scale. Therefore, it is expected that the above mentioned three components suffice to capture the scene angular variability, in accordance with previous works by Pinheiro et al. (2006) and Guillevic et al. (2013).

It is assumed that the pixel's radiance measured by the sensor can be estimated as a linear combination of the radiances emitted by each of the scene components weighted by their respective projected scene fractions. For our purposes, we assume that any angular variation in the observed radiance is exclusively due to changes in the scene fractions within the pixel (Pinheiro et al., 2006), i.e.:

$$L_{avg} = F_{sunlit} * L_{sunlit} + F_{shadow} * L_{shadow} + F_{canopy} * L_{canopy} \quad (2.2.4)$$

where L_{avg} is the pixel's radiance within a sensor FOV, L_{sunlit}, L_{shadow} and L_{canopy} are sunlit background, shaded background and canopy radiances, respectively, and F_{sunlit}, F_{shadow} and F_{canopy} are the corresponding component fractions, as seen by each space-borne sensor. Each component's radiance is obtained from *in situ* measurements of brightness temperature which are converted to radiances using Planck's Law. Here we use a representative wavelength of 10.55 μm for channel-effective emissivities for the KT-15.85 IIP radiometer band (Göttsche et al., 2013).

The estimation of the total radiance as a linear combination of each component's radiances implies that component radiances are uniform and additive, which might not be true. For example, the radiance of shaded background is brighter toward the edges of the shadow, instead of being uniform. Effects like differential absorption and multiple-scattering can be modeled by more sophisticated radiative-transfer models; however, we expect them to be negligible in this type of study (Strahler and Jupp, 1990).

Effective Emissivity

The radiance reaching the *in situ* radiometers facing the ground/canopy is a combination of the radiance emitted and reflected by the surface. Therefore, the reflected component needs to be removed from the averaged radiance, L_{avg}, using the measurements of the sky-facing radiometer (L_{sky}) and assuming the pixel effective emissivity is known:

$$L_{avg} = \varepsilon_{eff} * L_{sfc} + \left(1 - \varepsilon_{eff}\right) * L_{sky} \quad (2.2.5)$$

ε_{eff} is estimated as a weighted average of the emissivity of ground and tree components:

$$\varepsilon_{eff} = FVC * \varepsilon_{tree} + (1 - FVC) * \varepsilon_{ground} \quad (2.2.6)$$

where the FVC is the proportion of surface covered by vegetation operationally estimated and distributed by the LSA-SAF on a daily basis (García-Haro et al., 2005; Trigo et al., 2011). We consider that FVC provides a direct measure of green and non-green proportions of the pixel as seen by a remote sensor, being used here as monthly averages to provide monthly estimates of the pixel ε_{eff}. It should be noted that an estimate of the green and non-green proportions based on scene fractions may lead to unrealistic values of emissivity since the ground is usually covered by green/dry grass during winter/summer, with a significant impact on the overall emissivity. FVC is, therefore, more representative of this vegetative cycle. Emissivity values of 0.9934 for tree and 0.9689 for ground were attributed based on spectral emissivity libraries (Peres and DaCamara, 2005; Trigo et al., 2008b).

The composite radiance L_{sfc} is then estimated from equation (2.2.5) and converted back to temperature, i.e., the *in situ* composite temperature, using again Planck's Law.

THE BOOLEAN COMPONENT

Estimation of fractions of sunlit background, shaded background and canopy (F_{sunlit}, F_{shadow} and F_{canopy}) in equation (2.2.5) are derived using a Boolean Scene Model (Serra, 1982) that computes the gap probability $q(\theta,\phi)$ between randomly distributed objects according to:

$$q(\theta,\phi) = e^{-\zeta \bar{A}(\theta,\phi)} \tag{2.2.7}$$

where ζ is the density of object centers in [m^{-2}], θ is the considered zenith angle, ϕ is the considered azimuth angle and $\bar{A}(\theta,\phi)$ in [m^2] is the average area of an object projected at angles (θ,ϕ). A thorough description of the Boolean model is given by Liu et al. (2004) and Strahler and Jupp (1990).

Following Liu et al. (2004), the density of object centers was estimate:

$$\zeta = \frac{-\ln(1-PTC)}{\pi R^2} \tag{2.2.8}$$

where R is the average horizontal crown radius of an ellipsoidal tree (cf. Table 2.2.1) and PTC is the Percentage of Tree Cover, defined as the surface proportion covered by tree crowns. Given that trees at the Évora site are evergreen oak trees and PTC does not include ground vegetation (grass, shrub), it follows that PTC is virtually constant over the year, as opposed to FVC, which is highly variable and changes with the vegetative cycle of the ground vegetation.

Estimations of F_{sunlit}, F_{shadow} and F_{canopy} were obtained by applying equation (2.2.7) to both view (θ_v,ϕ_v) and illumination (θ_i,ϕ_i) angles. Considering the geometry of our problem, $q(\theta_v,\phi_v)$ will represent the proportion of background seen from the viewpoint at (θ_v,ϕ_v) when trees have an average areal projection $\bar{A}(\theta_v,\phi_v)$ onto the background. The complement $1-q(\theta_v,\phi_v)$ will correspond to the proportion covered by trees (Figure 2.2.3). On the other hand, the proportion of non-shaded background will be $q(\theta_i,\phi_i)$. Accordingly, the fractions of sunlit and shaded background and canopy can be estimated by:

$$F_{sunlit} = \exp\{-\zeta\left[\bar{A}(\theta_v,\phi_v) + \bar{A}(\theta_i,\phi_i) - \bar{A}_{overlap}\right]\} \tag{2.2.9}$$

$$F_{shadow} = \exp\{-\zeta \bar{A}(\theta_v,\phi_v)\} - F_{sunlit} \tag{2.2.10}$$

$$F_{canopy} = 1 - \exp\{-\zeta \bar{A}(\theta_v,\phi_v)\} \tag{2.2.11}$$

where $\bar{A}_{overlap}$ is the overlap, i.e., the shaded area that is also hidden by the tree crown (Figure 2.2.3).

Although the projected areas $\bar{A}(\theta,\phi)$ for certain shapes (e.g. spherical, ellipsoidal) are simple enough to be estimated analytically, the computation of the overlap area $\bar{A}_{overlap}$ is generally complex. Therefore, we use the projection of a single arbitrarily-shaped 3D vegetation element (an ellipsoidal tree in the case analyzed here) onto a fine scale regular grid to obtain the projected areas and respective overlap. This is a two-step procedure:

1) A tridimensional description of the canopy shape of a single tree element is obtained from the parametric equations of an ellipsoid.
2) The 3D shape of the canopy is then projected onto a 0.01m regular grid using parallel-ray geometry, and all areas ($\bar{A}(\theta_v,\phi_v)$, $\bar{A}(\theta_i,\phi_i)$ and $\bar{A}_{overlap}$) are estimated.

The accuracy of the projected areas depends only on the grid resolution. The output of the current configuration was validated against an analytical formulation of the projected area of an ellipsoidal shaped tree (Li and Strahler, 1992). The comparison of these two approaches for zenith angles 0°, 30°, 45°, 60° and 75° revealed relative differences between 0.18% and 0.25%.

Because it is based on a numerical procedure, the geometric model can be easily adapted to accommodate different shapes and sizes of trees in the landscape. Especially for practical applications, this is a significant advantage compared to the analytical approach of the GORT model.

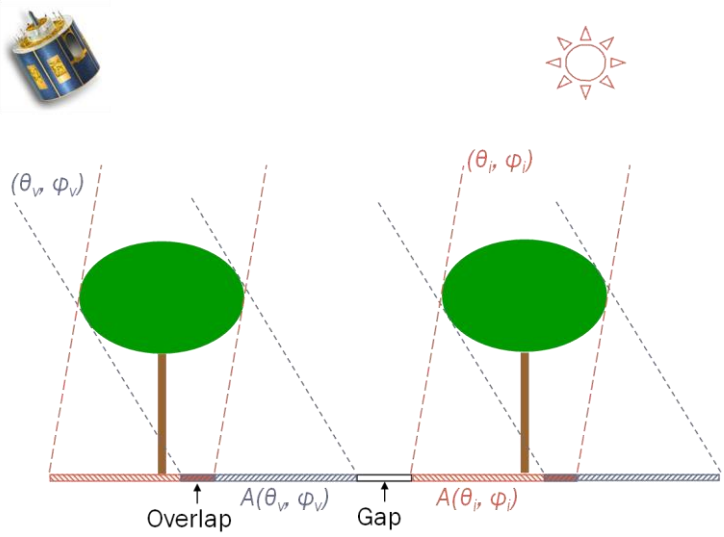

Figure 2.2.3 - Schematic representation of projected areas onto the fine regular grid, for a given viewing and illumination geometry. The red shaded area is the projection of the trees at the illumination zenith (θ_i) and azimuth (ϕ_i) angles, which physically represents tree shadow. The blue shaded area is the projection of the trees at the view zenith (θ_v) and azimuth (ϕ_v) angles which represents the area obscured by tree crown that will not be seen by the sensor. The sunlit background as seen by the sensor will be limited to the white area. Part of the shaded area will also be hidden by the crown, corresponding to the overlap area.

INPUT PARAMETERS

The input data for the geometric modeling the Évora validation site are summarized in Table 2.2.1. The tree shape parameters are in line with values attributed to the area surrounding the validation station measured by David et al. (2004, 2007). The chosen ellipsoidal shape for the tree crowns is the one that best reflects the traditional pruning of oak trees in southern Portugal, which is performed regularly to increase acorn production and provide shade for cattle (David et al., 2004).

Table 2.2.1 - Description of the input data for the model.

Parameter	Description	Value	Source
PTC	Percentage of Tree Cover: surface proportion covered by tree crowns.	-	-
R	Average canopy horizontal radius	5 m	Based on observations of the area surrounding Évora
b	Average canopy vertical radius	2.5 m	
H	Average height of crown center	6 m	
(θ_v, ϕ_v)	View zenith and azimuth angle	-	Available for each remote sensor
(θ_i, ϕ_i)	Illumination zenith and azimuth angle	Variable through the day	Calculated based on location, date and time of day

MODEL SENSITIVITY TO INPUT PARAMETERS

The geometric model was used to perform a sensitivity study of *in situ* LST to the parameters listed in Table 2.2.1. Results show that the impact is highest for daytime observations during summer months (June – September). An increase/decrease of 5% in PTC would lead to cooling/warming of daytime LST of up to 1°C between June and August and up to 0.5 °C in April-May. The impact is very small for the remaining months or at night-time. The variability in the canopy size has significantly lower impact than that of PTC. As an example, changing tree canopy horizontal radius R and vertical radius b by 20% (i.e. assuming R=5 ±1m and maintaining b=R/2 as in Table 2.2.1) leads to a maximum impact of about 0.25 °C for daytime summer observations, and negligible changes during the other periods of the day/year. However, considering different canopy shapes, e.g. assuming spheres instead of ellipsoids (b=R), generally increases the fractions of projected canopy and shaded areas and, therefore, decreases daytime summer temperature (about 1°C for R=b=5m and 2°C for R=b=6m).

Considering an uncertainty in FVC of 0.1, the emissivity differences among the local types of vegetation/bare soil and the inherent uncertainty of the vegetation cover method (eq. (2.2.6), we estimate an error for affective emissivity ε_{eff} of 1.2% to 1.4%. The propagation of these values through the model leads to an uncertainty in composite *in situ* LST of about 0.55°C.

The annual uncertainty budget for daytime and night-time observations is presented in Figure 2.2.4. The highest uncertainties with values of 1.4°C occur at daytime during summer. For night-time observations, the error in composite *in situ* LST is of the order of 0.6°C and is dominated by the uncertainty in emissivity; similar results are obtained at daytime between January and April.

As expected, the highest errors occur during daytime and during the part of the year when the contrast between sunlit/shaded ground and canopy temperatures is the highest. This sensitivity study confirms that night-time data are the most reliable for validating satellite LST products. Furthermore, the analysis of daytime LST provides useful insights about the variability among satellite products and shows that a considerable part of the observed differences can be explained by spatial heterogeneity of the surface and differences in viewing and illumination geometries.

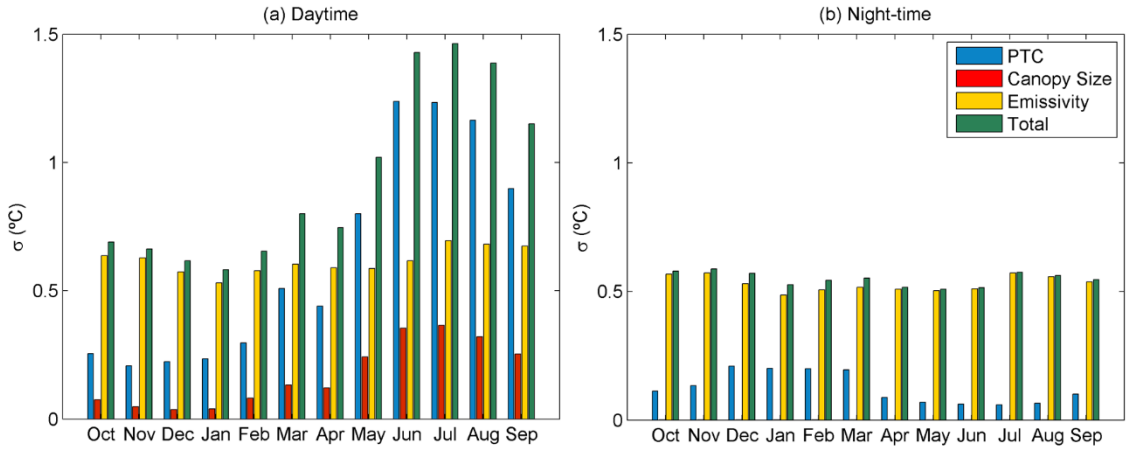

Figure 2.2.4 - Estimated monthly STD of composite *in situ* LST for (a) daytime and (b) night-time observations, associated to uncertainties in PTC (blue bar), canopy size (red bar), emissivity (yellow bar) and total budget (green bar).

ANGULAR DEPENDENCE OF COMPOSITE TEMPERATURE

The impact of changes in viewing geometry on surface temperature may be assessed by using the geometric model to compute composite temperature as a function of input viewing zenith and azimuth angles, for a PTC of 30%. Figure 2.2.5 presents *in situ* Évora temperatures, as they would be seen from nadir (Figure 2.2.5(a); i.e. $\theta_v = 0°$) and the respective deviations corresponding to a zenith angle $\theta_v = 45°$ (close to that of SEVIRI) when viewed from south, north and west (Figure 2.2.5(b),(c) and (d),

respectively). The LST composite and respective deviations are estimated for the whole period of study (October 2011 – September 2012).

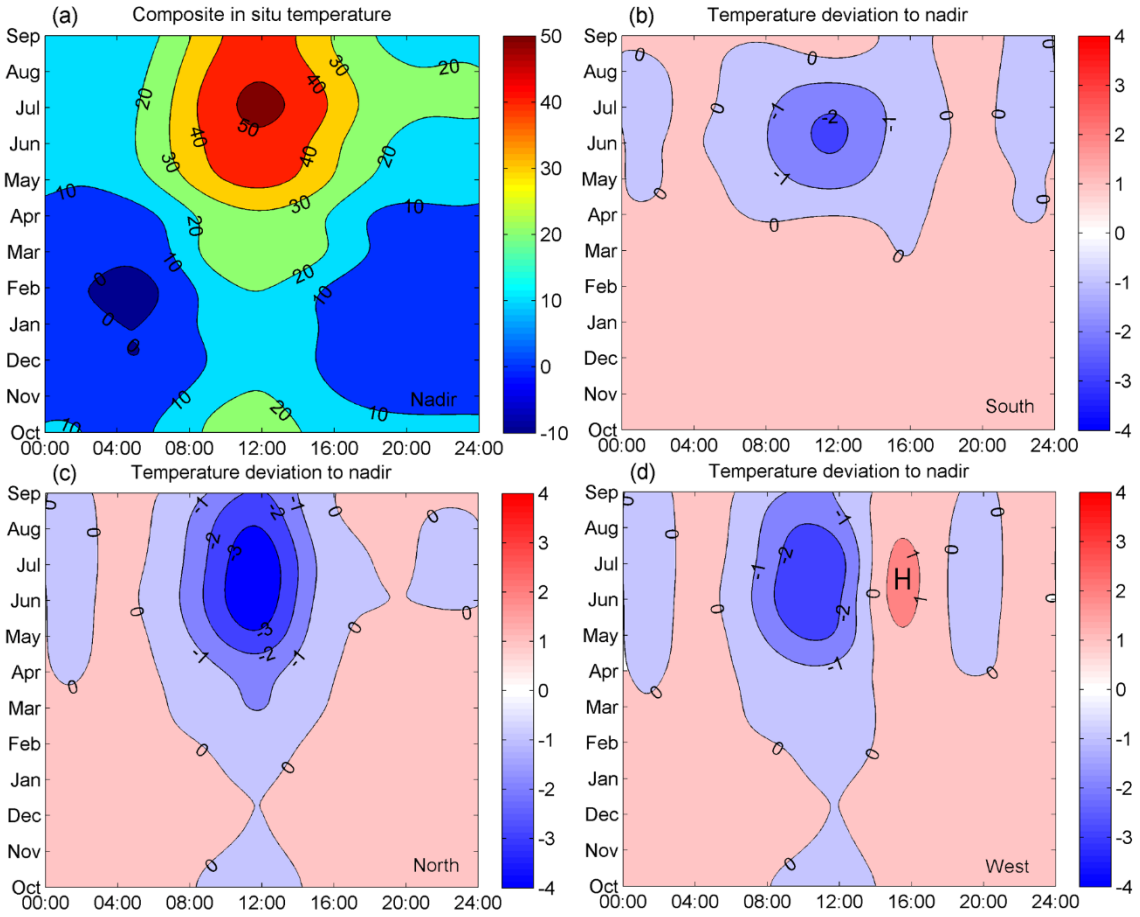

Figure 2.2.5 - (a) Average *in situ* temperatures (°C) per month (Oct 2011 to Sep 2012) and hour of the day estimated for nadir view; and temperature deviations with respect to nadir view (panel (a)) for different viewing geometries: (b) $\theta_v = 45°$ and $\phi_v = 180°$ (south view); (c) $\theta_v = 45°$ and $\phi_v = 0°$ (north view); and (d) for $\theta_v = 45°$ and $\phi_v = 270°$ (west view). Symbol "H" in panel d) indicates the hot spot.

Figure 2.2.5 shows that an increase in VZA results in a decrease in composite temperature, as the respective fractions of canopy, particularly of shaded background, increase. This is shown schematically in Figure 2.2.6 for nadir and for SEVIRI viewing geometries on a summer day: Figure 2.2.6 reveals that the fraction of shaded ground at noon is higher for the south (SEVIRI) view than for the nadir view. Moreover, Figure 2.2.6 illustrates how the area of shaded/sunlit ground is determined by the size of the tree shade, as well as by its position with respect to the canopy above. On top of this, the Boolean model provides the overlap probability of different tree canopies/shadows within the scene. This impact is stronger in summer months due to the higher contrast between shaded and sunlit background temperature – e.g., in July the differences in component temperatures can reach up to 30°C. During night-time the changes are negligible, as expected, since the temperature contrast between surface elements, i.e. background and canopy, is very small (Figure 2.2.1). For high zenith angles, however, the high fraction of tree canopy, which at night-time is warmer than the ground, leads to positive deviations. When considering changes in azimuth angle, it may be noted that viewing the scene from south (Figure 2.2.5(b)) results in higher temperatures than viewing the scene from north (Figure 2.2.5(c)), as easily explained by the sun position with respect to the observer (south view presented in the bottom row of Figure 2.2.6). A westward rotation leads to a decrease in composite temperature in the morning and an increase in the afternoon (Figure 2.2.5(d)). Again, this pattern is readily explained by the view-illumination geometries and the hot spot effect, i.e. in the afternoon the sun is located behind the sensor which results in a significant reduction of the shadow fraction.

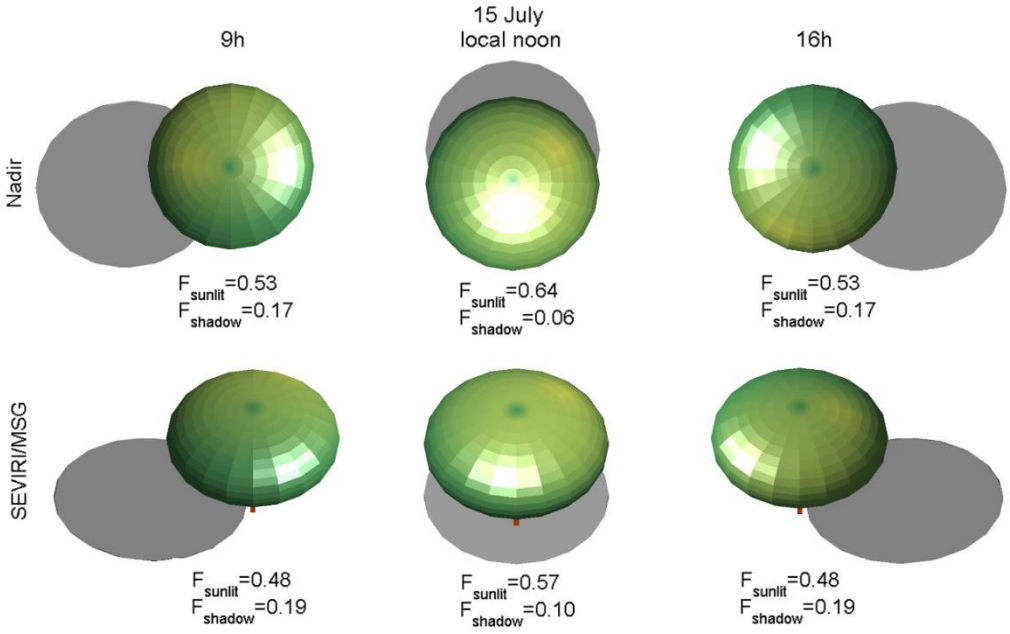

Figure 2.2.6 - Illustration of illumination and shadow produced by a single tree in Évora for a summer day (15 July), as seen from nadir (top row) and from SEVIRI zenith and azimuth angles (bottom row), corresponding to 9:00, 12:00, and 16:00 hours local time. The fractions of sunlit and shaded background that would be obtained with the geometric model are also indicated for each illumination/viewing configuration; the fraction of projected canopy is 0.30 for nadir and 0.33 for SEVIRI views, respectively.

SATELLITE VERSUS *IN SITU* MEASUREMENTS

Composited values of surface temperature as obtained with the geometric model were then used to assess SEVIRI and MODIS LST products. The comparison between satellite and *in situ* observations is performed for pixels closest to the Évora site and using the respective sensor viewing geometry to set up the appropriate composite *in situ* temperature. For both sensors, SEVIRI and MODIS, the composite temperature is calculated using the effective emissivity as defined in equation (2.2.6), yielding values between 0.9691 for the driest period in September, and 0.9773 for the greenest phase in April. It is assumed that this range reflects well the seasonal variability between dry and green understory that characterize the region. It is, however, acknowledged that emissivity uncertainties may be an important source of error for the *in situ* composite temperatures.

For reference, we also show the comparison between satellite LST and ground composites following a procedure where neither the daily and seasonal variations in the illumination geometry, nor the actual sensor viewing angles are taken into account. This procedure consists of a simple weighted average of sunlit background and tree crown temperatures, using the PTC, i.e. using fixed fractions of surface elements. This procedure is similar to that performed by Trigo et al. (2008a) for the same validation site.

Figure 2.2.7 presents scatterplots of satellite LST versus *in situ* temperature values obtained using the geometric model (lower panels) and using the above mentioned weighted temperature average where the effects of viewing and illumination geometry are not taken into account (upper panel). It is clear that both MODIS and SEVIRI-derived LST values are considerably closer to *in situ* composites obtained with the model (Figure 2.2.7c,d), which demonstrates the need to consider the directional character of LST products. This is further confirmed by the corresponding statistics shown in Table 2.2.2: taking all LST satellite products together, the daytime absolute bias (i.e. average of satellite LST minus *in situ* LST) and RMSE decrease by 1.5 to 2.5 °C when the viewing and illumination geometries of the scene are considered. It is worth noting that the STD of the difference between MODIS LST and *in situ* daytime temperature decreases by about 1.2 °C when the model is applied. The impact is smaller in the case of SEVIRI LST. In contrast to SEVIRI, which provides scene observations from a

fixed perspective, MODIS views the scene over a wide range of view angles (zenith angles up to 55°). As expected, the impact of the geometric correction on the night-time statistics is very small, while the large improvements at daytime considerably impact the overall statistics obtained for day and night-time data ("TOTAL" line in Table 2.2.2).

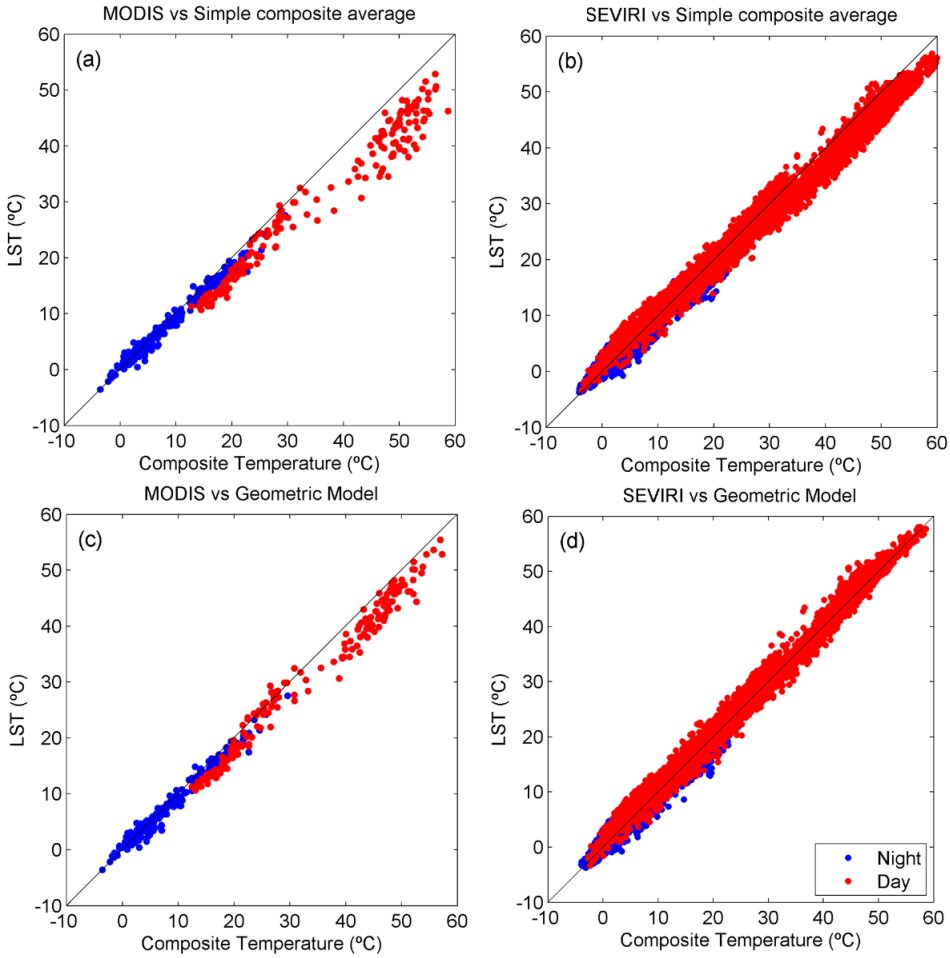

Figure 2.2.7 - Scatterplots of LST (°C) products as derived from MODIS (a, c) and SEVIRI (b, d) with the respective composite temperature as obtained using the geometric model (c, d) and using the composite with fixed fractions of surface elements (a, b). Blue dots indicate night-time measurements whereas red dots respect to daytime observations.

Overall MSG shows a better agreement with *in situ* observations than MODIS, presenting a lower RMSE, error standard deviation (STD) and bias for both daytime and night-time values (Table 2.2.2). MODIS LST tends to be cooler than composite temperature, keeping a bias of about -2.7 °C (-0.7 °C) for daytime (night-time) passages. In contrast, when the model is considered the biases of daytime SEVIRI LST values (about +0.5) are close to the uncertainty of *in situ* temperatures; RMSE are of the order of 1.5 °C during daytime. These results are not in agreement with the recent work by Guillevic et al. (2013), where MODIS LST (Collection 5) data are compared with *in situ* measurements taken in Évora; in that study, the application of a geometric model to upscale Évora measurements to MODIS observations leads to a negligible bias of satellite retrievals with respect to the *in situ* estimations. In the geometric model used by Guillevic et al. (2013), the area surrounding the station is populated with trees (similar percent to that used here) with crowns simulated as spheres of radius 6m. Although the referred study was carried out for a different period, we would obtain similar results for MODIS LST if the same tree shape parameters were introduced in our geometric model. A careful examination of the validation site suggests that 6m crowns may be oversized; the traditional pruning of trees also suggests these should be modeled as ellipsoids rather than spheres.

Table 2.2.2 - RMSE, error STD and bias for LST versus *in situ* composite temperature (°C) using the model (bold) and using the composite with fixed fractions of surface elements (italics). The values in parentheses correspond to the validation of MSG only using data for which MODIS observations are also available.

	RMSE		STD		BIAS	
	"simple composite"	modeled	"simple composite"	modeled	"simple composite"	modeled
			MODIS			
Daytime	*5.89*	**3.24**	*3.05*	**1.85**	*-5.04*	**-2.66**
Night-time	*1.34*	**1.35**	*1.19*	**1.17**	*-0.63*	**-0.68**
Total	*4.02*	**2.37**	*3.11*	**1.80**	*-2.56*	**-1.54**
			SEVIRI			
Daytime	*2.48* *(2.49)*	**1.50** **(1.51)**	*2.17* *(2.16)*	**1.42** **(1.33)**	*-1.19* *(-1.25)*	**0.50** **(0.72)**
Night-time	*1.27* *(1.21)*	**1.19** **(1.21)**	*1.27* *(1.22)*	**1.19** **(1.21)**	*-0.05* *(-0.04)*	**0.06** **(-0.08)**
Total	*1.90* *(1.88)*	**1.34** **(1.35)**	*1.82* *(1.80)*	**1.31** **(1.32)**	*-0.55* *(-0.57)*	**0.26** **(0.27)**

2.3 Assessing the potential of parametric models to correct directional LST

DATA PRE-PROCESSING

The geometric model is used to upscale the measurements performed at the Évora site for a variety of scenes. In particular, we consider a set of LST synthetic time-series generated for Évora-like sites, but with PTC varying from extremely sparse (in the limit with no trees, PTC=0%) to extremely dense (PTC=90%). In order to generate the LST values of scenes corresponding to varying viewing geometry, 100 view angles are selected randomly for each data point, with zenith angles ranging between 0º and 70º and azimuth angles ranging between 0º and 360º. This procedure results in 100 full-year LST time-series with varying sun-view configurations. The procedure is repeated for PTC values of 0%, 5%, and 10-90% with intervals of 10%.

EMISSIVITY PARAMETRIZATION

Effective emissivity is simulated for the wavelength range of the *in situ* radiometers using the Vegetation Cover method (Peres and DaCamara, 2005), as described in section 2.2. Following results suggested by previous works (Göttsche et al., 2013; Peres and DaCamara, 2005), vegetation emissivity is assumed to be constant with view angle. The rationale for this lies on the fact that reflectivity (and therefore emissivity) of rough surfaces is more likely to be related to volumetric effects rather than specular, explaining the absence (or weak) dependency of vegetation emissivity on viewing angles (Sobrino et al., 2005; Sobrino and Cuenca, 1999; Ulaby et al., 1981). On the other hand, the emissivity of bare ground surfaces often presents an angular dependence (Labed and Stoll, 1991; Ren et al., 2011; Sobrino and Cuenca, 1999).

Based on field measurements, García-Santos et al. (2012) found that soil emissivity decreases with VZA, following approximately:

$$\varepsilon_{soil}(\theta_v) = \varepsilon_0 - 8.7 \times 10^{-9}\theta_v^{\alpha} \quad (2.3.1)$$

with parameter α = 3.47, and where θ_v is the VZA and ε_0 is the soil emissivity at nadir. Here, we use equation (2.3.1) to model the variation of bare ground emissivity with view angle, but setting parameter α to 3.5, 3.3 and 3.1, representing different scenarios with a strong, moderate and weak dependence of emissivity on view angle, respectively (Figure 2.3.1).

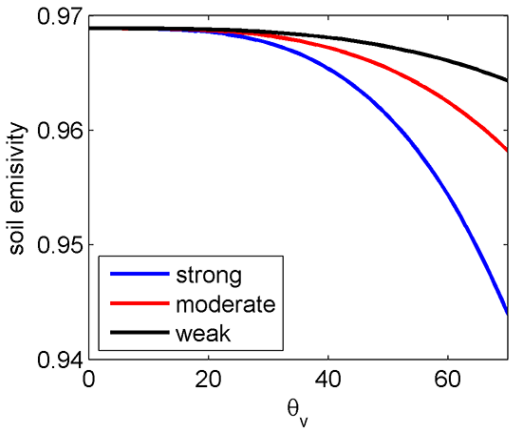

Figure 2.3.1 - Soil emissivity dependence on VZA (θ_v; in degrees) as given by eq. (2.3.1) with $\alpha = 3.5$ (strong dependence; blue), $\alpha = 3.3$ (moderate dependence; red) and $\alpha = 3.1$ (weak dependence; black).

The FVC of the scene is assumed to vary seasonally, a common behavior in most land cover types. This implies an important seasonality in the surface emissivity and, therefore, such marked seasonal cycle is simulated for different hypothetical tree coverages. In order to provide a realistic seasonal fraction of vegetation, the scene's fraction of vegetation is estimated from FVC as observed by SEVIRI over the in-situ station. Monthly averages of FVC were computed using data encompassing the years 2010-2012, providing realistic values at the location. A Fourier series was then fitted to the data in order to simulate the hypothetical seasonal variation of the FVC over the scene (Figure 2.3.2):

$$FVC(t) = \overline{FVC} + \Lambda \sin(\omega t + \chi) \tag{2.3.2}$$

where t is the month and $\overline{FVC} = 0.42$ is the annual mean FVC. The amplitude, frequency and phase of the FVC cycle are $\Lambda = 0.18$, $\omega = \pi/6$ and $\chi = -0.25$, respectively. It is assumed that the minimum of FVC corresponds to the PTC at the pixel. For the adjusted function, the minimum FVC is approximately 25% and occurs in September. The hypothetic seasonal cycle of FVC for other values of PTC is then obtained by shifting the curve, i.e.:

$$\overline{FVC}(PTC) = PTC + 0.17 \tag{2.3.3}$$

and all FVC values are saturated at 0% and 100%.

The geometric effects in the effective emissivity are accounted for using the Geometric model to calculate the increment in observed canopy with view angle. Figure 2.3.2b shows the variation of the fraction of canopy, f_{canopy}, seen with view angle θ_v for different values of PTC.

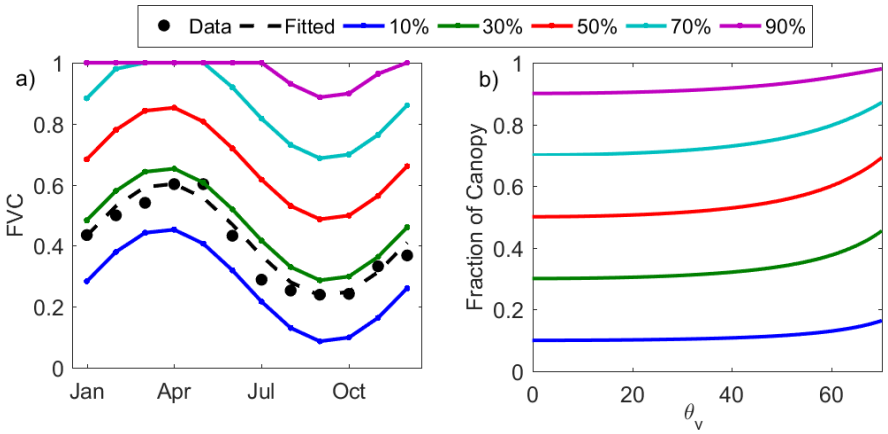

Figure 2.3.2 - a): Monthly fraction of vegetation cover (FVC) as measured by SEVIRI at Évora (dots), values provided by eq. (2.3.2) (dashed line) and respective values obtained for different PTC values as given by eq. (2.3.3) (colored lines). b): variation of the observed fraction of canopy for different values of PTC, as obtained using the Geometric model.

THE PARAMETRIC MODELS

THE KERNEL MODEL

As proposed by Vinnikov et al. (2012), the LST angular dependence may be modeled through a kernel approach, hereafter referred to as the Kernel model. The Kernel model provides the dependence of LST on viewing and illumination geometries by means of a statistical approach that is expressed by the following equation:

$$\frac{T(\theta_v, \theta_i, \Delta\phi)}{T_0} = 1 + A\Phi(\theta_v) + D\Psi(\theta_v, \theta_i, \Delta\phi) \quad (2.3.4)$$

where $(\theta_v, \theta_i, \Delta\phi)$ are the view zenith, sun zenith and sun-view relative azimuth angles, respectively, and $T_0 = T(\theta_v = 0, \theta_i)$ is the LST as viewed in the nadir direction. A and D are coefficients to be estimated from observations, that capture land cover structure. Following Vinnikov et al. (2012), the "emissivity kernel", $\Phi(\theta_v)$, and the "solar kernel", $\Psi(\theta_v, \theta_i, \Delta\phi)$, are defined by the following expressions:

$$\Phi(\theta_v) = 1 - cos(\theta_v) \quad (2.3.5)$$

$$\Psi(\theta_v, \theta_i, \Delta\phi) = sin(\theta_v)cos(\theta_i)sin(\theta_i)cos(\theta_i - \theta_v)cos(\Delta\phi) \quad (2.3.6)$$

The "emissivity kernel" is associated only to variations in the observation zenith angle, whereas the "solar kernel" models the shadowing/sunlit effects on the surface, which lead to inhomogeneous heating due to the different thermal behavior of the various surface components. It is worth emphasizing that the expressions used to model emissivity anisotropy when generating the synthetic data set (eq. (2.3.1)) are different from the one used here (eq. (2.3.5)).

The fit of this model is performed by linear regression using the procedure initially proposed by Vinnikov et al. (2012). The emissivity kernel coefficient, *A*, is first adjusted to night-time data (when *D* is null). The solar kernel coefficient, *D*, is then fitted by fixing the *A* value and using daytime data only. For consistency with the Hotspot model, eq. (2.3.4) is rearranged to allow a fit to LST differences instead of ratios:

$$T(\theta_v, \theta_i, \Delta\phi) - T_0 = AT_0\Phi(\theta_v) + DT_0\Psi(\theta_v, \theta_i, \Delta\phi) \quad (2.3.7)$$

THE HOTSPOT MODEL

The model proposed by Lagouarde and Irvine (2008), hereafter referred to as the Hotspot model, was heuristically derived from the parametric hot spot model developed by Roujean (2000) for the optical domain, with reflectance being formally replaced by LST (Duffour et al., 2016). The dependence of LST (*T*) on illumination and viewing geometries is expressed as:

$$T(\theta_v, \theta_i, \Delta\phi) - T_0 = \Delta T_H \frac{e^{-Kd} - e^{-Ktan\theta_i}}{1 - e^{-Ktan\theta_i}} \quad (2.3.8)$$

where θ_v, θ_i are again the view and illumination zenith angles, and $\Delta\phi$ the difference in azimuth angles and T_0 is the LST at nadir. K and ΔT_H are the model coefficients to be estimated and d is the hemispherical (angular) distance between the sun and viewing positions defined:

$$d = \sqrt{tan^2\theta_i + tan^2\theta_v - 2tan\theta_i tan\theta_v cos\Delta\phi} \quad (2.3.9)$$

taking the value $d_0 = tan\theta_i$ at nadir.

According to Roujean (2000), for the optical domain, k is closely related to canopy structure, in particular the Leaf Area Index (LAI). The parameter ΔT_H represents the deviation from T_0 of the LST observed under hotpot conditions, i.e., when the sun is effectively positioned behind the observer. ΔT_H therefore represents the anisotropy in the hotspot geometry and responds to thermal contrasts between the different surface components.

It may be noted that the Hotspot model formulation does not allow estimating LST directional effects during night-time. The model is fitted to daytime data by Mean Square Error (MSE) minimization, following the Nelder-Mead simplex method (Lagarias et al., 1998).

PARAMETERIZATION OF ΔT_H

Since ΔT_H is a parameter of the Hotspot model, it is implicitly assumed to be constant in the model formulation. However, ΔT_H is expected to depend on the temperature contrasts between the different surface components (sunlit/shadow ground, canopy), which in turn may vary with the time of day and day of year. As such, we propose that those contrasts may be simulated as a function of daily available top of the atmosphere (TOA) radiation and sun angle. We therefore propose using a more realistic representation of the hotspot geometry (i.e., relaxing the original assumption of a constant ΔT_H) by introducing the following parameterization:

$$\Delta T_H = \mathrm{B} \cdot \mathrm{Rad}^*_{TOA} \cdot \sin(2\theta_i) \quad (2.3.10)$$

where Rad^*_{TOA} is the daily TOA radiation normalized by the daily solar constant (Meeus, 1991), B is a new parameter of the model and $\sin(2\theta_i)$ is used to characterize the daytime cycle of surface temperature. Ultimately, this new formulation of the model leads to the same number of parameters but the dependence on Rad_{TOA} results in a seasonal and latitudinal variation of ΔT_H. The Hotspot model formulation together with the above-described parameterization of ΔT_H will be referred hereafter as Modified Hotspot model.

THE KERNEL-HOTSPOT MODEL

The hotspot model was designed to account for the variability in LST resulting from illumination and viewing geometries, alone. On top of these, the kernel model considers that directional effects in LST may also arise from changes in emissivity with view angle. As such, we propose a new scheme that results from the combination of the two models: we consider the characterization of the emissivity directionality proposed in the kernel model, together with the simulation of shadowing effects from the hotspot model:

$$T(\theta_v, \theta_i, \Delta\phi) - T_0 = AT_0\Phi(\theta_v) + \mathrm{B}\,\mathrm{Rad}^*_{TOA}\sin(2\theta_i)\frac{e^{-Kd} - e^{-Ktan\theta_i}}{1 - e^{-Ktan\theta_i}} \quad (2.3.11)$$

Here *A* is also first adjusted to night-time data by linear regression, and B and K are then calibrated with daytime data using MSE minimization.

PERFORMANCE OF THE KERNEL AND HOTSPOT MODELS

The Kernel and Hotspot models are adjusted to the synthetic LST time-series for each defined PTC value and each emissivity parametrization. As mentioned in methods section, for each PTC value, 100 time-series are available with varying view angles. Ultimately, 547 900 points are available for the fit of the emissivity kernel (night-time) and 688 400 data points are available for the fit of the solar kernel and the Hotspot model (daytime). Figure 2.3.3 shows the obtained parameters of the two models and the respective RMSE of fit.

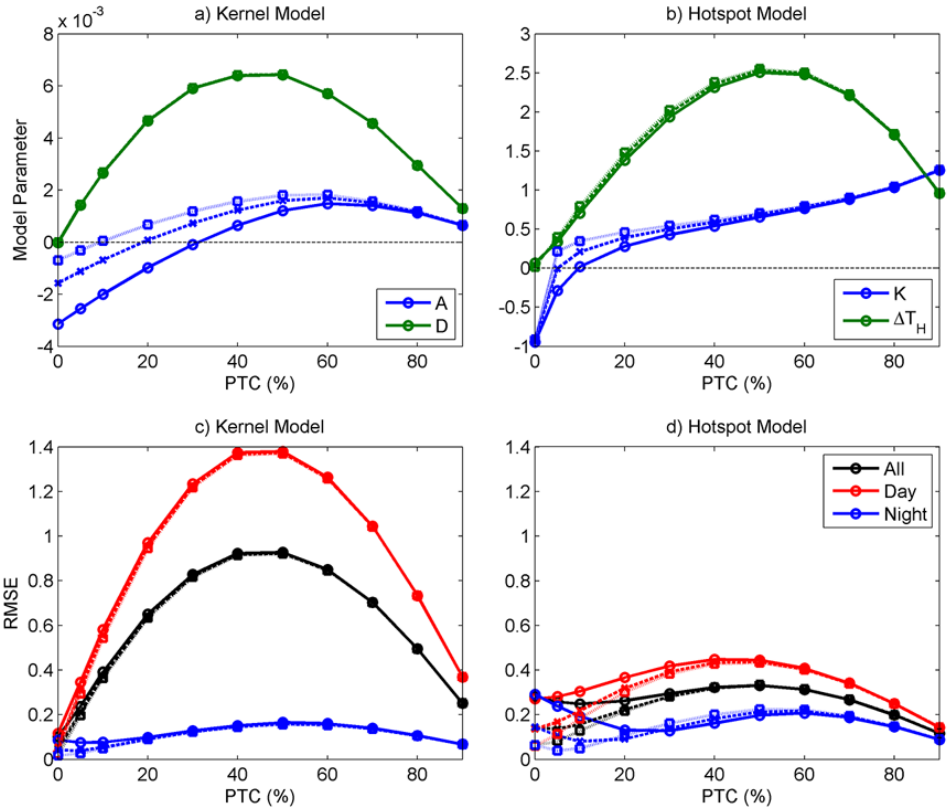

Figure 2.3.3 - Parameters of the Kernel model (a) and Hotspot model (b) as a function of the Percent of Tree Cover (PTC) for different scenarios of the dependency of bare ground emissivity with view angle: strong (circles), moderate (crosses) and weak (squares) dependence; respective RMSE (ºC) of fit (c,d).

Figure 2.3.3a reveals that the emissivity kernel parameter, *A*, is most relevant for 0% PTC and when soil emissivity presents the strongest variation with view angle. As expected, as the angular dependence of soil emissivity decreases, so does the absolute value of *A*. However, at PTC's of about 30%/20%/10% for strong/moderate/weak emissivity anisotropy, A is null because there is a balance between the emissivity decrease with view angle due to the soil emissivity anisotropy (intrinsic anisotropy) and the increase of emissivity with view angle as the fraction of seen canopy increases (geometric effect). For higher PTC, the latter effect seems to prevail, with *A* then reaching a maximum for 60% PTC. Since for PTC values around 60%, geometric effects play the major role (i.e. the scene is dominated by vegetated/high emissivity, and to a lesser extent by bare-soil/lower emissivity), *A* is positive. On the other hand, the shadowing effects are nonexistent for 0% (and 100%) PTC, which leads to a null solar kernel parameter, *D*. Parameter *D* is not sensitive to emissivity anisotropy. A

maximum of *D* is observed for 50% of PTC, which corresponds to the ideal shadow-to-sunlit fractions ratio that leads to the strongest LST directional effects.

Parameter ΔT_H of the Hotspot model (Figure 2.3.3b) presents a behavior similar to that of the solar kernel parameter *D*, with a maximum at 50% of PTC. Vegetation parameter, *K*, shows an approximately linear dependence with PTC, which is in agreement with the dependence on vegetation found by Roujean (2000) for the reflectance model. For very low PTC values, the emissivity has high impact on the LST directionality and *k* becomes erratic. Since the model was designed to simulate the hotspot geometry, when this geometry is very weak or absent (i.e. when ΔT_H is very close to zero, the model returns the best fit of the LST differences to a hotspot effect, resulting in negative values of *k*. This suggests the Hotspot model could benefit from adding an emissivity kernel term.

The Hotspot model presents an overall better agreement with the Geometric model, with exception of night-time and for very low PTC values (0-5%; Figure 2.3.3c,d). The Kernel model considers a sinusoidal dependence on incoming radiation (eq. (2.3.6)), while the hotspot model presents an exponential dependence on the tangent of the sun angle (eq. (2.3.10)). As a result, the Kernel model is not able to simulate the full amplitude of the thermal contrast between surface objects and underestimates the LST directionality. Nevertheless, the Kernel model shows a high potential to model LST anisotropy associated with emissivity, while the Hotspot scheme is unable to simulate such dependence.

Naturally, performance of the models depends on the strength of the soil emissivity anisotropy, especially in the case of the Hotspot model. To simplify our analysis, in the following sections we will only present results regarding the strongest emissivity angular dependence.

PARAMETERIZATION OF ΔT_H: THE MODIFIED HOTSPOT MODEL

Figure 2.3.4 shows the dependence of values of ΔT_H on sun zenith angle (θ_i) and day of the year (DOY) as given by the geometric model. As θ_i approaches zero, the hotspot occurs closer to the nadir and therefore ΔT_H is lower. For high values of θ_i, temperature contrasts are expected to be very low and hence ΔT_H approaches zero. The maximum of ΔT_H is obtained for θ_i values that simultaneously maximize the distance to nadir and the temperature contrasts. As expected, in summer the amplitude of the surface temperature is higher and consequently ΔT_H is higher. This suggests introducing a dependence of ΔT_H on θ_i that is related to the forcing by the radiation available for surface warming as expressed by equation (2.3.10).

The Modified Hotspot model was adjusted to the synthetic LST dataset with a bare-ground emissivity varying with VZA setting $\alpha = 3.5$ (eq. (2.3.1)). Figure 2.3.5 presents the parameters of the Modified Kernel-Hotspot model and the respective RMSE of fit, for different scenarios of PTC. Values obtained for the original Hotspot model are also shown for reference. It is worth noting that the introduction of a non-constant ΔT_H shows no impact on the values of *k*. However, the new formulation leads to an improvement of the RMSE values when compared to the old one, especially for PTC values in the range 20-60%.

COMBINATION THE MODELS: KERNEL-HOTSPOT MODEL

Results from the previous sections suggest that using the Hotspot or the Modified Hotspot models will allow a better characterization of shadowing effects. However, the model does not allow the simulation of emissivity anisotropy, which could largely affect its performance over desert areas and during night-time. A simple solution to this limitation is combining the Kernel and the Hotspot models in a formulation similar to the Kernel model, as expressed by eq. (2.3.11).

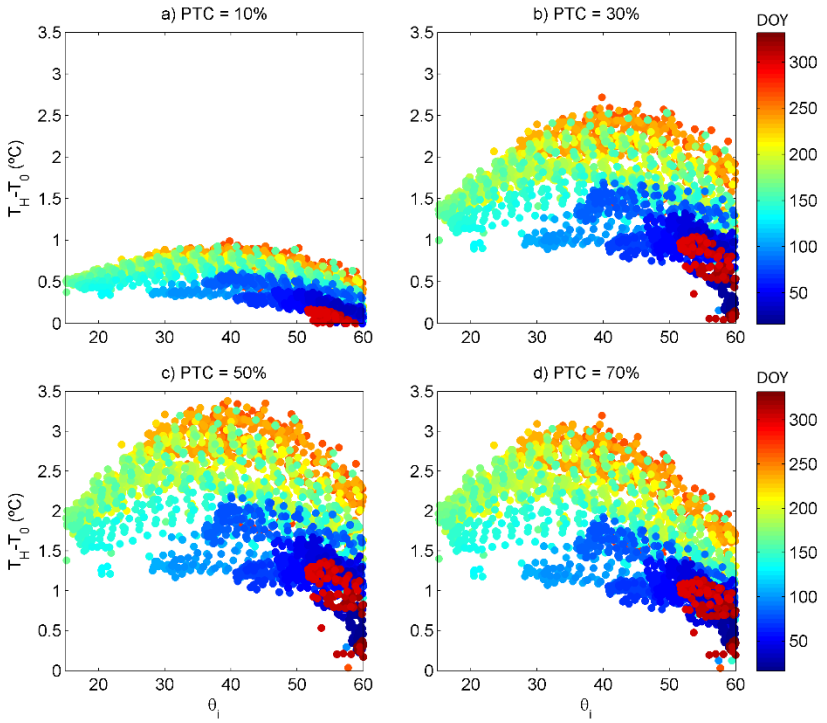

Figure 2.3.4 - LST difference between the hotspot geometry and the nadir ($T_H - T_0$) as function of the sun zenith angle (θ_i) and of the day of year (DOY; colorbar), for different values of PTC.

Figure 2.3.6 shows the parameters of the Kernel-Hotspot model and the respective RMSE of fit, for different scenarios of PTC. As in the previous sections, bare-ground emissivity varies with VZA following eq. (2.3.1), with $\alpha = 3.5$ (strong dependency on view angle). Values obtained for the Modified Hotspot model are also shown for reference. Since the emissivity kernel parameter, *A*, is calibrated with the same procedure as in the Kernel model (restricted to night-time data) there are no changes in A. When compared with the Modified Hotspot model, the Hotspot-Kernel parameters *B* and *k* show slight variations. These occur mostly for PTC ranges where *A* has higher impact, namely 0-20% and 40-90%. The RMSE values show an overall improvement compared with the Hotspot model, in particular for low PTC values and for night-time, with reductions as high as 0.2ºC.

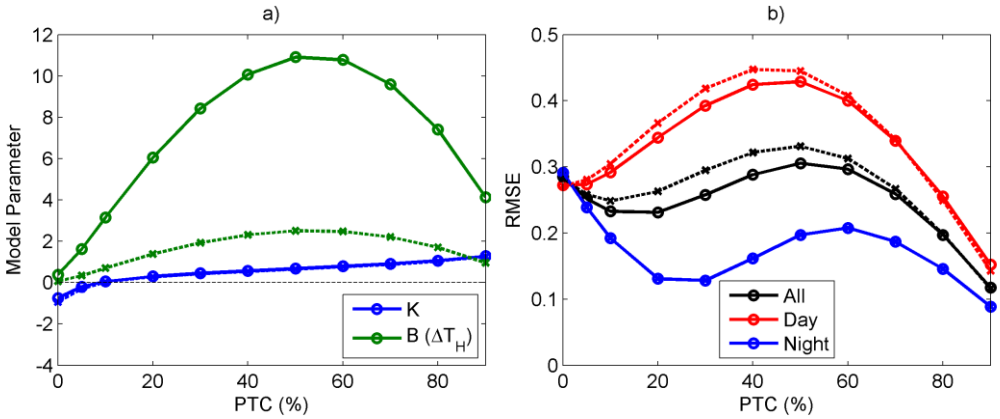

Figure 2.3.5 - Parameters of the Modified Hotspot model (a) as function of the PTC, and respective RMSE (ºC) of fit (b). The values obtained for the original Hotspot model (dashed lines) are also shown for reference.

In this case, the use of a different emissivity parameterization (i.e., using other values of parameter α in equation (2.3.1) has no impact on the hotspot parameters, affecting only the emissivity kernel as mentioned before. Consequently, for weaker emissivity angular dependence the impact on the RMSE when combining the models is reduced.

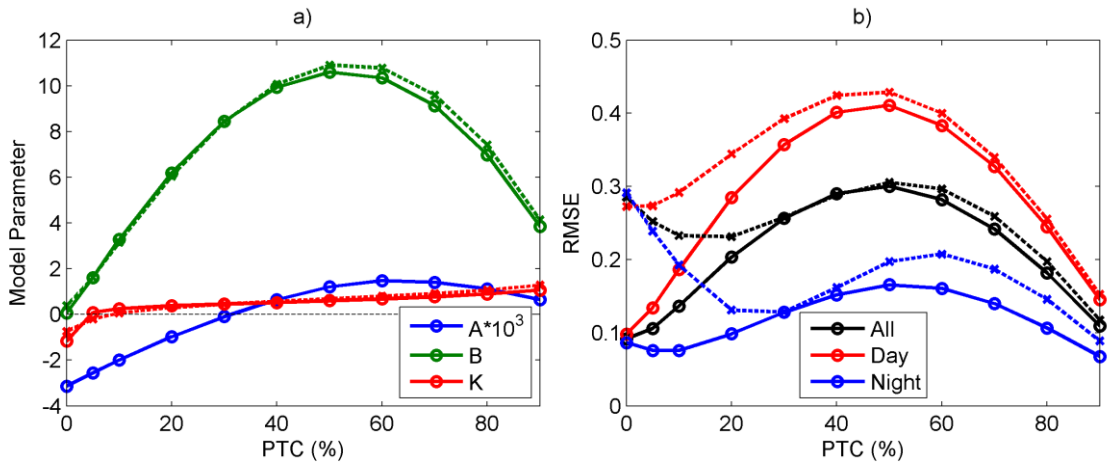

Figure 2.3.6 - Parameters of the Kernel-Hotspot model (a) as function of the PTC, and respective RMSE (ºC) of fit (b). The values obtained for the Modified Hotspot model (dashed lines) are also shown for reference.

MONTHLY ADJUSTMENT OF THE MODELS

LST directionality is expected to present a strong seasonal behavior, resulting from the different temperature amplitudes and from changes in the emissivity due to the vegetation cover. In order to better understand the impact of such seasonality on the parametric models, these are also calibrated on a month-by-month basis. Figure 2.3.7 shows the models' parameters obtained for August and January, as a function of PTC, and the respective annual RMSE values.

Parameters of the Kernel model present a pronounced seasonality (Figure 2.3.7a). Seasonal dependence of the emissivity kernel parameter, *A*, is associated with the impact of FVC on the emissivity anisotropy. Parameter *A* presents the lowest values during July-September, when the FVC is minimum and the intrinsic anisotropy dominates the directionality of emissivity resulting in negative *A* values. During January-March *A* is maximum since the high FVC values lead to emissivity anisotropy driven by geometric effects (hence positive *A* values). The seasonal change of the solar kernel, parameter *D*, is in turn associated with the annual cycle of the surface components' temperatures. As expected, *D* values are lower in November-January, when temperature contrasts are reduced, and are maximum in June-August.

As in the case of the Kernel parameter *D,* the seasonality of parameter ΔT_H of the Hotspot model (Figure 2.3.7b) and of parameter B of the Modified Hotspot (Figure 2.3.7c) and Kernel-Hotspot models (Figure 2.3.7d) is driven by the temperature contrast among surface elements, leading to a similar behavior in all of them. The lowest values of the parameters occur during December-February, while the highest occur during July-August. The vegetation parameter, *K*, shows a distinct behavior between the autumn/winter months (October to February) and the spring/summer months (March to September) for both the Hotspot (Figure 2.3.7b) and the Modified Hotspot models (Figure 2.3.7c). This contrasting behavior of *k* is not present in the Kernel-Hotspot model (Figure 2.3.7d), which suggests that this effect is related to emissivity seasonality that is accounted for with the emissivity kernel.

Despite the high variability shown by the models' parameters, the impact on the overall RMSE is small when compared to the original global models (Figure 2.3.7e,f). Monthly models may be more closely adjusted to conditions where directional effects are stronger (e.g., summer months), and therefore lead to slightly improved overall scores. However, the monthly calibration of the models has the caveat of being limited to a smaller range of illumination angles, which will greatly affect the robustness of the parameters. Besides, the seasonal variability of LST directionality may be incorporated, at least partially, in the annual models through the dependence on sun zenith angle, which is related to the amount of incoming radiation, and on daily TOA radiation (in the case of the Modified Hotspot and Kernel-Hotspot models).

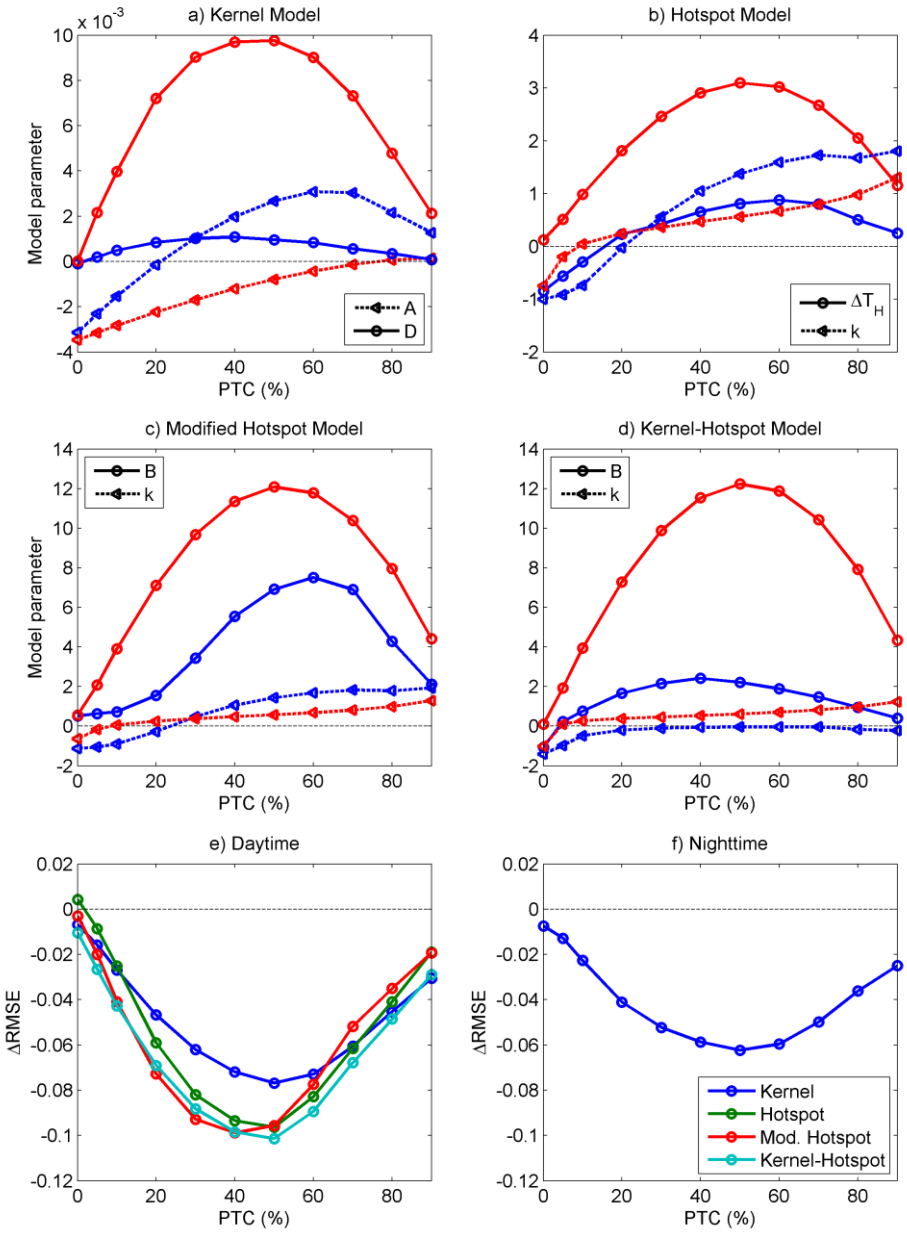

Figure 2.3.7 - Parameters of the Kernel (a), Hotspot (b), Modified Hotspot (c) and Kernel-Hotspot (d) models adjusted on a monthly basis for August (red) and January (blue), for different scenarios of PTC. The respective differences (ΔRMSE in °C) between the total annual RMSE obtained with the monthly models and the RMSE of the annual models (shown in Figure 2.3.3c,d, 6b and 7b) are shown in the lower panels, for each PTC scenario (e,f).

Nevertheless, there is an important seasonal change in the behavior of the emissivity kernel, resulting in the change of the signal of the parameter *A*. This is related to contrasting conditions in the simulated scenes that lead to a predominance of intrinsic anisotropy in summer and of geometric effects during winter. Since the emissivity kernel does not depend on sun angle, a seasonal fit of this kernel could be performed that is not susceptible to sampling problems.

SENSITIVITY TO VIEW ANGLE SAMPLING

We assume that models, such as those studied here, may be adjusted using collocated observations (or LST products) from geostationary and polar-orbiter platforms. However, sensitivity of the models to angle sampling is an important factor that must be taken into account when using satellite data, since it may significantly affect model calibration. The viewing angle sampling is particularly relevant when using geostationary sensors given their fixed viewing geometry. The impact of the view angle sampling

is analyzed using limited ranges of view angles to calibrate the models, namely for view zenith and azimuth angles (θ_v, ϕ_v) of $(20° \pm 10°, 100° \pm 15°)$, $(40° \pm 10°, 100° \pm 15°)$, $(60° \pm 10°, 100° \pm 15°)$, $(20° \pm 10°, 260° \pm 15°)$, $(40° \pm 10°, 260° \pm 15°)$, and $(60° \pm 10°, 260° \pm 15°)$. Each subset is generated using the procedure described in the Data section but limiting the view angles ranges.

In order to better analyze the impact of the parameters' variability on the LST RMSE between the Geometric model and the parametric models, the respective scores are calculated only for a fixed view geometry, namely $(\theta_v, \phi_v) = (60°, 180°)$, for which high angular effects are expected. Figure 2.3.8 shows the resulting RMSE change with respect to the global models for night and daytime. The impact is higher for the Kernel and Kernel-Hotspot models, with RMSE variations above 0.3ºC. The Kernel model is particularly sensitive to the sampling of the VZA (Figure 2.3.8a,b), in particular for low PTC values.

The Modified Hotspot model (Figure 2.3.8d) presents higher RMSE changes than the original Hotspot model (Figure 2.3.8c), reaching 0.3ºC and 0.1ºC, respectively. Both models are most sensitive to the azimuth angle. This is likely related to the configuration of the hotspot: a sensor observing the scene from the east $(100°)$ will be susceptible to the hotspot during the morning, while for a sensor observing from the west $(260°)$ the hotspot is likely to occur during the afternoon. This means that different temperature contrasts will impact the model's fit, resulting in a different retrieval of the parameters. This is an expected behavior for these types of models, suggesting that the Kernel model may be limited in the simulation of the hotspot effect.

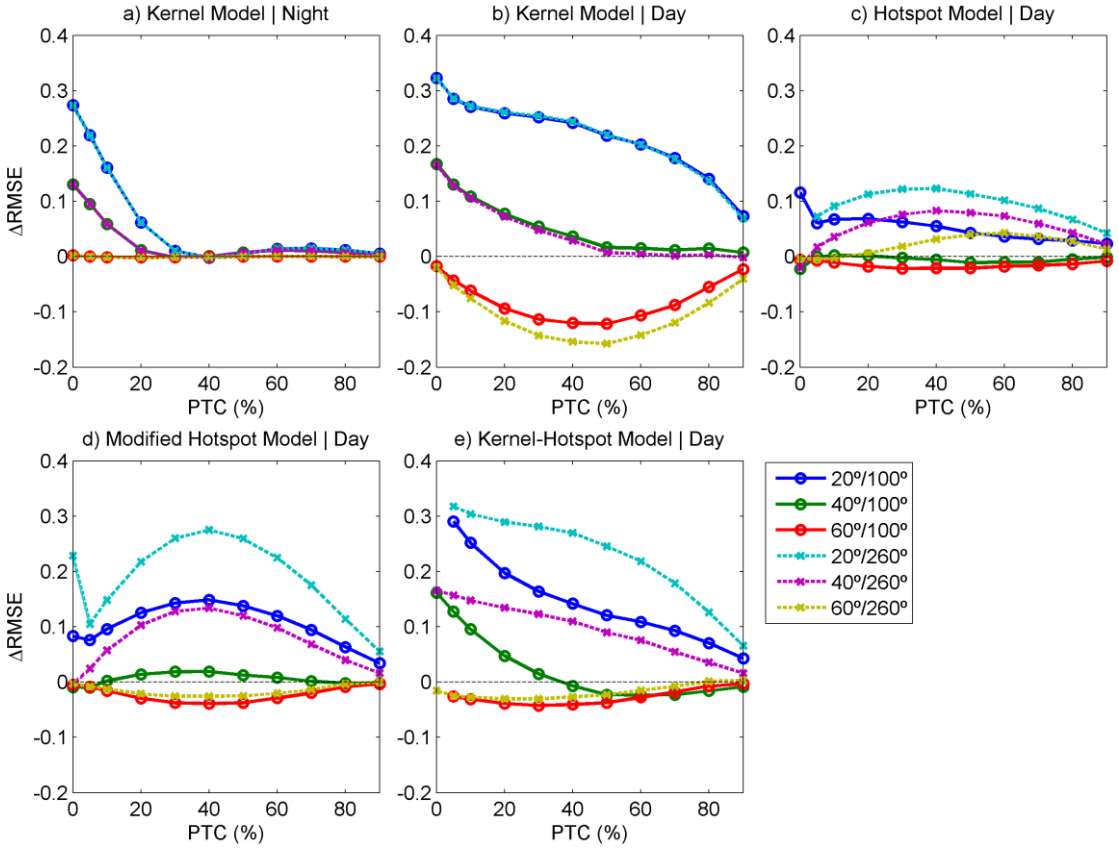

Figure 2.3.8 - Change of the RMSE (ºC) of the Kernel (a,b), Hotspot (c), Modified Hotspot (d) and Kernel-Hotspot (e) models with respect to the global models as function of the PTC, as obtained using the new subsets of LST with limited viewing angles, namely for (θ_v, ϕ_v) in the range $(20° \pm 10°, 100° \pm 15°)$, $(40° \pm 10°, 100° \pm 15°)$, $(60° \pm 10°, 100° \pm 15°)$, $(20° \pm 10°, 260° \pm 15°)$, $(40° \pm 10°, 260° \pm 15°)$, and $(60° \pm 10°, 260° \pm 15°)$. All RMSE values are calculated for a fixed view angle $(\theta_v, \phi_v) = (60°, 180°)$.

For the Kernel-Hotspot model (Figure 2.3.8e) there is a combination of the effects observed in the Kernel and the Modified Hotspot model, with the highest RMSE variations occurring for low PTC values. Moreover, there is a distinct impact on the RMSE associated with both the azimuth and zenith angles.

SENSITIVITY TO SUN ANGLE SAMPLING

Specific attention must be paid to the illumination angle sampling when using polar orbit sensors to calibrate the models, given the reduced frequency of observation. In order to study the models' sensitivity to sun angle sampling, the synthetic LST time-series used in the calibration are limited to a few hours of the day, namely for [8,10[, [10,12[, [12,14[, [14,16[and [16,18[UTC. Each parametric model is fitted to each subset with limited observation times and the respective RMSE is calculated for a fixed view geometry, namely $(\theta_v, \phi_v) = (60°, 180°)$. Figure 2.3.9 shows the RMSE change with respect to the global models.

The Kernel model (Figure 2.3.9a) presents the lowest sensitivity to the sun angle sampling, with RMSE changes up to 0.1ºC, while the Modified Hotspot (Figure 2.3.9c) and Kernel-Hotspot (Figure 2.3.9d) models present the higher sensitivity, with RMSE changes as high as 0.5ºC. The highest values of ΔRMSE occur for calibrations with early morning or late afternoon LST data, which is to be expected given the lower temperature contrasts observed at these times-of-day. The Hotspot model (Figure 2.3.9b) presents higher RMSE changes than the Kernel model. Since the Hotspot model includes an exponential dependence on the sun geometry (eq. (2.3.8)), it may be more sensitive to the sun angle sampling than the Kernel model. The introduction of an extra dependence on the sun angle through the parameterization of ΔT_H (eq. (2.3.10)) further increases the sensitivity of the models, which is well apparent in the high RMSE changes observed for the Modified Hotspot and Kernel-Hotspot models.

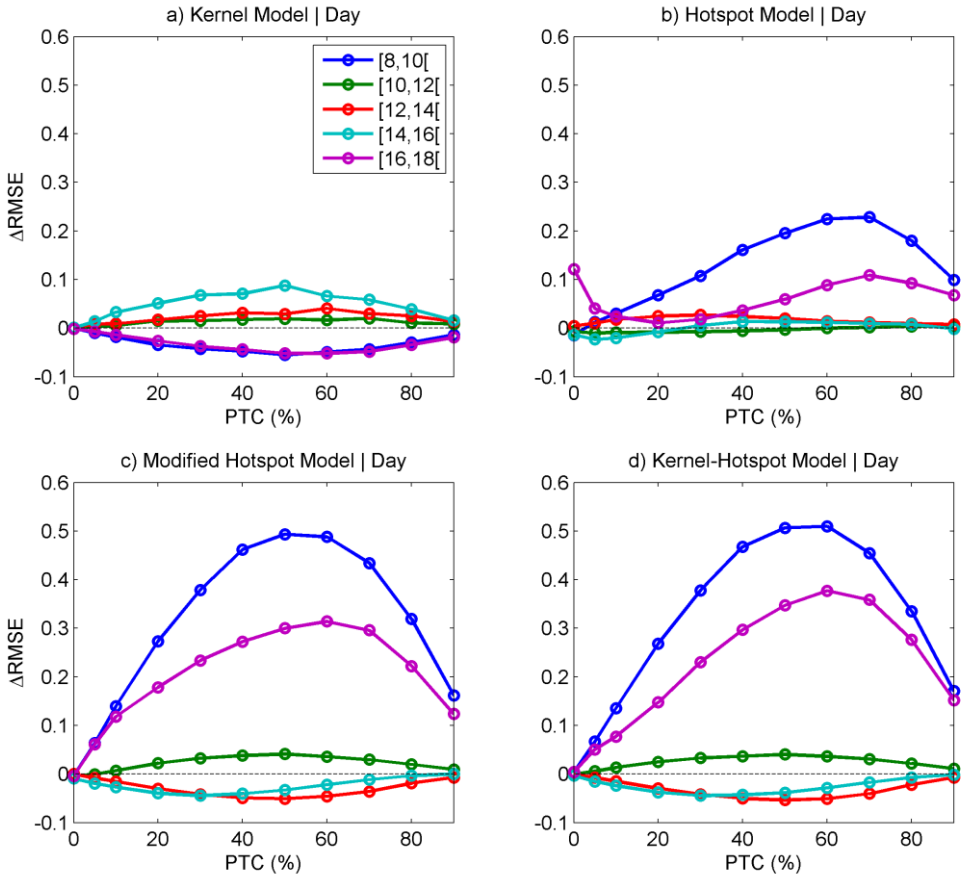

Figure 2.3.9 - Variation of the RMSE (ºC) of the Kernel (a,), Hotspot (b), Modified Hotspot (c) and Kernel-Hotspot (d) models with respect to the global models as function of the PTC, as obtained using the new subsets of LST with limited observation times, namely for [8,10[, [10,12[, [12,14[, [14,16[and [16,18[UTC. All RMSE values are calculated for a fixed view angle $(\boldsymbol{\theta_v, \phi_v}) = (\mathbf{60°, 180°})$.

SIMULATION OF THE ANGULAR CORRECTIONS ON LST

In order to further analyze the performance of the parametric models in simulating the LST directionality, the models are here used to compute a hypothetical angular correction to nadir. For different PTC scenarios and view angles, we estimate the average $(T - T_0)$ values for each month and time of the day using the geometric model (our reference model), as well as the Kernel, the Hotspot and the Kernel-Hotspot models. Figure 2.3.10 to Figure 2.3.12 show some examples of the obtained $(T - T_0)$ averages.

For a PTC of 0% (Figure 2.3.10) the Kernel model underestimates the maximum of the corrections by about 0.3ºC. There is a seasonal pattern in the Geometric model that is related to the vegetation cycle. Even though the tree coverage is null, a seasonal variation of understory vegetation is still considered. During winter, part of the ground will be covered by understory, which reduces the impact of emissivity anisotropy of soil on the LST directionality. Since emissivity presents a non-linear impact on LST, the higher corrections of LST will be observed during daytime, when LST presents higher amplitude. The seasonal pattern in the Geometric model is not fully reproduced by the Kernel model. This is to be expected, since the emissivity kernel has no information on illumination geometry. The model will fit to the average behavior of the full dataset, which partly explains the underestimation of the amplitude of the corrections, especially considering that this fit is performed with night-time data only. The pattern presented by the Hotspot model is completely different from the one by the Geometric model. The Hotspot model tries to fit a hotspot effect to the observed differences and this leads to a wrong result. The combined Kernel-Hotspot model presents an improvement with respect to the Kernel model in terms of the range of values, but the shape is slightly shifted, clearly influenced by the hotspot effect given by the Hotspot model.

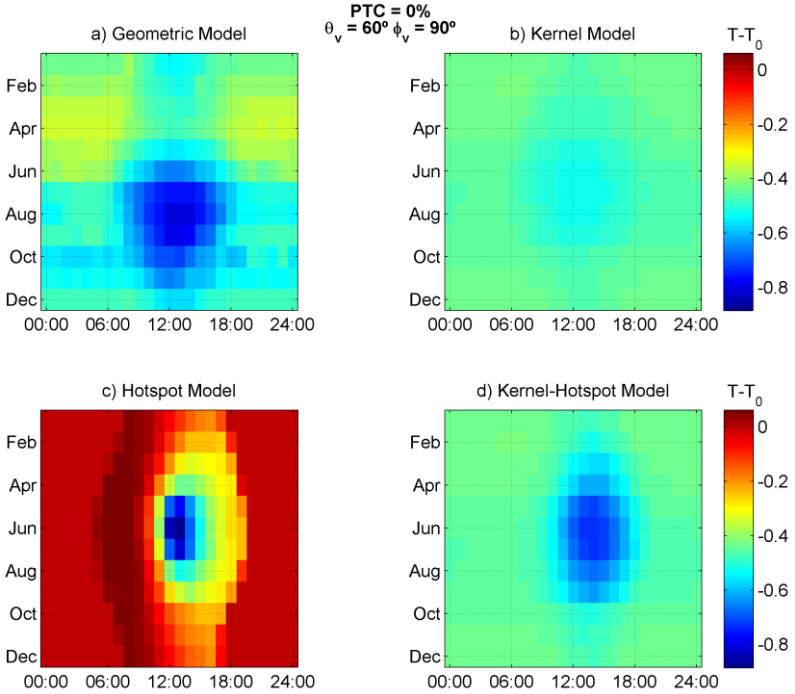

Figure 2.3.10 - Average $T - T_0$ (ºC) for each month and hour of the day (UTC) as given by the Geometric model (a), the Kernel model (b), the Hotspot model (c) and the Kernel-Hotspot model (d) for a PTC of 0% and view angles $(\theta_v, \phi_v) = (60°, 90°)$.

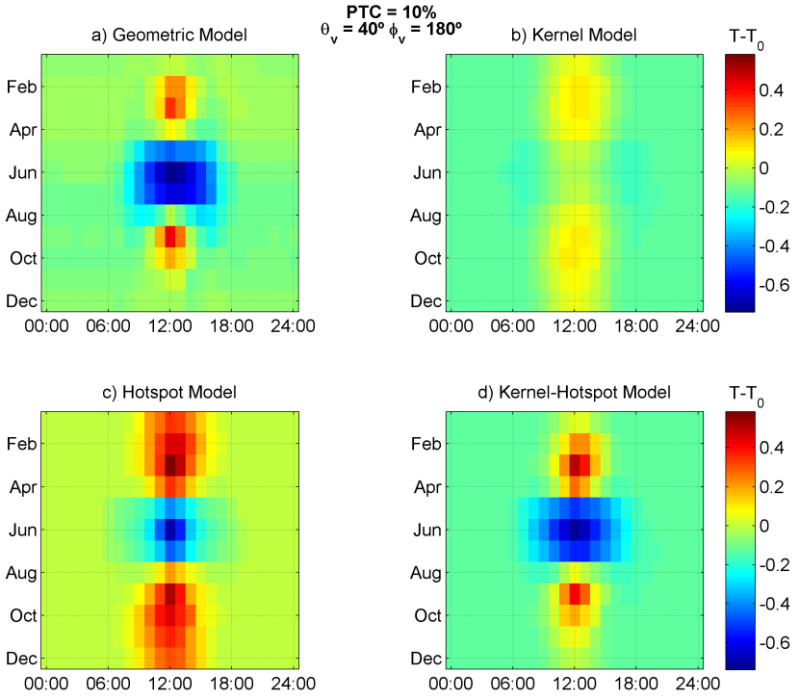

Figure 2.3.11 - As in Figure 2.3.10 but for a PTC of 10% and view angles $(\boldsymbol{\theta_v}, \boldsymbol{\phi_v}) = (\mathbf{40°}, \mathbf{180°})$.

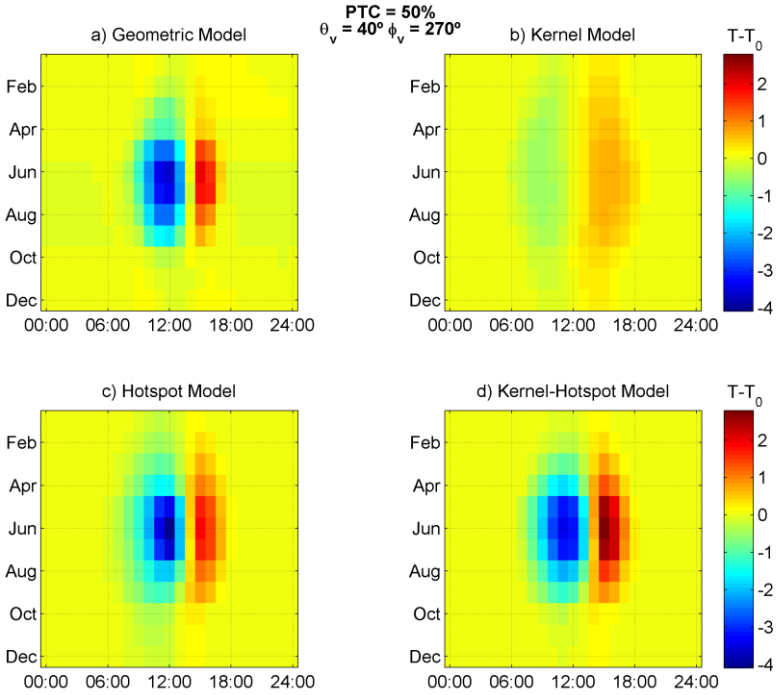

Figure 2.3.12 - As in Figure 2.3.10 but for a PTC of 50% and view angles $(\boldsymbol{\theta_v}, \boldsymbol{\phi_v}) = (\mathbf{40°}, \mathbf{270°})$.

For the other examples (Figure 2.3.11 to Figure 2.3.12), the corrections provided by the Geometric model are mainly associated to shadowing effects, being controlled by the position of the hot-spot. The sun is generally located south of Évora, with higher zenith angles during summer. As a result, for a view from south at 40º zenith angle (Figure 2.3.11), a nadir (off-nadir) observation will be closer to the hotspot during summer (winter) yielding negative (positive) $\mathrm{T} - \mathrm{T}_0$ values. For westward viewing

position (Figure 2.3.12) the hot-spot effect leads to a decrease in LST in the morning and an increase in the afternoon, i.e. in the afternoon the sun is located behind the sensor which results in a significant reduction of the shadow fraction. In all three cases presented, there is an overall underestimation of the amplitude of the corrections by the Kernel model when compared to the Geometric model (panel a of Figure 2.3.10 to Figure 2.3.12), particularly for the hotspot effect (associated with high positive differences in the other models). For a PTC of 10% (Figure 2.3.11) the Kernel-Hotspot model presents values closer to the Geometric model than the Hotspot model, especially for night-time. For a PTC of 50% (Figure 2.3.12), the Kernel-Hotspot model shows no significant improvement when compared to the Hotspot, which is to be expected given the low impact of emissivity anisotropy for these PTC ranges.

2.4 Analyzing the potential for operational use of the parametric models

DATA PRE-PROCESSING

Encompassing Mediterranean Europe, the study area for this section is defined as the region between the latitude circles of 34.5º and 45.8ºN and between the meridians of 12.4ºW and 30ºE (Figure 2.4.1). The region is covered by very heterogeneous vegetation, ranging from dense to sparse forest, cultivated areas and shrubland (Figure 2.4.1).

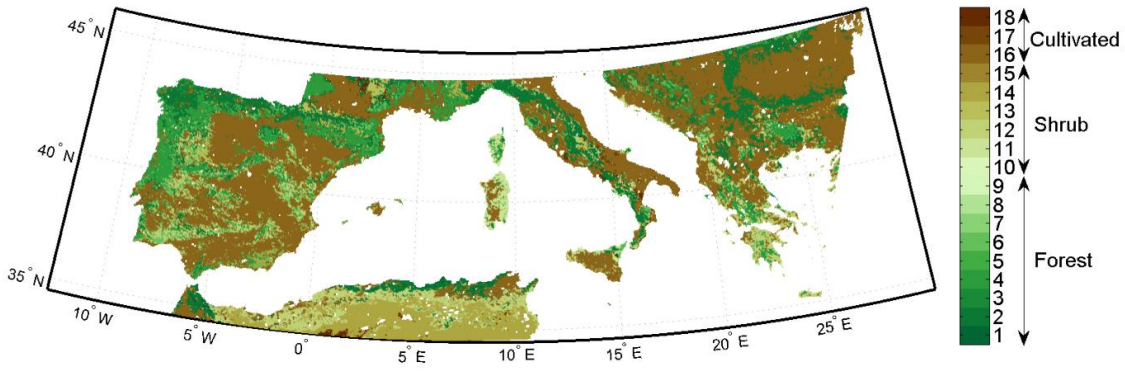

Figure 2.4.1 - ***Land cover classification according to GLC2000. Values of the colorbar correspond to GLC2000 labels. A detailed description may be found in*** http://bioval.jrc.ec.europa.eu/products/glc2000/legend.php**.**

The data were grouped into four datasets of geostationary (SEVIRI) and polar-orbiter (MODIS) based LST products collocated in space and time, according to the temporal coverage: the full years of 2011, 2012, 2013 and 2014 (referred hereafter as SEVMOD11, SEVMOD12, SEVMOD13 and SEVMOD14, respectively).

Space and time collocation was performed as follows:

1) MODIS LST were projected onto SEVIRI/MSG geostationary grid by attributing each MODIS pixel to the closest SEVIRI pixel center and averaging all MODIS pixels corresponding to each SEVIRI pixel. It is worth noting that this procedure takes into account the actual pixel sizes of SEVIRI and MODIS.

2) SEVIRI LST was then linearly interpolated to MODIS observation time using SEVIRI (15-minute) observations immediately preceding and succeeding MODIS observation. This interpolation is only performed if both SEVIRI observations are cloud-free, otherwise a single observation is used if the time difference between SEVIRI and MODIS retrievals is below 7.5 minutes.

HILL SHADE

The consistency of the obtained model coefficients over mountainous regions was assessed by comparing values of parameter *D* with the characteristics of illumination as estimated by an hill shading algorithm (Burrough and McDonell, 1998) applied to a Digital Elevation Model (DEM). The algorithm provides an hypothetical percentage of illuminated surface, F, based on light source and relief information:

$$\mathrm{F} = (\cos\theta_i \cos\theta_s) + (\sin\theta_i \sin\theta_s \cos(\phi_i - \phi_s)) \quad (2.4.1)$$

where θ_s and ϕ_s are respectively the slope and the aspect of the mountain. For any given position of the sun, the algorithm allows estimating the fraction of shaded and sunlit parts of the mountain that should translate into the values of the solar kernel parameter, *D*.

CALIBRATION

For this study, only the Kernel model (described in section 2.3) was analyzed. Since the model may be calibrated with a simple linear regression, it can be easily fitted on a pixel-by-pixel basis (unlike the Hotspot model). This allows a better analysis of the response of the model to surface characteristics of each pixel. The calibration of the kernel model was performed through the following procedure:

1. First, we need to remove any systematic differences between the two datasets, i.e., any offset or multiplicative factors that explain a significant part of MODIS – SEVIRI LST discrepancies. This broad sense bias was calculated by simple linear regression ($LST_{MOD} = a * LST_{SEV} + b$) restricted to night-time observations and to similar viewing configurations by the two satellites ($\left|\theta_{\mathrm{v},1} - \theta_{\mathrm{v},2}\right| \leq 5°$). Such restrictions are aimed to exclude cases where sources of non-systematic MODIS – SEVIRI LST differences are most relevant. Over the study area and for the 2013-2014 period there are a total of 7,844,745 available matchups resulting in values of slope $a = 0.981$ and intercept $b = 4.71$. This bias correction was then applied to the SEVIRI LST product.

2. For each SEVIRI pixel within the study area, parameter A was first calculated using MODIS and SEVIRI collocated LST (bias corrected) night-time observations (i.e., when $\Psi = 0$):

$$T_1 - T_2 = A(\Phi_1 \mathrm{T}_2 - \Phi_2 \mathrm{T}_1) \quad (2.4.2)$$

3. For each SEVIRI pixel within the study area, parameter D was then calculated using daytime observations only and using values of A obtained in the previous step:

$$T_1 - T_2 - A(\Phi_1 \mathrm{T}_2 - \Phi_2 \mathrm{T}_1) = D(\Psi_1 \mathrm{T}_2 - \Psi_2 \mathrm{T}_1) \quad (2.4.3)$$

To avoid taking into account LST values with very high uncertainties, only pixels with VZAs below 50º were considered for the bias correction (step 1 in the list above). For the same reasoning, the estimation of A (step 2) used MODIS observations limited to view angles up to 50º. The kernel parameters, *A* and *D* (steps 2 and 3), are adjusted on a pixel-by-pixel basis, i.e., each considers a fixed SEVIRI viewing geometry. As such, the restrictions imposed to MODIS observations were relaxed for SEVIRI in order to maintain the area of study (see Figure 2.4.1), where SEVIRI VZAs vary from 39.75º in the south-west to 59.5º in the far north-east of the domain. It is also assumed non-temporally dynamic values of A and D, although values are expected to change for cover types with a high seasonality. This calibration methodology was first applied to the time series given by combining *SEVMOD13* and *SEVMOD14* datasets. Obtained parameters of emissivity and solar kernels will be referred to hereafter as the reference model. For cross-validation purposes, the kernel model was also

calibrated using *SEVMOD13* (*SEVMOD14*) data only, and then verified through its application to *SEVMOD14* (*SEVMOD13*) data. Validation with independent data was accomplished by applying the reference model to the *SEVMOD11 and SEVMOD12* independent datasets.

ANALYSIS OF THE MODEL COEFFICIENTS

Figure 2.4.2 shows the fields of *A* and *D* parameters estimated over the study area for the reference model, which is calibrated with *SEVMOD13* and *SEVMOD14* combined datasets. It is clear that the kernel model captures vegetation and most notably orography patterns, which are known to have the most significant effects on directionality of LST (Trigo et al., 2008a).

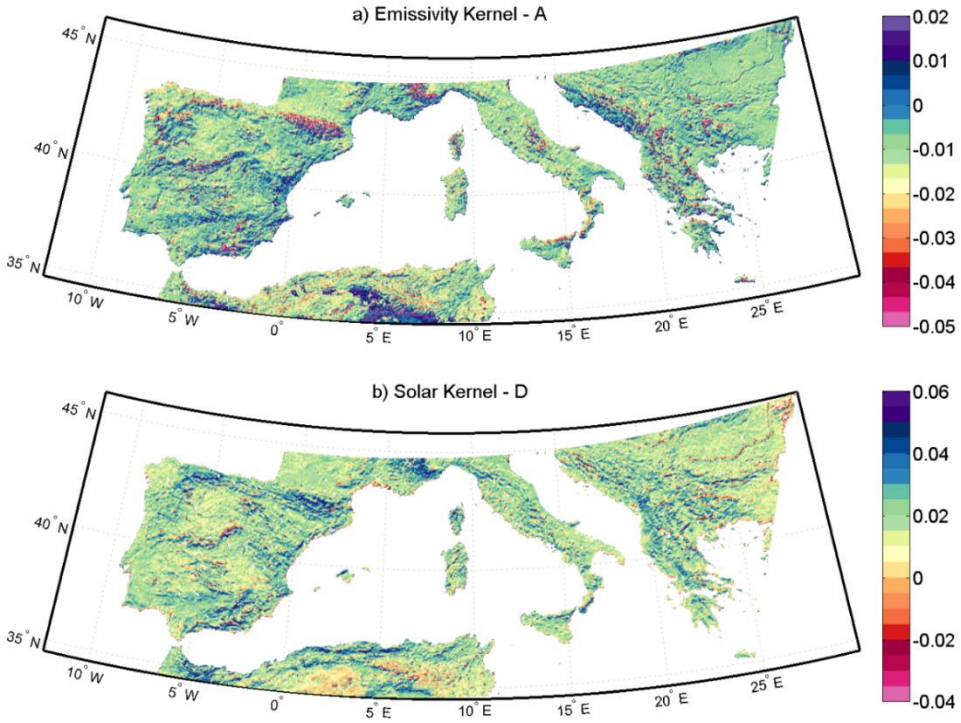

Figure 2.4.2 - ***Spatial distribution of coefficients of the reference kernel model for (a) A, the emissivity kernel (upper panel), and (b) D, the solar kernel. Colorbars are saturated at percentiles 0.2% and 99.0% for the emissivity kernel and at percentiles 0.5% and 99.7% for the solar kernel.***

Fitting the emissivity kernel to the data leads mostly to negative values of parameter *A* (Figure 2a), which indicates a decrease of the temperature relative to nadir for higher values of VZA. According to the formulation in Vinnikov et al. (2012), this could be associated to a dependence of emissivity on view angle, where negative values of *A* would be consistent with a decrease of emissivity with view angle. Emissivity is known to decrease with VZA for homogenous surfaces like sea and bare ground but this variation is expected to be negligible for other surfaces like grassland (Labed and Stoll, 1991; Sobrino and Cuenca, 1999). (Ren et al., 2011) assessed the pixel-scale directionality of emissivity and found that although emissivities in the thermal infrared band decrease with viewing angles, the angle dependency is very slight from 0° to 45° and only becomes significant for angles larger than 45°. Since only view angles up to 50º are considered in the adjustment of *A*, it is possible that the adjusted values do not translate to emissivity angular dependence but are rather a consequence of other factors that induce higher differences between the two LST products for large angles. Next, we take a closer look at the distribution of parameter *A* to further understand those factors.

Visual inspection of Figure 2.4.2(a) suggests a relation between values of parameter A and topography. Figure 2.4.3(a) shows the distribution of terrain topography (slope and orientation) per class of parameter *A*. It is shown that the highest absolute values of *A* are found over mountainous regions, while flat surfaces are associated to *A* values around -0.01. Although one should be cautious when

analyzing steep terrain, particularly because their geo-referencing errors tend to have a higher impact on LST uncertainties, Figure 2.4.2(a) and Figure 2.4.3(a) suggest a north-south gradient, with positive (negative) *A* values over pronounced slopes facing south (north). This is consistent with the strong contrasting negative/positive bias between MODIS and SEVIRI LST over mountains such as Pyrenees or the Alps (Figure 2.4.4): the fixed SEVIRI viewing geometry roughly observing the area from south favors measurements of higher surface elevations over the northern part of mountain ranges, since lower valleys are more likely to be obscured/hidden within the field-of-view; this shading of low surfaces within SEVIRI FOV is highly attenuated in the case of southern slopes.

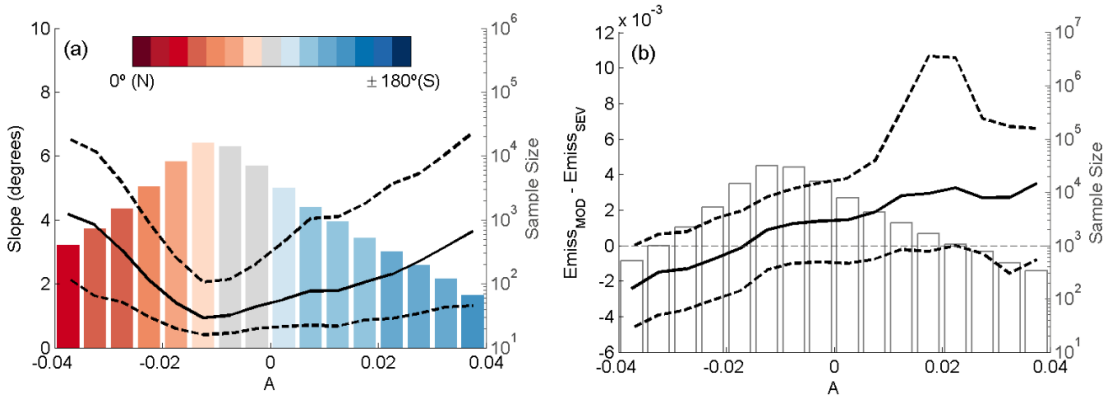

Figure 2.4.3 – Percentiles 50% (solid line), 25% and 75% (dashed lines) of a) surface slope and b) of average 10.8 µm emissivity differences between SEVIRI and MODIS over 2013 and 2014, for the classes of emissivity kernel parameter (A) indicated in the x-axis. The bars represent the sample size of each class (right y-axis). Colors of the bars in a) indicate the corresponding percentile 50% of slope orientation (in degrees from North to South, in the eastward (positive) or westward (negative) directions).

The spatial distribution of values of parameter A (Figure 2.4.2b) and of biases between MODIS and SEVIRI (Figure 2.4.4) suggest investigating the influence of the latter on the former. Figure 2.4.3b presents the distribution of differences in MODIS and SEVIRI surface emissivities at 10.8 µm per class of *A*. Regions where SEVIRI emissivity is higher than MODIS are associated to negative values of *A*, whereas regions with higher MODIS emissivity are associated to positive values of *A*. Figure 3b suggests that *A* tends to increase with increasing emissivity differences. The patch of very high *A* values observed over the northern part of Africa corresponding to desert is particularly conspicuous in Figure 2.4.2a, and is clearly associated to very high emissivity difference values between MODIS and SEVIRI over the same area (Figure 2.4.4); in Figure 2.4.3b, these correspond to the ridge in the 75% curve. Results from this analysis suggest that the adjustment of parameter *A* in the kernel model acts as a further correction for local effects between MODIS and SEVIRI, which end up being superimposed on the emissivity angular dependency.

Values of parameter *D* (Figure 2.4.2b) as obtained by fitting the solar kernel to the data are mostly positive (only 6.4% are negative), indicating that LST increases relative to nadir in hot-spot situations (i.e. when the sun is effectively positioned behind the sensor) and decreases with VZA for the remaining sun-sensor relative positions (as in the example shown in Figure 2.4.5). For heterogeneous pixels characterized by tree (or tall shrubs) coverage, the angular dependence of LST is mostly associated to shadowing effects. At the hot-spot the fraction of shadow observed by the sensor is significantly reduced as trees or other surface elements hide the shadow, leading the sensor to retrieve higher LST values. Off the hot-spot, the fraction of shadow observed by the sensor will increase with increasing VZA resulting in lower LST values. This effect should be more relevant in areas with sparse or moderately vegetated surfaces as opposed to more homogeneous areas (bare ground or highly dense forests).

The distribution of the PTC among several classes of *D* values (Figure 2.4.6b) reflects the consistency of the spatial distribution of parameter *D* with the patterns of vegetation (Figure 2.4.7). There is an increase of positive *D* values with increasing tree cover. This is consistent with higher shadowing effects present in moderately dense forested areas. In contrast, values of *D* closer to zero are

dominated by low PTC values that correspond to less representative shadowing effects. Moreover, very dense forested areas may lead to a reduction in the angular dependence as the tree crowns obscure the shadows. As a result, the larger values of PTC are associated to intermediate values of *D* (around 0.04).

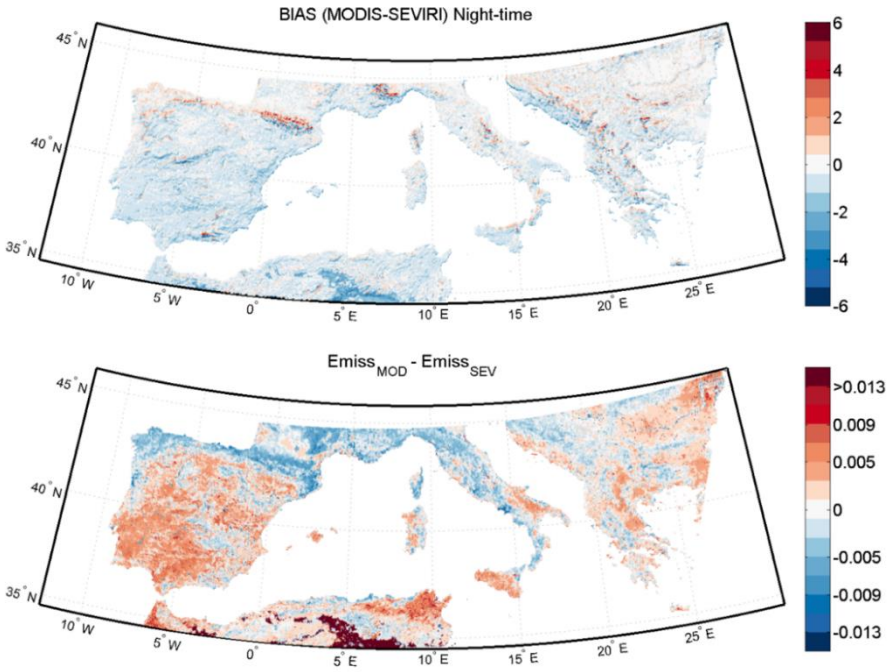

Figure 2.4.4 – Spatial distribution of values of night-time bias between MODIS and SEVIRI LST (upper panel) and of the average differences between MODIS and SEVIRI emissivity of the 10.8/11 µm channel over the years of 2013 and 2014 (lower panel).

More complex processes occur in mountainous areas, where LST retrievals depend not only on sensor-sun relative positions, but also on the relative orientation of slopes. There is an increase of D values with the surface slope (Figure 2.4.6a), which is consistent with the expected increased angular dependence. An illustration is provided of the case of the Guadarrama Mountains and the Pyrenes (Figure 2.4.8), two systems of mountain that range at the center and in the north of the Iberian Peninsula. The spatial distribution of parameter *D* over the areas located in these mountain ranges tend to form bands of markedly positive and negative values (Figure 2.4.8c,e), which are in very close agreement with the fraction of illumination (Figure 2.4.8b,d) as provided by a hill shading algorithm (eq. (2.4.1)) applied to a DEM model of the area (estimated for a solar zenith angle of 20º, i.e., close to local noon). Despite the relatively noisy field of D values (Figure 2.4.8c,f), higher positive (lower negative) values are associated to mountain slopes with higher (lower) fractions of illumination.

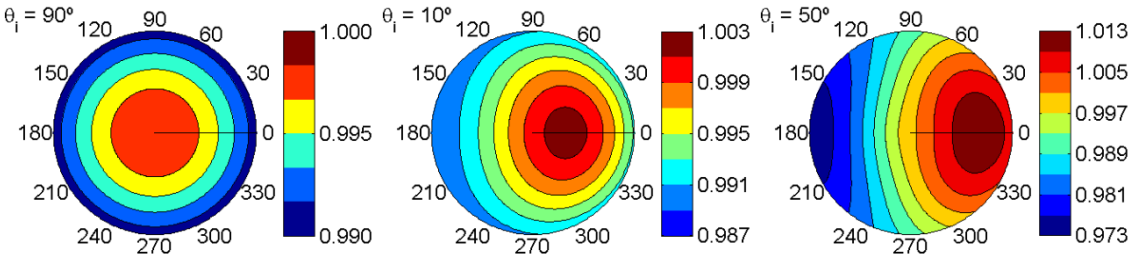

Figure 2.4.5 – Values of T/T_0 as given by the kernel model (eq. (2.3.4)) for a common pair of A and D values (A=-0.01 and D=0.04) and for three different values of solar zenith angle (θ_i) in a polar coordinate system: view zenith angle θ_v as radial coordinate (0-90º) and relative azimuth $\Delta\phi$ as angular coordinate (0-360º). Maximum of daytime T/T_0 is associated to the hot-spot effect – when the sun is effectively positioned behind the sensor.

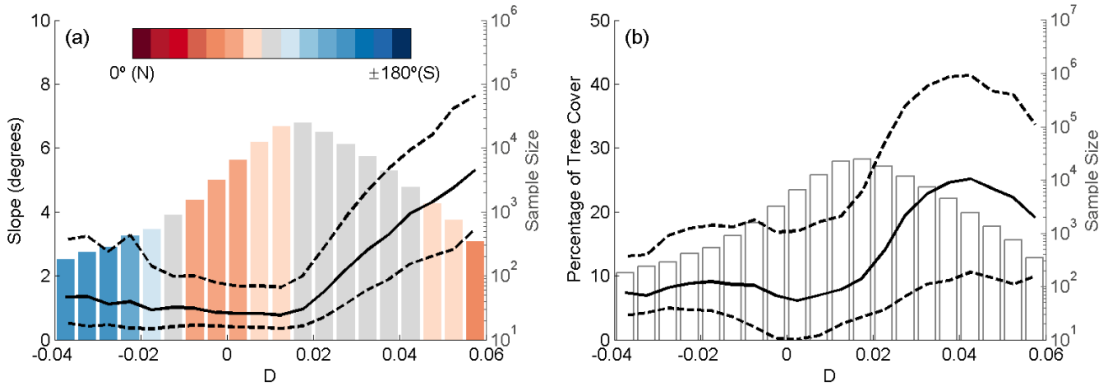

Figure 2.4.6 - Percentiles 50% (solid line), 25% and 75% (dashed lines) of a) surface slope and b) PTC over 2013 and 2014, for the classes of solar kernel parameter (D) indicated in the x-axis. The bars represent the sample size of each class (right y-axis). Colors of the bars in a) indicate the corresponding percentile 50% of slope orientation (in degrees from North to South, in the eastward (positive) or westward (negative) directions).

An example of use of the developed kernel model is provided in Figure 2.4.9 that shows two LST diurnal cycles estimated from SEVIRI over two pixels located at the northern and the southern slopes of the Guadarrama Mountains, respectively. The different exposure of the hill slopes leads to opposite behaviors of LST dependence on view angle. For the northern pixel, a viewing geometry from south (like that of SEVIRI instrument) prevents the satellite from seeing the valleys that have in general higher temperatures than those at higher altitudes; therefore, an observation from nadir may result in higher LST values than one from south, as shown in Figure 2.4.9a. In the case of the southern pixel, the sunlit surface dominates, leading to higher values of temperature when the surface is observed from the south (Figure 2.4.9b). These results are also consistent with the fixed SEVIRI viewing geometry (from south), leading to a higher probability of low altitude (and therefore higher LST) to be obscured in northern slopes. Moreover, it is worth emphasizing that estimates of fraction of illumination (Figure 2.4.9a) were derived from a hill shading algorithm based on a DEM and are therefore independent from the estimates of the kernel parameters (Figure 9b) that were obtained from observed pairs of collocated values of LST by the SEVIRI and MODIS instruments.

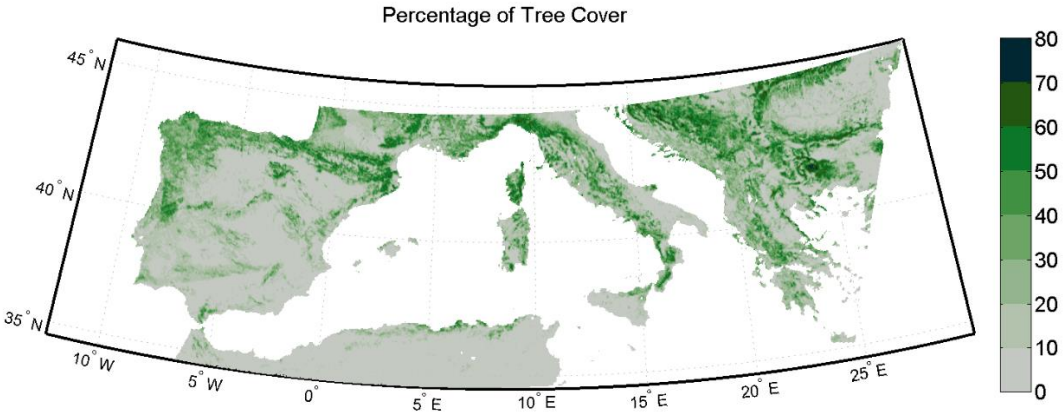

Figure 2.4.7 – PTC as obtained from MODIS Yearly Vegetation Continuous Fields (product MOD44B) for the years of 2013 and 2014.

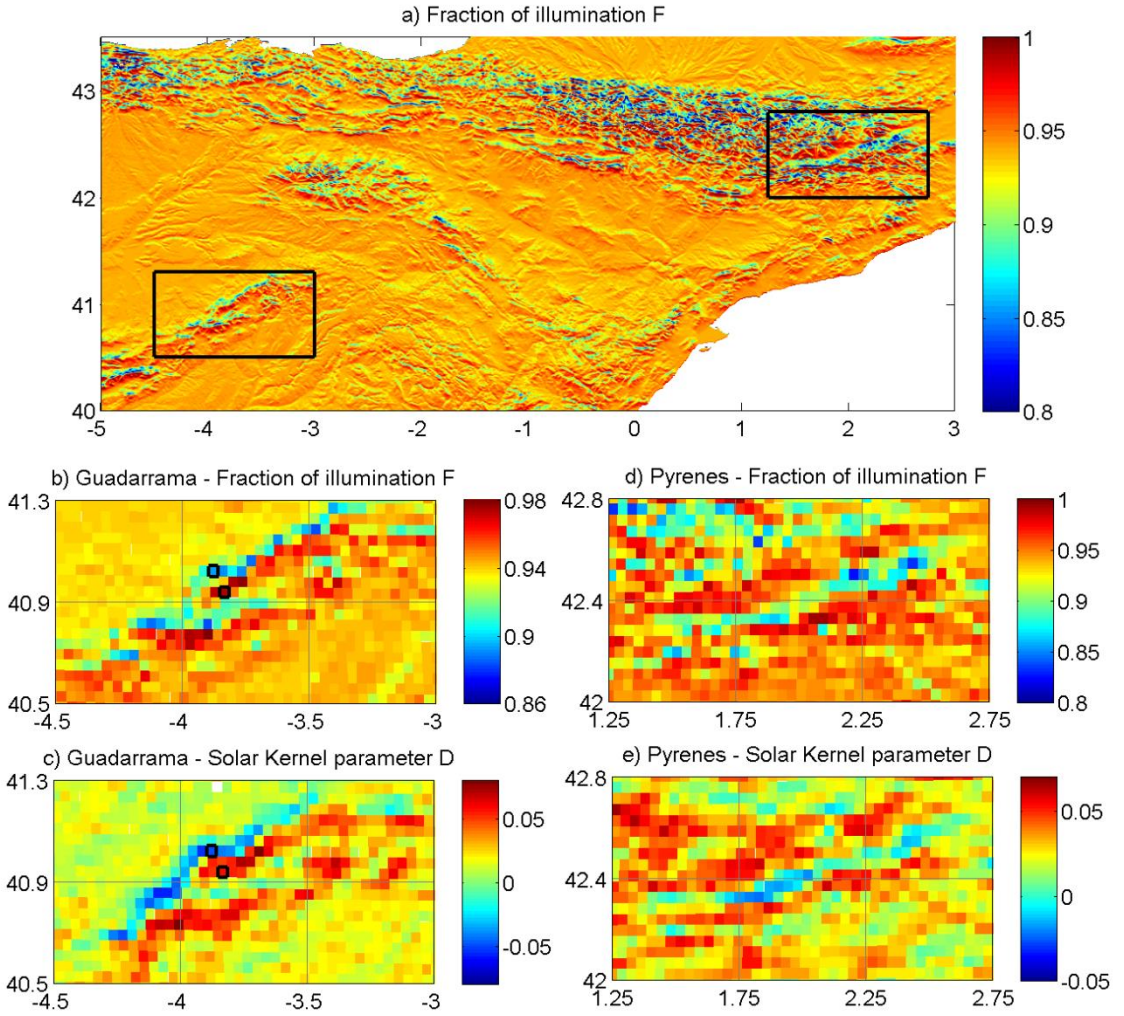

Figure 2.4.8 – a) Fraction of illuminated surface, F, for sun zenith and azimuth angles of 20º and 180º, respectively, as provided by a hill shading algorithm (eq. (2.4.1)) applied to a 1 km DEM model of an area in northern Iberian Peninsula (rectangles denote the areas shown in panels b-e); b,d) fraction of illumination, F, projected onto SEVIRI grid for the Guadarrama Mountains and the Pyrenes; and c,d) the corresponding values of the solar kernel parameter (D). The black squares in panels b) and c) indicate the location of the SEVIRI pixels from which the LST time-series in Figure 2.4.9 were extracted.

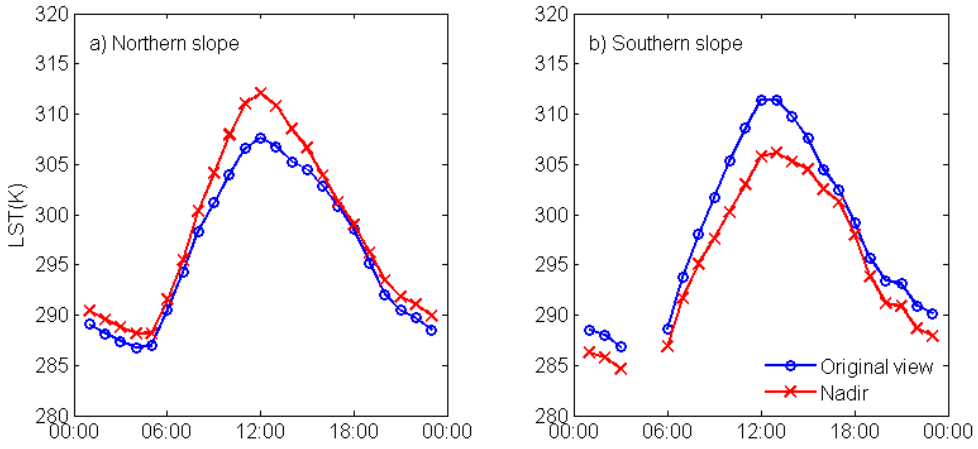

Figure 2.4.9 – Daily cycles of LST (K) as retrieved by SEVIRI (blue curves) and corrected to nadir view (red curves) on the 8th of July of 2013 at the two points marked in Figure 2.4.8, respectively located a) on the northern slope and b) on the southern slope of the Guadarrama Mountains.

MODEL VERIFICATION

Performance of the model may be inferred by first carrying out an angular correction on one of the sensors' LST to the viewing configuration of the other and then comparing LST differences before and after the correction. The angular correction should lead to closer values of LST between the sensors. The reference model was used to correct SEVIRI LST to MODIS viewing geometry. Figure 2.4.10 (lower panel) presents the impact of angular correction, showing the change in the root mean square differences (RMSD) of LST values (i.e., [RMSD after angular correction] – [original RMSD]). There is an overall significant decrease in LST differences, up to -3.6 K, with a very small percentage of pixels (5.9%) presenting an increase, but with lower amplitude. Larger RMSD decreases may be observed over mountainous areas as well as over a patch located in northern Algeria, where there are large differences in assigned values of emissivity by SEVIRI and MODIS.

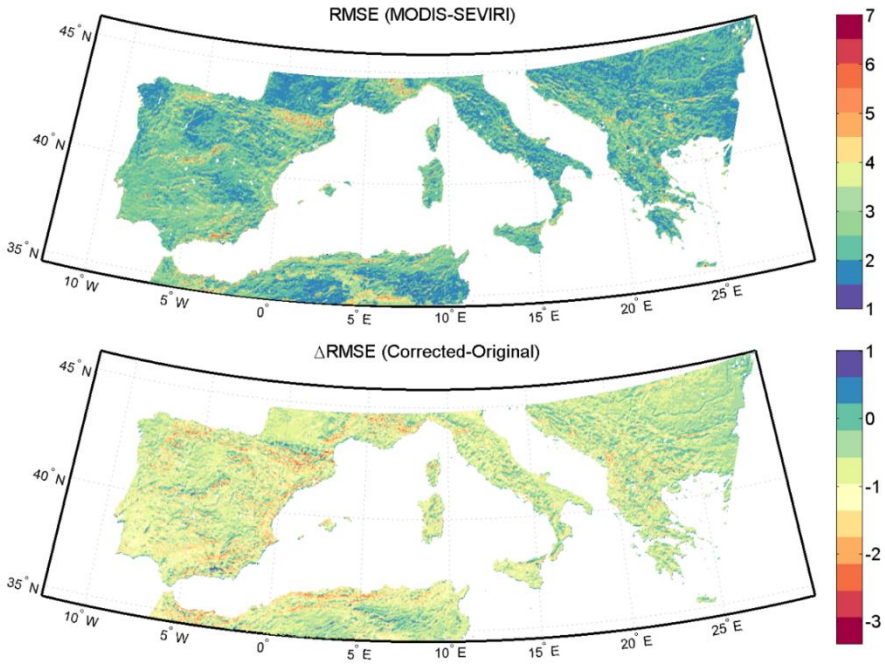

Figure 2.4.10 – RMSD between SEVIRI and MODIS (K) without angular correction (upper panel) and impact of LST angular correction on RMSD (in K) shown as RMSD after angular correction minus RMSD without correction (lower panel).

Since the angular correction is performed on data that were bias corrected (calibration), the role of both corrections was assessed by means of a histogram of RMSD (Figure 2.4.11). It may be noted that each step leads to a shift of the distribution of LST RMSD towards lower values. The angular correction performed by the kernel model is nevertheless significantly more effective; the overall RMSD of 2.7 K decreases to 2.3 K after the bias correction, and to 1.8 K after the angular adjustment. As expected, daytime values present the most significant angular correction.

A more detailed analysis reveals that only 3.7% of all pixels within the area of study present an RMSD degradation of 0.1 K or higher. These pixels, where discrepancies between SEVIRI and MODIS LST become larger after the angular correction, are associated to poor model fitting of equations (2.4.2) and (2.4.3) that lead to unlikely values of *A* and *D*, namely: pixels where there is a RMSD degradation correspond to positive values of A (51.6% of the pixels) and/or to negative values of D (77.5 of the pixels). As mentioned before, these pixels are mainly located in coastal and mountainous areas, where geo-referencing problems are likely to have a larger impact. In these cases, the quality or pixel representativeness of LST estimates may not be sufficient to perform a good calibration of the model.

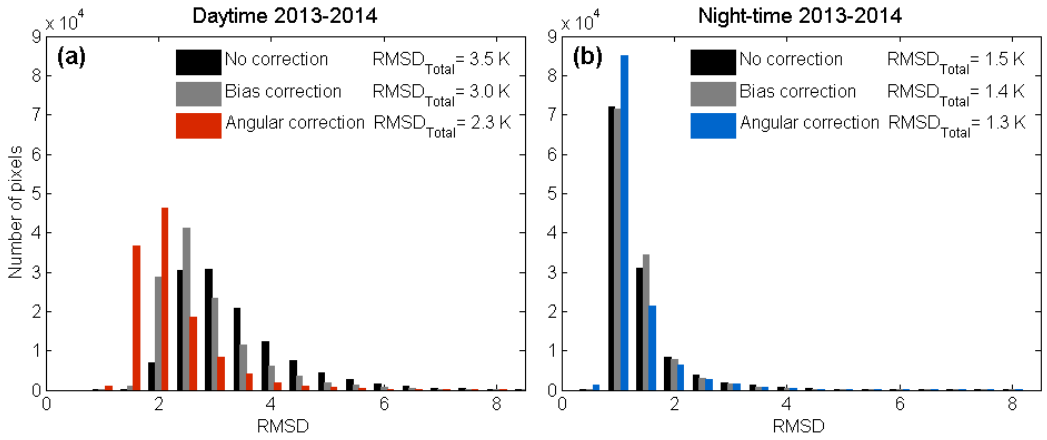

Figure 2.4.11 – Histograms of RMSD between SEVIRI and MODIS (in K) when no correction is applied (black), after applying the bias correction (grey) and after applying the angular correction with the reference model (red/blue) for (a) daytime and (b) night-time only observations.

MODEL VALIDATION

SATELLITE-BASED

The quality and robustness of the kernel model is assessed through two different processes: 1) a cross validation with *SEVMOD13* and *SEVMOD14* datasets; and 2) an independent validation with the *SEVMOD11* and SEVMOD12 datasets.

For the cross validation, the kernel model is calibrated using *SEVMOD13* and *SEVMOD14* datasets separately, and then assessed through the application of those model parameters to *SEVMOD14* and *SEVMOD13*, respectively. The aim of this procedure is to use independent datasets in the calibration and in the validation. The distribution of RMSD (Figure 2.4.12) is very similar to that obtained in the verification shown in Figure 2.4.11. It may be again noted that the angular correction presents the most pronounced impact on the retrievals, leading to the highest displacement of the histogram towards lower values. The performance of the kernel model seems therefore to hold, indicating that a kernel model calibrated with these data may be effectively applied to independent data.

Validation with independent data was performed by applying the reference model (i.e. calibrated with both *SEVMOD13* and *SEVMOD14)* to *SEVMOD11 and SEVMOD12*. This procedure allows assessing the quality of the reference model when applied to a different time period.

The distribution of RMSD between MODIS and SEVIRI LST for the *SEVMOD11* and SEVMOD12 datasets (Figure 2.4.12) presents characteristics very similar to those obtained before (Figure 2.4.11), with the highest impact being associated to daytime angular correction. These results together with those obtained in the verification and cross-validation processes strongly support the robustness of the kernel model.

IN SITU

The Évora site (Portugal) maintained by KIT presents a unique set of observations for the validation of LST. As detailed in section 2.1, *in situ* observations combined with a geometric model of the landscape surrounding the station allow the up-scaling of ground measurements for any viewing geometry and for a wide range of illumination angles. As a first step, the ability of the kernel model to reproduce the essential features of the geometric model designed for Évora was assessed by comparing the distributions of T/T_0 ratio (where T_0 is the nadir LST) as a function of VZA and relative azimuth valid for T, as obtained by each model. In the case of the kernel model (Figure 2.4.13, left panel) values of T/T_0 are those derived with the reference model at Évora. In the case of the geometric model (Figure 2.4.13, central panel), T/T_0 field corresponds the median values along the year *of in situ* LST derived for different view and illumination geometry configurations. Although there are noticeable differences between the kernel derived from SEVIRI and MODIS time series and that derived from *in situ*

observations, the main features are captured by the first one, namely the increase of T/T_0 towards nadir for geometries off the hot-spot zone. The ability of the kernel model to reproduce the patterns of the geometric model degrades as the solar zenith angle increases (not shown). This is to be expected since the kernel model does not take into account the lower differences in temperature among components that occur for higher solar zenith angles (namely, in winter and early morning and late afternoon). Indeed, while the sampling of the viewing geometry is restricted to collocated SEVIRI and MODIS observations in the case of the kernel model (Figure 2.4.13, right panel), the geometric space is entirely sampled in the case of the geometric model.

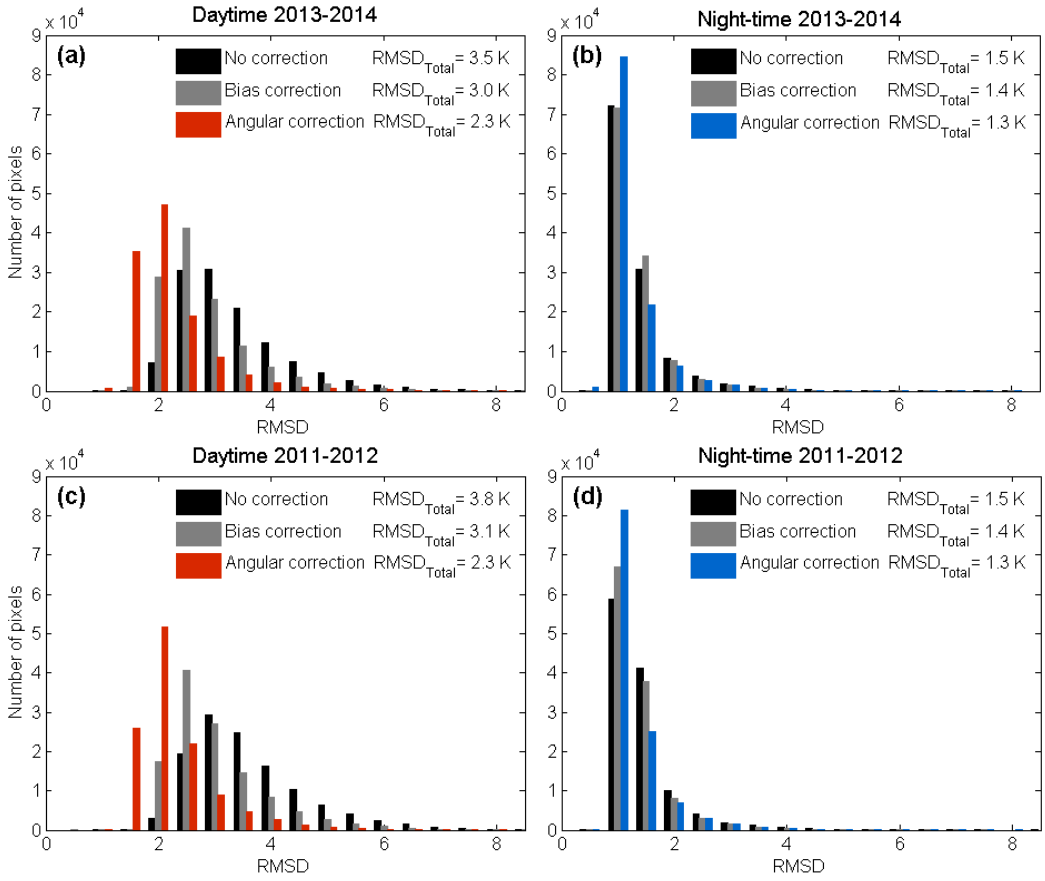

Figure 2.4.12- As in Figure 2.4.11, but a,b) in cross-validation mode, i.e. results obtained with a model calibrated with SEVMOD13 data and verified with SEVMOD14 data together with a model calibrated with SEVMOD14 and applied to SEVMOD13 data and c,d) applying the reference model (calibrated with SEVMOD13 and SEVMOD14 datasets combined) to SEVMOD11 and SEVMOD12 data.

Then, LST data retrieved by SEVIRI and MODIS (at their original resolution) for the nearest pixel to the Évora site were compared with respective *in situ* observations. The analysis covered the full year of 2010 and from October 2011 to September 2012 and the comparison exercise was performed before and after using the reference kernel model (calibrated with both SEVMOD13 and SEVMOD14) to correct satellite-observed LST to a nadir view. The model parameters at the site result in night-time corrections that are much lower than the uncertainty of both LST products. For that reason, the analysis was restricted to daytime.

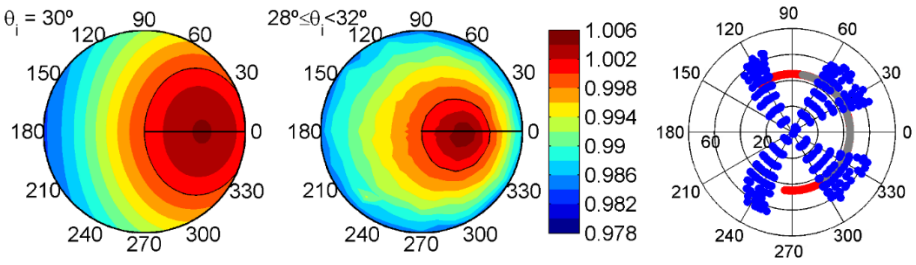

Figure 2.4.13 – As in Figure 2.4.5 but showing the values of T/T_0 as given by the reference kernel model at the Évora site (left panel) and as given by the geometric model (central panel), and showing the angle sampling of the LST time-series (right panel) of SEVIRI (red and grey dots), SEVIRI collocated with MODIS (grey dots) and MODIS (blue dots). The black lines in left and central panels corresponds to contour T/T_0=1.

For both SEVIRI and MODIS, the angular correction performed by the kernel model leads to LST values closer to the nadir *in situ* LST (Table 2.4.1). As expected, MODIS presents the largest reduction in the differences to *in situ*, given the larger VZA range of values of this sensor when compared with SEVIRI: SEVIRI VZA at the site is approximately 45º, whereas MODIS VZA varies between nadir and 65º (Figure 2.4.13, right panel). It is worth noting that changes in bias associated to the angular correction increase (decrease) when considering the whole SEVIRI dataset (when restricting to MODIS overpasses). This contrasting behavior is related to a reduce sampling of SEVIRI relative azimuth angles (Figure 2.4.13, right panel).

Table 2.4.1 - RMSE, error STD and bias for the differences between satellite LST and *in situ* LST (K), before (italics) and after (bold) using the kernel model to correct the satellite LST to nadir view. The number of available pairs of MODIS/station and SEVIRI/station LST is also shown (N). The second row in SEVIRI statistics corresponds to values obtained when limiting SEVIRI observations to MODIS overpass.

	VZA≤45º							VZA>45º						
	BIAS		STD		RMSE		N	BIAS		STD		RMSE		N
2010														
SEVIRI	*-0.8*	**-0.4**	*2.1*	**2.0**	*2.3*	**2.1**	2186							
	0.8	**-0.1**	*1.9*	**1.8**	*2.1*	**1.8**	133							
MODIS	*-0.6*	**-0.1**	*2.1*	**1.9**	*2.2*	**1.9**	99	*-3.2*	**-1.9**	*2.8*	**2.3**	*4.2*	**2.9**	46
2011-2012														
SEVIRI	*-0.5*	**-0.3**	*1.9*	**1.8**	*2.0*	**1.8**	5450							
	-0.7	**-1.4**	*2.1*	**1.7**	*2.2*	**2.2**	220							
MODIS	*-3.5*	**-3.1**	*2.3*	**2.0**	*4.2*	**3.7**	112	*-6.0*	**-4.3**	*3.7*	**3.7**	*7.0*	**5.6**	76

The seasonal variability of RMSE, STD and bias for the differences between satellite LST and *in situ* LST was also analyzed (Table 2.4.2). As might be expected, the discrepancies between satellite and *in situ* LST are smaller during winter (DJF) and larger during summer (JJA), in agreement with the respective magnitudes of LST. Most statistical measures for both satellites present an improvement after correction by the kernel model. In the case of SEVIRI, the bias is positive in winter and negative in summer, a behavior that is consistent with results obtained ins section 2.1 (Ermida et al., 2014). In the case of MODIS, the STD decrease after correction is more pronounced than in SEVIRI, reflecting the variable character of the viewing geometry of MODIS.

For the year of 2010 and for VZA values below 45º, MODIS and SEVIRI products present similar RMSE values. The same is not true for the 2011-2012 dataset, where MODIS presents a RMSE higher than SEVIRI (Table 2.4.1). During 2012, the Iberian Peninsula was affected by a strong drought (Trigo et al., 2013) that led to a strong decrease in green vegetation cover, particularly in late spring/summer months. In contrast with SEVIRI, MODIS emissivity does not show the signature of such strong vegetation anomaly for 2012 in the region surrounding Évora station, resulting in the higher discrepancies (underestimation) with *in situ* observations. Values of emissivity at 10.8 micrometer from both Seemann et al. (2008) and from SEVIRI present a seasonal cycle and a marked decrease from 2010 to 2011/2012. The former ranges from 0.946 to 0.968 (0.957 and 0.976) from summer

to winter in 2011/2012 (2010) and the latter from 0.969 to 0.977 (0.973 to 0.985). In the case of MODIS, both the seasonal cycle and the changes from 2010 to 2011/2012 are very weak, the values of emissivity ranging between 0.982 and 0.984 for both time periods. Nevertheless, the impact of the kernel model angular corrections is positive for both sensors despite being limited to values within the products uncertainty (improvement in RMSE of the order of 0.2 to 0.3K; Table 2.4.1). As expected, MODIS RMSE is higher for higher VZA values and it is in this case that the kernel model shows higher corrections, with RMSE reductions of 1.3 to 1.4 K (Table 2.4.1). For angles above 45º (MODIS retrievals only), the kernel model seems to be more efficient in reducing the bias with respect to *in situ* observations than the STD of the differences (positive impact in 2010 and neutral in 2011-2012; Table 2.4.1).

Table 2.4.2 – As in Table 2.4.1 but for inter-seasonal variability of RMSE, STD, and bias computed over the two periods of 2010 and 2011/2012. SEVIRI statistics corresponds to values obtained using all SEVIRI observations.

		BIAS		STD		RMSE		N
SEVIRI								
	DJF	*0.4*	**0.2**	*1.5*	**1.6**	*1.5*	**1.6**	1515
	MAM	*-0.7*	**-0.3**	*2.1*	**2.0**	*2.2*	**2.0**	1647
	JJA	*-1.5*	**-0.8**	*1.7*	**1.8**	*2.3*	**2.0**	3128
	SON	*0.1*	**0.1**	*2.0*	**1.9**	*2.0*	**1.9**	1346
MODIS								
	DJF	*-2.4*	**-1.3**	*1.7*	**1.4**	*2.9*	**1.9**	80
	MAM	*-2.6*	**-1.8**	*3.2*	**2.8**	*4.1*	**3.3**	63
	JJA	*-4.1*	**-3.4**	*4.0*	**3.5**	*5.8*	**4.9**	131
	SON	*-2.6*	**-1.8**	*2.9*	**2.4**	*3.9*	**3.0**	59

2.5 A methodology for the operational correction of angular effects on LST

CALIBRATION SETUP

The study area for this section corresponds to the full coverage of the SEVIR/MSG disk, encompassing Europe, Africa and part of South America. The full year of data of 2010 is used here.

All models are fitted to data corresponding to groups of pixels with similar surface characteristics. Clustering the pixels is essential since a pixel-by-pixel calibration of the Hotspot, and to a lesser extent of the Kernel model, is very demanding computationally. The pixel-by-pixel methodology presented in section 2.3 for the Kernel model is here used as a baseline for comparison.

In this study, both the Kernel (Vinnikov et al., 2012) and the Kernel-Hotspot (Ermida et al., 2018) models are adjusted per cluster, i.e., yielding a unique set of model coefficients which are applied to all pixels within the cluster. This approach contrasts with the methodology used in section 2.4, where the calibration of the Kernel model was performed for each individual pixel. The method used to find the Kernel model coefficients (A and D) is described in section 2.4. In the case of the Kernel-Hotspot model, eq. (2.3.11) must be rewritten to accommodate two LST time-series with different viewing configurations:

$$T_1 - T_2 = A(\Phi_1 \mathrm{T}_2 - \Phi_2 \mathrm{T}_1) + \mathrm{B} \cdot \mathrm{Rad}^*_{TOA} \cdot \sin(2\theta_i) \frac{e^{-Kd_1} - e^{-Kd_2}}{1 - e^{-K \tan \theta_i}} \quad (2.5.1)$$

where sub-indices 1 and 2 denote the two considered LST time-series, T_1 and T_2. Here *A* is again first adjusted to night-time data by linear regression. B and K are fitted to daytime data by MSE minimization, using the Nelder-Mead simplex method (Lagarias et al., 1998).

SURFACE CLASSIFICATION

We perform a clustering of the pixels using information indicative of vegetation characteristics and topography, namely surface elevation, land cover and FVC. First, four main land cover classes are defined based on ALB2: crops, forests, shrubland and deserts. Then, for each main land cover, a cluster analysis is performed using the elevation and monthly maximum and minimum FVC (Seber, 1984). Maximum and minimum FVC are here used to account for both vegetation density and its seasonal variability. This classification is performed at global scale at a resolution of 0.05ºx0.05º to allow the application of this method to other sensors, as required within the scope of the GlobTemperature project.

Figure 2.5.1 shows the spatial distribution of the resulting classification and Figure 2.5.2 presents the clusters' centroids. The classification is then projected onto SEVIRI grid using the nearest-neighbor approach.

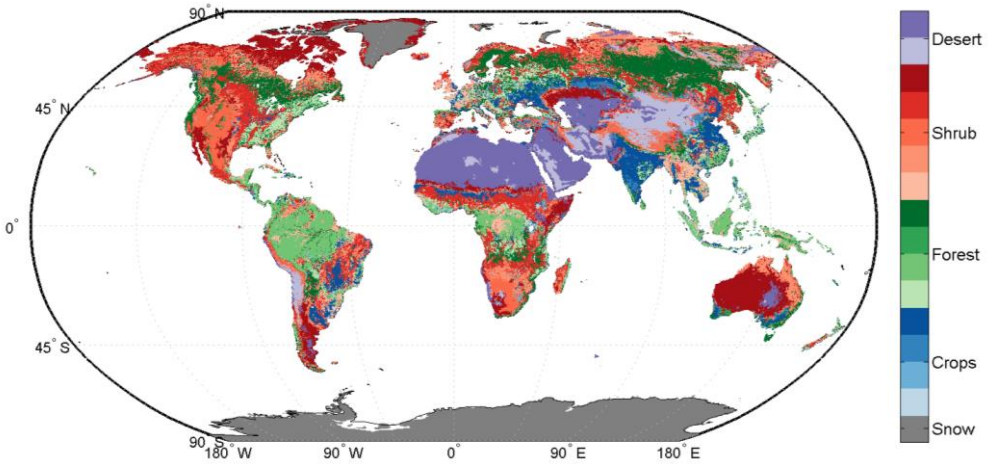

Figure 2.5.1 - Spatial distribution of the cluster-based surface classification.

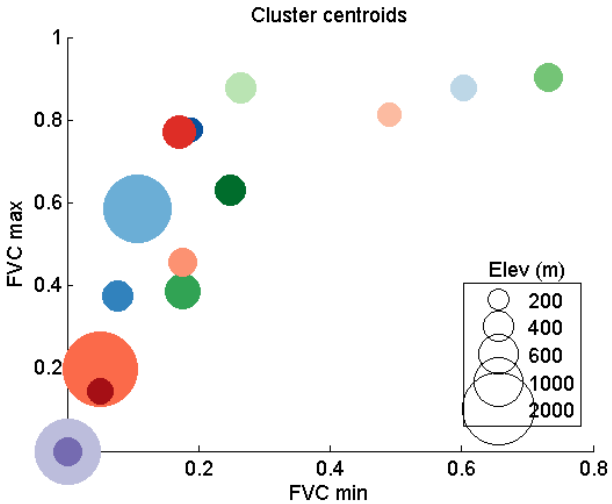

Figure 2.5.2 - Cluster centroids of the surface classification. Colors correspond to the colorbar of Figure 2.5.1.

ANALYSIS OF THE MODELS COEFFICIENTS

The parametric models are fitted to the LST datasets of each cluster of pixels, and Figure 2.5.3 shows the respective parameters. The emissivity kernel parameter, *A*, presents only negative values. This indicates a decrease of the LST with VZA, which is consistent with a decrease of emissivity with view

angle. Emissivity is known to decrease with VZA for homogenous surfaces like bare ground (e.g., McAtee et al., 2003) but this variation is expected to be negligible for rough surfaces like those that are vegetated (Labed and Stoll, 1991; Ren et al., 2011; Sobrino and Cuenca, 1999). The highest absolute values of *A* are obtained for clusters with low FVC and there is a tendency for absolute values of A to decrease with the increase of FVC (Figure 2.5.4). The impact of emissivity anisotropy on LST is likely to be related with the percentage of bare ground which is visible within the satellite FOV, and therefore it is expected that this impact will be larger for lower vegetation cover.

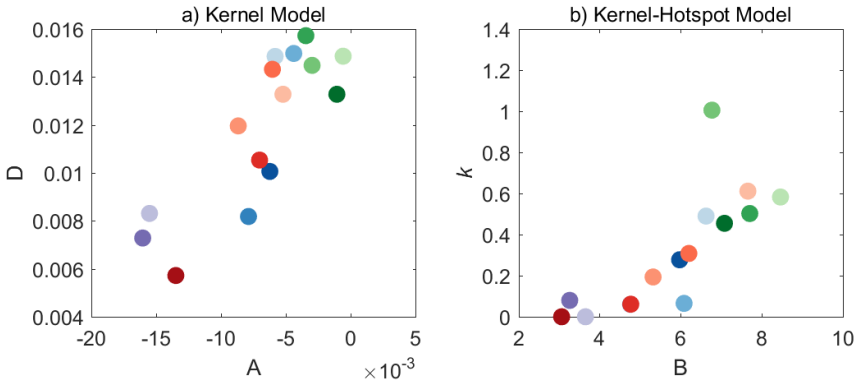

Figure 2.5.3 - Coefficients of the a) Kernel model and b) Kernel-Hotspot models. Values of the parameter *A* of the Kernel-Hotspot model are the ones of the Kernel model (a). Colors indicate the different clusters of pixels and correspond to the colorbar of Figure 2.5.1. Values of *A* of the Kernel-Hotspot model (b) are the same as in the Kernel model (a).

The fitting of the solar kernel lead to positive values of parameter *D* (Figure 2.5.3a), which indicates that LST tends to increase with view angle in hot-spot situations (i.e. when the sun is effectively positioned behind the sensor) and decreases for the remaining sun-sensor relative positions. For heterogeneous surfaces (e.g. tree/shrub covered), the LST anisotropy is mostly related to shadowing effects and, therefore, this effect is expected to be more relevant over moderately vegetated surfaces. Moreover, the higher *D* values are obtained for intermediate FVC values, although the relation to FVC is not as clear as in the case of *A* (see Figure 2.5.4a and Figure 2.5.4b). Other factors are also relevant in this case, e.g. typical temperature contrasts, height and volume of the vegetation objects, surface topography (Ermida et al., 2014, 2017; Franklin and Strahler, 1988; Lagouarde et al., 1995; Li and Strahler, 1986).

The calibration of the Kernel-Hotspot model also leads to positive values of parameter *B* (Figure 2.5.3), indicating that the hot-spot configuration is associated with LST values that are warmer than those that would be measured from the nadir configuration. As in the case of the solar kernel parameter, *D*, the higher values of *B* are associated to intermediate values of FVC although this quantity does not translate the full variability of *B* (Figure 2.5.4c). The fit also results in positive values of *K* for the majority of the clusters (Figure 2.5.3b). According to Roujean (2000) this parameter is closely linked to the density of vegetation in the reflectance model, and the study of section 2.2 (Ermida et al., 2018) showed a linear dependence of *K* with the PTC. We found that *K* tends to increase with the average FVC (Figure 2.5.4), in agreement with these studies. Near-zero values of *K* occur for very low values of FVC, when shadowing effects are very weak or absent. Although the emissivity effect is here accounted for, values of *B* are still significant for very low FVC, which suggests that geometric effects that are not related to emissivity may still exists or that the emissivity kernel is not able to fully represent the LST anisotropy.

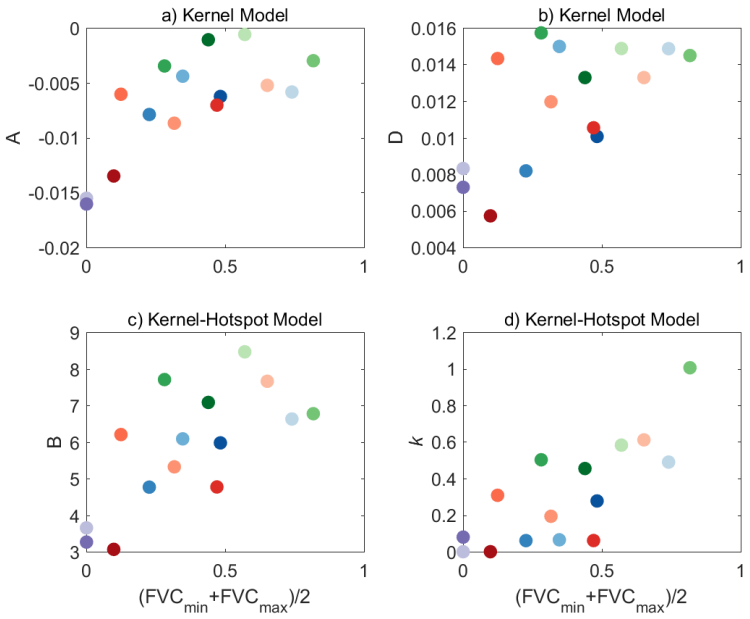

Figure 2.5.4 - Parameters of the Kernel (a,b) and Kernel-Hotspot (c,d) models as function of the average FVC of the cluster. Colors indicate the different clusters of pixels and correspond to the colorbar of Figure 2.5.1.

ASSESSMENT OF MODELS' PERFORMANCE

The performance of each model is analyzed based its capability to simulate the differences in LST fields estimated from different sensors (and different viewing geometries) collocated in space and time. As such, we first use the model to correct one of the sensors' LST to the viewing configuration of the other and then compare LST differences before and after the correction. The angular correction should lead to closer values of LST between the sensors (Ermida et al., 2017a). The models are here used to correct SEVIRI LST to the viewing geometry of MODIS. Figure 2.5.5 presents the spatial distribution of RMSD between MODIS and SEVIRI LST, and the impact of the angular corrections as given by each model, showing the change in the RMSD of LST values (i.e., [RMSD after angular correction] – [original RMSD]). Since the angular correction is performed on data that were bias corrected, the role of both corrections was assessed by means of a histogram of RMSD change (Figure 2.5.6). The performance of the models with respect to the Kernel model calibrated on a pixel-by-pixel basis is also analyzed in the histogram of Figure 2.5.6.

During daytime, the Kernel model leads to an overall decrease of the RMSD between the sensors, with only a small percentage of the pixels (5.7%) presenting an increase of the LST differences. LST RMSD corrections (ΔRMSD) are as high as -1.6 K (percentile 0.1%) and -0.5 K on average. For the Kernel-Hotspot model the angular correction also leads mostly to a decrease of the RMSD, with a slightly lower percentage of the pixels (3.2%) presenting an increase. The average ΔRMSD given by this model is -1.1 K, and corrections are as high as -5.5 K (percentile 0.1%).

During night-time, there is also a general decrease in the LST RMSD when the Kernel model is used to correct angular effects. As expected, corrections are lower than during daytime, leading to an average ΔRMSD of -0.2 K, with values up to -1.4 K (percentile 0.1%). In this case, a larger percentage of pixels (15.6%) show an increase in RMSD, but for most of these (84.2%) the increase is below 0.2 K.

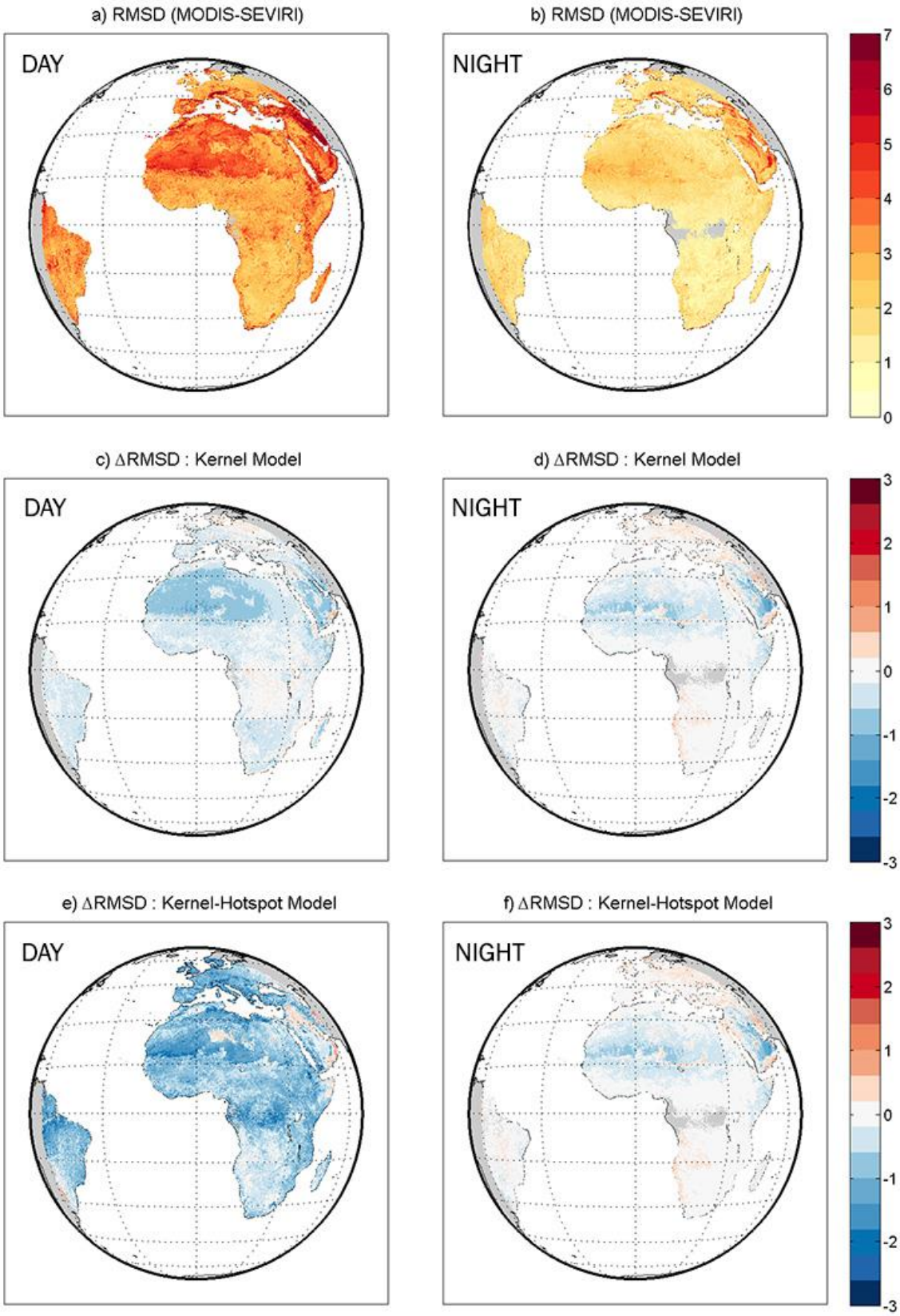

Figure 2.5.5 – Spatial distribution of Root Mean Square Differences (RMSD) between SEVIRI and MODIS (K) without angular correction (a,b) and impact of LST angular correction on RMSD (in K; as [RMSD after angular correction] – [RMSD without correction]), as given by the Kernel model (c,d) and the Kernel-Hotspot model (e,f) .

It may be noted that all models lead to a displacement of the distribution of ΔRMSD towards lower values (Figure 2.5.6), and that the displacement is higher for the Kernel-Hotspot model. This indicates that the Kernel-Hotspot model presents an overall better performance than the Kernel model. There is also a larger displacement of the RMSD distribution of the pixel-based Kernel model than the cluster-based one, but the displacement resulting from the combined Kernel-Hotspot is larger. This suggests a better performance of the Kernel-Hotspot model than that of the Kernel model for both the cluster-based and the pixel-based approaches.

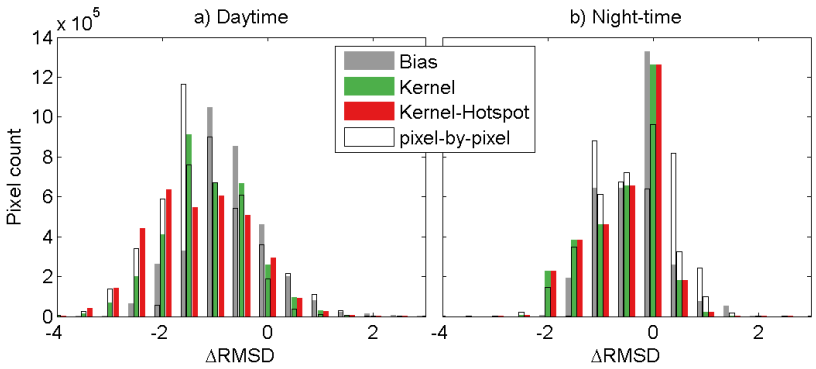

Figure 2.5.6 - Histograms of variation of the root mean square differences (ΔRMSD) between SEVIRI and MODIS (in K) after applying the bias correction (grey) and after applying the angular correction with the Kernel model (green) and the Kernel-Hotspot model (red), for (a) daytime and (b) night-time only observations. The open bars are the respective values for the pixel-based model.

The performance of the Kernel-Hotspot model was further analyzed for each cluster separately (Figure 2.5.7). During daytime, the highest angular corrections are generally found for forest and shrubland, namely the shrub clusters associated to savanna-like vegetation cover (e.g. in central Africa and Iberian Peninsula). These land cover types are particularly prone to shadowing effects (Ermida et al., 2014; Guillevic et al., 2013; Rasmussen et al., 2010). The desert areas also present large corrections, being more susceptible to anisotropic effects associated to the emissivity (McAtee et al., 2003; Ren et al., 2011). The higher percentages of positive values of ΔRMSE are found for the second cluster of the forest group (Figure 2.5.7b) and for the first cluster of the desert group (Figure 2.5.7d). For the forest cluster, the respective *K* parameter is much larger than the remaining clusters (Figure 2.5.3b), which might indicate problems in the calibration. This cluster is associated to equatorial forests (Figure 2.5.1) where there is generally higher cloud coverage. This not only strongly limits the amount of available observations but could also be associated to a higher frequency of cloud contamination of the LST estimates. The desert cluster, being associated to high elevation values, corresponds to areas with high topography heterogeneity (Figure 2.5.2). These areas are particularly challenging since the high heterogeneity enhances geo-referencing errors. Also, slope and orientation of the mountain ridges could introduce shadowing effects that are not fully accounted for by the Kernel model (Ermida et al., 2017a).

SIMULATION OF THE ANGULAR CORRECTIONS ON LST

The Kernel and Kernel-Hotspot models calibrated per cluster may finally be used to quantify the expected angular effects on LST retrieved by any given sensor. Examples of the $T - T_0$ (ΔLST) given by the Kernel and Kernel-hotspot models are shown in Figure 2.5.8 and Figure 2.5.9 for SEVIRI/MSG based observations.

During night-time (00 UTC; Figure 2.5.8a,c,e), the angular corrections should be solely due to emissivity effects, which are simulated by the emissivity kernel. As such, night-time corrections are the same for the Kernel and Kernel-Hotspot models. The largest corrections are observed over the desert areas over the eastern-most part of the disk, encompassing the Arabian Peninsula and Asian regions surrounding the Caspian Sea.

The angular corrections provided by the by the Kernel model are particularly conspicuous at 12 UTC (Figure 2.5.8d), showing high discrepancies when compared to the Kernel-Hotspot. At this time of the day over Europe, SEVIRI is particularly prone to hotspot effects, which lead to high negative corrections as shown in Figure 2.2.4b. The corrections obtained with the Kernel-Hotspot model over the Iberian Peninsula are in agreement with those found with the Geometric model for Évora (Figure 2.2.4b). The Kernel model, however, shows a very contrasting behavior presenting positive corrections over most Europe. This seems to be related to limitations in the simulation of the hotspot effect by the Kernel model, as previously pointed out in section 2.3.

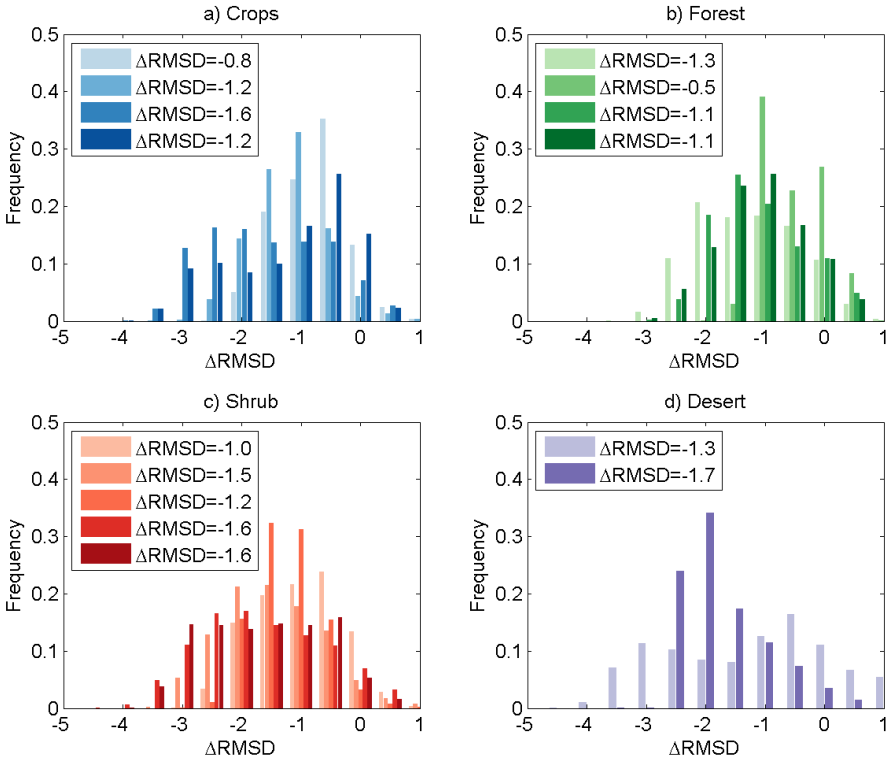

Figure 2.5.7 – Within cluster frequency of variation of the daytime root mean square differences (ΔRMSD) between SEVIRI and MODIS (in K) after applying the angular correction of the Kernel-Hotspot model. Colors correspond to the colorbar of Figure 2.5.1. The legend shows the average ΔRMSE for each cluster.

Examples of the expected angular corrections are also shown for mid-morning (09 UTC; Figure 2.5.9a,c,e) and mid-afternoon (15 UTC; Figure 2.5.9b,d,f). At these times of the day, corrections seem to be mostly controlled by the view angle. Close-to-hotspot geometries occur over the western and eastern parts of the disk for 09 and 15 UTC, respectively, which result in enhanced corrections over these regions (Figure 2.5.9e and f, respectively)). Corrections are particularly high over the eastern part of the disk (Figure 2.5.9f). The angular corrections depend on the LST values and therefore higher corrections are expected during the day, even for desert areas where shadowing effects are reduced. Nevertheless, values of *B* over desert clusters are still significant, despite the emissivity effect being accounted for by the emissivity kernel. As such, during the day the hotspot part of the Kernel-Hotspot model will enhance corrections over desert areas, an effect that may contribute to the high values observed in Figure 2.5.9f.

The values of *B* obtained over the desert areas could be associated to discrepancies in the LST products not related to viewing geometries. This indicates that the Kernel-Hotspot model is particularly sensitive to the LST dataset, and that an optimally calibrated dataset (with the same algorithm and the same input parameters) should preferably be used to avoid overfitting of the model.

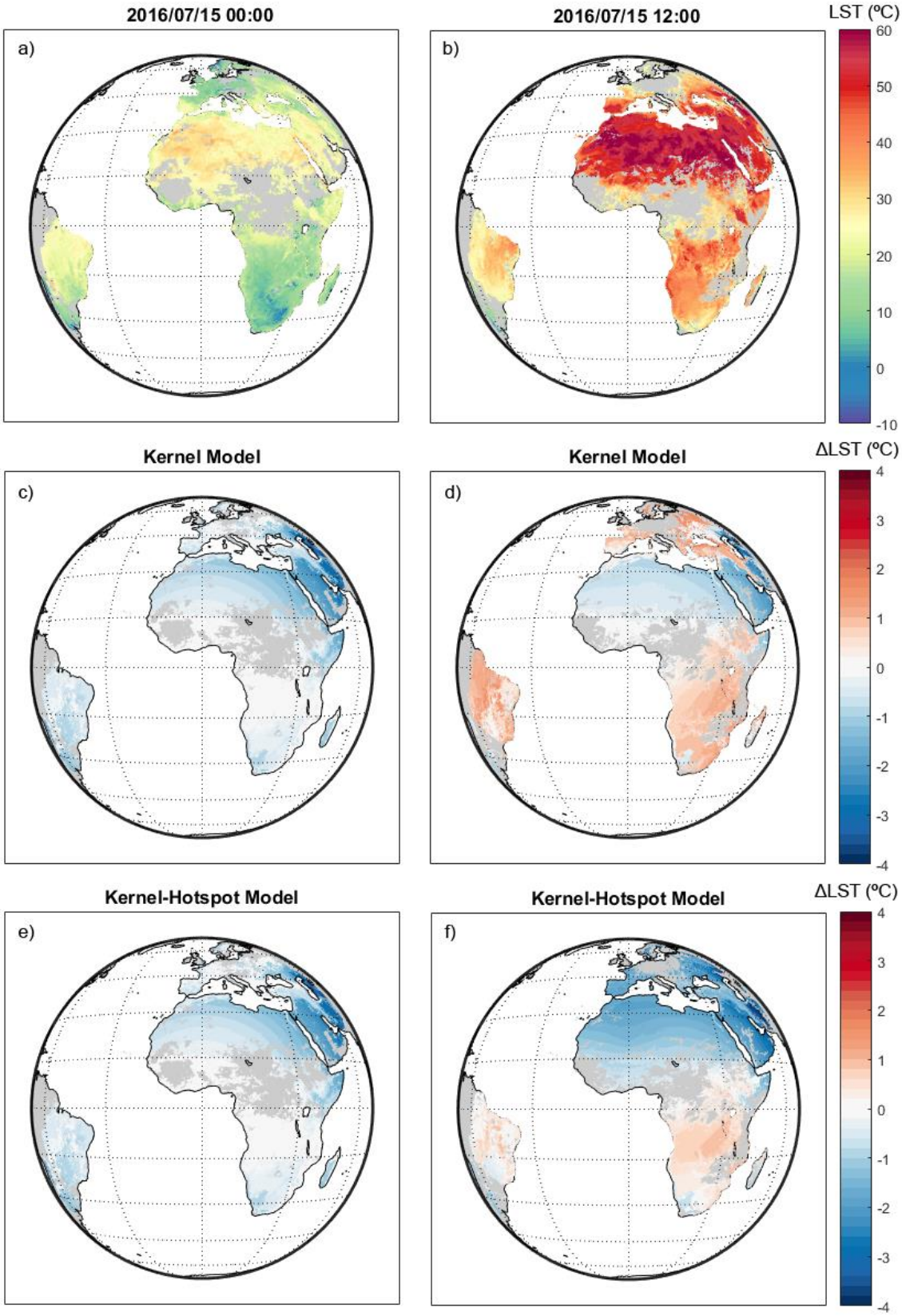

Figure 2.5.8 – Examples of LST (a,b) as retrieved by SEVIRI and respective angular corrections to nadir ($T - T_0$ = ΔLST) as given by the Kernel model (c,e) and the Kernel-Hotspot model (d,f), for the 15th of July of 2016 at 00UTC (a,c,e) and 12UTC (b,d,f). Cloudy land pixels are represented in grey.

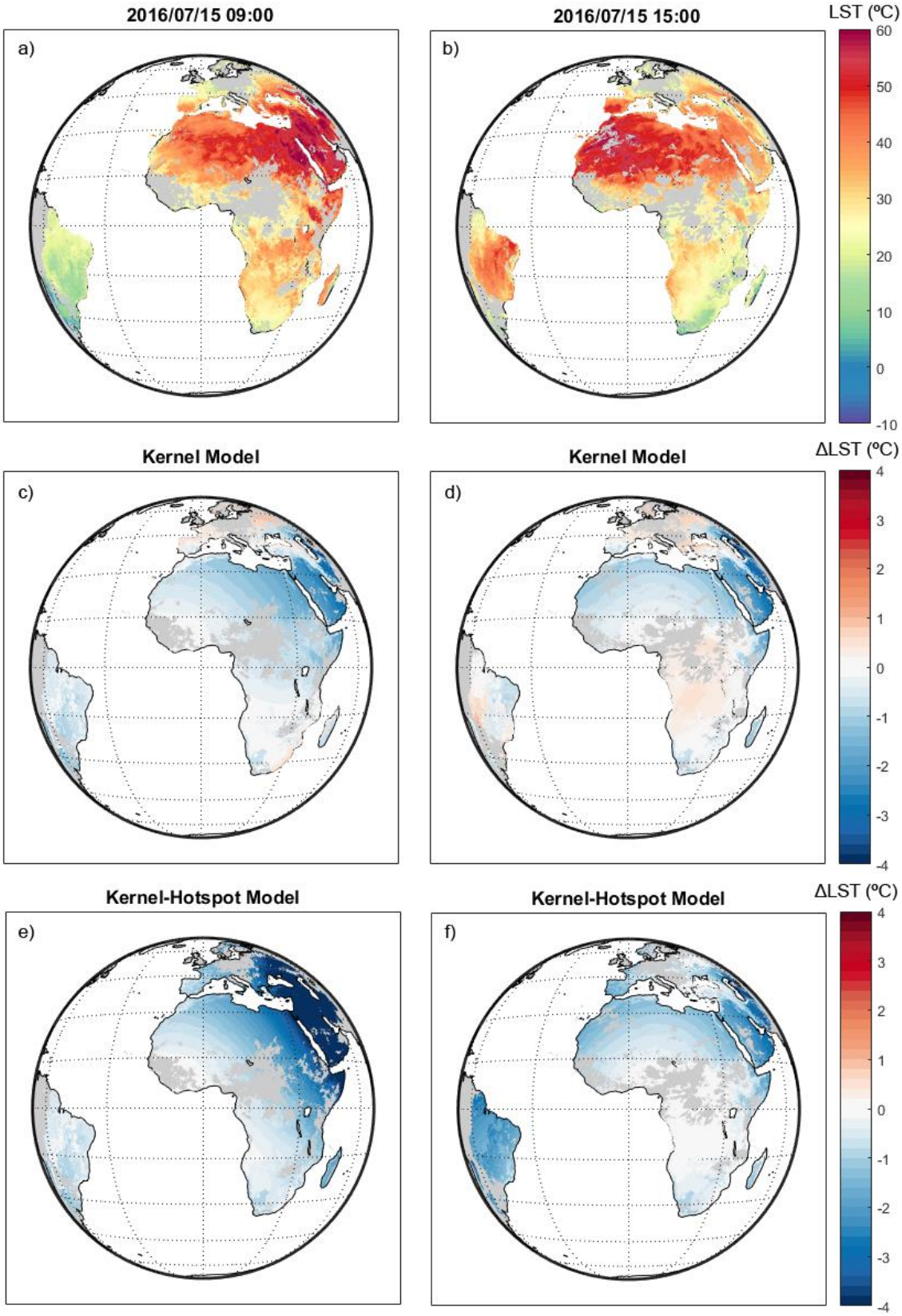

Figure 2.5.9 – As in Figure 2.5.8 but at 09UTC (a,c,e) and 15UTC (b,d,f).

2.6 Summary and Concluding remarks

The correction of directional effects on satellite-retrieved LST is of high relevance for a proper interpretation of spatial and temporal features contained in LST fields. LST differences between products induced by geometric effects may be as high as 15ºC (Ermida et al., 2014; Lagouarde et al., 2014; Rasmussen et al., 2011).

This chapter presents and discusses different approaches to quantify the impact of viewing and illumination geometries on LST. In a first step, we have developed a method to estimate the LST values that are expected to be observed from space for any view/illumination angle, if appropriate ground measurements are available, while keeping assumptions at a minimum. The methodology is based on the identification of the main elements that compose a given scene followed by a statistical estimation of the respective fractions seen by the sensor. The LST within the sensor's FOV can then be estimated if the temperature of each individual element is known. Since the model relies on a computational method that allows calculating the geometrical projections of arbitrary objects, it can be applied to any land surface as long as average tree shape and size and tree density are known, together with the respective temperatures.

The application of the model to ground measurements shows that there is a significant impact of land heterogeneities and viewing geometry on LST. The effect varies throughout the year and over the day as it depends on the relative temperatures of the shaded and sunlit ground and tree components within the viewed scene. The proposed model proved to be a useful tool in the validation of satellite LST against *in situ* measurements, since it allows the effective correction of discrepancies related to viewing and illumination geometry. The use of the model to estimate the ground temperatures to the FOVs of SEVIRI and MODIS sensors reduces the daytime LST bias values by 1 to 2.5 °C, when compared with a simpler upscaling method where the viewing geometry and shadowing effects are not taken into account.

Dependence of emissivity on viewing geometry is complex and difficult to assess and therefore it was assumed that directional differences in emissivity are negligible when compared to variations due to shadowing effects. The directional variability of emissivity should be more important for flat homogeneous surfaces (Cuenca and Sobrino, 2004; Dash et al., 2002; Labed and Stoll, 1991; McAtee et al., 2003; Ren et al., 2011). Also, terrain slope could be incorporated for an improved formulation. The correction involves adjusting the proportions of shaded crown and shaded background according to the specific slope angle and aspect of the site. For the Évora site the slope is small, but this correction should be included for more sloping terrains.

The developed geometric model provides a useful tool for the validation of LST products over heterogeneous landscapes, if the main surface components and respective temperatures are known. Beyond this important aspect, the proposed model serves as a practical baseline for understanding directional effects on LST retrievals.

In this chapter we went further to analyze the adequacy of parametric models to estimate angular effects on LST, using the developed geometric model and *in situ* data acquired at Évora to generate a set of reference data. The Évora station, surrounded by wide area of savanna-type land-cover a (i.e., homogeneous at the large scale), has the right conditions for the application of the geometric model. However, this is rarely the case for most areas, which largely limits the applicability of such type of models to represent LST anisotropy. Parametric models constitute an alternative approach, and in order to offer a better understanding of their performance over different surface conditions we propose the simulation of surface leaving radiance for a wider range of land cover characteristics, both in terms of vegetation density and surface emissivity anisotropy. For that purpose, we perform LST simulations based on the geometric model, for different tree coverages. This allows assessing the changes in the shadowing effects with tree density. It is assumed that the simulated scenes consist of bare ground (instead of desiccated grass, as in Évora) and trees, constituting a good test-bed for simulating emissivity anisotropy, as well as shading effects. These assumptions on the land cover characteristics

are not meant to represent the real conditions at any specific site, although actual measurements of brightness temperatures taken at Évora are used in the simulations. There may be inconsistencies between the imposed surface conditions and the brightness temperatures being measured. For instance, typical surface temperature values observed over deserts or dense forests are not expected to be the same as for a savanna. Nevertheless, we assume that the measured temperatures represent a close enough approximation to the diurnal cycles of other land covers. As such, the observations taken at the site, together with the different configurations of the geometric model (i.e., different vegetation and bare ground conditions) allow building a wide range of scenarios that can be used to test parameterizations of LST directional effects. Furthermore, the high contrasts between shadow and sunlit ground temperature observed at the Évora station lead to high LST directionality, making these observations particularly appropriate to evaluate such parametric models.

In order to introduce a realistic seasonal variability to the simulations, we chose to maintain the FVC seasonal cycle observed over Évora for the calculation of the emissivity. Since PTC affects FVC, this implies the adjustment of FVC values, for different PTC values. We also considered bare-ground emissivity to be lower than that of vegetation or of tree tops (e.g., Peres and DaCamara, 2005; Trigo et al., 2008b), which allows a reduction of the emissivity when the radiometer is measuring bare soil (summer) when compared to green grass (winter). The angular dependence of soil emissivity is simulated with a simple parametrization derived from experimental setups. In real conditions, especially considering the large footprint of a satellite, this dependence is expected to be much more complex given the heterogeneity introduced by the surface composition and roughness. Nevertheless, the proposed parameterization effectively allows an evaluation of the parametric models' response to emissivity anisotropy. In this respect, it is worth emphasizing that the expressions used to model emissivity anisotropy when generating the synthetic data set (eq. (2.3.1)) are different from the one used in the Kernel model (eq. (2.3.5)).

The Hotspot model shows a very good agreement with the reference dataset generated by the Geometric model in the simulation of shadowing effects, while the Kernel model allows a good simulation of emissivity anisotropy. Results show that the Hotspot model presents a better performance for most sun-view configurations, with the Kernel model significantly underestimating the amplitude of the angular corrections. In turn, one limitation of the Hotspot model is its inability to simulate emissivity anisotropy, which could be overcome through the combination of the Kernel and Hotspot models. The Hotspot model was designed to simulate the hotspot geometry associated with shadowing effects. When tree coverage is low or nonexistent the model will fit the best hotspot geometry to the LST anisotropy in the data, leading in this case to negative *K* values.

We propose a parameterization of the hotspot-to-nadir LST differences that depends on daily input radiation and sun zenith angle, derived from the differences found with the Geometric model. The ΔT_H value depends on the contrasts between the temperature of shade and sunlit ground and of the tree canopies, which ultimately leads to a dependence of ΔT_H on the amplitude of the different temperatures. The amplitude of the surface temperature is primarily controlled by the daily available TOA radiation and, as such, this variable constitutes a good proxy for ΔT_H. The TOA radiation dependence introduces seasonal and spatial variability in ΔT_H, while the sun zenith angle represents the diurnal variation.

Tests on the seasonality of the models show no significant improvement of the quality of fit, which suggests that to some extent the models incorporate this seasonality through the dependence on the illumination angle. Furthermore, a seasonal fit of the models leads to a limitation of the sun angle sampling that impacts the quality of the fit. Nevertheless, there is an important seasonal change in the behavior of the emissivity kernel, resulting in the change of the signal of the parameter *A*. This is related to contrasting conditions in the simulated scenes that lead to a predominance of intrinsic anisotropy in summer and of geometric effects during winter. Since the emissivity kernel does not depend on sun angle, a seasonal fit of this kernel could be performed that is not susceptible to sampling problems.

The sensitivity of the models to view and solar angles sampling was also analyzed. Results suggest that, if the models are to be calibrated with satellite data, special attention must be paid to sampling problems as they may affect the quality of the fit. We found that the average impact on LST may be as high as 0.5ºC, which means that local impacts might be significant.

The present chapter further addressed the problem of modelling directional effects of LST products using time series of observations collocated in space and time from SEVIRI on-board MSG satellites, and MODIS on-board Aqua and Terra. For each pixel, the kernel model is statistically fitted to unbiased pairs of SEVIRI and MODIS observations using a linear regression. The spatial distributions of parameters *A* and *D*, the coefficients of the emissivity and solar kernels, respectively, reflect the characteristics of the landscape, both in terms of vegetation cover and topography. Values of A are mainly influenced by local biases between MODIS and SEVIRI LST products, which in turn are associated to a wide range of factors (e.g. emissivity differences, biases induced by surface heterogeneity and SEVIRI fixed viewing geometry). Those factors overlap the impact of emissivity angular dependence, which only has a relevant impact on LST for large VZAs. The higher values of parameter *D* (solar kernel) are associated to areas dominated by moderately dense forest and indicate a strong dependence of LST on shadowing effects.

Over mountainous regions, there is a close agreement between the spatial distribution of *D* and that of the fraction of illumination. Both quantities tend to form stripes on the images corresponding to valeys, those with higher (lower) values of *D* being associated to higher (lower) values of fraction of illumination. The kernel model originally proposed by Vinnikov et al. (2012) did not take into account shading geometry associated with sloping terrain. However, and despite the caveats referred above for those surfaces, the model is able to simulate LST anisotropy associated with heterogeneities induced either by vegetation or local orography. Improvement of the model by explicitly including these features may help increase quality of the regressions, leading to better quality of parameters over these regions. It is also worth noticing that vegetation cover and orography are generally correlated, which might make the partitioning between vegetation and topographic effects difficult. Nevertheless, the obtained *D* parameters seem to be consistent with the expected slope shading (Figure 2.4.8), which suggests that the solar kernel is able to statistically depict these features from the LST data.

The performance of the kernel model was assessed through several comparison exercises over the 3-year period under analysis, where the differences between collocated LST values obtained from MODIS and SEVRI/Meteosat are considered before and after the angular effects are taken into account. Since there is no method available that would allow the validation of the model over the whole region of study, LST differences between the sensors were used as a measure of quality and consistency of the model. It is shown that the use of the kernel model to describe the angular variability of LST effectively reduces the differences between the two products. A cross-validation of the kernel model revealed that the RMSD between SEVIRI and MODIS daytime (night-time) products changed from the original values of 3.5 K (1.5 K) to 2.3 K (1.3 K), once the correction was considered. The larger decreases in local RMSD were observed over mountainous regions and over an arid patch over northern Algeria, reflecting the roles played by the solar and the emissivity kernels, respectively. The cross-validation and evaluation with independent data show that LST differences present a decrease that is consistent with the previous results, indicating that the model is robust. Robustness is very import in this case since it will allow for the model to be used operationally without the need of frequent recalibration, although the model parameters should be checked on a regular basis since changes in land cover may require recalibration.

Results of this study demonstrate that it is possible to use LST estimates collocated in space and time, but obtained with different viewing geometries, to calibrate a simple model capable of characterizing the LST angular variability. It has been shown that the model calibration is stable, and it can be easily extended to other areas. As such, the kernel model may be viewed as a tool to estimate the expected LST uncertainty associated with viewing and illumination angles.

Quality of estimated parameters of the kernel model depend on an adequate sampling of viewing and illumination angles. This is a general issue when calibrating parametric models based on information from geostationary and polar orbit satellites. In the present study, a representative sampling of illumination angles is achieved by calibrating the model using full-year time-series. In the case of the viewing angles, there are only limitations in azimuth angles (no observations from north) but these are expected to have small impact on the parameters because the solar kernel is symmetric for relative azimuth angles.

The main limitation found in the calibration of parametric models with satellite-retrieved LST seems to be associated to the high impact on the obtain parameters of LST discrepancies not related to the viewing geometry. To partially overcome such problems, we propose a methodology to calibrate the models where a cluster approach is used to aggregate pixels with similar surface conditions, allowing an effective reduction of overfitting to local biases and a better sampling of view and illumination angles.

The distributions of the models' parameters reflect the main characteristics of the clusters' landscape. Values of *A* (emissivity kernel) are always negative and show an inverse relation with the density of vegetation, while parameters *D, K* and *B* generally present an increase with increasing fraction of vegetation. This is in agreement with the relationships previously found between these models and vegetation indicators (sections 2.3 and 2.4). It is shown that the use of the models calibrated per cluster to correct for angular effects reduces the differences between the two products. Decreases in RMSD are found to be larger for the Kernel-Hotspot model than for the Kernel model, which is in agreement with the assessment shown in section 2.3.

However, the Kernel-Hotspot seems to be particularly sensitive to the calibration database. This is to be expected as this model is able to provide larger corrections than the Kernel model. As a result, LST discrepancies between the LST products non-associated to viewing geometry that were not fully accounted for in the bias correction could lead to overfitting of the model. Consequently, angular corrections may be overestimated by this model. As such, to avoid overfitting problems, the model should be fitted to LST data that were previously calibrated and processed using the same algorithm and input data.

This study shows that collocated satellite observations may be used to calibrate a parametric model that in turn allows an effective representation of directional effects on LST. The method can easily be extended for other sensors and the simplicity of the model makes it particularly appropriate to be used in an operational context. This methodology is currently being used in the framework of the ESA DUE GlobTemperature project (http://www.globtemperature.info/) and was extend to the other geostationary sensors: the Japanese Meteorological Imager (JAMI) on-board the Japanese Meteorological Association (JMA) Multifunction Transport SATellite 2 (MTSAT-2), the Advanced Himawari Imager (AHI) on-board Himawari 8, and NASA's Geostationary Operational Environmental Satellites (GOES). Information on angular effects on LST is provided in a data layer in the Merged LST product that consists in an estimate of LST difference from the nadir to the satellite view.

We are currently working on a methodology to retrieve emissivity directionality from collocated radiance measurements performed by multiple sensors. A brief description of the methodology and preliminary results are shown in Appendix A.

CHAPTER 3

QUANTIFYING THE CLEAR-SKY BIAS OF IR LST WITH MW LST

CONTENTS

3. Quantifying the clear-sky bias of IR LST with MW LST

3.1 Introduction

The estimation of LST from space-borne sensors has been systematically performed on a global scale for over three decades and geostationary and polar orbiter LST climate data records are now available e.g. from the International Satellite Cloud Climatology Project (Rossow and Schiffer, 1999) and Pathfinder Atmospheres-Extended dataset (Heidinger et al., 2013), opening new perspectives for climate monitoring (Arnfield, 2003; Hansen et al., 2010; Liang et al., 2013; Sellers et al., 1992; Thies and Bendix, 2011; Weng, 2009; Yang et al., 2013). The compilation of a 30+ year LST CDR with a 30-min temporal and 5-km spatial resolution over Africa and Europe is currently under way using information from EUMETSAT Meteosat First and Second Generation series of geostationary satellites (Duguay-Tetzlaff et al., 2015).

The retrieval of LST from satellite observations generally relies on measurements in the TIR window, the spectral band that contains the peak of Earth's spectral radiance and presents relatively weak atmospheric attenuation under clear-sky conditions. Although there is a large number of IR sensors on-board geostationary satellites and polar orbiters performing LST retrievals with different temporal and spatial resolutions, the use of IR observations limits LST retrievals to clear-sky conditions. As a consequence, climate studies based on IR LST are likely to be affected by the restriction of LST data to cloudless conditions. However, such "clear-sky bias" has never been quantified and, therefore, the true impact of relying only on clear-sky data is uncertain.

Passive MW measurements, on the other hand, are much less affected by clouds than IR observations. LST estimates can in principal be derived from MW measurements, regardless of the cloud conditions, e.g. Prigent et al. (2003a). Over the last decades, several algorithms have been proposed for the retrieval of LST from passive MW observations.

The first attempt to obtain LST from passive MW imagers was carried out by McFarland et al. (1990). The proposed method used a linear regression model dependent on surface type to determine surface temperature from brightness temperatures retrieved by the Special Sensor Microwave Imager (SSM/I) at 19, 22, 37 and 85 GHz. However, serious limitations were found in deriving the LST over surface types like snow cover or wet ground and the method could not be used over these areas. Basist et al. (1998) also proposed a LST retrieval scheme for SSM/I were the different channels are used to obtain information on vegetation cover, snow cover and ground wetness, allowing an effective correction of the surface emissivities. Ultimately, a relationship is derived between LST and the observed brightness temperatures for different surface conditions and using the corrected emissivities. Such methodology permitted the retrieval of LST over areas previously considered problematic by McFarland et al. (1990).

For the same sensor, Weng and Grody (1998) proposed a physical algorithm based on the 19 and 22 GHz channels, where it is assumed that surface emissivity is the same for such closely spaced channels and brightness temperature differences are mainly due to differential atmospheric water vapor emission. Njoku and Li (1999) developed an approach for the retrieval of surface parameters (soil moisture, vegetation water content, and surface temperature) using brightness temperature measured by the Advanced MW Scanning Radiometer (AMSR), launched on the Japanese Advanced Earth Observing Satellite (ADEOS)-II and the Earth Observing System (EOS) PM-1 platforms. The model was based on a radiative transfer model applied to brightness temperature data from the 6 to 18 GHz channels.

Aires et al. (2001) proposed a new method using a neural network approach to retrieve surface skin temperature, integrated water vapor content, cloud liquid water path and surface emissivities between 19 and 85 GHz over land from SSM/I observations. The algorithm showed high accuracy however, the LST inversion requires a large range of ancillary data. An analytical algorithm for the determination of land surface temperature and soil moisture from the Tropical Rainfall Measuring Mission/MW Imager (TRMM/TMI) was also developed by Wen et al. (2003). The method was based on radiative transfer equations applied to the 19.65 and 21.3 GHz channels. Later on, Holmes et al. (2009) proposed a retrieval scheme based on a simple linear relationship between 37GHz vertical polarized brightness temperature and LST. However, barren, sparsely vegetated, and open shrublands cannot be accurately described with this single channel approach because variable surface conditions become more relevant.

In a recent paper Prigent et al. (2016) presented a simplified methodology to retrieve LST from brightness temperatures (Tb) acquired by MW connical scanners and applied the methodology to invert SSM/I Tbs. This methodology used the experience gained by retrieving atmospheric and land surface parameters from the inversion method presented in Aires et al. (2001) and proposed a simplified scheme to minimize the number of ancillary inputs required in the processing. Given their objectives of building a climatological record of LST and preparing for a potential near-real-time processing, a small number of auxiliary inputs was considered a priority in order to avoid discontinuity in the data record related to changes or absences of input sources, and to avoid waiting until the ancillary inputs are processed and disseminated. In essence, the proposed methodology consisted in training a neural network with a database of Tb and LST built from the detailed inversions of Aires et al. (2001) to provide a fast global transfer function approximating the Tb-LST relationship. The only required inputs (apart from the MW Tb) were pre-calculated MW monthly mean emissivities available from the Tool to Estimate Land Surface Emissivity in the MW (Aires et al., 2011). Given the large impact of the land surface emissivity on the observed Tb, adding emissivity estimates helps to constrain the inversion problem. Although instantaneous emissivities at the observation time will result in more accurate retrievals for locations with large emissivity variability, climatological estimates were found to be a good compromise for this simplified methodology.

In section 3.2, we present a methodology adapted from Prigent et al. (2016) to retrieve LST from the Advanced Microwave Scanning Radiometer–EOS (AMSR-E) observations and evaluate the produced estimates at a number of ground stations. First, the methodology to invert the AMSR-E observations and the data used to evaluate the retrieved LST are presented. This is followed by characterizing the AMSR-E inversions, and an evaluation of the produced LST at a selection of ground stations.

We also perform a comprehensive comparison between LST derived from AMSR-E passive MW observations and LST derived from IR sensors, namely, from MODIS onboard Aqua, SEVIRI on board the MSG satellites, the GOES Imager, and JAMI on board the MTSAT-2. This comparison exercise is presented in section 3.3. The consistency between MW and IR-derived LST is analyzed for clear-sky observations under different surface conditions and using the IR LST products as the baseline. First, the satellite data and the space-time collocation methodology are described. Then, results of the comparison between MODIS and AMSR-E, together with a detailed analysis for different surface conditions, are presented. Lastly, an intercomparison is performed of all IR and MW products.

A 3-year record of all-weather MW LST is then used to quantify the clear-sky bias of IR LST at the global scale (section 3.4). The associated cloud coverage to each pixel is here obtained from measurements performed by MODIS on-board the same satellite. The bias is analyzed in terms of spatial and temporal distribution.

DATA DESCRIPTION

MW LST is derived from AMSR-E brightness temperatures (Tb), extracted from the National Snow and Ice Data Center archive (Shcroft and Wentz, 2013). For the inversions, the 18.7, 23.8, and 36.5 GHz channels are applied at their original resolutions (27 × 16, 31 × 18, and 14 × 8 km, respectively),

while the 89.0 GHz channels with an original resolution of 6 × 4 km are resampled to the 36.5 GHz resolution. The highest resolution channels are likely to have more weight on the retrieval at most locations, potentially resulting in a LST retrieval with an "effective" spatial mean resolution closer to 12 km (36.5 GHz) than to 21 km (18.7 GHz). According to this, the LST retrieval is placed in the 14 × 8 km swath grid of the 36.5 GHz channel, although information from a larger footprint is likely to affect the retrieval.

To evaluate the AMSR-E inversions, data records of LST estimated from ground IR measurements at 10 stations in the year 2010 were available from an evaluation data set compiled by the ESA DUE GlobTemperature project. The stations are listed in Table 3.1.1, grouped by climate types. Three of them (EVO, GBB, and KAL) are run by the Land Surface Analysis Satellite Applications Facility (LSA SAF) (Trigo et al., 2011) and have narrowband IR radiometers dedicated to the validation of satellite LST. The remaining seven (GCM, BND, PSU, SFA, FPK, DRA, and TBL) belong to the Surface Radiation Network (SURFRAD) (Augustine et al., 2005) and use broadband IR radiometers that are part of a suite of different instruments dedicated to measure radiation-related variables. Notice that apart from the difference in radiometers, the data at the stations are not identically processed. For the SURFRAD stations, the emissivity required to derive the LST from the radiometric observations comes from the database of Seemann et al. (2008). For the LSA SAF stations, EVO and KAL use the emissivity retrieved for the LSA SAF satellite LST inversions (Trigo et al., 2008a), while the emissivity at GBB is estimated following Göttsche and Hulley (2012). Notice that for EVO, apart from the radiometers measuring the upwelling and downwelling radiation, there is a third radiometer measuring canopy Tb, which is combined with the other measurements assuming a fixed fraction of vegetation cover (Ermida et al., 2014). Together with the LST estimates, an estimation of the uncertainty is provided by error propagating the broadband emissivity uncertainty and the measurement uncertainty of the radiances (Göttsche et al., 2016). The resulting overall LST uncertainty lies in a range between 0.6 and 2 K for all stations (Martin and Göttsche, 2015).

Table 3.1.1 – Station Location, Climate, and Surface Type.

ID	Latitude, Longitude	Location	Climate	Surface
		Temperate		
EVO	38.5, -8.00	Évora, Portugal	Mediterranean	Forest
GCM	34.2, -89.9	Goodwin Creek, Miss., USA	Humid subtropical	Forest
BND	40.0, -88.4	Bondville, Illinois, USA	Humid subtropical	Cropland
		Boreal		
PSU	40.7 -77.9	Pennsylvania State University, Pennsylvania, USA	Humid continental	Forest, cropland
SFA	43.7, -96.6	Sioux Falls, South Dakota, USA	Humid continental	Cropland
FPK	48.3, -105.1	Fort Peck, Montana, USA	Semiarid	Cropland
		Subtropical		
DRA	36.6, -116.0	Desert Rock, Nevada, USA	Arid	Rock
GBB	-23.5, 15.0	Gobabeb, Namib Desert, Namibia	Arid	Rock, sand
KAL	-23.0, 18.3	Kalahari, Namibia	Arid	Rock
		Highlands		
TBL	40.1, -105.2	Table Mountain, Boulder, Colorado, USA	Highland	Rock, shrub

The stations are associated with different environments and were accordingly organized into four main climate types: temperate, boreal, subtropical, and highlands. The stations EVO, GCM, and BND are located in temperate climate areas; the EVO station presents a drier Mediterranean climate, and the remaining ones belong to more humid environments. The stations PSU, SFA, and FPK have boreal climates; PSU and SFA are typical of humid environments, while FPK represents a very dry environment. DRA, GBB, and KAL are desert stations, characteristic of the subtropical climate. The last station, TBL, although belonging to a temperate climate, is located in a mountainous region; because of the high spatial heterogeneity, this station is analyzed separately. For each station, AMSR-E overpasses are matched to the station available LST observations allowing a maximum distance of

7 km between the station location and the pixel center, and a maximum difference of 5 min between the AMSR-E and the station time acquisitions. As the station data are recorded every minute and the records are quite continuous, in practical terms the time difference is in most cases within one minute.

To provide a satellite IR reference to the AMSR-E evaluations, MODIS LST (Wan and Li, 2008) is also compared to the station data. MODIS-Aqua and AMSR-E are on board the same satellite platform, so they are closely collocated in time. Regarding the spatial matching, MODIS 1 km data were averaged to the 14 × 8 km swath grid adopted for the AMSR-E LST retrieval to assure that surface heterogeneity impacts equally both LST estimations. Only MODIS pixels with the best quality flag were considered. Grid cells where less than 100% of MODIS pixels are valid are considered as cloudy, and the resulting cloud mask is used to separate AMSR-E estimates into clear and cloudy-sky.

SEVIRI LST (Trigo et al., 2008a) covering the study time period is also used to assess AMSR-E LST. Spatial collocation is performed as for the MODIS data set, and only observations with a time difference up to 7.5 min are considered.

GOES and MTSAT LST data are produced by the Copernicus Global Land Service within the framework of the GEOLAND-2 (Lacaze et al., 2011). LST is estimated using a Dual Algorithm (Freitas et al., 2013) applied to TOA brightness temperature measurements from one middle IR and one thermal window channel overnight and from a single thermal window channel during day. Both products are available in the geostationary projection (as for SEVIRI) with a 4 km resolution at subsatellite point and with a 3-hourly temporal resolution. The GOES disk encompasses all the American continent, while MTSAT covers the eastern most part of Asia and Australia. Space and time collocation is as described for SEVIRI.

All IR LST data sets were extracted from the product versions archived at the data portal of the ESA DUE GlobTemperature project. The AMSR-E data set was specifically processed for this comparison, but the 3-year period from 2008 to 2010 is available from the same data portal.

Backscattering coefficients (σ_0) are estimated from active MW observations performed by a wind scatterometer operating at 5.25 GHz on board the European Remote Sensing (ERS) satellite (Frison and Mougin, 1996) and are used here to indicate regions with large MW penetration depth. As the radar backscattering is a combination of surface and volume scattering, at places where surface roughness is low and wave penetration is large very little power is reflected back to the instrument and the backscattering coefficient takes small values. A threshold of −20 dB is used here to identify places with large penetration depth, selected by comparison of maps of the backscattering coefficient with maps of variables that help identify these locations, such as maps of sand dunes and shifting sands, roughness lengths, and MW surface emissivity variability (Prigent et al., 2005). The coefficients are estimated globally for a viewing angle of 45◦, at 0.25◦ spatial resolution, averaged over 8 years (1993–2000).

To identify snow/ice-covered surfaces in this comparison, the Global Multisensor Automated Snow and Ice (GMASI) Mapping System product developed by NOAA National Environmental Satellite, Data, and Information Service (NESDIS) is used (Romanov, 2016). The snow and ice mask are derived from combined observations in the visible, IR, and MW bands from different sensors, on a daily basis, with a 0.04◦ × 0.04◦ resolution.

Information on land surface cover is obtained from ESA Global Land Cover Product (v2.2) (Bicheron et al., 2008). This land cover map is derived from surface reflectance as measured by the Medium Resolution Imaging Spectrometer Instrument on board the Envisat satellite with a resolution of 300 m. The product is characterized by 22 land cover classes and represents the period from December 2004 to June 2006. The 22 original classes were grouped into eight main classes as follows: (1) permanent or regularly flooded forest and croplands, (2) cropland, (3) equatorial forest, (4) high-latitude forest, (5) shrubland/grassland, (6) sparse vegetation, (7) bare areas, and (8) other (urban, water, and permanent snow).

Information on cloud coverage is obtained from the Level-3 MODIS/Aqua Atmosphere Daily Global Product from collection 6 (MYD08_D3; Platnick et al., 2015), which correspond to daily daytime and night-time mean cloud fraction at a resolution of $1^{o}x1^{o}$.

3.2 All-weather LST retrieval from MW observations

INVERSION METHODOLOGY

The AMSR-E Tbs are inverted with the methodology presented in Prigent et al. (2016), with some minor adaptations to deal specifically with the AMSR-E observations. Similar to the SSM/I inversions presented in Prigent et al. (2016) work, a neural network is trained with a database of coincident AMSR-E Tbs, retrieved LST from the 2003 AMSR-E inversions presented in Lipton et al. (2015) (referred to as Ts*), and a monthly AMSR-E emissivity climatology derived using as ancillary LST data from MODIS on the same Aqua spacecraft (Moncet et al., 2011).

As for the SSM/I inversions, a strategy of having separate neural networks for (1) Greenland and Antarctic, referred to as permanent snow, and (2) the remaining continental land is also adopted. Unlike SSM/I, inversion tests showed that independent trainings for the night-time and daytime retrievals were more effective at approximating the Tb-LST relationship. The AMSR-E close to midnight and midday overpasses typically result in quite different surface-atmosphere conditions with a more different range of LST (compared with the closer conditions between the SSM/I early morning and late afternoon overpasses), and an inversion having two dedicated setups (one for night-time and one for daytime) for each of the two geographical selections was adopted.

Multilayer perceptrons are used to implement each neural network. The input layer has as many nodes as the number of frequency channels and associated emissivities used for the inversion. It is followed by a hidden layer of 10 nodes, and the output layer with one node for the retrieved LST. For the training, 105 cases are randomly selected from the Tb-LST database. The initial weights of the neural network are randomly initialized by the Nguyen-Widrow algorithm (Nguyen and Widrow, 1990), and the final weights are assigned by a Marquardt-Levenberg backpropagation algorithm (Hagan and Menhaj, 1994). To prevent overfitting to the training data set, a cross-validation technique is used to monitor the evolution of the training error function.

Once the neural network is trained, it becomes a transfer function to produce LST from the observed Tb and associated emissivities. The training of the neural network corresponds to the minimization of an error function, here the sum of squared differences between the neural network response to the training input vector and the corresponding target vector. The initial weights are slightly changed to minimize the error function, which results in a new set of final weights and therefore a new transfer function. In most cases the resulting transfer functions are very close, and for well-constrained inversion situations the variability in the output (here the retrieved LST) by applying the neural networks from different trainings is small. Likewise, a large variability is an indication of inversion situations where the neural network has difficulties to solve the inverse problem. To use this variability as a form of quality control for the inversions, 50 neural networks for each of the four retrieval setups (continental land and permanent snow, each with daytime and night-time separated inversions) are trained with different initial conditions. The neural network with the smallest training error is selected to produce the retrieved LST, and the variability of the 50 final LST for each inversion is monitored to capture cases where the inversion situation seems problematic.

The AMSR-E 18.7, 36.5, and 89.0 GHz vertically and horizontally polarized channels and the 23.8 GHz vertically polarized channel are used for the retrieval, in a similar configuration to the SSM/I retrievals of Prigent et al. (2016). In principle, the 6.9 and 10.6 GHz lower frequency channels could also have been considered for the retrieval. They are more transparent to clouds, but their spatial resolution is coarser, they sample a deeper surface layer, and they are more sensitive to surface characteristics, requiring a more accurate estimate of the surface emissivity to derive LST. In addition, they are known to suffer from radio frequency interference (Li et al., 2004). The spatial resolution of the 6.9 GHz

channels is approximately 3 times coarser than at 18.7 GHz channels, so we did not consider it any further as we attempt to produce LST retrievals at a relatively fine spatial resolution. The 10.6 GHz channels are closer in spatial resolution to the 18.7 GHz channels, but inversion tests with the training database did not show any improvement in performance when these channels were added to the higher-frequency channels. With our inversion methodology relying on monthly climatological emissivity, it is possible that any positive effects on the inversion related to a larger transparency to clouds are compensated by unaccounted variability of the surface emissivity at this frequency. Therefore, we favored the channel selection without the 10.6 GHz in order to have an inversion algorithm as close as possible to the SSM/I inversions.

An estimate of retrieval uncertainty is always useful and required for some applications (e.g., in data assimilation), and a simple uncertainty map has been derived by analyzing the total retrieval errors in the training database. The selected final neural network is applied to a new subset of the training database not seen by the neural network during the training phase, and the differences between the target surface temperature in the database Ts* and the retrieved LST are used to infer an uncertainty estimate for a range of emissivity and LST values. The result is a lookup table storing the mean difference for 56 combinations of LST and emissivity, using the 18.7GHz horizontally polarized channel. This emissivity has a slightly larger variability than the other emissivities, so it is well indicated to classify diverse inversion situations. For a given retrieval of LST and associated emissivity, the lookup table is searched and the found value is used as a simple estimation of the inversion uncertainty. It should be stressed that the uncertainty is derived from the difference with the MW LST of the training database, but not with the unavailable real ground LST corresponding to the database Tb.

As the MW Ts* in the training database is the product of an inversion subject to retrieval errors (see Aires et al. (2001) for a discussion), the uncertainty from the derived lookup table should be considered as a lower estimate of the “true” retrieval error.

INVERSIONS CHARACTERIZATION

Following the methodology described before, inversions of AMSR-E Tb have been conducted at the sensor ground location. The retrievals are conducted in the AMSR-E swath grid of 14 × 8 km of the 36.5 GHz channel, but the retrievals are also affected by observations with coarser resolution from the lower frequency channels. Spatial coverage is global, twice a day at ~1:30 A.M./P.M., but the 1–2 days revisiting time and some missing AMSR-E acquisitions result in gaps in the data record.

The inversions corresponding to 4 days in 2008 are presented in Figure 3.2.1 as an example of retrieved LST. With the 1–2 days revisiting time, full coverage only happens at the higher northern and southern latitudes. Missing night-time orbits are also noticeable for these specific days. The expected LST geographical patterns are well reproduced, with the warm and cold regions associated with the different climate regions clearly visible in the maps. The night-time/daytime differences are also as expected, with the largest gradients occurring over arid and semiarid areas. More detailed discussions are provided below.

AMSR-E RETRIEVAL UNCERTAINTY

The ability of the neural network to approximate the Tb-LST relationship under different inversion situations is shown in Figure 3.2.2 (black lines). The figure shows histograms of the night-time/daytime difference between the MW Ts* (the target variable during the neural network training) and the retrieved LST (the output from the neural network once it is trained) for three ranges of the 18.7 GHz horizontally polarized emissivity and two ranges of LST. As described before, this difference is used to build a lookup table to produce an approximated uncertainty characterization for the LST retrievals.

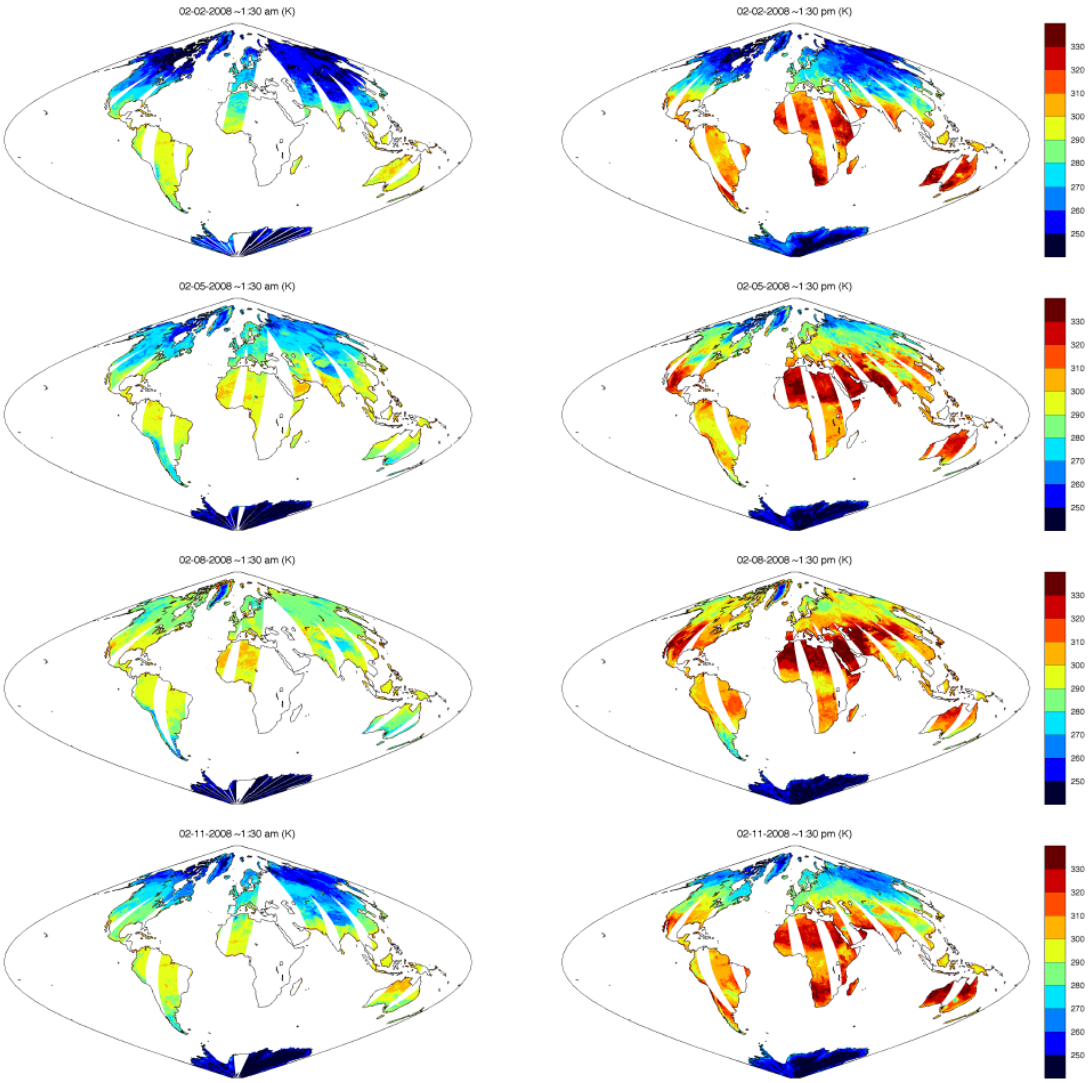

Figure 3.2.1 - Example of AMSR-E retrieved LST for 2 February, 2 May, 2 August, and 2 November 2008. (left column) night-time overpass retrieval; (right column) the daytime overpass. The gaps over land correspond to areas where there are no AMSR-E data available for the inversions; most of them are due to the AMSR-E swath, but missing portion of orbits are also visible during the night.

Global maps of this retrieval uncertainty are plotted in Figure 3.2.3 for 4 days in 2008. RMSD ranging from 2.0 K (warm LST, high emissivity) to 4.0 K (cold LST, low emissivity) are shown in Figure 3.2.2, with the RMSD below 2.8 K for ~75% of the global land surface. Large uncertainty can be observed for snow-covered and humid surfaces, conditions where the climatological emissivities can be poorly representing the true emissivity, implying larger difficulties in retrieving the surface LST. This is also visible in Figure 3.2.3, where large uncertainty is estimated for the snow-covered regions. The smallest uncertainty occurs over tropical forests. This possibly reflects a better match between the climatological emissivity used in the inversion and the real emissivity. In these regions, the surface is temporarily more stable and the relatively simple surface emission models used to derive the emissivity from the MW observations are closer to reality. The opposite happens in snow-covered regions, where melting and snow metamorphisms result in a more varying emissivity and more difficulties to estimate the surface emission. For most cases, the RMSD in Figure 3.2.2 is larger in the daytime than at night. This is likely to reflect the most challenging inversion situation for the daytime overpasses. Strongest subsurface thermal gradients are more likely at daytime and can accentuate the impact of MW penetration in the retrieval (i.e., the LST to be retrieved is not just a skin temperature but represents a temperature derived from the emission of a nonuniform temperature layer of a

certain depth). Figure 3.2.3 also shows that in general the retrieval uncertainty is lower at night than in the daytime.

For reference, Figure 3.2.2 also shows the LST uncertainty characterization when SSM/I Tb are inverted using the SSM/I retrieval scheme presented in Prigent et al. (2016) (i.e., similar retrieval algorithm but trained with a database of SSM/I Tb and corresponding Ts*). The histograms (blue lines) are comparable to the AMSR-E inversions presented here, with RMSD ranging from 2.1 to 3.8 K. For these inversions, night-time and daytime denote the early morning and late afternoon overpasses of SSM/I. The differences between those surface-atmosphere conditions are smaller than for the AMSR-E overpasses, and the RMSD for night-time/daytime are closer than for AMSR-E. Overall, these figures suggest that inversions with comparable uncertainty are possible from the SSM/I/SSMIS and AMSR-E/AMSR2 sensors, which is a good outcome for a future product that combines estimates from all sensors.

Inversion With SSM/I Emissivity

A future joint SSM/I/SSMIS and AMSR-E/AMSR2 inversion is planned, and for those inversions, using a common emissivity climatology may help reduce differences in the retrieved LST related to differences in the estimated emissivities. Compared with AMSR-E, some of the SSM/I(SSMIS) channels are centered at slightly different frequencies, but the frequency dependence of the emissivity is rather limited and not likely to bring any significant differences in the monthly emissivity from the different sensors (Prigent et al., 2008). Most significant can be the differences caused by the coarser spatial resolution of SSM/I (AMSR-E roughly improving the SSM/I spatial resolution by a factor of 2), specially for regions with large surface heterogeneity.

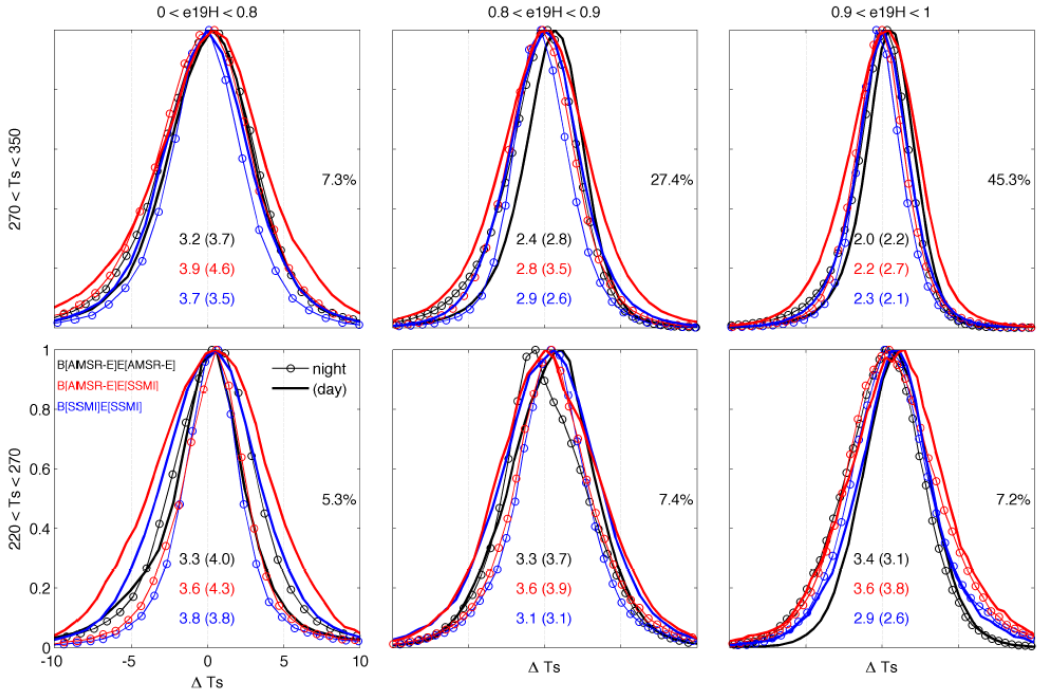

Figure 3.2.2 - Histograms of the difference between the retrieved LST from the neural network inversion and the original MW Ts* (ΔTs). The differences are plotted for two LST (Ts) ranges (top to bottom) and three 18.7 GHz horizontally polarized emissivity ranges (left to right). AMSR-E inversions using AMSR-E emissivities are plotted in black; AMSR-E inversions using SSM/I emissivities are plotted in red; SSM/I inversions using SSM/I emissivities are plotted in blue. Open circles represent the night-time overpass inversions, and solid lines represent the daytime. The numbers in the middle give the RMSD for each combination and overpass (daytime in brackets). The numbers on the right give the percentage of cases in the global training database for each emissivity and LST combination.

To test the impact of using SSM/I emissivities, inversions of AMSR-E Tb were conducted using the same methodology used previously but replacing the AMSR-E emissivities with the same SSM/I

climatological emissivity as in Prigent et al. (2016). Figure 3.2.2 (red lines) shows the same histograms as before, but this time for the AMSR-E (Tb) and SSM/I (emissivity) inversions. RMSDs are only slightly larger than for the all (Tb and emissivity) AMSR-E inversions, ranging from 2.2 to 4.6 K instead of 2.0 to 4.0 K, suggesting that using a common climatology for the SSM/I(SSMIS) and AMSR-E inversions could be considered.

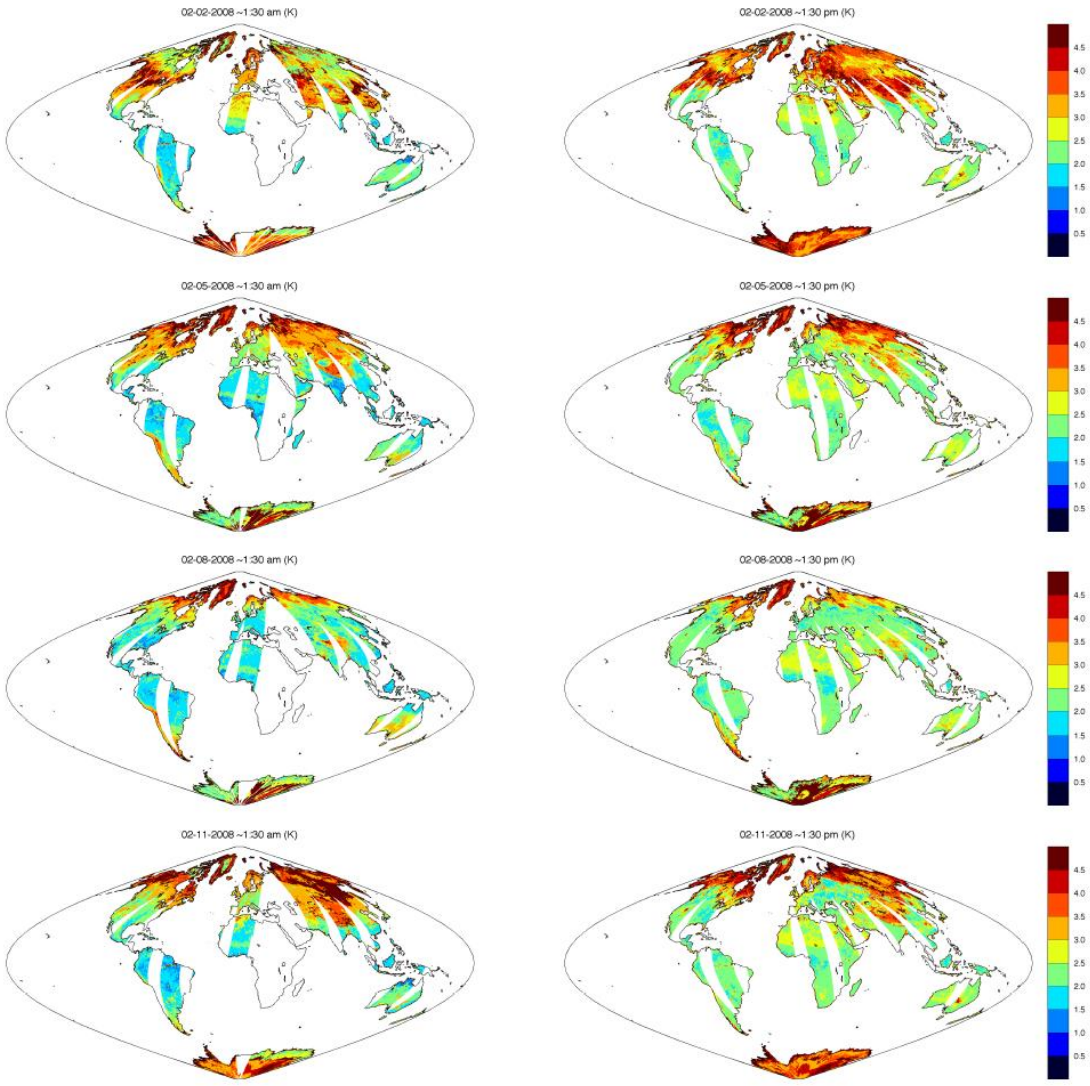

Figure 3.2.3 - As in Figure 3.2.1 but showing the retrieval error.

Differences With MODIS LST

A true LST to evaluate the retrieval uncertainty at the global scale of the AMSR-E inversions does not exist. But a comparison with another LST product could also be useful under the assumption that these new LST estimates are a reasonable representation of the unknown true LST. This is illustrated in Figure 3.2.4, where histograms of the difference between the original AMSR-E Ts* from the training database and collocated MODIS LST (black lines) are compared with histograms of the difference between the neural network retrieved LST and the MODIS LST (green lines). The RMSD are close for both differences (original AMSR-E retrieval and our neural network scheme), indicating that the new AMSR-E inversion methodology trained on the original AMSR-E inversions does not notably degrade the level of agreement with the IR LST estimates from MODIS. For ~75% of the global land surface, RMSD are below 3.9 K. A much more detailed comparison of the AMSR-E and MODIS LST is presented in section 3.3.

RETRIEVAL VARIABILITY

The retrieval variability defined as the standard deviation of the estimates at each pixel from the multineural network retrievals is displayed in Figure 3.2.5 for 4 days in 2008. For a large part of the globe the variability is below 1.5 K but can show larger values specially over some arid and snow-covered areas. For instance, in Northern Africa the locations with sand dunes are clearly associated with a larger variability, indicating the difficulties of the inversion in regions with large penetration depth and emission emanating from subsurface layers.

The retrieval variability increases for locations where we expect inversion difficulties. In most cases, they correspond to areas where the emissivity applied in the retrieval can be poorly representing the true conditions. This is the case for snow-covered areas and humid surfaces. For coastal regions the situation is similar, with very low emissivities if water is present in the swath position of the AMSR-E observation, which are not always properly captured by the closest emissivity estimate selected from the climatology. Convection activity in the overlying atmosphere can also result in difficult inversions. In this case, the problem is impact of the hydrometeors (rain and clouds) in the brightness temperatures of the different frequency channels, which is not quantified by the retrieval as the inversion assumes that most of the MW emission comes from the surface.

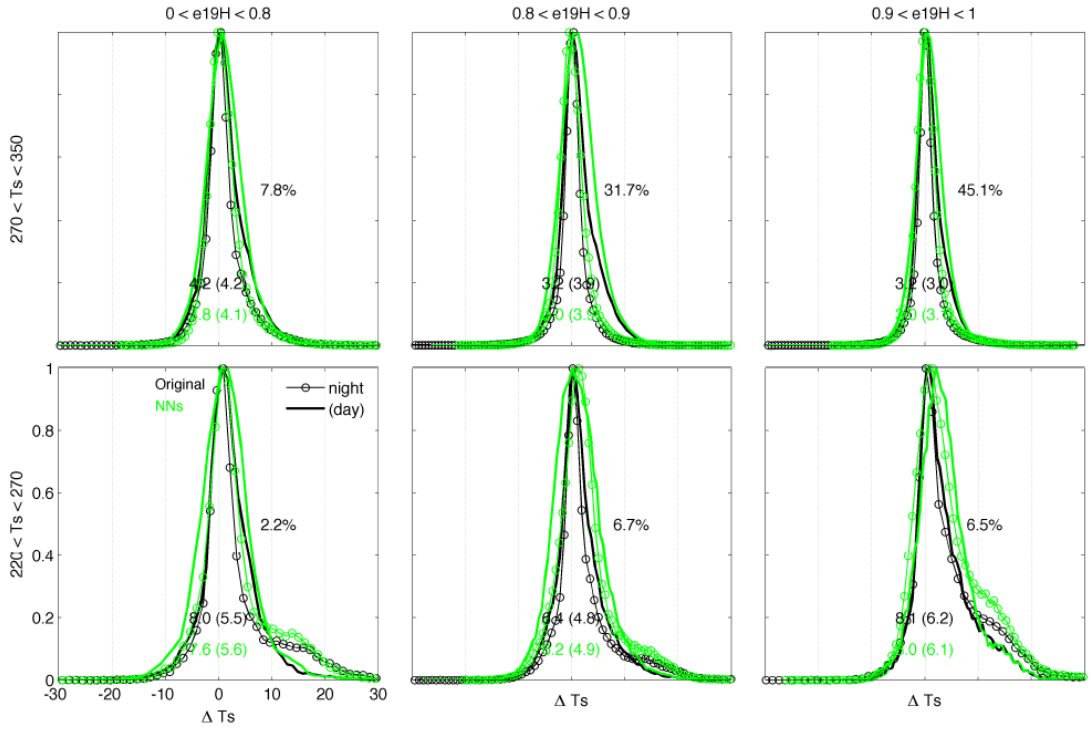

Figure 3.2.4 - Similar to Figure 3.2.2 but showing histograms of the difference between the MODIS LST and (1) the original MW Ts* (black lines) and (2) the LST from the neural network inversion (green lines).

To help identify these situations, a series of flags have been added to the retrieval product. The flags signal (a) snow-covered pixels, using the snow water equivalent (SWE) product from GlobSnow (Takala et al., 2011); (b) inundated pixels, using a monthly climatology from the Global Inundation Extension from Multi-Satellites (GIEMS) (Prigent et al., 2012); (c) coastal pixels; (d) pixels with large MW penetration depth, using a monthly climatology of radar backscattering from (Prigent et al., 2005); and (e) pixels with atmospheric convection activity, by looking at Tb depressions in the 89.0 GHz channels caused by ice clouds. Figure 3.2.6 (top) shows for 2 May 2008 the retrieval variability for the pixels flagged for different conditions (the median of the variability of all pixels for a given condition), and for the nonflagged pixels, together with the percentage of pixels for each condition. For the nonflagged pixels night-time and daytime variability are well below 1.0 K, while for the flagged pixels it is above 1.0 K, with the largest variability for the pixels with large penetration depth.

Figure 3.2.6 (bottom) also shows the retrieval uncertainty for different biome types (the median of the uncertainty of all pixels for a given biome, only including the nonflagged pixels). The uncertainty is around 2.0 K for all biomes apart from the tundra, where it reaches over 3.0 K. The tundra biome has a very small number of pixels (most of them were flagged as snow covered). Some of those pixels can still be snow contaminated (even if not detected by the snow product) or can correspond to very wet areas with abundance of water streams during the warm season, in both cases having the typical large uncertainty associated with cold and low emissivity conditions (see Figure 3.2.2). The smallest uncertainty corresponds to the forest and woodlands, with quite stable surface conditions and the emissivity climatology likely capturing the true emissivity and constraining well the inversion problem. It is worth noticing that the arid regions also have comparable uncertainty once pixels with possible MW penetration are removed. Still, some specific difficulties may be encountered for situations where changes in moisture and vegetation are not well captured by the monthly climatology.

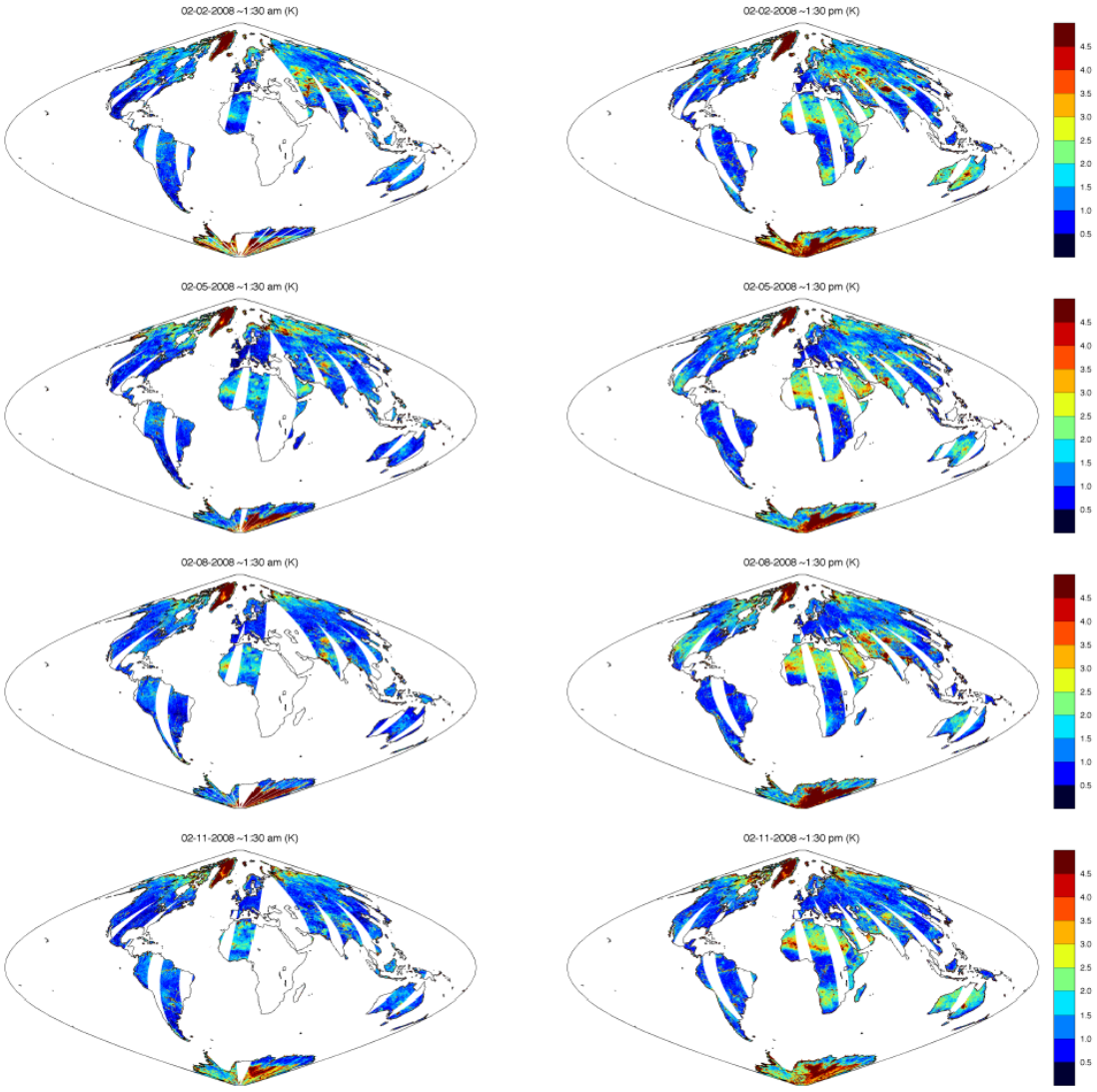

Figure 3.2.5 - As in Figure 3.2.1 but showing the retrieval variability.

Evaluation With *In situ* Measurements

An evaluation of the AMSR-E inversions at the 10 stations listed in Table 3.1.1 is presented here. For reference, a comparison with MODIS LST is also included. As main statistics, the bias (mean of the difference between the satellite and the *in situ* LST), the STD of the same difference, and the RMSD

are calculated for the AMSR-E and MODIS differences, for clear-sky (MODIS and AMSR-E) and cloudy-sky (AMSR-E), and for night-time/daytime separately.

Annual Evaluation

The statistics of the 2010 full year comparison are summarized in Figure 3.2.7, together with the number of matches for each situation (daytime/night-time, clear/cloudy-sky). At most stations night-time/daytime conditions are closely sampled in terms of number of cases; an exception is the arid DRA station, where the number of night-time cases is more than double the number of daytime cases due to the quality filtering of MODIS data at this specific location. Over these stations the number of cloudy-sky cases is in general much larger than the clear-sky cases; the only exception is the arid GBB station. The ratio of available AMSR-E matched MODIS LST estimates to AMSR-E LST estimates is ~0.3. This highlights the importance of having LST products that can provide estimates also for cloudy conditions.

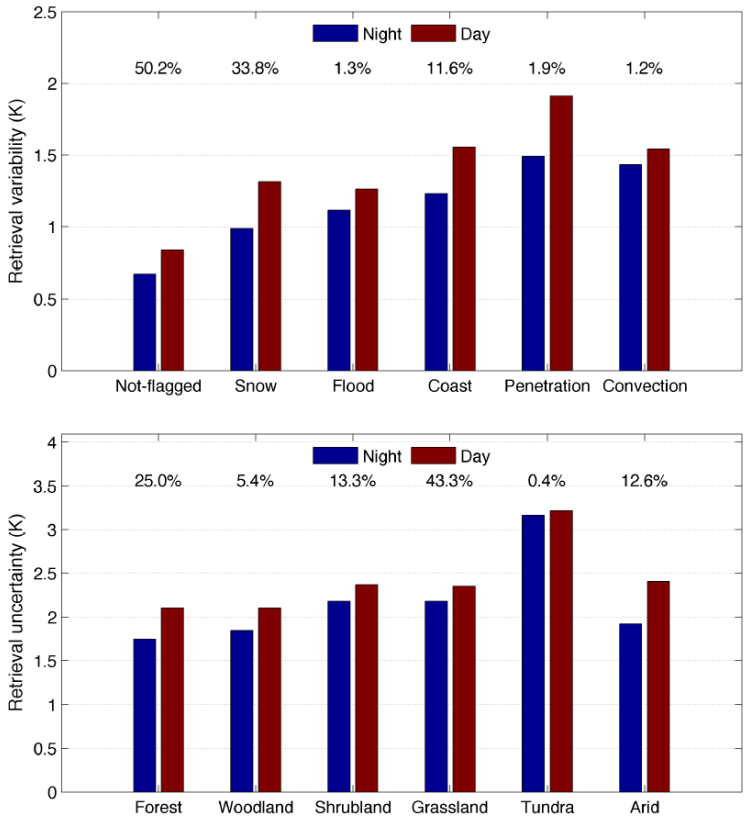

Figure 3.2.6 - Statistics of the AMSR-E inversion for 2 May 2008. (top) The retrieval variability for different conditions: pixels identified as being snow covered (snow), close to the coastal line (coast), with convection activity in the overlying atmosphere (convection), with the thermal radiation likely emanating from deep layers within the underlying soil (penetration), with a large possibility of being flooded (flood), and for the remaining pixels (not flagged). The bars display the median of the retrieval variability of the individual pixels for each surface condition (blue for night-time inversions, red for daytime inversions). The numbers above the bars indicate the percentage of pixels corresponding to a given surface condition. (bottom) Similar to the top panel but giving the retrieval error for the not-flagged pixels classified as a function of land cover.

The overall picture given by the annual biases does not show a clear direction (positive or negative) in terms of daytime/night-time, clear-/cloudy-sky, climate group, or sensor is not obvious. An exception is the DRA station, where both MODIS and AMSR-E have large negative biases for all situations. At many stations, the RMSD of the AMSR-E clear-sky and cloudy-sky are comparable, highlighting the ability of the MW inversions to provide LST estimates under most atmospheric conditions. The AMSR-E all-stations mean RMSD for clear-sky is 4.0 K, and only slightly larger for cloudy-sky at 4.3 K. Comparing the MODIS and AMSR-E STD for clear-sky conditions, for all stations the MODIS STD is

smaller than the AMSR-E STD. The same happens for the RMSD, with an all-stations mean RMSD of 2.4 K for MODIS, lower than the 4.0 K for AMSR-E.

Closer RMSD for MODIS and AMSR-E is observed for the temperate stations, compared with most of the boreal and subtropical stations. The MW emissivity is less seasonally varying than at other stations (e.g., EVO and GCM are less affected by snow episodes), and the presence of vegetation at these locations reduces the issues with MW penetration, likely resulting in less uncertain inversions. For the EVO station, AMSR-E and MODIS present a high positive bias for night-time clear-sky observations, in accordance with previous studies for MODIS and SEVIRI for the same location (Trigo et al., 2008a). There is also a degradation of MODIS night-time bias from 1.5 K at the original resolution to 2.0 K at the AMSR-E resolution, suggesting that the station representativeness degrades with distance to the station, particularly during the night. This night-time/daytime variation of the bias is also present at the GCM and BND station.

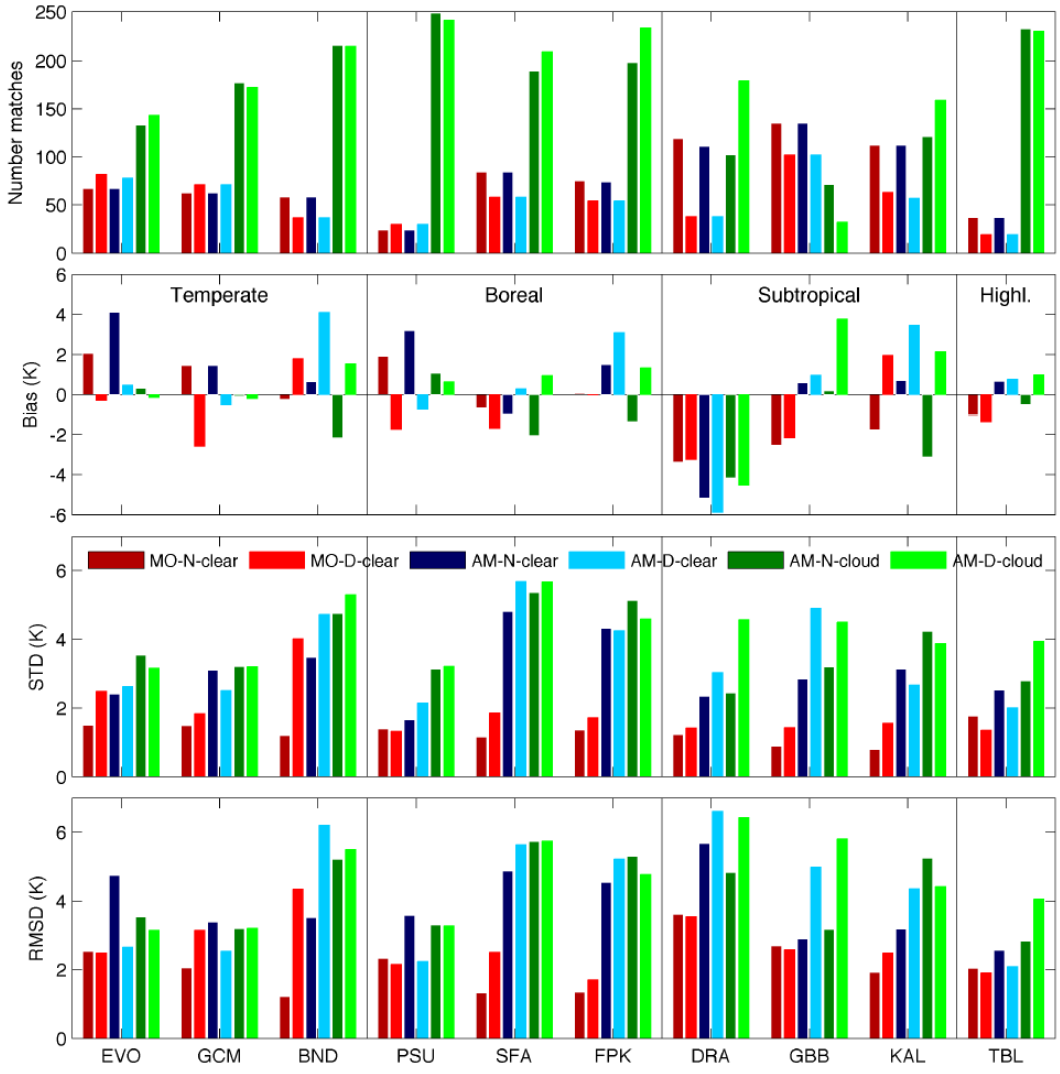

Figure 3.2.7 - Statistics of the 2010 comparison of MODIS and AMSR-E LST with *in situ* measurements at 10 stations. From top to bottom: (1) Number of matches between satellite and *in situ*; (2) bias, average of the difference between satellite and *in situ* LST; (3) STD, standard deviation of the difference; and (4) RMSD, root-mean-square of the difference. For each station there are six bars corresponding to clear-sky MODIS (MO, red) night-time (N, dark color) and daytime (D, light color), and AMSR-E (AM, blue and green) night-time/daytime and clear (blue)/cloudy (green) sky.

Compared with MODIS, AMSR-E presents a much larger RMSD at the boreal stations. The large differences are mainly associated with very low LST values when the surface is likely to be covered with ice or snow. If only *in situ* LST observations above 274 K are considered, the overall AMSR-E STD

of 3.1/5.6/4.6 K at PSU/SFA/FPK stations decreases to 2.7/3.9/3.8 K. At the PSU station, there is again a contrasting bias from daytime to night-time for the clear-sky comparisons, which is consistent between AMSR-E and MODIS. The PSU station is located in an agricultural area that is surrounded by forests; trees tend to have higher (lower) temperatures than the surface during night-time (daytime) resulting in higher (lower) remotely sensed LST values, in agreement with the positive (negative) bias observed. A change in the MODIS bias when using the closest 1 km pixel or the resampled MODIS LST also points to discrepancies in the point versus area-integrated LST (from−0.3 to 0.8 K). The SAF and FPK stations are located in more homogeneous cultivated areas but still subject to snow coverage in the winter period resulting in difficulties for the AMSR-E inversions.

The three subtropical stations discussed here are representative of arid conditions. For these stations, the larger AMSR-E RMSD compared with MODIS is related to these regions being prone to large MW penetration depth (i.e., the skin temperature at the station can be different from the subsurface-integrated MW temperature). The DRA station is located in an area of very irregular surface relief, and both MODIS and AMSR-E compare very poorly with the *in situ* measurements. MODIS bias presents a large degradation in the statistics from the original 1 km resolution to the AMSR-E resolution, especially for daytime, which supports the negative impact of a high surface heterogeneity on the LST comparison. For the GBB station, there is a high AMSR-E bias for daytime cloudy-sky. This station is located over rocky terrain but there are sand dunes at a distance of ~2.5 km from the station, which can be part of the AMSR-E pixel and negatively impact the comparison due to the expected MW emission from subsurface layers. At the KAL station, there is also a high contrast between daytime and night-time AMSR-E bias values, which is also occurring for MODIS. MODIS daytime bias values also present a degradation from 0.9 K at the 1 km resolution to 2.0 K at the AMSR-E resolution, which suggests again representativity issues between the *in situ* and satellite spatial scales.

The highland station TBL is located in a very heterogeneous region both in terms of orography (being close to a mountain range) and of vegetation cover. Nevertheless, at this station the agreement of MODIS and AMSR-E is relatively good compared with the other stations.

In summary, MODIS agrees better with the station measurements than AMSR-E. This can be expected due to the fact that both MODIS and the station instruments measure IR radiation, while AMSR-E operates in the MW; i.e., MODIS and the station measure a skin temperature, while AMSR-E observes a depth-integrated temperature, which can be different if there are subsurface thermal gradients at the depths where the MW observations are sensitive. The larger MW emissivity variability can also play a role given the satellite area-integrated to station point-observation disparity. The area surrounding the station is likely to be thermally more heterogeneous in the MW given the smaller dependence of the IR radiation on the emissivity and a generally more stable IR emissivity. Nevertheless, the differences in RMSD are significantly large at some stations, pointing also to difficulties in the AMSR-E inversions.

Seasonal Evaluation

Seasonal changes in the differences with the station were observed at the DRA, EVO, and GCM stations. Figure 3.2.8 illustrates this behavior for the two temperate stations by plotting the seasonal bias of MODIS (clear-sky) and AMSR-E (all weather). At the EVO station (Figure 3.2.8, top) there are night-time and daytime seasonal changes in the AMSR-E bias, although it is more pronounced for night-time. The bias is negative in winter (January-February-March), and positive in summer (July-August-September). MODIS also presents a negative daytime bias in winter and positive in summer (although very small for summer). In contrast, the night-time MODIS bias is positive for all seasons with close values. At the GCM station (Figure 3.2.8, bottom), at daytime MODIS and AMSR-E have a larger bias in summer compared with winter, although in this case the negative bias is in summer. The night-time seasonal changes are less pronounced for AMSR-E, while MODIS bias is always positive for night-time, similar to the EVO station. Figure 3.2.8 also illustrates again the much larger number of available AMSR-E LST estimates, compared with MODIS (a ratio of ~3 for the EVO and GCM stations for most seasons).

It is difficult to identify the causes of this seasonal behavior, but we could hypothesize that something changes with season in either the representativeness of the station, or the quality of the LST retrievals. Depending on land cover, the surroundings of the station might present some seasonal variability of surface conditions that is not represented at the station scale, resulting in seasonal discrepancies between the station and the satellite measurements. Regarding retrieval quality, snow conditions and occurrence and type of clouds are examples of seasonal changes that can have an impact for both MW and IR retrievals. Emissivity can also play a role: the MODIS retrieval uses a fixed emissivity, while the station LST is processed with a seasonally changing emissivity, which can also induce changes in the comparison; for AMSR-E, the representativeness of the emissivity climatology can change along the year, with some seasons more prone to have large deviations from the expected surface conditions.

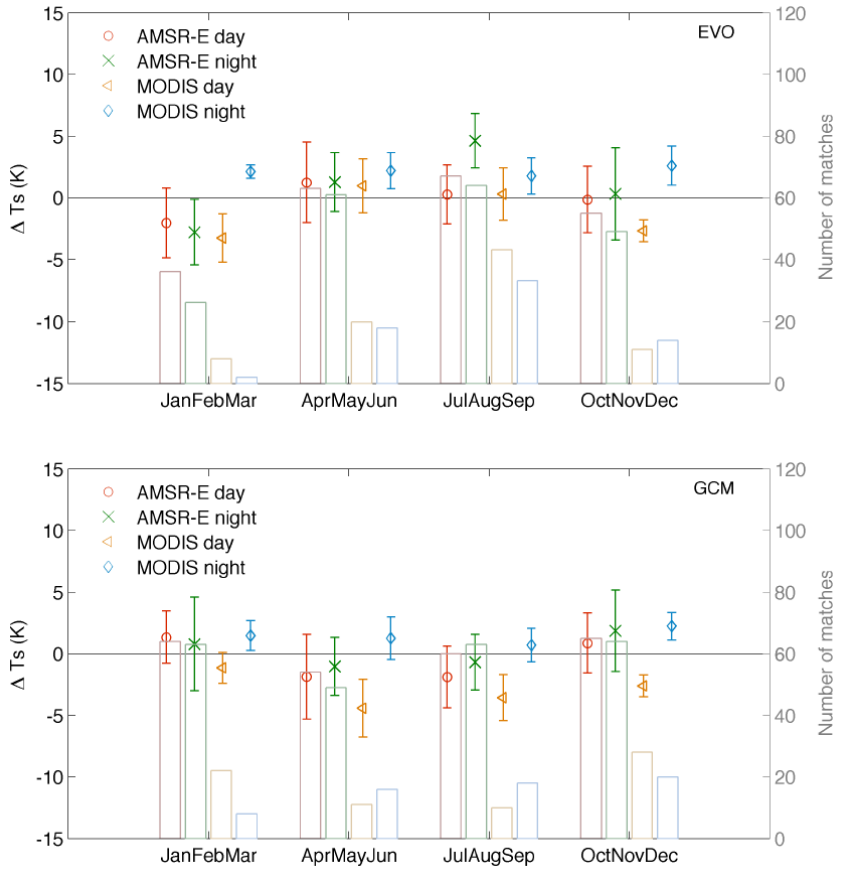

Figure 3.2.8 - Seasonal statistics of the MODIS and AMSR-E LST comparison with the *in situ* measurements at the (top) EVO and (bottom) GCM stations. The symbols (left y axis) give the satellite seasonal biases for night-time/daytime as indicated in the legend, with the length of the line centered at each bias value showing the seasonal standard deviation of the difference. The number of matches (right y axis) is indicated by bars.

Evaluation Artifacts

Broken clouds can have an impact on the comparison between satellite and ground LST estimates. This is illustrated in Figure 3.2.9, where time series of *in situ*, AMSR-E and MODIS LST at the PSU station are plotted. To help the figure readability, the time series is plotted from 29 June to 4 July, but similar behavior was observed at other occasions at this station. The first 3 days are cloudy at daytime and MODIS LST is not available. Scattered clouds are present and result in highly variable *in situ* LST values due to the transition between shaded and non-shaded surfaces. At the AMSR-E scale this effect is attenuated given the spatial integration over a much larger area. This *in situ* LST variability linked to scattered clouds will penalize the AMSR-E cloudy-sky comparisons for those stations and periods with frequent broken clouds.

Another source of instantaneous LST variability impacting the comparisons is the changing location of the AMSR-E observations. The closest pixel to the station changes position at each satellite overpass. If surface heterogeneity at the station surroundings is significant, this will result in variability in the averaged MODIS and AMSR-E LST that cannot be captured by the station measurements. Given the identified lack of surface homogeneity at the AMSR-E scale at most stations, it is very likely that this issue is contributing to the large STD observed at many stations. In principle, the impact of this will be larger for the AMSR-E observations. The largest dependence of MW LST in emissivity results in a larger LST variability among satellite footprints.

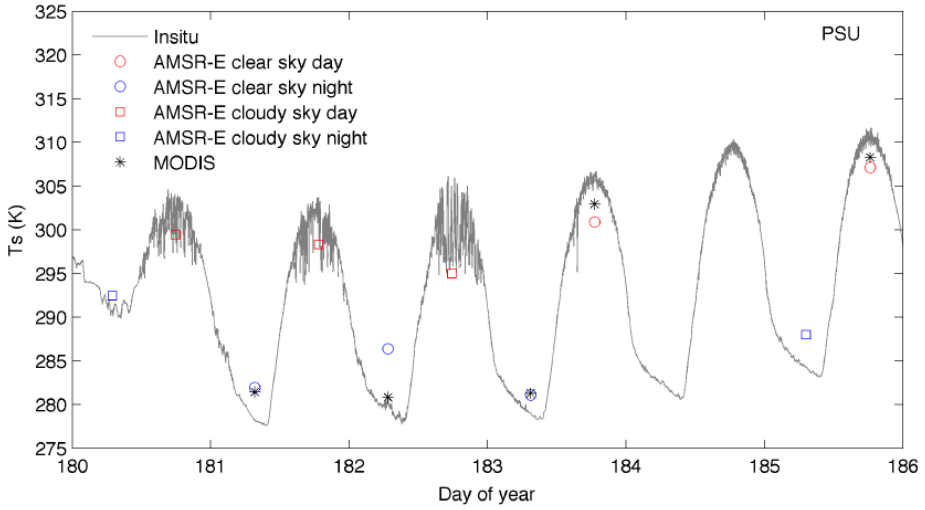

Figure 3.2.9 - Example of *in situ* LST (Ts) time series at the PSU station. Plotted the 1 min sampled *in situ* LST (solid line) from 29 June to 4 July 2010 and the available MODIS and AMSR-E estimates (symbols).

3.3 IR-MW LST comparison

Data Pre-processing

The time period under analysis corresponds to the first 6 days of each month from January to September 2011. Collocation of MODIS and each geostationary satellite (GEO) LST data sets was performed within the GlobTemperature project and was only available for the full year 2011. Unfortunately, due to malfunctioning of the AMSR-E sensor the respective data production ceased on 4 October 2011. Nevertheless, the chosen time period still encompasses different seasons and is representative of intra-annual variability. MODIS and AMSR-E sensors are on board the same satellite, and therefore, observation times are coincident. GEO data were matched to MODIS/AMSR-E observation time by using the closest observation, up to 7.5 min.

All data sets were reprojected onto an equal-area grid with a resolution of 0.125◦ × 0.125◦ at the equator and fixed latitude intervals. IR LST data sets were reprojected by plain averaging, while the MW LST and backscatter data were reprojected using the nearest neighbor. Statistics are only performed for grid cells where 100% of MODIS (or GEO) pixels have LST values with the best quality, in order to limit cloud contamination in the IR data. Snow cover data were reprojected to the comparison grid by counting the number of GMASI pixels within each grid cell where snow was identified; if at least one GMSASI pixel is identified as snow or ice, the grid cell is marked as being snow/ice covered. Land cover data were reprojected using the mode value.

Comparison Between MODIS and AMSR-E LST

Figure 3.3.1 shows maps of the overall bias (a, b) and STD (c, d) of the differences between AMSR-E and MODIS, for daytime (a, c) and night-time (b, d) separately. Overall, AMSR-E presents a root-mean-square difference relative to MODIS of 7.76/9.16 K, a bias of 2.64/4.64 K, and STD of 7.29/7.90 K

for daytime/night-time. There is a positive bias associated to desert areas, where penetration effects are more prone, especially for daytime observations. High latitudes are associated to a positive bias and high standard deviation that may be attributed to the presence of snow/ice cover. A high positive bias near the coast is also noticeable.

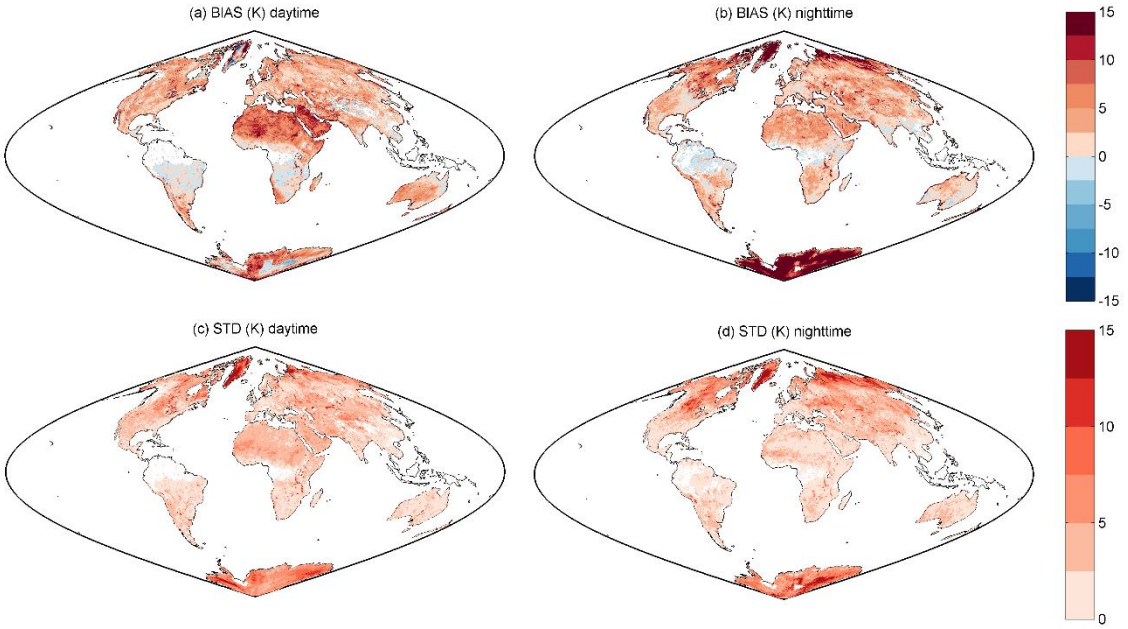

Figure 3.3.1 - Spatial distribution of (a, b) bias and (c, d) standard deviation of LST differences between AMSR-E and MODIS for daytime (a, c) and night-time (b, d) observations.

A great advantage of MW over IR observations is the ability to estimate LST in cloudy-sky conditions. Figure 3.3.2 shows the number of available observations for AMSR-E and MODIS as a function of latitude for the considered time period. It is evident that, even after masking problematic areas like sand deserts and snow-covered areas (as will be described), MW observations represent a significant increase of the sampling. Regions with high cloud coverage like equatorial areas present an increase of more than 250% in sampling size, and subtropical areas show an increase of more than 150%.

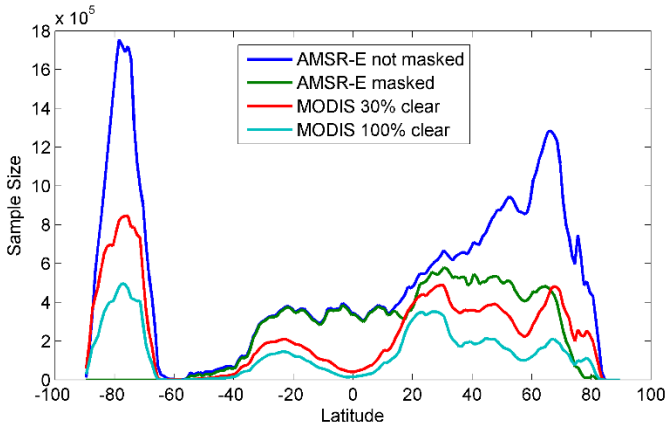

Figure 3.3.2 - Latitudinal distribution of the number of observations available in the considered time period for AMSR-E with (green) and without (blue) snow and desert masking and for MODIS (red/cian). For this specific figure, the criterion to have a valid MODIS observation has been relaxed (a MODIS observation is considered valid here if at least 30% of MODIS pixels within the grid cell are valid, while for the comparison 100% is required).

Arid and Semiarid Areas

As discussed in section 3.2, MW radiation penetration is one of the factors that can affect the LST differences between MODIS and AMSR-E, and may lead to significantly different LST values for AMSR-

E. This effect is especially relevant over bare ground and for the lower frequencies (Prigent et al., 1999). For this reason, arid and semiarid regions are here analyzed to assess the impact of such effects on the retrieved MW LST.

Regions where penetration is more likely to occur may be identified using the backscattering coefficient (σ_0) obtained from active MW observations (Prigent et al., 2005). Figure 3.3.3 (top) shows the global averaged σ_0. Vegetated areas like the equatorial forests present large σ_0 values due to the high volume scattering. Arid regions, on the other hand, are associated to low σ_0 values due to the combined effects of low surface roughness and wave penetration.

The bias between AMSR-E and MODIS LST is shown in Figure 3.3.3 (bottom), as a function of the backscattering coefficient. The biases between AMSR-E and MODIS LST show an increase as the backscattering coefficient decreases, but this effect cannot be directly attributed to penetration. As penetration increases (lower values of σ_0), the MW sensor measures radiation emitted from layers below the surface, usually resulting in lower (higher) temperature values during daytime (night-time) and therefore negative (positive) bias values (Prigent et al., 1999). For night-time, the temperature gradient below the surface is reduced compared to midday, penetration having an almost null impact. The histograms show a dependence of the night bias values with backscattering that is very close to the one observed for daytime, which suggests that penetration does not play a major role in the observed bias values.

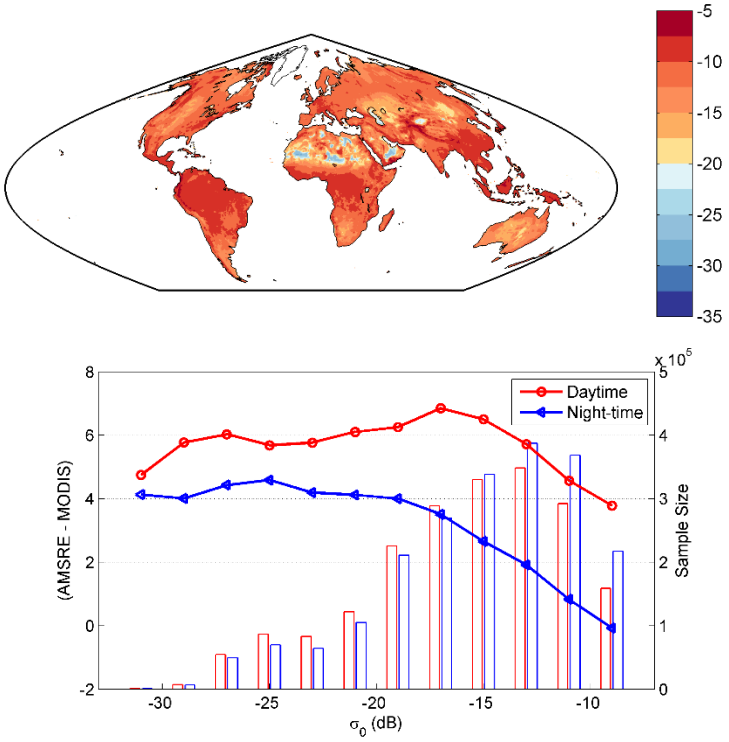

Figure 3.3.3 - (top) Global map of 8-year mean backscattering ERS coefficient σ_0 and (bottom) bias between AMSR-E and MODIS LST as a function of backscattering coefficient σ_0 (dB), for daytime (red) and night-time (blue), for the region encompassing the Sahara and Arabian Peninsula between the latitude circles of 0∘ and 40∘ and between longitude −20∘ and 70∘. Respective sample size of each backscattering coefficient bin is represented by the bars (right y axis).

Moreover, the visual comparison of the bias maps (Figure 3.3.1a) and the σ_0 map (Figure 3.3.3, top) suggests limited correspondence between high bias values and the backscattering. There is a conspicuous positive bias over the whole Sahara and Arabian Peninsula during daytime. However, it was expected that penetration effects would lead to negative bias values and the observed spatial patterns do not resemble those of the backscattering. This suggests that these high positive bias values could also be related to a LST underestimation by MODIS over arid regions. Several studies (e.g., Trigo et al., 2008a; Ermida et al., 2014) have reported an underestimation of LST by MODIS that

is likely related to an overestimation of IR land surface emissivity over those areas (Göttsche and Hulley, 2012). Desert areas tend to present higher uncertainties for IR LST retrievals, particularly for the products used in this comparison. The major drawback is the use of IR emissivity based on biome classification, which results in a single emissivity value for all desert areas, independent of the soil type (Göttsche and Hulley, 2012). As pointed by Jimenez et al. (2010) the IR emissivity may vary with soil type for desert areas. Recently, NASA's Land Processes Distributed Active Archive Center team reported that LST values over bare soil/sand sites were underestimated by more than 3 K, for both versions 4 and 5 of the product (Wan, 2014). This systematic underestimation may explain part of the bias observed between MODIS and AMSR-E over the deserts.

These results suggest that the neural network approach used to estimate MW LST is able to compensate some of the penetration effects described. Nevertheless, MW inversions in these locations have higher uncertainties, and the threshold of −20 dB in σ_0 is used to flag the dry sand regions that are likely affected by penetration in the AMSR-E product. In the global comparisons with MODIS discussed here, masking regions below this threshold change the overall bias, from 2.64/4.64 K to 2.48/3.75 K for daytime/night-time.

Snow-Covered Areas

The largest differences between AMSR-E and MODIS LST are observed over high latitudes, where the surface is covered by snow or ice. Figure 3.3.4 shows the biases between AMSR-E and MODIS as a function of the MODIS LST, separating snow-covered and snow-free areas. Snow pixels are associated to larger bias, as expected. There is still a small number of pixels with LST lower than 270 K that are not marked as snow but present large bias, indicating that they are probably covered by snow. The MW response over snow is highly variable in space and time. This response is related to the MW signature over snow that may vary between a blackbody behavior for wet snow to high reflectivities associated to strong volume scattering by a very inhomogeneous snowpack (Cordisco et al., 2006; Prigent et al., 2003b). Therefore, MW emissivities are particularly sensitive to snow water equivalent, grain size, and snow wetness, resulting in a large emissivity variability. As the retrieval uses a monthly mean emissivity value, large differences with the real emissivity are likely, which can translate into a large retrieval error. Therefore, it is still possible to estimate LST from MW observations but with higher uncertainties, especially for conditions of highly variable snow (e.g., melting and refreezing over a short time period). For regions with more stable snow properties and coverage, the uncertainties are expected to be much lower. For instance, the large oscillation in the daytime bias observed around 270 K in Figure 3.3.4 may reflect the higher uncertainty for highly variable snow, which is more prone to occur during the warmer seasons and close to 270 K.

Snow-covered surfaces may also present higher IR LST uncertainties. First, the cloud masking presents higher errors/uncertainties over these surfaces, especially at night-time when the visible channels cannot be used to derive the cloud mask (which corresponds to the winter time in the poles). Second, IR emissivity is also affected by snow coverage. Snow presents higher emissivity (above 0.99 at 10.8 μm) than vegetated soil (around 0.97 to 0.98 at 10.8 μm). This means that if a pixel is erroneously masked as snow (vegetation) by MODIS, LST will be estimated with an emissivity larger (lower) than the real surface emissivity leading to LST values that are lower (higher) than the real skin temperature and inducing a positive (negative) bias in the comparison with AMSR-E. This feature could partially explain the strong oscillation observed in the bias for LST values around 270 K (Figure 3.3.4).

At the global scale, masking of snow pixels leads to a change in bias from 2.64/4.64 K to 3.20/1.64 K for daytime/night-time and a significant decrease in STD from 7.29/7.90 K to 5.10/3.88 K. The increase in bias observed for daytime snow pixels seems to be associated to the daytime bias oscillation described above (Figure 3.3.4).

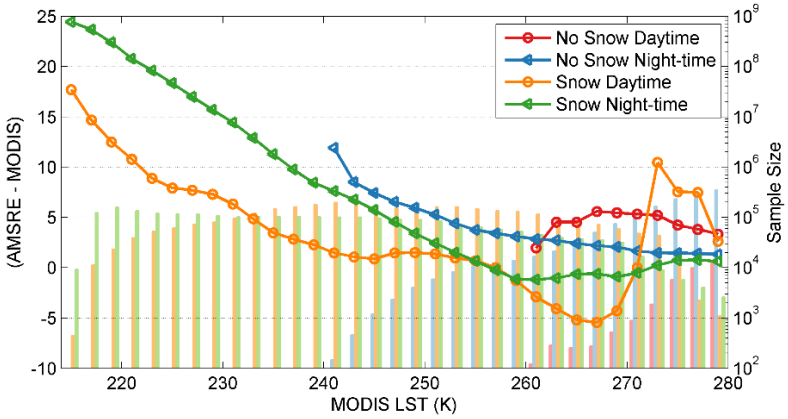

Figure 3.3.4 - Bias between AMSR-E and MODIS as function of MODIS LST, for pixels marked as snow (orange/green) and clear of snow (red/blue), for daytime (red/orange) and night-time (blue/green). Respective sample size of each MODIS LST bin is represented by the bars (right y axis in logarithmic scale).

Coastal Areas

Proximity to water bodies may have a strong impact on MW LST estimates because of the very low MW emissivity of water. For that reason, and considering the lower resolution of MW observations, AMSR-E LST presents larger differences from MODIS close to the coast. Figure 3.3.5 shows the bias and standard deviation of these LST differences as a function of the distance from the coast line. There is a maximum of the bias around 20 km for both daytime and night-time, and the STD presents a slow decrease with distance up to approximately 30 km. These are reasonable values considering that the spatial resolution of AMSR-E is ~21 km at the lower frequencies (18.7 GHz and 23.8 GHz) and ~12 km at the higher frequencies (36.5 GHz and 89.0 GHz). These resolutions correspond to the 3 dB FOV of the antenna, but energy measured by the antenna sidelobes can also be affected by ocean emission, contaminating the measured radiances. Water contamination of the FOV is particularly relevant in the case of the emissivity estimation since water presents values much lower than land (~0.4 over water compared to ~0.9 over land). For this reason, climatological emissivity values attributed to coastal pixels are generally lower than inland pixels. In the case of the Tb, however, this effect is not systematic as the fraction of sensed water surface depends on the swath position. The observed positive biases indicate that for many swath positions close to the coast the climatological values underestimate the real emissivity, resulting in an overestimation of the LST.

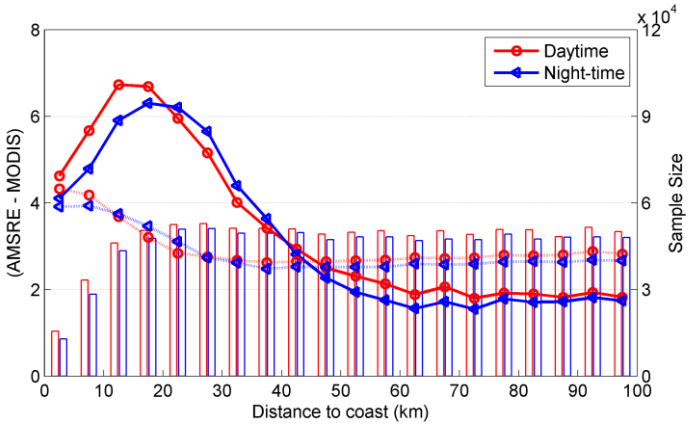

Figure 3.3.5 - Bias (solid line) and standard deviation (dashed line) of the LST differences between AMSR-E and MODIS as function of the distance to the coast up to 100 km, for daytime (red) and night-time (blue). Respective sample size of each LST difference bin is represented by the bars (the right y axis).

VEGETATION COVER

LST differences between AMSR-E and MODIS are further evaluated here as a function of land cover. Figure 3.3.6 (top) shows the spatial distribution of the aggregated seven main classes. Figure 3.3.6 (bottom) presents the distribution of the bias of LST differences between AMSR-E and MODIS for the regrouped land cover classes. Note that the distributions were calculated from snow-masked LST.

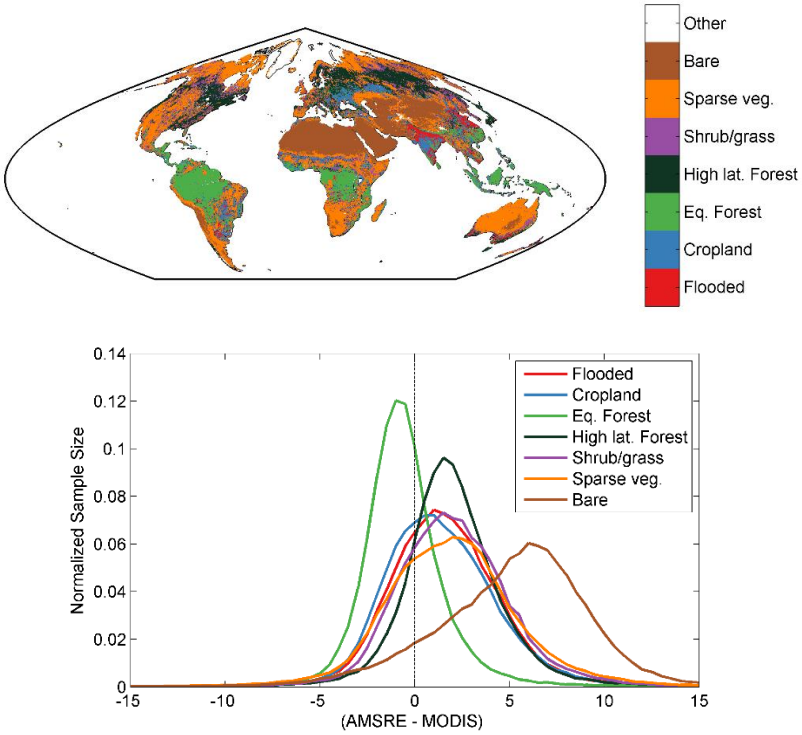

Figure 3.3.6 - (top) Classes of land cover as defined by ESA Globcover and (bottom) distribution of the bias between AMSR-E and MODIS for classes of vegetation cover. Sample size is normalized by the total number of observations in each class.

Most classes present similar distributions centered at approximately 2 K. Vegetation classes associated to dense forest show contrasting behaviors between equatorial forests (light green line) and high-latitude forests (dark green line), the former presenting a negative bias. This could be attributed to the different seasonal behaviors of the two types of forests. Equatorial forests present a fairly constant coverage throughout the year, and for that reason, emissivity values are closer to the climatological emissivity resulting in lower biases. High-latitude forests, in contrast, may present a significant foliage reduction during winter and may even be covered by snow. Desert areas present a larger positive bias, as it was discussed previously.

COMPARISON BETWEEN LST FROM GEOSTATIONARY SATELLITES, MODIS, AND AMSR-E

ASMR-E and MODIS differences were extensively analyzed given the common platform and near to perfect time agreement. Here we compare both MODIS and AMSR-E with the other IR sensors to place the AMSR-E-MODIS biases in perspective. The biases between the GEOs and AMSR-E and between the GEOs and MODIS are presented in Figure 3.3.8, for daytime and night-time. A summary of the LST comparisons is given in Table 3.3.1 by presenting the bias and standard deviation of the differences between each GEO and AMSR-E, between each GEO and MODIS, and between AMSR-E and MODIS over the GEO area.

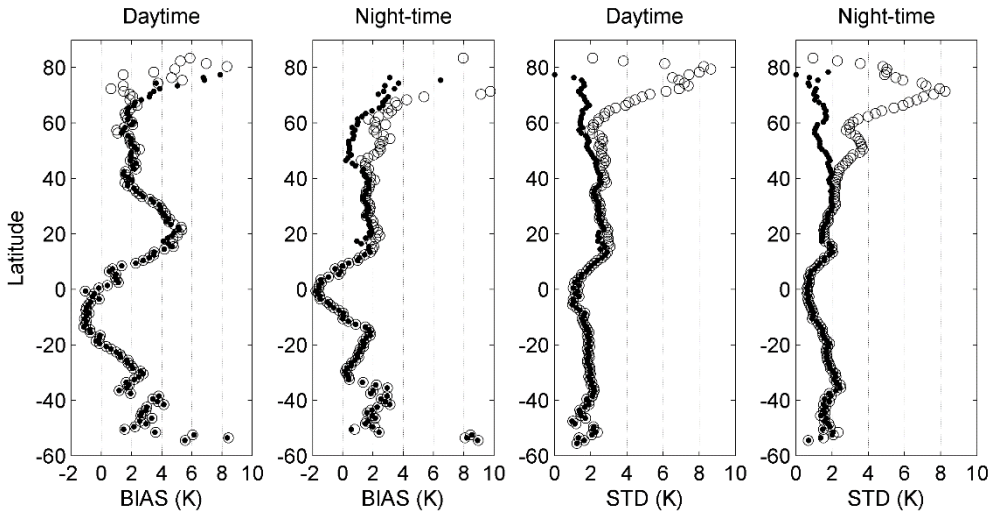

Figure 3.3.7 - Bias and standard deviation (STD) of the LST differences between AMSR-E and MODIS for 1∘ latitude bands before (open circles) and after (filled circles) removing snow and desert areas.

GEO-MODIS COMPARISON

Discrepancies between IR LST products are generally attributed to differences (1) in the top-of-atmosphere measurements (sensor calibration, spatial resolutions, and spectral channels), (2) in the algorithm and auxiliary data used for atmospheric and surface emissivity correction, (3) in cloud mask, and (4) in angular anisotropy (Barroso et al., 2005; Ermida et al., 2014; Pinheiro et al., 2006; Rasmussen et al., 2010; Trigo et al., 2008a).

MODIS presents overall lower LST values than the GEOs (Table 3.3.1). Bias values tend to be positive over most of the GEO scan area but negative close to the scan edge (Figure 3.3.8). At the edge of the geostationary disk, high view angles favor the observation of shadows and vegetation objects by the sensor resulting in lower LST retrievals. This is particularly noticeable in heterogeneous surfaces during daytime (Ermida et al., 2014; Guillevic et al., 2013; Pinheiro et al., 2006; Rasmussen et al., 2010). Emissivity anisotropy may also impact the LST retrieval. Studies indicate that IR emissivity decreases with view angle for bare ground, but this dependence is negligible for heterogeneous surfaces (Labed and Stoll, 1991; Ren et al., 2011; Sobrino and Cuenca, 1999). At the scale of the satellite FOV, however, it is likely that emissivity increases with view angle for sparsely vegetated surfaces, as the fraction of vegetation objects seen by the satellite increases.

Table 3.3.1 - Bias and standard deviation (in parenthesis) of the difference between AMSR-E and each geostationary sensor (GEO), between AMSR-E and MODIS (limited to the GEO area) and between each GEO and MODIS, for daytime (upper row) and night-time (lower row), and with and without deserts and snow masking.

	SEVIRI				GOES				MTSAT			
	Not masked		Masked		Not masked		Masked		Not masked		Masked	
AMSRE-GEO	2.29	(5.51)	2.15	(5.50)	0.63	(5.25)	0.45	(5.96)	2.41	(4.85)	2.51	(4.55)
	1.66	(4.34)	1.46	(4.30)	1.70	(4.71)	1.38	(3.88)	1.87	(5.56)	0.26	(4.06)
AMSRE-MODIS	3.66	(5.13)	3.45	(5.13)	1.22	(4.47)	1.05	(4.04)	1.54	(4.46)	1.47	(4.00)
	1.91	(4.18)	1.67	(4.12)	1.74	(4.77)	1.40	(3.90)	2.40	(5.46)	0.85	(3.79)
GEO-MODIS	1.37	(3.03)	1.31	(3.03)	0.59	(2.71)	0.60	(2.72)	-0.87	(3.20)	-1.03	(3.03)
	0.25	(1.90)	0.21	(1.86)	0.04	(1.73)	0.01	(1.67)	0.52	(2.08)	0.59	(1.91)

Overall, SEVIRI presents the highest discrepancies when compared to MODIS (Table 3.3.1 and Figure 3.3.8), despite having the closest algorithm and spectral channels (Freitas et al., 2013). SEVIRI LST is warmer than MODIS LST for most of the scan disk, which may be attributed to the contrasting emissivity values used in each retrieval (Ermida et al., 2014; Qian et al., 2013). As already mentioned,

at the scan edge SEVIRI LST values tend to be cooler due to the angular effects. GOES shows a similar behavior (Figure 3.3.8) but presenting overall lower bias values (Table 3.3.1). GOES LST is retrieved using emissivity values estimated from the same library as for SEVIRI but using different methods. Emissivity is estimated as a weighted average of vegetation and bare ground in both cases, but for SEVIRI daily values of fraction of vegetation cover are used as weight, while for GOES (and MTSAT) a static land cover classification is used instead (Freitas et al., 2013). MODIS has a similar LST algorithm to SEVIRI, but the emissivity is estimated with a methodology similar to GOES and MTSAT, which might contribute to the lower differences between GOES/MTSAT and MODIS LST (Wan and Dozier, 1996). MTSAT presents contrasting bias values, characterized by a negative overall bias during the day and a positive one at night (Table 3.3.1 and Figure 3.3.8): this is likely related to the predominance of high view angles for MTSAT. Over Australia, biases are much lower. That supports the fact that the high negative bias observed over Asia is likely related to angular effects as seen in the other sensors.

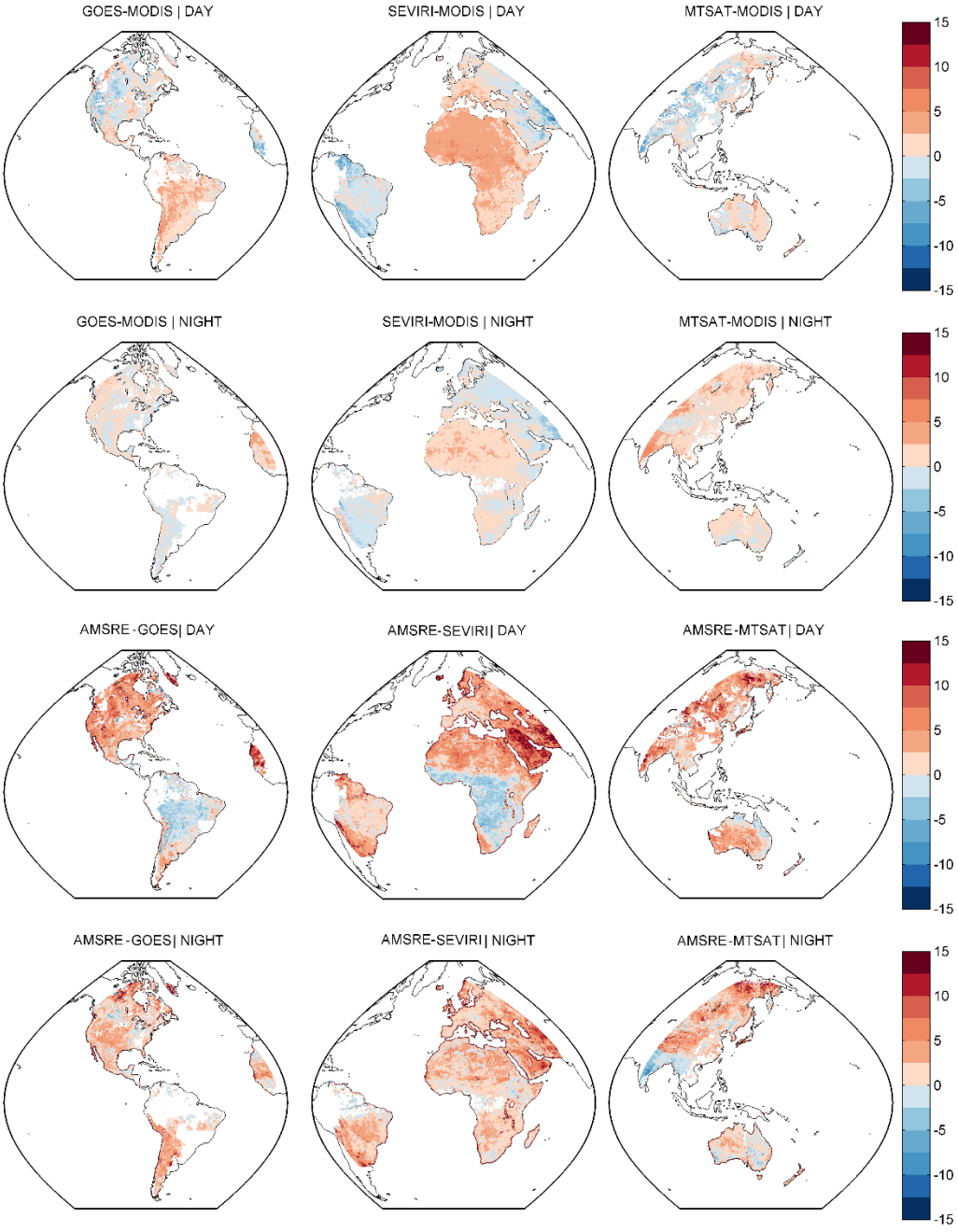

Figure 3.3.8 - Spatial distribution of the bias (K) of LST differences between the GEOs and MODIS and between the GEOs and AMSR-E for daytime and night-time observations.

GEO-AMSR-E COMPARISON

AMSR-E shows better agreement with SEVIRI LST than with MODIS LST, especially during daytime (Table 3.3.1). AMSR-E also agrees better with GOES than with MODIS. Regarding MTSAT, AMSR-E is in closer agreement with MTSAT during night-time, with lower bias than with MODIS, but for daytime the bias with respect to MTSAT is much larger than with MODIS. Overall, the agreement between the different sensors improves when problematic areas such as snow and sandy deserts are masked. Arid, semiarid areas, and high latitudes are characterized by positive bias, while tropical forests are associated to negative biases (Figure 3.3.8). This is consistent with the result obtained when comparing AMSR-E and MODIS (Figure 3.3.1 and Figure 3.3.6). Values of the bias between the GEOs and AMSR-E tend to increase toward the GEO scan edge, as a result of the angular effects on the GEO LST.

Table 3.3.1 shows that, in some cases, the biases between AMSR-E and the GEOs are of the same order as the ones observed between MODIS and the GEOs. For instance, GOES presents a daytime bias with respect to AMSR-E of 0.45 K, whereas the bias with respect to MODIS is 0.60 K. MTSAT also presents a night-time bias with respect to AMSR-E of 0.26 K, while MODIS bias is 0.59 K. However, the standard deviation of the differences between AMSR-E and the GEOs or MODIS is generally higher when compared to the ones observed between MODIS and each GEO. This can be partially related to the differences between measuring a skin temperature (MODIS and GEOs) and measuring a depth-integrated temperature (AMSR-E), i.e., that MODIS and the GEOs observe a more similar physical temperature by using similar wavelengths and also to more uncertain MW retrievals associated to a relatively large dependence of the MW radiation processes on the emissivity (emission in the IR regime is less dependent on the emissivity) and how this is captured in the retrieval. To reduce the dependence on ancillary data, the AMSR-E inversion approach uses a climatological monthly emissivity, instead of the actual emissivity estimates corresponding to the specific date of the inversion (see section 3.2). At location and times where the emissivity is highly variable, the climatological emissivity may poorly represent the real emissivity, resulting in larger retrieval errors. A similar result was found in section 3.2 when AMSR-E and MODIS were compared with ground IR LST from a selection of stations, with overall larger standard deviations in the differences between the AMSR-E and the *in situ* LST compared with MODIS.

3.4 Quantifying the clear-sky bias of satellite LST using MW-based estimates

The MW LST dataset described in the previous sections was then used to estimate the impact of the clear-sky bias at multiple spatial and temporal scales.

DATA PRE-PROCESSING

The MW LST dataset used here covers the 3-year period from 2008 to 2010 that is available through the GlobTemperature portal. LST data are then projected onto a 1^{o}x1^{o} grid by simply averaging all retrievals falling into each grid-box, creating daily daytime and night-time composites, respectively.

In the results presented below, “clear-sky bias” refers to the difference between clear-sky and all-sky AMSR-E LST retrievals, averaged over the same period. The analysis is performed at seasonal scale (averaging all-sky/clear-sky per 3-month periods) and for daytime and night-time, respectively. A given pixel is considered clear (cloudy) if the cloud fraction is below 30% (above 70%). The choice of thresholds represents a compromise between an “accurate” definition of clear/cloudy conditions and the number of cases for analysis, so that a sufficiently dense spatial coverage remains available, especially over regions with high cloud coverage (e.g. tropical and mountainous regions). A sensitivity analysis performed on the thresholds to classify pixels as clear shows that when applying thresholds of 30% over the results obtained using thresholds of 1%, there is an absolute change in the bias of less than 0.5K for the majority of the pixels (85%), but of the number of pixels that are flagged because

of reduced number of available clear-sky observations (dotted pixels of Figure 3.4.2 and Figure 3.4.3) is reduced by more than half when using the 30% threshold.

CHARACTERIZING THE CLEAR-SKY BIAS

Latitudinal profiles of the clear-sky bias and the percentage of clear-sky days averaged over the whole 3-year period are presented in Figure 3.4.1. The daytime clear-sky bias takes positive values over most of the globe, i.e. the increased input of solar radiation under clear-sky conditions leads to higher LST values. The bias is negative only over regions with very low LST values, which are likely covered with snow. In this case, the high albedo of the snow may lead to a significant reduction of the absorbed short-wave solar radiation under clear-skies, and at the same time, the downwelling longwave radiation emitted by clouds contributes to the warming of the surface.

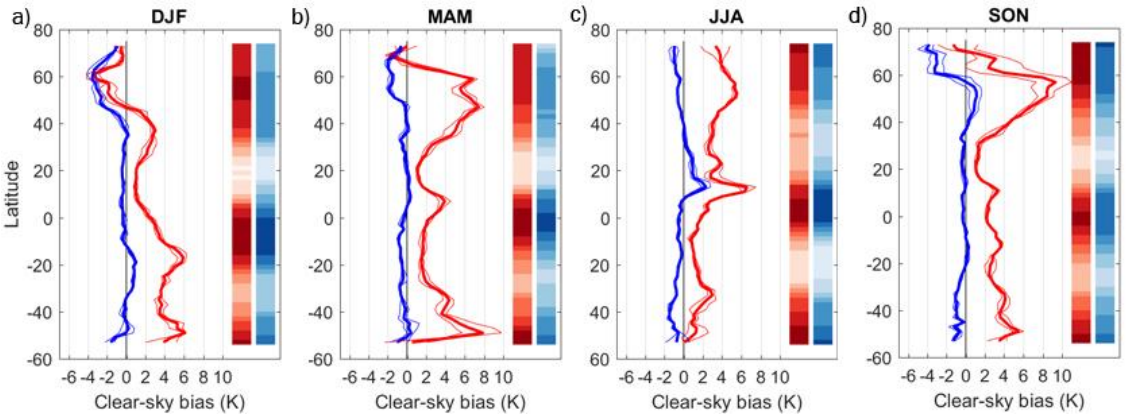

Figure 3.4.1 - Latitudinal profiles of the clear-sky bias for a) December-January-February (DJF), b) March-April-May (MAM), c) June-July-August (JJA), d) September-October-November (SON), for daytime (red) and night-time (blue). The thick line is the average value for the 3-year-period and the thin lines represent minimum and maximum values of the yearly-averages. The color shades in the two vertical bars represent the latitudinal distribution of the percentage of clear-sky days for daytime (red shades) and night-time (blue shades), with light colors indicating high percentages (clear-sky) and darker colors indicating low percentages (cloudy-sky).

Cloud coverage has high an impact on absolute values of the clear-sky bias, since ultimately all-sky LST is dictated by the balance between cloudy and clear-sky LST at any given point. The seasonal displacement of the Intertropical Convergence Zone (ITCZ) may be identified by larger values of bias (around 20ºS in DJF and around 15ºN in JJA). The near-null biases associated to a very high frequency of clear-sky over the deserts are also conspicuous. The highest biases occur during the intermediate seasons over mid-latitudes, when weather conditions are more variable. Since we are considering land surface temperature only, it is not surprising that northern hemisphere profiles present larger seasonal variability, as will be further detailed below.

For night-time, the values of clear-sky bias are much lower and generally negative (Figure 3.4.1). During night-time, clear-sky conditions generally lead to a stronger cooling of the surface since the cloud coverage leads to a decrease in the outgoing long-wave radiation.

Global maps of seasonal all-sky LST, averaged over the whole 3-year period, are shown in Figure 3.4.2Figure 3.4.3 (a, b, g, h), for day and night-time, respectively. The corresponding maps of clear-sky bias (i.e., clear-sky minus all-sky averaged LST) are also presented (Figure 3.4.2Figure 3.4.3c, d, i, j), as well as the percentage of clear-sky days (Figure 3.4.2Figure 3.4.3e, f, k, l). These were accordingly generated for December-January-February (DJF; Figure 3.4.2a-f), March-April-May (MAM; Figure 3.4.3a-f), June-July-August (JJA; Figure 3.4.2g-l) and September-October-November (SON; Figure 3.4.3g-l).

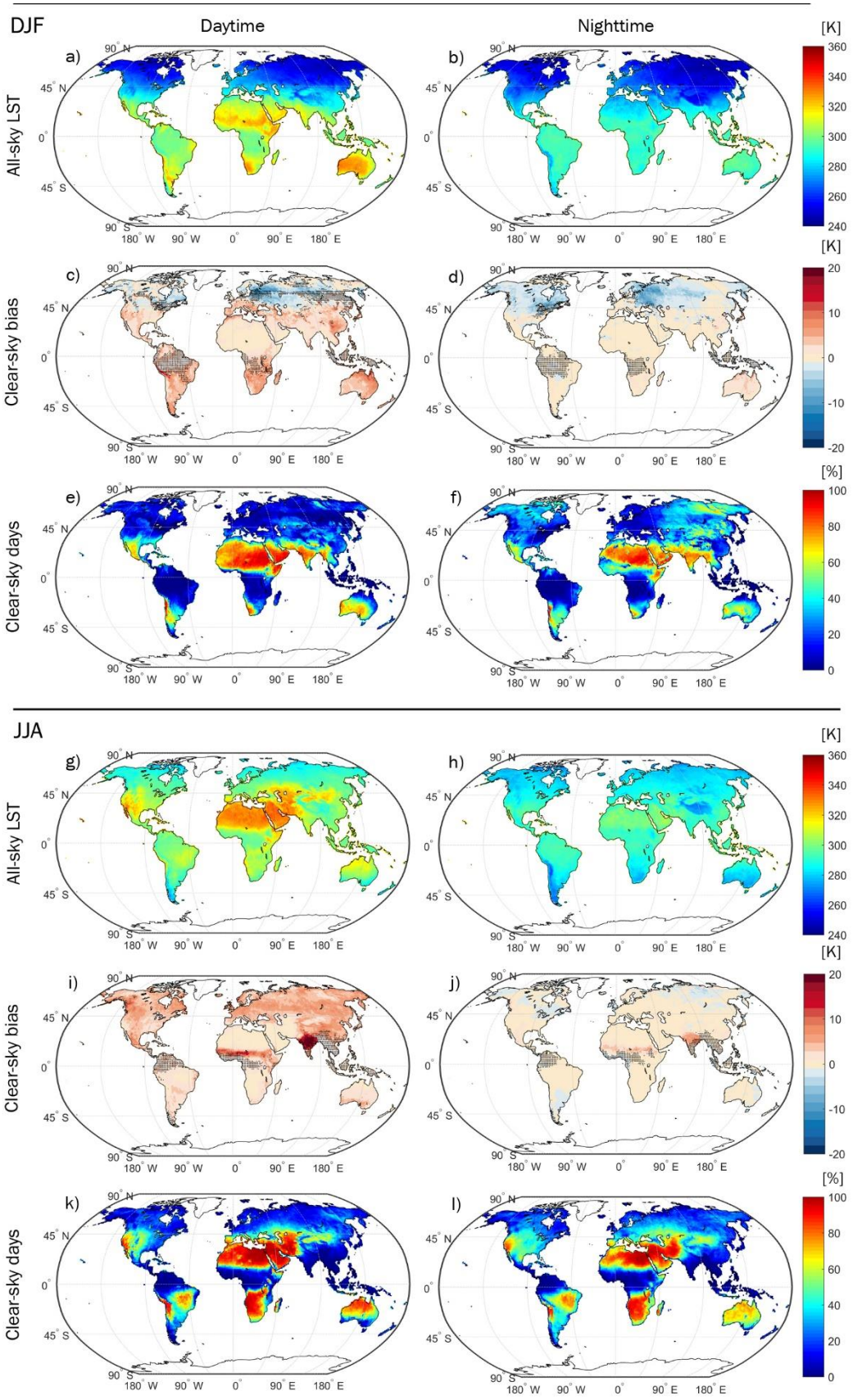

Figure 3.4.2 - Spatial distribution of 3-year average all-sky LST (K; a, b, g, h), clear-sky bias (K; c, d, i, j) and percentage of clear-sky days (e, f, k, l), for DJF (a-f) and for JJA (g-l), for daytime (left panels) and night-time (right panels). Dotted pixels in the clear-sky bias maps (c, d, l, j) indicate that less than 50 days of data are available for that pixel.

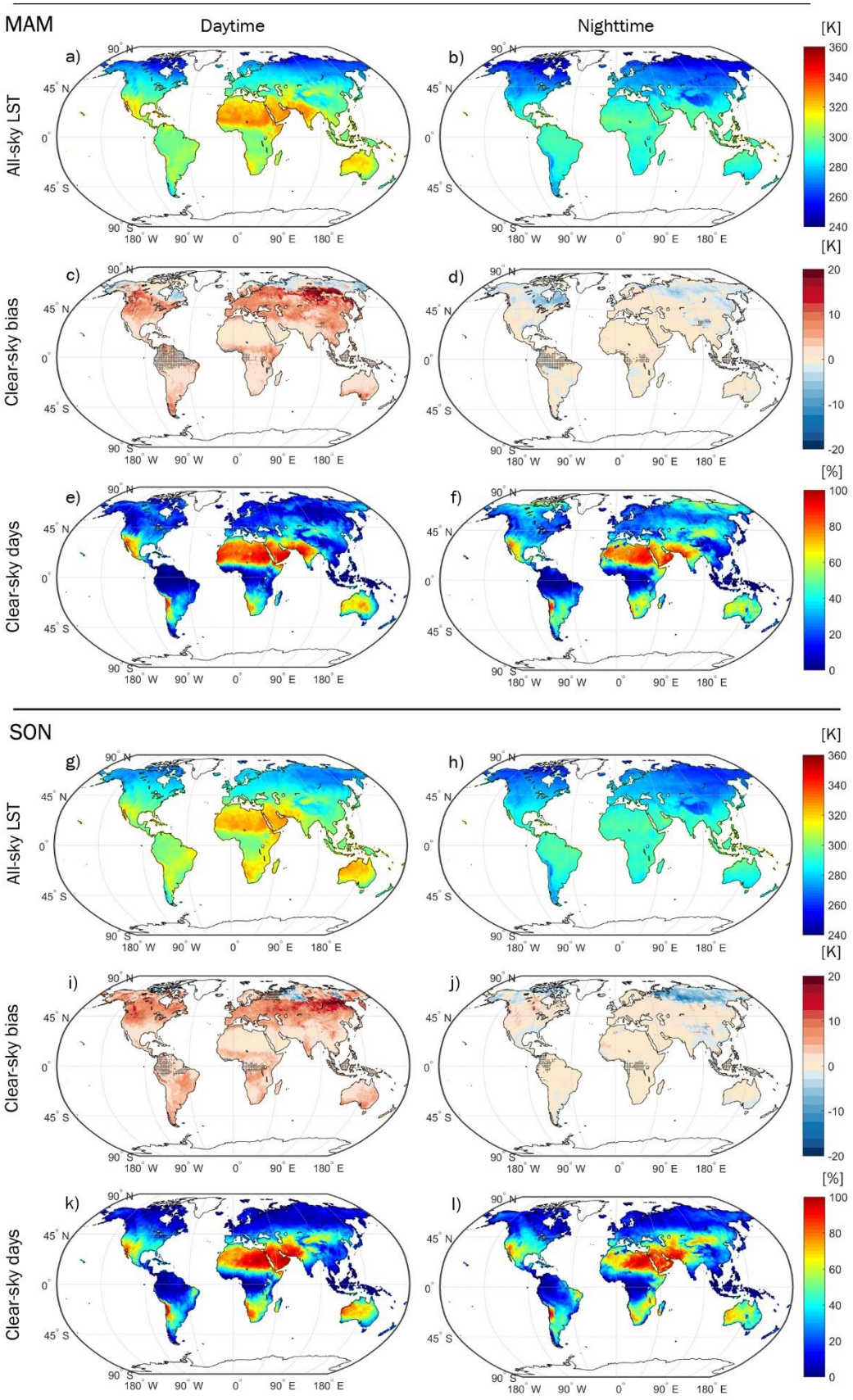

Figure 3.4.3 - As in Figure 3.4.2 but respecting to the 3-year average for MAM (a-f) and for SON (g-l).

The spatial maps of clear-sky biases in LST reveal a large variability both in space and time, which follows to some extent the patterns seen in the frequency of clear-sky events. This sustains the strong links between clear-sky bias and local radiation budget at the surface, or with the lack of cloudy events. Thus, the spatial distribution of clear-sky bias confirms the tendency for warmer daytime LSTs under clear-sky conditions (Figure 3.4.2Figure 3.4.3c,i), with negligible clear-all sky differences in areas where the cloud frequency is very low (Figure 3.4.2Figure 3.4.3d,j), such as over all major deserts. However, this pattern is reversed over Eurasia in winter (Figure 3.4.2c), where negative LST clear-sky biases are present for both daytime and night-time. In those cases, the incoming solar radiation at rather low sun angles does not compensate for the higher radiative cooling associated with the dry atmospheres, which are frequent over those regions. As referred above, this is further enhanced by large albedos, as part of those areas will be snow-covered during winter. The most pronounced night-time cold biases are, therefore, also observed over regions where the atmospheric moisture content is low, favoring night-time radiative cooling under clear skies (see northern continents in DJF and SON).

Nevertheless, surface temperature is not uniquely determined by local radiation budget, but instead it is the result of the overall energy budget at the surface. As such, local weather conditions, and particularly the advection of warm/cold air, can also play a significant role in determining the clear-sky biases shown in Figure 3.4.2 and Figure 3.4.3. In South-western Europe, as an example, the higher availability of solar radiation at the surface in clear-sky conditions in DJF is partly compensated by the advection of warmer air (and moist) from the Atlantic, which leads to rather low clear-sky LST bias in DJF.

Figure 3.4.4 presents the clear-sky bias averaged over defined areas of interest (Figure 3.4.5), together with the respective spatial STD. The mid-latitudes (South Europe, South of North America, South of South America, China) are representative of the common clear-sky situation where the increased input of solar radiation leads to higher daytime LSTs. The biases are higher during the intermediate seasons (MAM and SON), when the frequencies of clear and cloudy-sky conditions are closer, having about the same weight on the all-weather LST (Figure 3.4.6). In mid-latitude regions, the contrast between cloudy and clear-sky LST is largest in the summer season and lowest in the winter season (Figure 3.4.6c,d,e,h). However, in the latter period, it is worth noting that the weight of cloudy conditions on all-weather LST is relatively low.

As mentioned before, advection of oceanic air may also contribute to compensate for the lower incoming solar radiation under cloudy conditions, and therefore to reduce the clear-sky biases during the winter season in areas such as South Europe (DJF) and South of South America (JJA) (Figure 3.4.4).

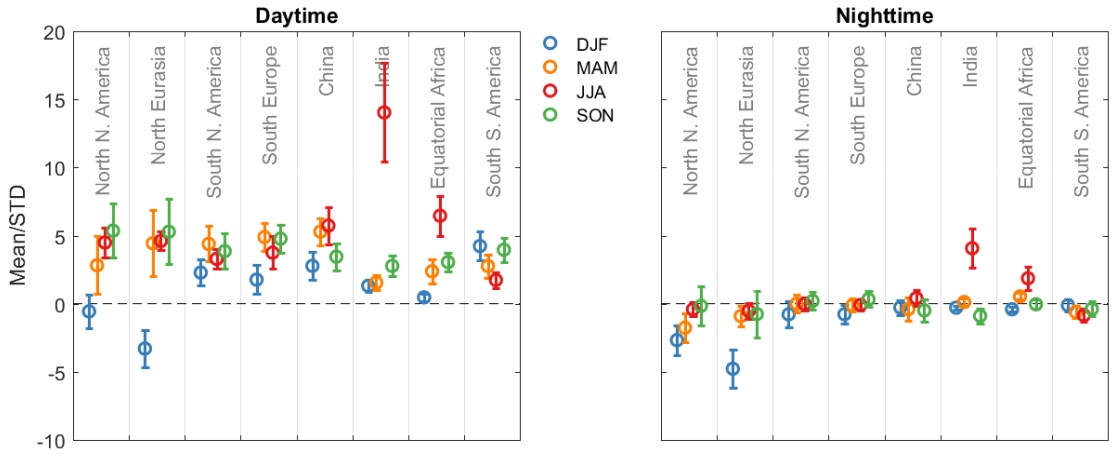

Figure 3.4.4 - Spatial mean (circles) and standard deviation (STD; bars) of the clear-sky bias over the defined areas of interest.

The impact of snow coverage is evident in the northernmost regions (North of North America, North Eurasia; Figure 3.4.4), leading to high negative biases being observed during daytime DJF. During the remaining seasons, the clear-sky bias seems to be mostly controlled by the available solar radiation.

Night-time biases are also more pronounced over these regions, being associated to the drier atmosphere that facilitates the radiative cooling. During MAM and SON there is a higher variability of surface conditions (e.g. snow coverage, soil water content) that results in a higher spatial heterogeneity of the biases leading to higher STD values.

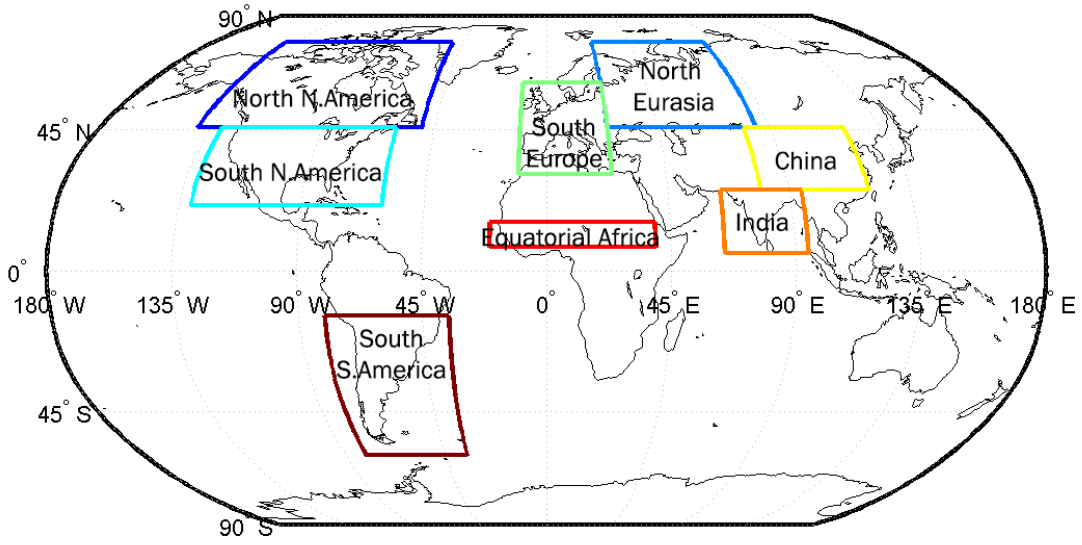

Figure 3.4.5 - Geographical location of the areas of interest described in Figure 3.4.4.

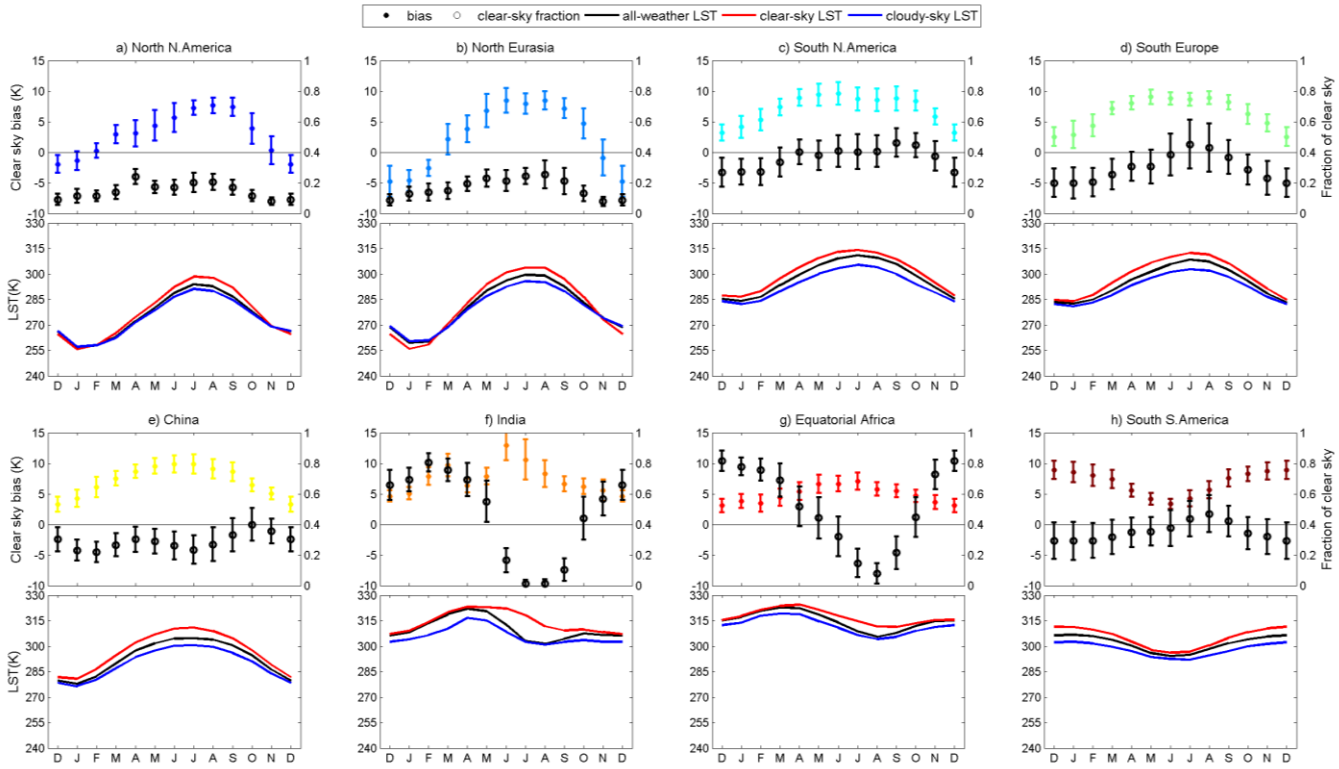

Figure 3.4.6 - Top panel: monthly average and standard deviation of the clear-sky bias (left axis; color) and clear-sky fraction (right axis; black) over the areas of interest described in Figure 3.4.4. Bottom panel: monthly average clear-sky (red), all-weather (black) and cloudy-sky (blue) LST over the interest areas.

3.5 Summary and Concluding remarks

Inversions of AMSR-E brightness temperatures to derive LST are presented. Targeting limited dependence on ancillary data sets and rapid conversion of Tb into LST estimates, the methodology is based on approximating the Tb-LST relationship by a global transfer function built by neural networks trained with a database of coincident AMSR-E Tb and retrieved MW Ts* from Lipton et al. (2015). A close methodology was already presented in Prigent et al. (2016) to invert SSM/I observations, and similar to those inversions, climatological MW emissivity (here from the database of Moncet et al. (2011)) is added as an input to the neural network together with the Tb to help constraining the inversion problem.

The retrieval of LST from MW observations is subject to difficulties for some atmospheric and/or surface conditions. They are mainly related to a rather large emissivity variability (e.g., related to snowpack metamorphism or changes in soil water content) and emission from subsurface layers for some specific soil types and conditions (e.g., sandy soils). To help identify these conditions, the inversion is accompanied by a coarse estimation of retrieval uncertainty based on estimating the retrieval error for a selection of LST and emissivity conditions from the training database. Given that the target Ts* is already the product of an inversion, this retrieval uncertainty has to be considered as a low error estimate, with real uncertainty likely to be larger (i.e., the uncertainty with respect to the true LST). For ~75% of the land surface the RMSD (difference between the training target Ts* and the retrieved LST by the neural network) is below 2.8 K.

To further characterize the inversions, a simple estimate of the quality of the retrieval and a series of flags to signal potentially difficult inversion situations are also provided. The estimate of retrieval quality is based on looking at the LST variability from multiple trainings of the neural network with slightly different initial conditions. Regarding the flags, a series of ancillary products are used to identify snow and water covered ground, inversions close to the coastal line, strong cloud convection, and soils with large MW penetration depth. For nonflagged inversions, where we expect the best retrieval performance, the retrieval variability shows median values of ~0.7 K. That value can reach close to 2.0 K for difficult inversions (e.g., over sandy soils with large MW penetration depth).

Further strengths and issues of the LST product are discussed by evaluating one year of (2010) AMSR-E inversions at 10 selected ground stations. To provide a satellite IR reference to the AMSR-E evaluations, MODIS LST (MYD11A1, collection 5) (Wan and Li, 2008) is also compared to the station data. The MODIS LST is averaged over the 14 × 8 km resolution AMSR-E swath grid used for the LST retrieval. Overall, MODIS agrees better with the station LST than AMSR-E (all-station mean RMSD of 2.4 K for MODIS and 4.0 for AMSR-E), but since MODIS is an IR instrument, the corresponding LST retrievals are limited to clear-sky and are much more prone to contamination by undetected clouds. AMSR-E provides a much larger number of LST estimates, with an approximated ratio of 3 to 1 over the analyzed stations. At many stations, the RMSD of the AMSR-E clear-sky and cloudy-sky are comparable, highlighting the ability of the MW inversions to provide LST estimates under most atmospheric conditions. Closest level of agreement of MODIS and AMSR-E with the *in situ* LST occurs at the temperate stations, likely the result of a more stable MW emissivity well captured by the monthly climatological emissivity used for the inversions. Surface heterogeneity impacted the comparisons due to the large mismatch between the area-integrated satellite LST and the point LST estimate at the station. As the area surrounding the station is likely to be thermally more heterogeneous in the MW than in the IR, this may penalize the AMSR-E comparison. At a large number of stations, the biases between the satellite and station LST change sign between night-time and daytime and were also noticed to seasonally change, but the causes of the observed patterns cannot be clearly identified.

An intercomparison study was performed between LST retrieved from MW and IR sensors. MW LST values were compared against clear-sky IR LST estimates recorded by MODIS, SEVIRI, GOES, MTSAT. First, LST differences between AMSR-E and MODIS products were analyzed globally taking into account the surface conditions, paying special attention to the cases where larger discrepancies are expected

due to the contrasting physical behavior of IR and MW radiation. To put in perspective, the AMSR-E and MODIS LSTT differences, AMSR-E and MODIS were then compared with each GEO product.

The largest differences between AMSR-E and MODIS products, characterized by high (positive) bias and standard deviation, are found over regions prone to the occurrence of snow/ice. These regions are particularly problematic for both MW and IR LST retrievals. MW emissivity is highly variable for snow-covered ground and not always properly accounted for by the climatological emissivity used in the retrieval. Concurrently, IR emissivity despite presenting a lower contrast between snow and snow-free conditions, is highly dependent on the correct snow masking, with misclassifications impacting the retrieval. Desert areas also present large discrepancies between the AMSR-E and MODIS LST products, also with a positive bias in the AMSR-E and MODIS difference. LST differences over these regions seem mostly related to an underestimation of LST by MODIS. Nevertheless, MW inversions over dry sand areas with larger penetration depth are prone to larger uncertainties and are, for that reason, flagged in the AMSR-E LST product. Coastal areas present overall higher MW LST values than IR due to the emission from the water within the observations footprint not correctly accounted for in the MW retrieval. LST differences between AMSR-E and MODIS are significantly reduced after masking out snow/ice and sandy deserts, with a bias change from 2.64/4.64 K to 2.99/1.45 K for daytime/night-time and a STD decrease from 7.29/7.90 K to 5.06/3.87 K.

Results from the comparison between AMSR-E and the GEOs and between MODIS and the GEOs point out that some of the high discrepancies observed between AMSR-E and MODIS are reduced when the comparison is performed against other IR sensors. This is the case of the positive bias observed over the Sahara and the Arabian Peninsula. AMSR-E LST presents a better agreement with SEVIRI over these regions, and the bias between MODIS and SEVIRI is as high as 5 K for daytime. This means that the IR retrieval is very sensitive to the emissivity hypothesis over desert, and additional work has to be done in this area. The high discrepancies associated to snow coverage are consistent when comparing MW and IR estimates from the different sensors. Bias values between AMSR-E and the GEOs are, in some cases, of the same order as the ones observed between MODIS and the GEOs. In particular, GOES presents a daytime bias with respect to AMSR-E of 0.45 K, whereas the bias with respect to MODIS is 0.60 K. MTSAT presents a night-time bias with respect to AMSR-E of 0.26 K, while with MODIS the bias is 0.59 K.

Most LST products currently being disseminated rely on IR measurements and, therefore, are restricted to clear-sky conditions. This means that IR LST datasets are susceptible to clear-sky biases. The study of section 3.4 quantifies the spatial and seasonal variations of “clear-sky bias”, defined as the difference between average clear-sky and average all-weather LST. An all-weather LST dataset is available from MW measurements, allowing a full characterization of the bias at the global scale. However, it should be noted that this dataset corresponds to overpass times around 1.30 AM/PM and therefore is not to be taken as representative of the full diurnal cycles of both LST and cloud coverage.

The amplitude of the bias is closely related to the fraction of clear-sky days and, therefore, arid or tropical regions are associated to very low values of clear-sky bias whereas mid-latitudes present the highest values. During daytime, the input of solar radiation for clear-sky situations leads to higher LST values and therefore the bias is generally positive over most areas of the mid and high latitudes. For some periods (DJF, MAM and SON), the bias is negative over high latitudes due to the very own radiative properties of snow and to less accurate values of snow emissivity. During night time, the bias is generally negative although with lower amplitude, because of the increased radiative cooling for clear-sky situations. The remarkably high biases over the monsoon regions are likely to be related to an underrepresentation of clear-sky conditions throughout the season, since there is a higher percentage of clear-sky days before the monsoon.

Although MW LST is here used to characterize the expected clear-sky biases present in IR LST datasets, It should be noted that MW LST may not always be compatible with IR LST due to the higher penetration of MW radiation in the surface. As shown in section 3.3, higher inter-sensor biases were found over

snow covered areas, especially for night-time. The high clear-sky biases found over high latitudes during the intermediate seasons may be partly attributed to high uncertainties of the LST associated to melting and refreezing of snow.

To the best of our knowledge, this study represents a first attempt to quantify clear-sky bias of remotely sensed LST at the global scale. All-weather LST datasets are not readily available and the MW LST dataset that was here used certainly constitutes an important added value. Although MW LST generally presents higher uncertainties than IR LST, the obtained spatial and seasonal variations of the clear-sky bias are within the expected range when considering the radiative properties of the different surfaces.

Satellite observations have been used to monitor surface temperature for over three decades, opening new perspectives to climate applications. In particular, it is expected that climate studies focusing on climate change monitoring will benefit from a better knowledge of the impact of using satellite observations restricted to clear-sky conditions.

CHAPTER 4

CONCLUDING REMARKS AND FUTURE WORK

CONTENTS

4. Concluding remarks and future work

4.1 Concluding remarks

The current availability of long-term time series of physical and biophysical parameters derived from remotely sensed observations has opened new perspectives in the monitoring of the Earth's surface. It is possible to estimate a wide range of land surface variables, including LST, from many different sensors on-board geostationary or polar orbit platforms. In the case of LST, the use of various algorithms, often based on very different assumptions, together with the diverse sensor spatial and temporal samplings and viewing perspective, makes it difficult to harmonize the various satellite products available (e.g., Barroso et al., 2005; Pinheiro et al., 2006; Rasmussen et al., 2010; Ermida et al., 2014).

The correction of directional effects on satellite-retrieved LST is of high relevance for a proper interpretation of spatial and temporal features contained in LST fields. LST differences between products induced by geometric effects may be as high as 15 K (Ermida et al., 2014; Lagouarde et al., 2014; Rasmussen et al., 2011). A methodology to correct such directional effects at local to global scales is proposed in Chapter 2. This methodology relies on parametric models since they are computationally more efficient and require few input information, which makes them particularly appropriate for an operational context. These parametric models were also evaluated against datasets based on a Geometric model of the local landscape and *in situ* radiometric temperatures of different surface elements.

The results presented in section 2.3 show that the parametric models are able to provide corrections on LST directionality with reliable quality, and in particular the combined Kernel-Hotspot model presents the best performance. The model is able to account for both shadowing effects and emissivity anisotropy with high accuracy. However, this model shows a higher sensitivity to the sampling of sun and view angles. This indicates that special care must be taken to the angle sampling when compiling the calibration database.

The analysis performed in sections 2.4 and 2.5 show that the parametric models may effectively be calibrated with observations performed by geostationary and polar orbit satellites collocated in time and space. The spatial distributions of the model parameters reflect the characteristics of the landscape, both in terms of vegetation cover and topography. Still, results show that the models' calibration are highly susceptible to LST differences in the products related to other sources of uncertainty (e.g. prescribed emissivity, algorithm, atmospheric correction). Despite these limitations, the work presented here demonstrates that the developed methodology can be used to harmonize LST products for a reference view angle (e.g. nadir).

In contrast with MW sensors, IR measurements are not sensitive to the surface under cloudy conditions. MW brightness temperatures, available from, e.g., AMSR, AMSR-E and SSM/I, have been demonstrated to provide all-weather LST (e.g. Aires et al., 2001; Prigent et al., 2003, 2016). However, it should be recognised that there are differences in the surface layer being sensed in the thermal IR domain (sensitive to the first ~ 50 μm of the soil) and MW domain (sensing depth ranging between 1 mm and a few cm). Furthermore, MW emissivity presents higher variability associated to surface properties such as soil moisture, vegetation cover, or presence of snow. Before assessing the clear-sky bias associated to IR LST measurements, the differences between IR and MW estimates of land surface temperature must be fully characterised.

Chapter 3 presents a methodology to retrieve LST from MW measurements based on a neural network approach. The use of IR LST to train the MW LST algorithm acts to attenuate the differences in the products that would be caused by the different penetration depths of IR and MW. The MW LST is fully analysed and compared with both *in situ* and IR LST obtained from different sensors. Ultimately, the

obtained MW all-weather LST is used to characterize the clear-sky bias expected to be found when using IR LST.

Results presented in sections 3.2 and 3.3 indicate that discrepancies between MW and IR may be close to the ones observed among IR-based products. The highest discrepancies were found for snow covered areas, where MW emissivity is highly variable and not always properly accounted for by the climatological emissivity used in the retrieval. There is no indication that penetration of the MW is significantly affecting the LST retrievals, and this likely due to the use of IR LST in the calibration of the algorithm, as referred above. The estimation of LST from MW measurements represents an added value to IR estimates, providing consistent global all-weather LST estimates. This advantage is especially relevant over areas of prevailing cloudy conditions, where the amount of available observations in the MW is more than double that in the IR. As such, the two types of LST estimates can be considered to provide complementary information, and the combined use of MW and IR would be highly advantageous. However, inconsistencies between the products need to be further studied before a merging strategy can be designed, paying attention not only to differences between MW and IR but also to those among IR-based products.

Section 3.4, presents comprehensive analysis of the clear-sky bias estimated using MW LST. To the best of our knowledge, this study represents a first attempt to quantify clear-sky bias of remotely sensed LST at the global scale, i.e. the systematic deviations with respect to all-weather conditions associated to the use of IR-based LST data. Results suggest a high temporal and spatial variability of those differences, following the local radiative balance, with bias values as high as 10 K over a large portion of Earth's land surface. As such, it is expected that climate studies focusing on climate change monitoring will benefit from a better knowledge of the impact of using satellite observations restricted to clear-sky conditions.

OUTCOME OF RESEARCH

Research carried out during this PhD resulted in the publication of several articles in international peer-reviewed scientific journals. Three papers were published in *Remote Sensing of Environment*, a scientific journal with an *Impact Factor* of 6.265, ranking 2/29 in the "Remote Sensing" category according to *ISI Journal of Citation Report*s edition of 2016:

- Ermida, S.L., Trigo, I.F., Dacamara, C.C., Göttsche, F.M., Olesen, F.S., Hulley, G. (2014). Validation of remotely sensed surface temperature over an oak woodland landscape — The problem of viewing and illumination geometries. Remote Sens. Environ. 148, 16–27.
- Ermida, S.L., DaCamara, C.C., Trigo, I.F., Pires, A.C., Ghent, D., Remedios, J., (2017). Modelling directional effects on remotely sensed land surface temperature. Remote Sens. Environ. 190, 56–69.
- Ermida, S.L., Trigo, I.F., Dacamara, C.C., Roujean, J.-L. (2018). Assessing the potential of parametric models to correct directional effects on local to global remotely sensed LST. Remote Sens. Environ. 209, 410-422.

Two papers were published in *Journal of Geophysical Research: Atmospheres*, a scientific journal with an *Impact factor* of 3.454, ranking 20/85 in the "Meteorology & Atmospheric Sciences" category according to *ISI Journal of Citation Report*s edition of 2016:

- Jiménez, C., Prigent, C., Ermida, S.L., Moncet, J.-L. (2017). Inversion of AMSR-E observations for land surface temperature estimation: 1. Methodology and evaluation with station temperature. J. Geophys. Res. Atmos. 122, 3330–3347.
- Ermida, S.L., Jiménez, C., Prigent, C., Trigo, I.F., DaCamara, C.C. (2017). Inversion of AMSR-E observations for land surface temperature estimation: 2. Global comparison with infrared satellite temperature. J. Geophys. Res. Atmos. 122, 3348–3360.

Research performed in this PhD was also used in the framework of the ESA DUE GlobTemperature project to produce an "angular corrected LST" for the Merged LST product. In the framework of the

LSA-SAF, the same methodology based on the kernel model (calibrated per vegetation and orography clusters – see section 2.5) have also been proposed to be operationally implemented with the aim of generating an additional data layer to be disseminated within the LST product. This layer will consist of an estimate of the LST difference from the nadir to the SEVIRI view, thus providing the user with information on the expected deviation of the actual retrieval due to angular effects, on a pixel-by-pixel basis.

Ongoing research is presented in Appendix A. This was partly carried out at NASA's Jet Propulsion Laboratory (JPL) under a Visiting Student Researchers Program with the mentorship of Dr. Glynn Hulley, supported by FCT and Fulbright.

4.2 Future work

The full characterization of angular effects on LST is a complex task. Although radiative transfer models may provide information on directionality of LST with high accuracy, they require detailed information on the surface which is not always readily available. For that reason, parametric models are much more appealing. However, resulting from the research performed in this PhD, several limitations were found that may be addressed in future studies:

1. Terrain slope and orientation may be important factors determining LST directional effects, which could be incorporated in improved model formulations. The parametric models considered here were not designed to simulate topography effects. However, given their statistical nature, they may be able to accommodate shadowing effects resulting from topography at sub-pixel scale. The shadowing effects resulting from sloping terrain is nonetheless complex since it combines the effects at the local (pixel) scale and at larger scales (e.g. mountain ranges) and should therefore be further studied.
2. Other parametric models of surface reflectivity (e.g. Li and Strahler, 1992; Qin and Gerstl, 2000) could be adapted for the temperature domain and compared against with the presented methodologies. The Hapke soil model (Hapke, 1981) could also be considered for the simulation of soil emissivity directionality.
3. The parametric models were found to be highly sensitive to LST discrepancies between the products associated to uncertainties in the retrieval methodology. As such, coefficients with better quality may be obtained by performing the fit of the models with a database of fully calibrated LST, where LST products would be retrieved using the same algorithm and input data.

The use of MW observations to obtain LST under all weather conditions represents a great advantage towards a better characterization of LST spatio-temporal variability. MW LST may complement the wide use of IR measurements, contributing to overcome one of the main limitations of IR LST: the availability of the latter under clear-sky only. The research performed within this PhD contributed to a better understanding of intrinsic physical differences between IR and MW LST and of the impact of the use of clear-sky only datasets of LST. In this context, there is a number of open threads, some of which resulted from the research work conducted for this thesis:

1. The algorithm used to derive MW LST (Jiménez et al., 2017) may be adapted for new and upcoming MW sensors to provide longer time records. In particular, the Advanced Microwave Scanning Radiometer 2 (AMSR2) on board JAXA's GCOM-W1 spacecraft is the successor of the AMSR-E sensor, presenting the same orbit and equator crossing time. The spacecraft was launched in May 2012 and is currently operational. The AMSR2 presents similar channel configurations to the AMSR-E making it ideal to provide temporal continuity to the MW LST product generated with AMSR-E, which stopped rotating in October 2011.
2. Further work should be carried out to further reduce discrepancies observed between the IR and MW products, addressing the limitations and sources of uncertainties of both IR and MW retrieval algorithms. This should address in particular the training databases for the MW LST

algorithms referred in the previous point, which include also IR LST and must ensure a wide and realistic representativeness of all possible retrieval conditions.

3. The clear-sky bias analysis presented here would benefit from the use of longer datasets and of an intercomparison of results obtained using different datasets to provide a more robust assessment of the impact of such bias at different temporal and spatial scales.
4. The best strategy to merge multiple LST products from IR and MW sensors is still far from being settled. Its objective would be to create a harmonized LST dataset with the best possible temporal and spatial sampling. Such merge could be produced at different spatio-temporal scales to meet the requirements of different users.
5. Other methods to obtain all-weather LST should also be taken into consideration. Since LST is mostly determined by incoming radiation, vegetation cover and soil moisture availability, LST can also be indirectly derived from satellite-based estimates of all these variables via models of the surface energy budget. The advantages and caveats of such an approach - somehow less close to the observations than a more direct retrieval of LST from IR or MW - are still to be further investigated.

Appendix A

A RADIANCE-BASED METHOD TO RETRIEVE EMISSIVITY ANGULAR DEPENDENCE FROM SATELLITE OBSERVATIONS

As discussed in Chapter 2, bare ground areas may present significant variations of emissivity with view angle and several studies have shown this dependence from experimental measurements (Cuenca and Sobrino, 2004; García-Santos et al., 2012; Labed and Stoll, 1991; Lagouarde et al., 1995; Sobrino and Cuenca, 1999). However, the dependence found in such experimental setups is not always translated into the pixel scale, as the heterogeneity (e.g. in soil composition) and roughness of the surface within the FOV of the satellite may impact that dependence. Methodologies have been proposed to retrieve LST and emissivity that would in theory allow the characterization of such dependence (e.g. García-Santos et al., 2015; Masiello et al., 2015; Ren et al., 2011). However, these methodologies depend directly on the quality of the algorithm and a proper validation of the obtained dependences is difficult.

We are currently studying the use of TOA radiance measurements as obtained by different sensors collocated in space and time to retrieve the angular dependence of emissivity over desert areas. This method would benefit from the multiple viewing geometries that could be obtained by collocating a geostationary and a polar orbit satellite without requiring a LST retrieval. In this study, we use TOA radiances provided by three sensors, namely SEVIRI/MSG, MODIS/Aqua and the Visible Infrared Imaging Radiometer Suite (VIIRS) on-board the joint NASA/NOAA Suomi National Polar-orbiting Partnership (NPP), covering the year of 2016 and over selected locations of the Namib and Sahara deserts, i.e. surfaces where shadowing effects can be neglected and where, therefore, any directional effects observed on emitted radiance at the surface must be essentially attributed to emissivity. The locations selected for this preliminary study are shown in Figure A.1 for Namib and Sahara deserts.

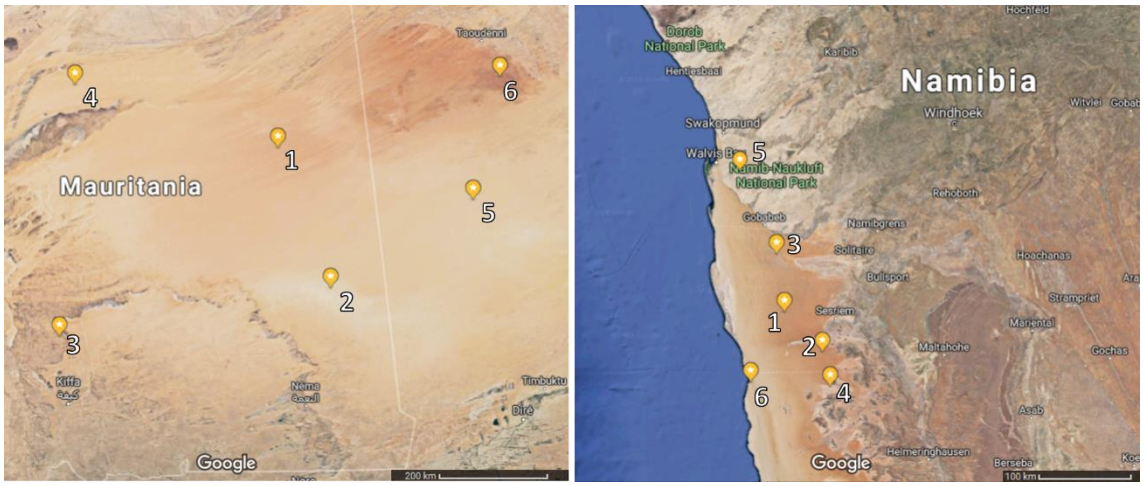

Figure A.1 – Geographical location of the selected study sites at the Sahara (left panel) and Namib (right panel) deserts. Photos courtesy of Google Earth™ mapping service.

The method is derived directly from the radiative transfer equation (eq. 1.2.5) obtained for a GEO and polar orbit (or low earth orbit; LEO) satellite. For that purpose, it is assumed that at a given location emissivity depends only on zenith angle. It is also assumed that LST is invariant with viewing angle (i.e., the surface is homogeneous and there are no shadowing effects), which means that the value to be retrieved by both sensors, T_{skin}, will be the same, given a proper space-time collocation. As a result, $B_{\lambda,GEO}(T_{\mathrm{skin}})/B_{\lambda,LEO}(T_{\mathrm{skin}}) \approx 1$ and from eq. 1.2.5:

$$\frac{\tau_{\lambda,LEO}}{\tau_{\lambda,GEO}}\left(L_{\lambda,GEO}-\tau_{\lambda,GEO}L_{\mathrm{at}_\lambda\downarrow,GEO}-L_{\mathrm{at}_\lambda\uparrow,GEO}\right)+\varepsilon_{\lambda,GEO}\left(\tau_{\lambda,LEO}L_{\mathrm{at}_\lambda\downarrow,GEO}-\tau_{\lambda,GEO}L_{\mathrm{at}_\lambda\downarrow,LEO}\right)$$
$$=\frac{\boldsymbol{\varepsilon_{\lambda,GEO}}}{\boldsymbol{\varepsilon_{\lambda,LEO}}}\left(L_{\lambda,LEO}-\tau_{\lambda,LEO}L_{\mathrm{at}_\lambda\downarrow,LEO}-L_{\mathrm{at}_\lambda\uparrow,LEO}\right) \quad \textbf{(A.1)}$$

$L_{\mathrm{at}_\lambda\downarrow}$, $L_{\mathrm{at}_\lambda\uparrow}$ and τ_λ are obtained using a radiative transfer model applied atmospheric data obtained from an atmospheric model and using the respective view angles of the LEO and GEO sensors. In this study we use the RTTOV model with atmospheric profiles (temperature and specific humidity) from the Modern-Era Retrospective analysis for Research and Applications, Version 2 (MERRA-2). For consistency, all terms are derived for the GEO channels, and $L_{\lambda,LEO}$ is converted to these channels using the respective response functions.

Given that emissivity ratios will be small when compared to radiance values, the method requires prescribed values of $\varepsilon_{\lambda,GEO}$ for a proper calibration. SEVIRI emissivities are therefore derived using a Temperature Emissivity Separation (TES) algorithm developed for the MODIS sensor (Hulley et al., 2016; Hulley and Hook, 2011). $\varepsilon_{\lambda,GEO}$ is then set as the average of the values obtained with the TES for the full 2016 period. The TES algorithm has shown great accuracy in retrieving emissivity over deserts, especially for dry atmospheres and low view angles (Göttsche and Hulley, 2012; Hulley et al., 2012; Hulley and Hook, 2011). As such, a better quality of the $\varepsilon_{\lambda,GEO}$ value is achieved by using only emissivity values retrieved for very dry atmospheres and the locations under study are all within low SEVIRI view angles (below 35º). Uncertainties obtained following the methodology described in Hulley et al. (2012) are all below 0.1% for these cases. For reference, directional emissivity is also derived for MODIS and VIIRS using the TES algorithm.

This method also requires information on the atmospheric conditions and, therefore, quality of the emissivity retrievals will depend on the quality of the atmospheric data. To reduce uncertainty of the atmospheric correction, only observations with total column water vapour (TCWV) below 1 cm are considered.

From a first assessment of the results, we found that the TOA radiances needed further calibration between sensors. Therefore, a pre-calibration of the radiances is performed by fitting a linear regression to observations with similar view angles between the GEO and the LEO ($|VZA_{GEO} - VZA_{LEO}| < 7.5°$). This regression is then used to correct the LEO radiances towards the GEO. An example of such regression is shown in Figure A.2.

The ratio $\boldsymbol{\varepsilon_{\lambda,GEO}/\varepsilon_{\lambda,LEO}}$ is then derived from eq. (A.1) by robust regression using a bi-square weighting function (Holland and Welsch, 1977), forcing the intersection at (0,0). The regressions are performed for classes of VZA of the LEO with intervals of 10º, in order to assess the VZA dependence. Figure A.3 shows the VZA dependence of the LEO emissivity as obtained for some of the selected locations. The channel at 8.7 µm shows the highest anisotropy of the emissivity with variations as high as 0.06, followed by the 10.8 µm channel with variations as high as 0.03, while the variations in 12 µm channel are negligible. As expected, the emissivity anisotropy varies also with location. The highest anisotropy of the 8.7 µm channel is found over the sand dune areas of both Namib and Sahara (locations 1 of both areas), but the dependence for the 10.8 µm channel is higher at the Sahara site.

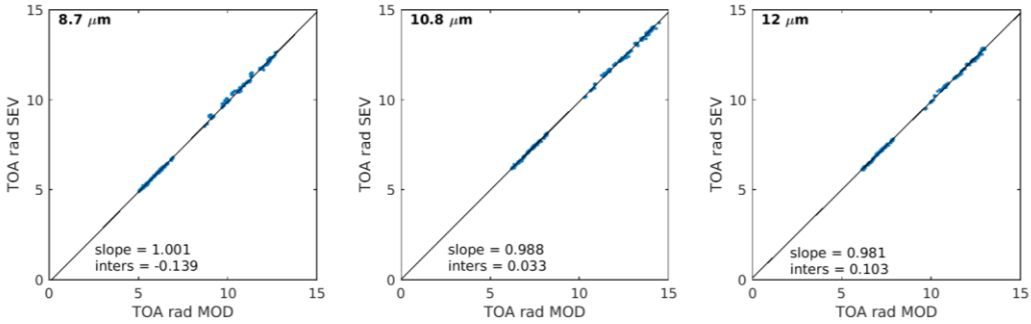

Figure A.2 – Scatterplots of SEVIRI TOA radiances with respect to MODIS, for each channel and for VZA differences below 7.5° and TCWV below 1 cm. The respective coefficients of the linear regression are also shown.

It is worth noting that results are consistent for both MODIS and VIIRS, emphasizing the robustness of the results. The dependence obtained for TES agrees with the one with the radiance-based method, except for the 10.8 μm channel. The TES relies on an empirical relationship (the so-called calibration curve) to predict emissivity spectral contrasts, which is derived from a spectral library of emissivities of different materials (Hulley and Hook, 2011). This spectral library does not include emissivity dependence with view angle and consequently changes of spectral contrasts with view angle are not taken into account. Results shown in Figure A.3 indicate that emissivity spectral contrasts are expected to increase with view angle and therefore it is likely that the calibration curve used in the TES is constraining variations of the emissivity at 10.8 μm.

Emissivities derived from the radiance method are less stable for the 12 μm. This channel is associated to higher atmospheric absorption/emission than the 10.8 μm, which combined a likely lower emissivity dependence on view angle, resulting in a higher sensitivity to the atmospheric correction. The TES, on the other hand, benefits from the information provided by the other channels and therefore presents more stable results for this channel.

The radiance-based method presented here, complemented by the TES algorithm, shows promising results in the retrieval of directional emissivity from satellite observations. The method will be further analyzed to quantify the sensitivity to uncertainties in the atmospheric correction. For that purpose, other radiative-transfer and atmospheric models could be used to confirm these results. The method could also be applied using other sensors, to obtain information on emissivity anisotropy over other desert areas.

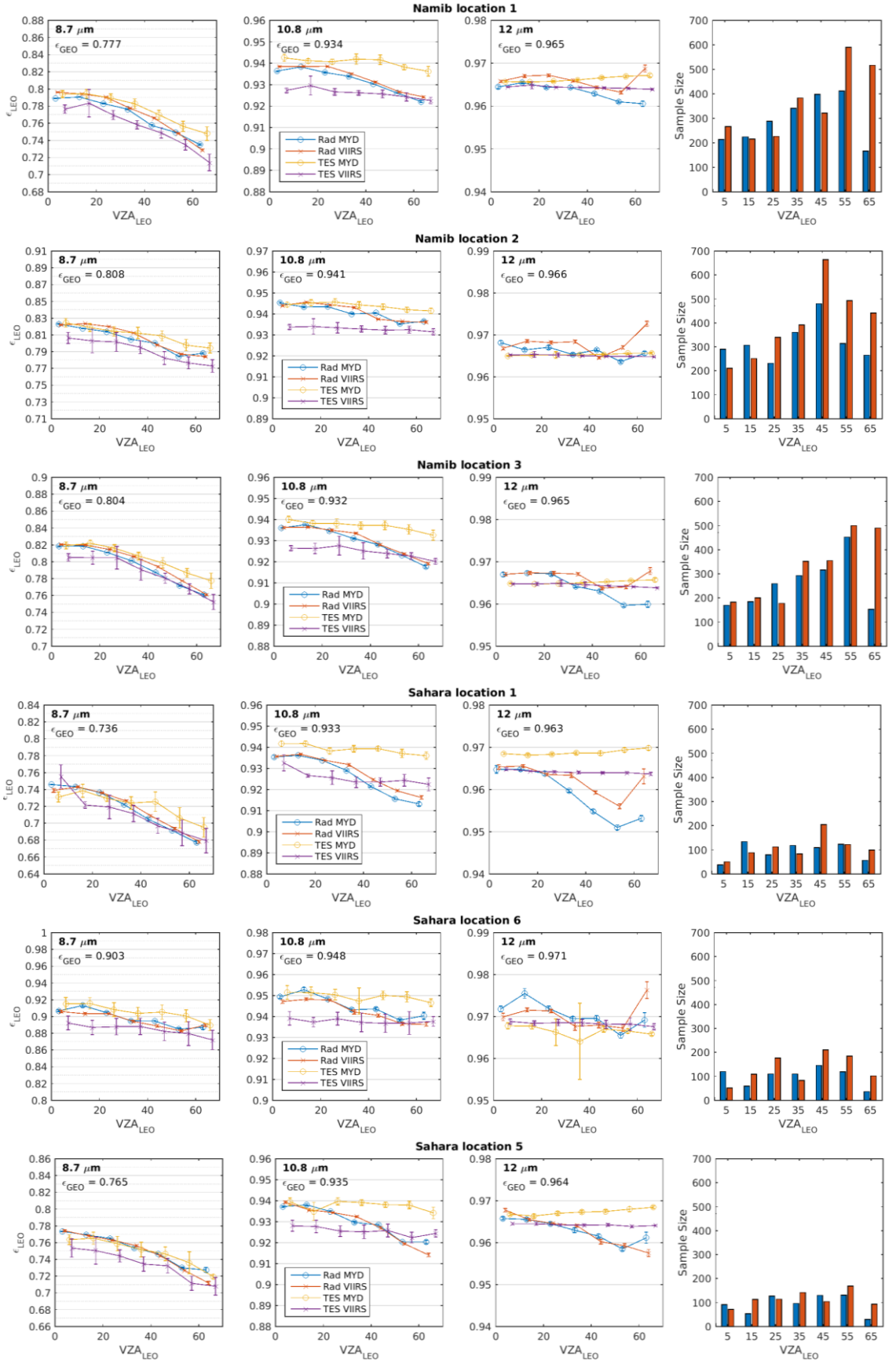

Figure A.3 – Emissivity values of the LEO sensor as function of the VZA for each channel and for some of the locations indicated in Figure A.1. Values obtained from the radiance method (Rad) are shown in blue for MODIS and orange for VIIRS, and values obtained with the TES are shown in yellow and purple, respectively.

REFERENCES

Aires, F., Prigent, C., Bernardo, F., Jiménez, C., Saunders, R., Brunel, P., 2011. A Tool to Estimate Land-Surface Emissivities at Microwave frequencies (TELSEM) for use in numerical weather prediction. Q. J. R. Meteorol. Soc. 137, 690–699.

Aires, F., Prigent, C., Rossow, W.B., Rothstein, M., 2001. A new neural network approach including first guess for retrieval of atmospheric water vapor, cloud liquid water path, surface temperature, and emissivities over land from satellite microwave observations. J. Geophys. Res. Atmos. 106, 14887–14907.

Arnfield, A.J., 2003. Two decades of urban climate research: A review of turbulence, exchanges of energy and water, and the urban heat island. Int. J. Climatol. 23, 1–26.

Augustine, J.A., Hodges, G.B., Cornwall, C.R., Michalsky, J.J., Medina, C.I., Augustine, J.A., Hodges, G.B., Cornwall, C.R., Michalsky, J.J., Medina, C.I., 2005. An Update on SURFRAD—The GCOS Surface Radiation Budget Network for the Continental United States. J. Atmos. Ocean. Technol. 22, 1460–1472.

Barroso, C., Trigo, I.F., Olesen, F., DaCamara, C., Queluz, M.P., 2005. Intercalibration of NOAA and Meteosat window channel brightness temperatures. Int. J. Remote Sens. 26, 3717–3733.

Basist, A., Grody, N.C., Peterson, T.C., Williams, C.N., Basist, A., Grody, N.C., Peterson, T.C., Williams, C.N., 1998. Using the Special Sensor Microwave/Imager to Monitor Land Surface Temperatures, Wetness, and Snow Cover. J. Appl. Meteorol. 37, 888–911.

Becker, F., Li, Z., 2009. Surface temperature and emissivity at various scales: Definition, measurement and related problems. Remote Sens. Rev. 12, 225–253.

Belward, A.S., Office, I.-D., 1996. The IGBP-DIS global 1 km land cover data set “DISCover”: Proposal and implementation plans. Rep. L. Cover Work. Gr. IGBP-DIS 18, 3289–3295.

Bicheron, P., Defourny, P., Brockmann, C., Schouten, L., Vancutsem, C., Huc, M., Bontemps, S., Leroy, M., Achard, F., Herold, M., Ranera, F., O., A., 2008. GLOBCOVER Products Report Description and Products Description and Validation Report. ESA Globcover Proj. led by MEDIAS Fr. 33, 140–7.

Burrough, P.A., McDonell, R.A., 1998. Principles of Geographical Information Systems. Oxford university press, New York.

Caselles, V., Sobrino, J.A., 1989. Determination of frosts in orange groves from NOAA-9 AVHRR data. Remote Sens. Environ. 29, 135–146.

Caselles, V., Sobrino, J., Coll, C., 1992. A physical model for interpreting the land surface temperature obtained by remote sensors over incomplete canopies. Remote Sens. Environ. 39, 203–211.

Chen, L., Zhuang, J., Liu, Q., Xu, X., Tian, G., 2000. Study on the law of radiant directionality of row crops. Sci. China Ser. E Technol. Sci. 43, 70–82.

Cordisco, E., Prigent, C., Aires, F., 2006. Snow characterization at a global scale with passive microwave satellite observations. J. Geophys. Res. 111, 1–15.

Cuenca, J., Sobrino, J.A., 2004. Experimental measurements for studying angular and spectral variation of thermal infrared emissivity. Appl. Opt. 43, 4598.

Dash, P., Göttsche, F.-M., Olesen, F.-S., Fischer, H., 2002. Land surface temperature and emissivity estimation from passive sensor data: Theory and practice-current trends. Int. J. Remote Sens. 23, 2563–2594.

Dash, P., Olesen, F., Prata, A., 2004. Optimal land surface temperature validation site in Europe for MSG, in: Proceedings of EUMETSAT Meteorological Satellite Conference. Prague, p. 41.

David, T.., Ferreira, M.., Cohen, S., Pereira, J.., David, J.., 2004. Constraints on transpiration from an evergreen oak tree in southern Portugal. Agric. For. Meteorol. 122, 193–205.

David, T.S., Henriques, M.O., Kurz-Besson, C., Nunes, J., Valente, F., Vaz, M., Pereira, J.S., Siegwolf, R., Chaves, M.M., Gazarini, L.C., David, J.S., 2007. Water-use strategies in two co-occurring Mediterranean evergreen oaks: Surviving the summer drought. Tree Physiol. 27, 793–803.

Duffour, C., Lagouarde, J.-P., Roujean, J.-L., 2016. A two parameter model to simulate thermal infrared directional effects for remote sensing applications. Remote Sens. Environ. 186, 250–261.

Duffour, C., Olioso, A., Demarty, J., Van der Tol, C., Lagouarde, J.P., 2015. An evaluation of SCOPE: A tool to simulate the directional anisotropy of satellite-measured surface temperatures. Remote Sens. Environ. 158.

Duguay-Tetzlaff, A., Bento, V.A., Göttsche, F.M., Stöckli, R., Martins, J.P.A., Trigo, I., Olesen, F., Bojanowski, J.S., da Camara, C., Kunz, H., 2015. Meteosat land surface temperature climate data record: Achievable accuracy and potential uncertainties. Remote Sens. 7, 13139–13156.

English, S.J., 2008. The importance of accurate skin temperature in assimilating radiances from satellite sounding instruments, in: IEEE Transactions on Geoscience and Remote Sensing. pp. 403–408.

Ermida, S.L., DaCamara, C.C., Trigo, I.F., Pires, A.C., Ghent, D., Remedios, J., 2017a. Modelling directional effects on remotely sensed land surface temperature. Remote Sens. Environ. 190, 56–69.

Ermida, S.L., Jiménez, C., Prigent, C., Trigo, I.F., DaCamara, C.C., 2017b. Inversion of AMSR-E observations for land surface temperature estimation: 2. Global comparison with infrared satellite temperature. J. Geophys. Res. Atmos. 122, 3348–3360.

Ermida, S.L., Trigo, I.F., DaCamara, C.C., Göttsche, F.M., Olesen, F.S., Hulley, G., 2014. Validation of remotely sensed surface temperature over an oak woodland landscape - The problem of viewing and illumination geometries. Remote Sens. Environ. 148.

Ermida, S.L., Trigo, I.F., DaCamara, C.C., Roujean, J.-L., 2018. Assessing the potential of parametric models to correct directional effects on local to global remotely sensed LST. Remote Sens. Environ. 209, 410–422.

Franklin, J., Strahler, a. H., 1988. Invertible canopy reflectance modeling of vegetation structure in semiarid woodland. IEEE Trans. Geosci. Remote Sens. 26, 809–825.

Freitas, S.C., Trigo, I.F., Bioucas-dias, J.M., Göttsche, F., 2010. Quantifying the Uncertainty of Land Surface Temperature Retrievals From SEVIRI / Meteosat. IEEE Trans. Geosci. Remote Sens. 48, 523–534.

Freitas, S.C., Trigo, I.F., Macedo, J., Barroso, C., Silva, R., Perdigão, R., Freitas, S.C., Trigo, I.F., Macedo, J., Barroso, C., Silva, R., Perdigão, R., 2013. Land surface temperature from multiple geostationary satellites 1161.

Frison, P.-L., Mougin, E., 1996. Use of ERS-1 wind scatterometer data over land surfaces. IEEE Trans. Geosci. Remote Sens. 34, 550–560.

García-Haro, F.J., Sommer, S., Kemper, T., 2005. A new tool for variable multiple endmember spectral mixture analysis (VMESMA). Int. J. Remote Sens. 26, 2135–2162.

García-Santos, V., Coll, C., Valor, E., Niclòs, R., Caselles, V., 2015. Analyzing the anisotropy of thermal infrared emissivity over arid regions using a new MODIS land surface temperature and emissivity product (MOD21). Remote Sens. Environ. 169, 212–221.

García-Santos, V., Valor, E., Caselles, V., Ángeles Burgos, M., Coll, C., 2012. On the angular variation of thermal infrared emissivity of inorganic soils. J. Geophys. Res. Atmos. 117 (D19).

Ghent, D., Kaduk, J., Remedios, J., Ardö, J., Balzter, H., 2010. Assimilation of land-surface temperature into the land surface model JULES with an Ensemble Kalman Filter. J. Geophys. Res. 115, 1–16.

Göttsche, F.-M., Hulley, G.C., 2012. Validation of six satellite-retrieved land surface emissivity products over two land cover types in a hyper-arid region. Remote Sens. Environ. 124, 149–158.

Göttsche, F.-M., Olesen, F.-S., Bork-Unkelbach, A., 2013. Validation of land surface temperature derived from MSG/SEVIRI with in situ measurements at Gobabeb, Namibia. Int. J. Remote Sens. 34, 3069–3083.

Göttsche, F.-M., Olesen, F.-S., Trigo, I.F., Bork-Unkelbach, A., Martin, M.A., 2016. Long term validation of land surface temperature retrieved from MSG/SEVIRI with continuous in-situ measurements in Africa. Remote Sens. 8, 410.

Gray, W.A., Müller, R., W., H.D., 1974. Engineering Calculations in Radiative Heat Transfer, Progress i. ed. Elsevier Ltd.

Guillevic, P., Gastellu-Etchegorry, J.P., Demarty, J., Prévot, L., 2003. Thermal infrared radiative transfer within three-dimensional vegetation covers. J. Geophys. Res. 108, 4248.

Guillevic, P.C., Bork-unkelbach, A., Göttsche, F.M., Hulley, G., Gastellu-Etchegorry, J.-P., Olesen, F.S., Privette, J.L., 2013. Directional Viewing Effects on Satellite Land Surface Temperature Products Over Sparse Vegetation Canopies — A Multisensor Analysis. IEEE Geosci. Remote Sens. Lett. 10 (6), 1464-1468.

Hagan, M.T., Menhaj, M.B., 1994. Training feedforward networks with the Marquardt algorithm. IEEE Trans. Neural Networks 5, 989–993.

Hansen, J., Ruedy, R., Sato, M., Lo, K., 2010. Global surface temperature change. Rev. Geophys. 48, RG4004.

Hapke, B., 1981. Bidirectional reflectance spectroscopy 1. Theory. J. Geophys. Res. 86, 3039–3054.

Hatsopoulos, G.N., Keenan, J.H., 1965. Principles of General Thermodynamics. John Wiley & Sons, Inc.

Heidinger, A.K., Laszlo, I., Molling, C.C., Tarpley, D., 2013. Using SURFRAD to verify the NOAA single-channel land surface temperature algorithm. J. Atmos. Ocean. Technol. 30, 2868–2884.

Holland, P.W., Welsch, R.E., 1977. Robust regression using iteratively reweighted least-squares. Commun. Stat. - Theory Methods 6, 813–827.

Holmes, T.R.H., De Jeu, R.A.M., Owe, M., Dolman, A.J., 2009. Land surface temperature from Ka band (37 GHz) passive microwave observations. J. Geophys. Res. 114, D04113.

Hulley, G.C., Hook, S.J., 2011. Generating Consistent Land Surface Temperature and Emissivity Products Between ASTER and MODIS Data for Earth Science Research. IEEE Trans. Geosci. Remote Sens. 49, 1304–1315.

Hulley, G.C., Hughes, C.G., Hook, S.J., 2012a. Quantifying uncertainties in land surface temperature and emissivity retrievals from ASTER and MODIS thermal infrared data. J. Geophys. Res. Atmos. 117.

Jimenez, C., Catherinot, J., Prigent, C., Roger, J., 2010. Relations between geological characteristics and satellite-derived infrared and microwave emissivities over deserts in northern Africa and the Arabian Peninsula. J. Geophys. Res. Atmos. 115, 1–11.

Jiménez, C., Prigent, C., Ermida, S.L., Moncet, J.-L., 2017. Inversion of AMSR-E observations for land surface temperature estimation: 1. Methodology and evaluation with station temperature. J. Geophys. Res. Atmos. 122, 3330–3347.

Jones, H.G., Vaughan, R.A., 2010. Remote sensing of vegetation: principles, techniques, and applications. Oxford university press.

Jupp, D., 2000. A Compendium of Kernel & Other (Semi-)empirical BRDF Models, Report Earth Observation Center, Office of Space Science Applications, CSIRO, Clayton, Victoria, Australia.

Kabsch, E., Olesen, F.-S., Prata, F., 2008. Initial results of the land surface temperature (LST) validation with the Evora, Portugal ground-truth station measurements. Int. J. Remote Sens. 29, 5329–5345.

Kerr, Y.H., Lagouarde, J.P., Nerry, F., Ottlé, C., 2004. Land surface temperature retrieval techniques and applications, in: Thermal Remote Sensing in Land Surface Processes. CRC Press, Boston, USA, pp. 33–109.

Kimes, D.S., 1983. Remote sensing of row crop structure and component temperatures using directional radiometric temperatures and inversion techniques. Remote Sens. Environ. 13, 33–55.

Kimes, D.S., 1981. Remote Sensing of Temperature Profiles in Vegetation Canopies Using Multiple View Angles And Inversion Techniques. IEEE Trans. Geosci. Remote Sens. GE-19, 85–90.

Kimes, D.S., Kirchner, J.A., 1983. Directional radiometric measurements of row-crop temperatures. Int. J. Remote Sens. 4, 299–311.

Kimes, D.S., Smith, J.A., Link, L.E., 1981. Thermal IR exitance model of a plant canopy. Appl. Opt. 20, 623.

Labed, J., Stoll, M.P., 1991. Angular Variation of Land Surface Spectral Emissivity in the Thermal Infrared - Laboratory Investigations on Bare Soils. Int. J. Remote Sens. 12, 2299–2310.

Lacaze, R., Balsamo, G., Baret, F., Bradley, A., Calvet, J.-C., Camacho, F., D'Andrimont, R., Freitas, S.C., Makhmara, H., Naeimi, V., Philippe, P., Poilvé, H., Smets, B., others, 2011. GEOLAND2 – Towards an Operational GMES Land Monitoring Core Service; First Results of the Biogeophysical Parameter Core Mapping Service, in: Wagner, W., Székely, B. (Eds.), ISPRS TC VII Symposium – 100 Years ISPR. ISPRS, pp. 354–359.

Lagarias, J.C., Reeds, J.A., Wright, M.H., Wright, P.E., 1998. Convergence Properties of the Nelder-Mead Simplex Method in Low Dimensions. SIAM J. Optim. 9, 112–147.

Lagouarde, J.P., Ballans, H., Moreau, P., Guyon, D., Coraboeuf, D., 2000. Experimental study of brightness surface temperature angular variations of maritime pine (Pinus pinaster) stands. Remote Sens. Environ. 72, 17–34.

Lagouarde, J.P., Dayau, S., Moreau, P., Guyon, D., 2014. Directional anisotropy of brightness surface temperature over vineyards: Case study over the Medoc Region (SW France). IEEE Geosci. Remote Sens. Lett. 11, 574–578.

Lagouarde, J.P., Irvine, M., 2008. Directional anisotropy in thermal infrared measurements over Toulouse city centre during the CAPITOUL measurement campaigns: First results. Meteorol. Atmos. Phys. 102, 173–185.

Lagouarde, J.P., Kerr, Y.H., Brunet, Y., 1995. An experimental study of angular effects on surface temperature for various plant canopies and bare soils. Agric. For. Meteorol. 77, 167–190.

Lagouarde, J.P., Moreau, P., Irvine, M., Bonnefond, J.M., Voogt, J.A., Solliec, F., 2004. Airborne experimental measurements of the angular variations in surface temperature over urban areas: Case study of Marseille (France). Remote Sens. Environ. 93, 443–462.

Li, L., Njoku, E.G., Im, E., Chang, P.S., St.Germain, K., 2004. A Preliminary Survey of Radio-Frequency Interference Over the U.S. in Aqua AMSR-E Data. IEEE Trans. Geosci. Remote Sens. 42, 380–390.

Li, X., Strahler, A., 1986. Geometric-optical bidirectional reflectance modeling of a conifer forest canopy. Trans. Geosci. Remote Sens. GE-24, 906–919.

Li, X., Strahler, A., 1985. Geometric-Optical Modeling of a Conifer Forest Canopy. IEEE Trans. Geosci. Remote Sens. GE-23, 705–721.

Li, X., Strahler, A.H., 1992. Geometric-Optical Bidirectional Reflectance Modeling of the Discrete Crown Vegetation Canopy : Effect of Crown Shape and Mutual Shadowing. Trans. Geosci. Remote Sens. 30, 276–292.

Li, Z.-L., Tang, B.-H., Wu, H., Ren, H., Yan, G., Wan, Z., Trigo, I.F., Sobrino, J. a, 2013. Satellite-derived land surface temperature: Current status and perspectives. Remote Sens. Environ. 131, 14–37.

Liang, S., Zhao, X., Liu, S., Yuan, W., Cheng, X., Xiao, Z., Zhang, X., Liu, Q., Cheng, J., Tang, H., Qu, Y., Bo, Y., Qu, Y., Ren, H., Yu, K., Townshend, J., 2013. A long-term Global LAnd Surface Satellite (GLASS) data-set for environmental studies. Int. J. Digit. Earth 6, 5–33.

Lipton, A.E., Liang, P., Jimenez, C., Moncet, J.-L., Aires, F., Prigent, C., Lynch, R., Galantowicz, J.F., D'Entremont, R.P., Uymin, G., 2015. Sources of discrepancies between satellite-derived and land surface model estimates of latent heat fluxes. J. Geophys. Res. Atmos. 120, 2325–2341.

Liu, J., Melloh, R. a., Woodcock, C.E., Davis, R.E., Ochs, E.S., 2004. The effect of viewing geometry and topography on viewable gap fractions through forest canopies. Hydrol. Process. 18, 3595–3607.

Martin, M., Göttsche, F.M., 2015. Satellite LST validation report WP4-DEL-12, Tech. Rep., ESA DUE GLOBTEMPERATURE Project,. Karlsruhe, Germany.

Masiello, G., Serio, C., Venafra, S., Liuzzi, G., Goettsche, F., Trigo, I.F., Watts, P., 2015. Kalman filter physical retrieval of surface emissivity and temperature from SEVIRI infrared channels: A validation and intercomparison study. Atmos. Meas. Tech. 8, 2981–2997.

McAtee, B.K., Prata, A.J., Lynch, M.J., McAtee, B.K., Prata, A.J., Lynch, M.J., 2003. The Angular Behavior of Emitted Thermal Infrared Radiation (8–12 μm) at a Semiarid Site. J. Appl. Meteorol. 42, 1060–1071.

McFarland, M.J., Miller, R.L., Neale, C.M., 1990. Land surface temperature derived from the SSM/I passive microwave brightness temperatures. IEEE Trans. Geosci. Remote Sens. 28, 839–845.

McGuire, M.J., Balick, L.K., Smith, J.A., Hutchison, B.A., 1989. Modeling directional thermal radiance from a forest canopy. Remote Sens. Environ. 27, 169–186.

Meeus, J., 1991. Astronomical Algorithms, 2nd ed, Astronomical Algorithms. Willmann-Bell, Incorporated.

Minnis, P., Khayer, M.M., 2000. Anisotropy of Land Surface Skin Temperature Derived from Satellite Data. J. Appl. Meteorol. 39, 1117–1129.

Moncet, J.L., Liang, P., Galantowicz, J.F., Lipton, A.E., Uymin, G., Prigent, C., Grassotti, C., 2011. Land surface microwave emissivities derived from AMSR-E and MODIS measurements with advanced quality control. J. Geophys. Res. Atmos. 116.

Nguyen, D., Widrow, B., 1990. Improving the learning speed of 2-layer neural networks by choosing initial values of the adaptative weights, in: International Joint Conference on Neural Networks (IJCNN). IEEE, New York, pp. 21–26.

Ni, W., Li, X., Woodcock, C.E., Caetano, M.R., Strahler, A.H., 1999. An analytical hybrid GORT model for bidirectional reflectance over discontinuous plant canopies. IEEE Trans. Geosci. Remote Sens. 37, 987–999.

Niu, Z., Liu, Q., Gao, Y., Zhang, Q., Wang, C., 2000. The gap probability model for canopy thermal infrared emission with non-scattering approximation. Sci. China Ser. E Technol. Sci. 43, 83–94.

Njoku, E.G., Li Li, 1999. Retrieval of land surface parameters using passive microwave measurements at 6-18 GHz. IEEE Trans. Geosci. Remote Sens. 37, 79–93. doi:10.1109/36.739125

Norman, J.M., Becker, F., 1995. Terminology in thermal infrared remote sensing of natural surfaces. Agric. For. Meteorol. 77, 153–166.

Otterman, J., Brakke, T.W., Fuchs, M., Lakshmi, V., Cadeddu, M., 1999. Longwave emission from a plant/soil surface as a function of the view direction: Dependence on the canopy architecture. Int. J. Remote Sens. 20, 2195–2201.

Otterman, J., Brakke, T.W., Susskind, J., 1992. A model for inferring canopy and underlying soil temperatures from multi-directional measurements. Boundary-Layer Meteorol. 61, 81–97.

Pampaloni, P., Paloscia, S., 2000. Microwave Radiometry and Remote Sensing of the Earth's Surface and Atmosphere, 1st ed.

Peres, L.F., DaCamara, C.C., 2005. Emissivity maps to retrieve land-surface temperature from MSG/SEVIRI. IEEE Trans. Geosci. Remote Sens. 43, 1834–1844.

Pinheiro, a. C.T., Privette, J.L., Guillevic, P., 2006. Modeling the observed angular anisotropy of land surface temperature in a Savanna. IEEE Trans. Geosci. Remote Sens. 44, 1036–1047.

Pinheiro, a. C.T., Privette, J.L., Mahoney, R., Tucker, C.J., 2004. Directional effects in a daily AVHRR land surface temperature dataset over Africa. IEEE Trans. Geosci. Remote Sens. 42, 1941–1954.

Platnick, S., et. all, 2015. MODIS Atmosphere L3 Daily Product. NASA MODIS Adapt. Process. Syst. Goddard Sp. Flight Center, USA.

Prigent, C., Aires, F., Rossow, W., 2003a. Land surface skin temperatures from a combined analysis of microwave and infrared satellite observations for an all-weather evaluation of the differences between air and skin temperatures. J. Geophys. Res. 108 (D10)

Prigent, C., Aires, F., Rossow, W.B., 2003b. Retrieval of Surface and Atmospheric Geophysical Variables over Snow-Covered Land from Combined Microwave and Infrared Satellite Observations. J. Appl. Meteorol. 42, 368–380.

Prigent, C., Jaumouille, E., Chevallier, F., Aires, F., 2008. A Parameterization of the Microwave Land Surface Emissivity Between 19 and 100 GHz, Anchored to Satellite-Derived Estimates. IEEE Trans. Geosci. Remote Sens. 46, 344–352.

Prigent, C., Papa, F., Aires, F., Jimenez, C., Rossow, W.B., Matthews, E., 2012. Changes in land surface water dynamics since the 1990s and relation to population pressure. Geophys. Res. Lett. 39 (8).

Prigent, C., Rossow, W.B., Matthews, E., Marticorena, B., 1999. Microwave radiometric signatures of different surface types in deserts. J. Geophys. Res. 104, 12147.

Prigent, C., Tegen, I., Aires, F., Marticorena, B., Zribi, M., 2005. Estimation of the aerodynamic roughness length in arid and semi-arid regions over the globe with the ERS scatterometer. J. Geophys. Res. 110

Qian, Y.-G., Li, Z.-L., Nerry, F., 2013. Evaluation of land surface temperature and emissivities retrieved from MSG/SEVIRI data with MODIS land surface temperature and emissivity products. Int. J. Remote Sens. 34, 3140–3152.

Qin, W., Gerstl, S.A.W., 2000. 3-D scene modeling of semidesert vegetation cover and its radiation regime. Remote Sens. Environ. 74, 145–162.

Rahman, H., Pinty, B., Verstraete, M.M., 1993. Coupled surface-atmosphere reflectance (CSAR) model: 2. Semiempirical surface model usable with NOAA advanced very high resolution radiometer data. J. Geophys. Res. 98, 20791.

Rasmussen, M.O., Göttsche, F., Olesen, F., Sandholt, I., 2011. Directional Effects on Land Surface Temperature Estimation From Meteosat Second Generation for Savanna Landscapes. IEEE Trans. Geosci. Remote Sens. 49, 4458–4468.

Rasmussen, M.O., Pinheiro, A.C., Proud, S.R., Sandholt, I., 2010. Modeling Angular Dependences in Land Surface Temperatures From the SEVIRI Instrument Onboard the Geostationary Meteosat Second Generation Satellites. IEEE Trans. Geosci. Remote Sens. 48, 3123–3133.

Ren, H., Yan, G., Chen, L., Li, Z., 2011. Angular effect of MODIS emissivity products and its application to the split-window algorithm. ISPRS J. Photogramm. Remote Sens. 66, 498–507.

Romanov, P., 2016. NOAA NESDIS global automated satellite-based snow mapping system and products, in: SPIE Asia-Pacific Remote Sensing. p. 987712.

Rossow, W.B., Schiffer, R.A., 1999. Advances in Understanding Clouds from ISCCP. Bull. Am. Meteorol. Soc. 80, 2261–2287.

Roujean, J.-L., Leroy, M., Deschamps, P.-Y., 1992. A bidirectional reflectance model of the Earth's surface for the correction of remote sensing data. J. Geophys. Res. 97, 20455.

Roujean J.-L., 2000. A Parametric Hot Spot Model for Optical Remote Sensing Application. Remote Sens. Environ. 71, 197–206.

Schanda, E., 1986. Physical fundamentals of remote sensing, 1st ed. Springer-Verlag Berlin Heidelberg.

Schott, J.R., 2007. Remote sensing: the image chain approach, 2nd editio. ed. Oxford University Press on Demand, New York.

Schroeder, D. V., 2000. An Introduction to Thermal Physics. Addison Wesley.

Seber, G.A., 1984. Multivariate Observations. John Wiley & Sons.

Seemann, S.W., Borbas, E.E., Knuteson, R.O., Stephenson, G.R., Huang, H.-L., 2008. Development of a global infrared land surface emissivity database for application to clear sky sounding retrievals from multispectral satellite radiance measurements. J. Appl. Meteorol. Climatol. 47, 108–123.

Sellers, P.J., Hall, F.G., Asrar, G., Strebel, D.E., Murphy, R.E., 1992. An Overview of the 1st International Satellite Land Surface Climatology Project (ISLSCP) Field Experiment (FIFE). J. Geophys. Res. Atmos. 97, 18345–18371.

Serra, J., 1982. Image Analysis and Mathematical Morphology, Academic Press.

Shcroft, P., Wentz, F.J., 2013. AMSR-E/Aqua L2A Global Swath Spatially-Resampled Brightness Temperatures, version 3.

Smith, J.A., Goltz, S.M., 1994. A thermal exitance and energy balance model for forest canopies. IEEE Trans. Geosci. Remote Sens. 32, 1060–1066.

Snyder, W.C., Zhengming, W., Zhang, Y., Feng, Y.Z., 1997. Thermal infrared (3-14 µm) of bidirectional reflectance measurements of sands and soils. Remote Sens. Environ. 60, 101–109.

Sobrino, J.A., Caselles, V., Becker, F., 1990. Significance of the remotely sensed thermal infrared measurements obtained over a citrus orchard. ISPRS J. Photogramm. Remote Sens. 44, 343–354.

Sobrino, J.A., Cuenca, J., 1999. Angular variation of thermal infrared emissivity for some natural surfaces from experimental measurements. Appl. Opt. 38, 3931–3936.

Sobrino, J.A., Jiménez-Muñoz, J.C., Verhoef, W., 2005. Canopy directional emissivity: Comparison between models. Remote Sens. Environ. 99, 304–314.

Sobrino, J., Caselles, V., 1990. Thermal infrared radiance model for interpreting the directional radiometric temperature of a vegetative surface. Remote Sens. Environ. 33, 193–199.

Steane, A.M., 2016. Thermodynamics: A complete undergraduate course. Oxford University Press.

Strahler, A.H., Jupp, D.L.B., 1990. Modeling bidirectional reflectance of forests and woodlands using boolean models and geometric optics. Remote Sens. Environ. 34, 153–166.

Takala, M., Luojus, K., Pulliainen, J., Derksen, C., Lemmetyinen, J., Kärnä, J.-P., Koskinen, J., Bojkov, B., 2011. Estimating northern hemisphere snow water equivalent for climate research through assimilation of space-borne radiometer data and ground-based measurements. Remote Sens. Environ. 115, 3517–3529.

Thies, B., Bendix, J., 2011. Satellite based remote sensing of weather and climate: Recent achievements and future perspectives. Meteorol. Appl. 18, 262–295.

Townshend, J.R.., Hansen, M.C., Carroll, M., DiMiceli, C., Sohlberg, R., Huang, C., 2011. Vegetation Continuous Fields MOD44B, 2010 Percent Tree Cover. Collect. 5, Univ. Maryland, Coll. Park. Maryl. 1–12.

Trigo, I.F., Boussetta, S., Viterbo, P., Balsamo, G., Beljaars, A., Sandu, I., 2015. Comparison of model land skin temperature with remotely sensed estimates and assessment of surface-atmosphere coupling. J. Geophys. Res. Atmos. 120, 12096–12111.

Trigo, I.F., Dacamara, C.C., Viterbo, P., Roujean, J.-L., Olesen, F., Barroso, C., Camacho-de-Coca, F., Carrer, D., Freitas, S.C., García-Haro, J., Geiger, B., Gellens-Meulenberghs, F., Ghilain, N., Meliá, J., Pessanha, L., Siljamo, N., Arboleda, A., 2011. The Satellite Application Facility for Land Surface Analysis. Int. J. Remote Sens. 32, 2725–2744.

Trigo, I.F., Monteiro, I.T., Olesen, F., Kabsch, E., 2008a. An assessment of remotely sensed land surface temperature. J. Geophys. Res. 113, 1–12.

Trigo, I.F., Peres, L.F., Dacamara, C.C., Freitas, S.C., 2008b. Thermal land surface emissivity retrieved from SEVIRI/Meteosat. IEEE Trans. Geosci. Remote Sens. 46, 307–315.

Trigo, R.M., Añel, J.A., Barriopedro, D., García-Herrera, R., Gimeno, L., Nieto, R., Castillo, R., Allen, M.R., Massey, N., 2013. The record winter drought of 2011-12 in the Iberian peninsula. Bull. Am. Meteorol. Soc.

Ulaby, F.T., Moore, R.K., Fung, A.K., 1986. Microwave remote sensing: Active and passive. Volume 3 - From theory to applications, Microwave Remote Sensing Active and Passive.

Ulaby, F.T., Moore, R.K., Fung, A.K., 1981. Microwave remote sensing: Active and passive. Volume 1 - Microwave remote sensing fundamentals and radiometry, Microwave Remote Sensing Active and Passive.

Vinnikov, K.Y., Yu, Y., Goldberg, M.D., Tarpley, D., Romanov, P., Laszlo, I., Chen, M., 2012. Angular anisotropy of satellite observations of land surface temperature. Geophys. Res. Lett. 39, L23802.

Wan, Z., 2014. New refinements and validation of the collection-6 MODIS land-surface temperature/emissivity product. Remote Sens. Environ. 140, 36–45.

Wan, Z., Dozier, J., 1996. A generalized split-window algorithm for retrieving land-surface temperature from space. Geosci. Remote Sensing, IEEE Trans. 34, 892–905.

Wan, Z., Li, Z. -L., 2008. Radiance-based validation of the V5 MODIS land-surface temperature product. Int. J. Remote Sens. 29, 5373–5395.

Wan, Z., Zhang, Y., Zhang, Q., Li, Z., 2002. Validation of the land-surface temperature products retrieved from Terra Moderate Resolution Imaging Spectroradiometer data. Remote Sens. Environ. 83, 163–180.

Wang, A., Barlage, M., Zeng, X., Draper, C.S., 2014. Comparison of land skin temperature from a land model, remote sensing, and in situ measurement. J. Geophys. Res. Atmos. 119, 3093–3106.

Wanner, W., Li, X., Strahler, A.H., 1995. On the derivation of kernels for kernel-driven models of bidirectional reflectance. J. Geophys. Res. 100, 21077.

Wen, J., Su, Z., Ma, Y., 2003. Determination of land surface temperature and soil moisture from Tropical Rainfall Measuring Mission/Microwave Imager remote sensing data. J. Geophys. Res. 108, 4038.

Weng, F., Grody, N.C., 1998. Physical retrieval of land surface temperature using the special sensor microwave imager. J. Geophys. Res. Atmos. 103, 8839–8848.

Weng, Q., 2009. Thermal infrared remote sensing for urban climate and environmental studies: Methods, applications, and trends. ISPRS J. Photogramm. Remote Sens. 64, 335–344.

Yan, G., Jiang, L., Wang, J., Chen, L., Li, X., 2003. Thermal bidirectional gap probability model for row crop canopies and validation. Sci. China Ser. D Earth Sci. 46, 1241–1249.

Yang, J., Gong, P., Fu, R., Zhang, M., Chen, J., Liang, S., Xu, B., Shi, J., Dickinson, R., 2013. The role of satellite remote sensing in climate change studies. Nat. Clim. Chang. 3, 875–883.